UNIVERSIDAD DE CASTILLA-LA MANCHA

Instituto de Nanociencia, Nanotecnología y Materiales Moleculares (INAMOL)

Departamento de Química Inorgánica, Orgánica y Bioquímica

Facultad de Ciencias Ambientales y Bioquímica

NOVEL PORPHYRINS FOR DSSC AND BHJ SOLAR CELLS

Memoria que presenta:
Marlene Susana Arrechea Alvarado

Dirigida por:
Fernando Langa de la Puente y Ana Isabel Aljarilla Jiménez

Toledo, octubre de 2015

UNIVERSIDAD DE CASTILLA-LA MANCHA

Instituto de Nanociencia, Nanotecnología y Materiales Moleculares (INAMOL)

Departamento de Química Inorgánica, Orgánica y Bioquímica

Facultad de Ciencias Ambientales y Bioquímica

NOVEL PORPHYRINS FOR DSSC AND BHJ SOLAR CELLS

Memoria que presenta Marlene Susana Arrechea Alvarado para optar al Doctorado en Nanociencia y Nanotecnología por la Universidad de Castilla La Mancha

Toledo, octubre de 2015

El trabajo descrito en esta Tesis Doctoral del programa de Doctorado en Nanociencia y Nanotecnología (Verificado según R.D. 99/2011), ha sido realizado en el laboratorio de Materiales Moleculares del Instituto de Nanociencia, Nanotecnología y Materiales Moleculares de la Universidad de Castilla-La Mancha, bajo la dirección del Dr. Fernando Langa de la Puente y la Dra. Ana Isabel Aljarilla Jiménez quienes autorizan el presente trabajo para su presentación y defensa.

En Toledo, octubre de 2015

Marlene Susana Arrechea Alvarado

NOMBRE LANGA DE LA PUENTE FERNANDO - NIF 01801922X

Firmado digitalmente por NOMBRE LANGA DE LA PUENTE FERNANDO - NIF 01801922X
Nombre de reconocimiento (DN): c=ES, o=FNMT, ou=FNMT Clase 2 CA, ou=500880177, cn=NOMBRE LANGA DE LA PUENTE FERNANDO - NIF 01801922X
Fecha: 2015.11.26 17:16:09 +01'00'

Prof. Fernando Langa de la Puente
Director

Dra. Ana Isabel Aljarilla Jimenez
Co-Director

Agradecimientos a:

Fernando Langa y Ana Aljarilla: Por su trabajo como directores para la realización de esta tesis.

Profesor Dr. Luis Echegoyen, Departament of Chemistry, University of Texas at El Paso (UTEP), USA: Por su valiosa colaboración en las medidas de las propiedades fotovoltaicas de los dispositivos **SA1**-**SA4**.

Profesor Emilio Palomares y equipo de trabajo, Institute of Chemical Research of Catalonia (ICIQ), Tarragona, España: Por su valiosa colaboración y medidas de todas las propiedades fotovoltaicas de los dispositivos **SA5-18** y por haberme permitido realizar una estancia corta de investigación en ICIQ.

A Fundación Carolina, Universidad de San Carlos de Guatemala (USAC) y Universidad de Castilla-La Mancha (UCLM): Por la beca que me otorgaron y que me permitió realizar esta tesis doctoral.

PUBLICATIONS:

To date, the results reported in this thesis have been published in the following journals:

1. Effect of porphyrin loading on Dye Sensitized Solar Cell performance based on iodide/tri-iodide and cobalt electrolytes
   Aljarilla, A.; Clifford, J. N.; Pelleja, L.; Moncho, A.; Arrechea, S.; de la Cruz, P.; Langa, F.; Palomares, E. *J. Mat. Chem. A.* **2013**, *1*, 13640.

2. New Acceptor-π-Porphyrin-π-Acceptor Systems for Solution-Processed Small Molecule Organic Solar Cells
   Arrechea, S.; Molina-Ontoria, A.; Aljarilla, A.; de la Cruz, P.; Langa, F.; Echegoyen, L. *Dyes Pigm.* **2015**, *121*, 109.

3. Charge Recombination Losses in Thiophene-Substituted Porphyrin Dye-Sensitized Solar Cells.
   Arrechea, S.; Clifford, J. N.; Pelleja, L.; Aljarilla, A.; de la Cruz, P.; Palomares, E.; Langa, F. *Dyes Pigm.* Manuscript Number: DYPI-D-15-00841R1, 2016 (manuscript in press).

Manuscript in preparation

1. Porphyrin systems for Solution-Processed Small Molecule Organic Solar Cells
   Arrechea, S.; Molina-Ontoria, A.; Montcada, N. F.; Aljarilla, A.; de la Cruz, P.; Palomares, E.; Echegoyen, L.; Langa, F.

Other publications

To date, the results not included in this thesis have been published in the following journals:

1. Push-Pull cromophores based on triphenylamine as photosensitizers and electron donors for molecular solar cells
   Aljarilla, A.; Herrero-Ponce, P.; Atienzar, P.; Arrechea, S.; de la Cruz, P.; L.; Langa, F.; García, H. *Tetrahedron.* **2013**, *69*, 6875.

Abbreviation list

δ	Chemical shift
λ	Wavelength
ε	Molar extinction coefficient
^{13}C-NMR	Nuclear Magnetic Resonance carbon-13
^{1}H-NMR	Nuclear Magnetic Resonance proton
ATR	Attenuated total reflectance
CV	Cyclic Voltammetry
d	Doublet
dd	Doublet of doublets
DSSC	Dye-sensitized solar cell
DMF	N,N-Dimethylformamide
Et al	and others
eV	Electronvolt
FF	Fill factor
FT-IR	Fourier transform infrared spectrometry
HOMO	Highest occupied molecular orbital
Hz	Hertz
IPCE	Incident photon to current efficiency
J	Coupling constant
J_{sc}	Short circuit current
LUMO	Lowest unoccupied molecular orbital
NMR	Nuclear Magnetic Resonance
NBS	N-bromosuccinimide
*n*TV	Oligothienylenevynilene)
OSWV	Oyster-Young square-wave voltammetry
ppm	Parts per million
s	Singlet
t	Triplet
THF	Tetrahydrofurane
TMEDA	N,N,N,N-Tetramethyl ethylene diamine
UV-Vis	Ultraviolet-Visible spectroscopy
V_{oc}	Open circuit voltage

Molecules abbreviation list

Molecules synthetized in this thesis were named with the following abbreviation:

Chapter 1. *p*-Semiconductor

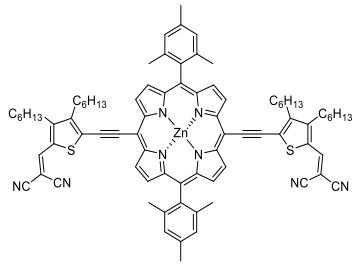

SA1

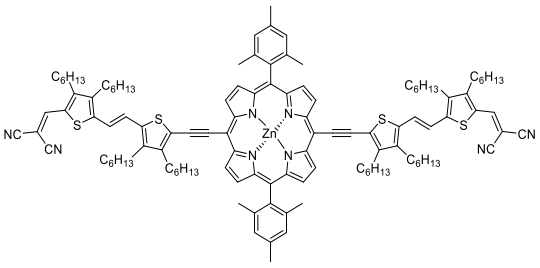

SA2

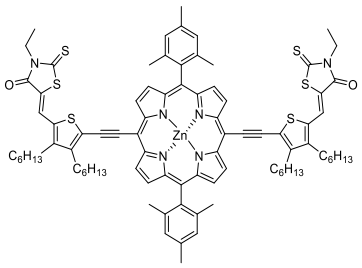

SA3

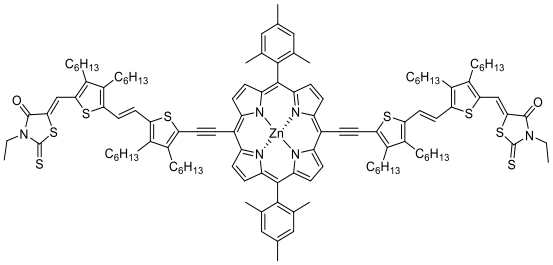

SA4

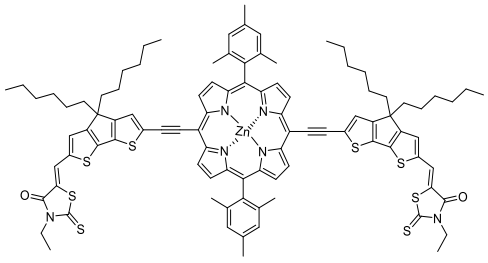

SA5

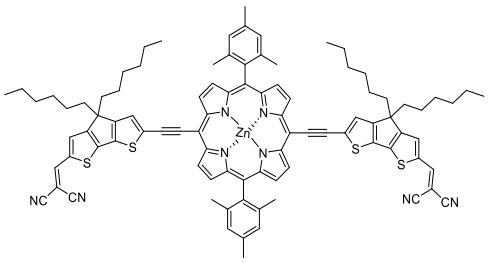

SA6

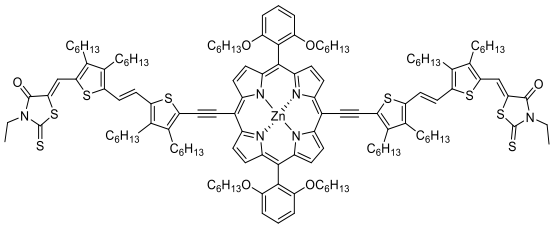

SA7

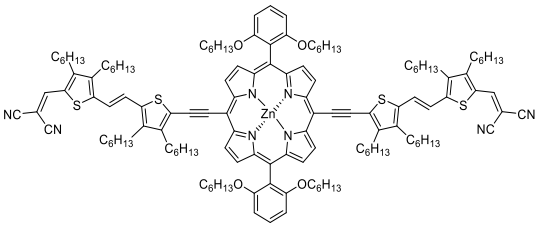

SA8

Chapter 1. Connectors

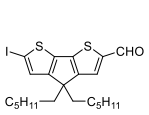

C1

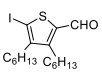

C2

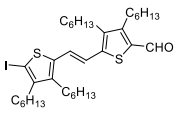

C3

Chapter 1. *p*-Semiconductors

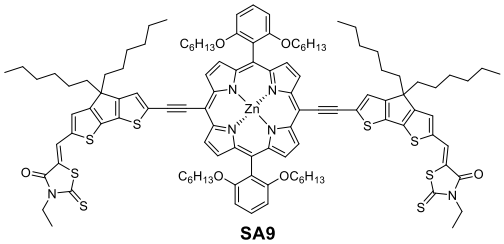

SA9

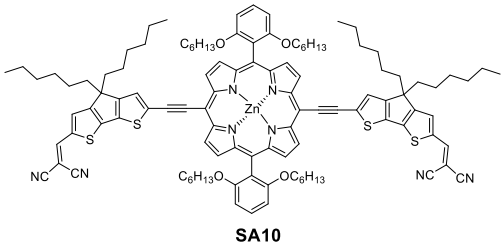

SA10

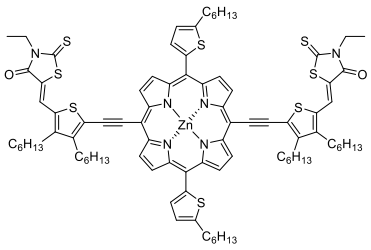

SA11

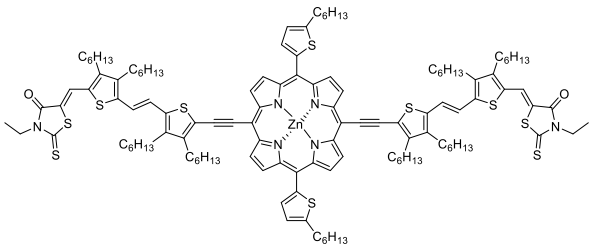

SA12

Chapter 1. Porphyrin cores

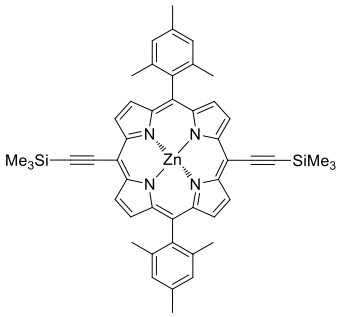

P1

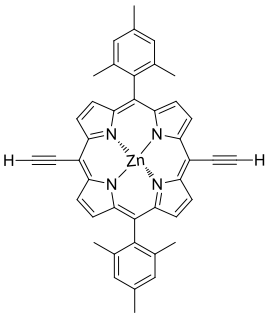

P1S

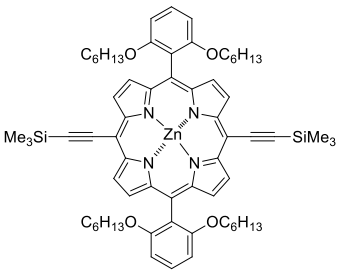

P2

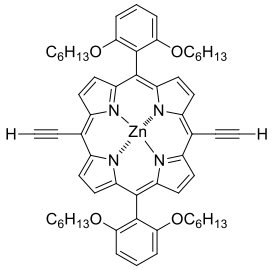

P2S

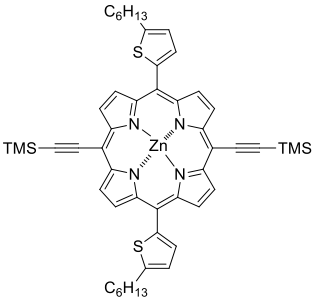

P3

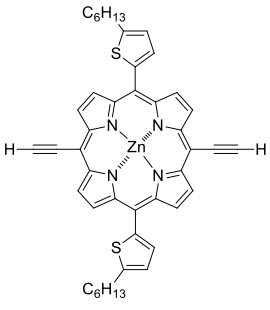

P3S

Chapter 1. Precursor porphyrin aldehydes

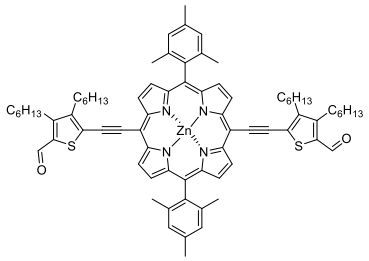

A1

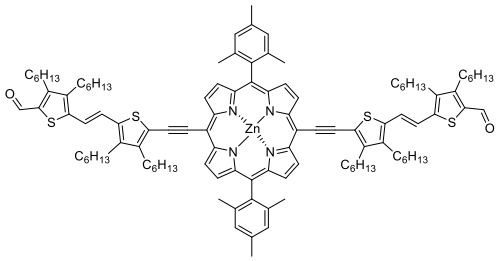

A2

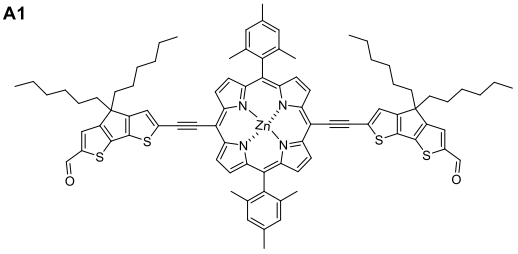

A3

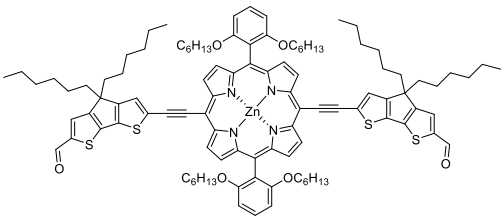

A4

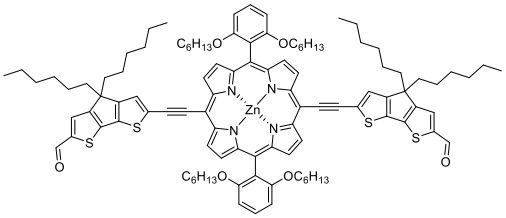

A5

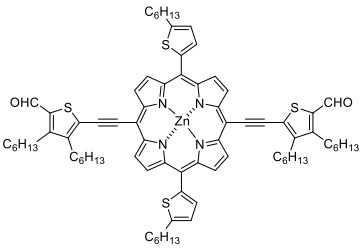

A6

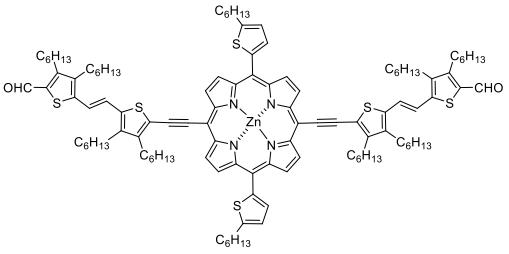

A7

Chapter 2. Dyes

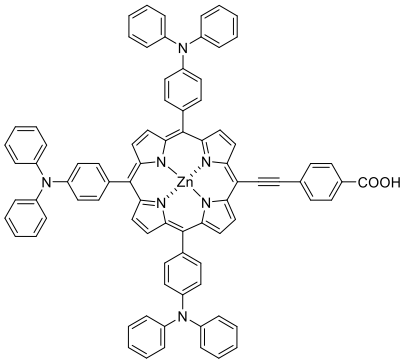

SA13

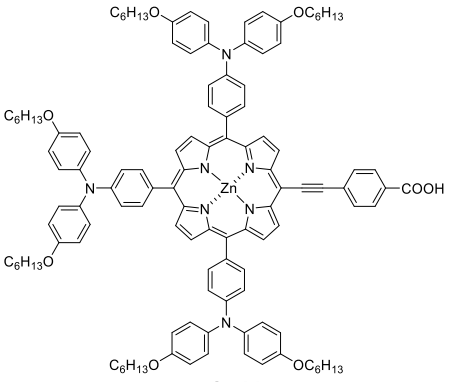

SA14

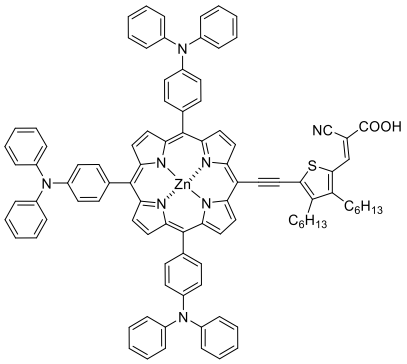

SA15

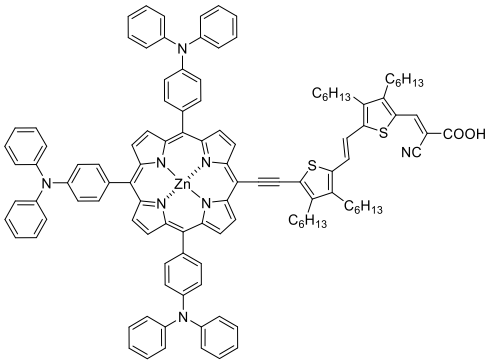

SA16

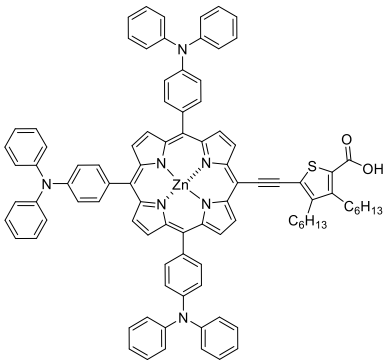

SA17

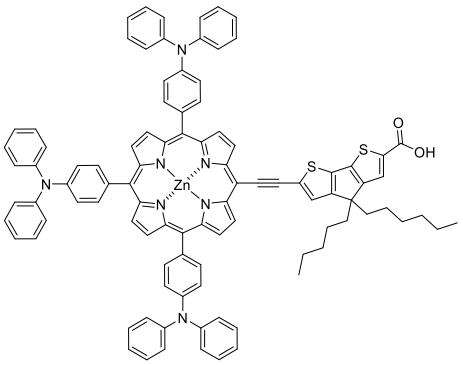

SA18

Chapter 2. Porphyrin core

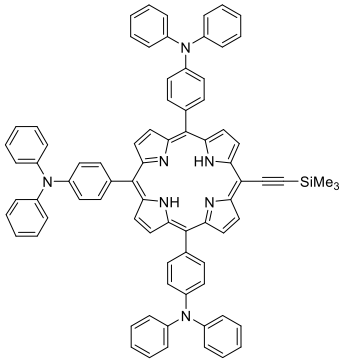

P4

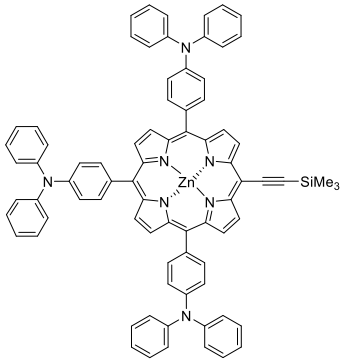

P4S

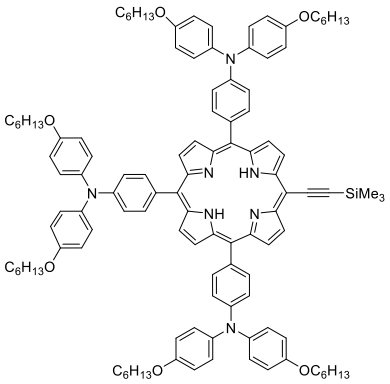

P5

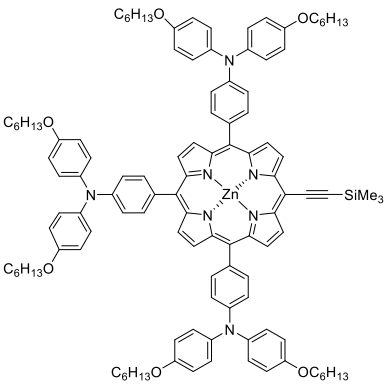

P5S

Chapter 2. Aldehydes

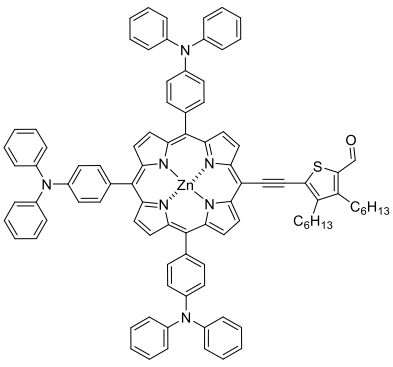

A8

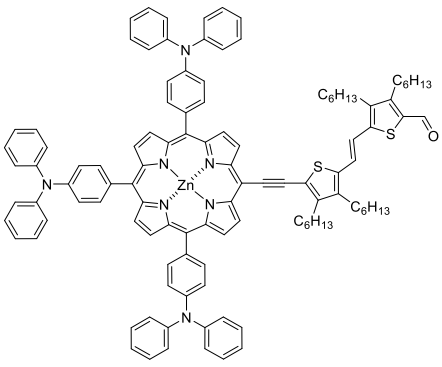

A9

Abstract

The global challenge of sustainable development, clean energy and climate change needs to be pursued by development of energy technologies. Moreover the energy sector is responsible of two thirds of the world's greenhouse-gas (GHG) emissions; therefore the world needs to change the inefficient energy system based on fossil fuels to renewable sources as sunlight, wind, rain, waves, tides, biomass and geothermal heat. Moreover, solar energy is available throughout the world as radiant light or heat from the sun, using technology such as photovoltaics devices. New generation of photovoltaics can provide an alternative and complementary approach for the exploitation of solar energy; offers low manufacture cost, they are flexible, light, and more environmental friendly; the most promising for their remarkable progress are: organic solar cells, hybrid dye sensitized solar cells, and perovskite solar cells. Nevertheless, in this thesis the first two types of cells will be widely described focusing on devices comprising porphyrins, these molecules have been explored due to their robustness, thermal stability, rich metal coordination chemistry, strong aromaticity, optical, electronic and magnetic properties.

In the first chapter twelve novel symmetrical small molecules based on porphyrins, with configuration A-π-D-π-A, were synthesized and characterized to be applied in solution processed Bulk Heterojunction Solar Cells (BHJSC). Zinc porphyrin core (D) and π conjugated linker were separated by an ethynyl group, to improve the planarity and enhance the π conjugation of the system. Furthermore, each molecule comprise two strong π electron withdrawing moieties (A) to control the absorption spectrum in the near infrared region, by a conjugation with electron rich aromatic units. In order to study, all molecules were synthesized and properly characterized, photophysical and electrochemical properties were measured, and theoretical HOMO-LUMO orbitals and optimized geometries were calculated. Additionally, to complete these studies, devices were prepared and their performance was evaluated; the best PCE (4.24%) was achieved with $PC_{71}BM$:**SA4** (4:1 *w/w*) (comprising a mesityl zinc porphyrin core, *(E)*-1,2-bis(3,4-dihexylthiophen-2-yl)ethylene as π conjugated linker and 3-ethylrhodanine as acceptor), with a high short circuit current of 13.2 $mAcm^{-2}$.

In the second chapter six novel dyes bearing triphenylamine substituted porphyrins, A_3B, were synthesized and characterized by spectroscopic techniques. The optical and electrochemical properties were investigated to determine the electronic features of these compounds. Moreover these molecules were employed as sensitizers in Dye Sensitized Solar Cells (DSSCs) hybrid devices with nanocrystalline TiO_2, and their efficiencies were measured in. The best PCE (6.0%) was achieved for **SA15** employing one thiophene ring connected between the conjugated porphyrin core and the anchoring cyanoacrylate group.

Novel designs of porphyrin and improvements in photovoltaic devices can be achieved. Therefore, there is still much work to be done to improve solar cells for commercial applications

INTRODUCTION

Solar cells, background

Energy, a global challenge

The global challenge of sustainable development, clean energy and climate change needs to be pursued by development of energy technologies. The report of the Intergovernmental Panel on Climate Change (IPCC) 2014, informed that scientist were more than 95% certain that the most of the global warming is caused by increasing concentration of the greenhouse-gas (GHG, carbon dioxide, methane, nitrous oxide, fluorinated gases) and other anthropogenic activities. Figure 1 shows global emissions of GHG in 2012 provided by the World Resources Institute (WRI).[1]

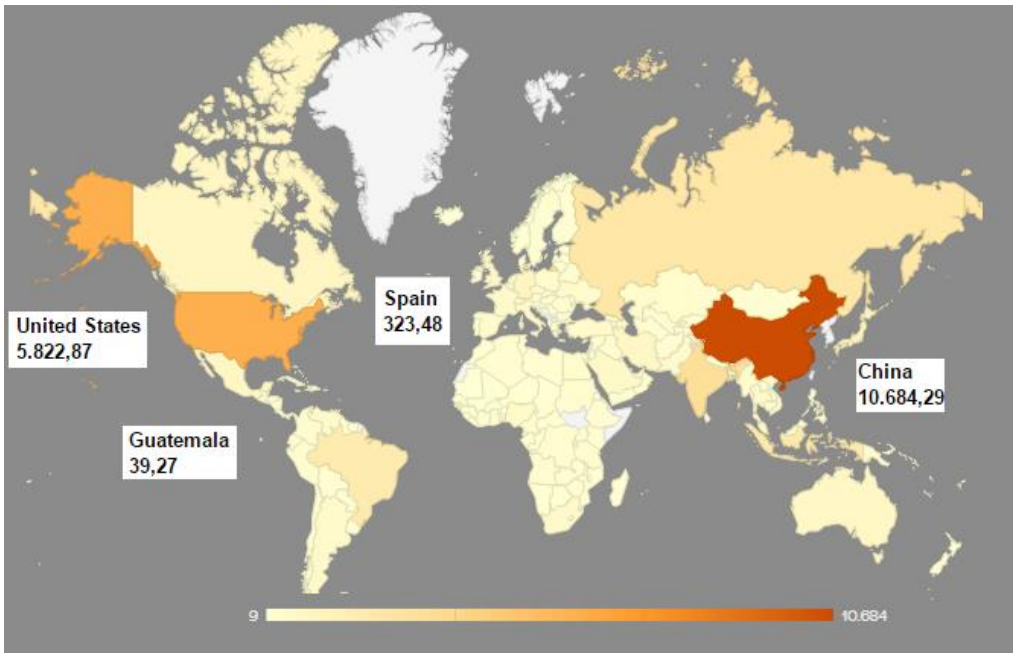

Figure 1. GHG emission in 2012[1]

The energy sector is responsible of two thirds of the world's GHG emissions.[2] Since 1995 to 2012 the concentration of GHG emissions have raised to 435 ppm CO_2 eq. and these gases have increased more than one quarter[3] (Figure 2).

The BP energy outlook 2035 in the edition 2015 described the energy landscape and the projection to the next 20 years: according to this publication, fossil fuel lose share by 2035 but remain the dominant form of energy, with 25-26%, and renewables including biofuels, gain share, from around 3% in 2015 to 8% in 2035[4] (Figure 3).

The world needs to change the inefficient energy system based on fossil fuels to renewable sources as sunlight, wind, rain, waves, tides, biomass and geothermal heat. The renewable energy directive of the European Commission sets rules for 20% renewables target by 2020 to ensure secure, affordable and climate friendly energy.[5]

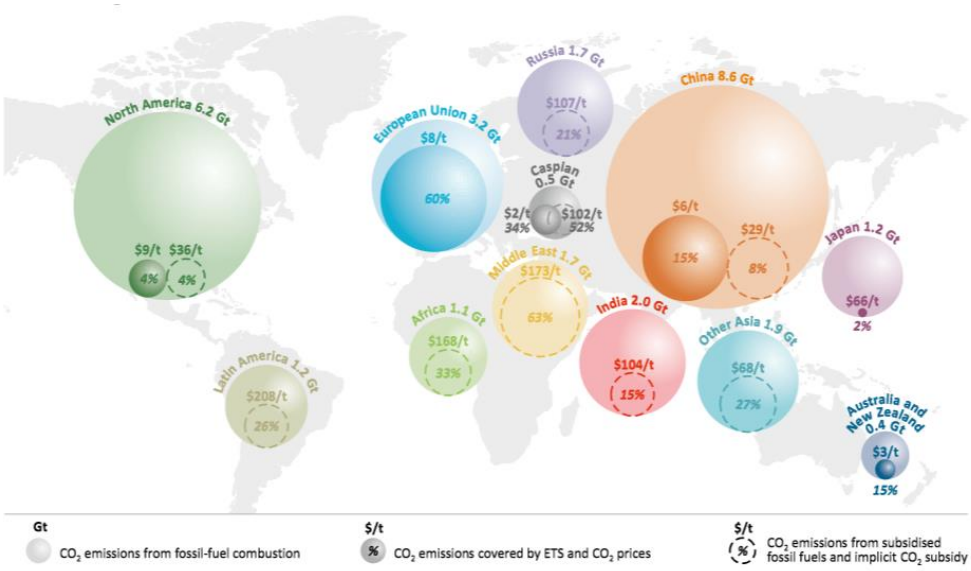

Figure 2. Energy CO_2 emissions in selected regions[2]

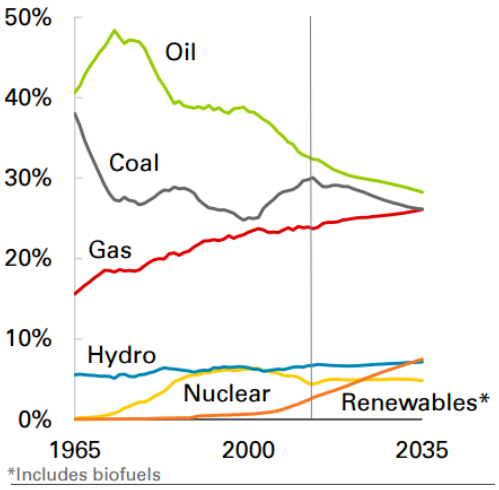

Figure 3. Graph of energy landscape (BP energy outlook 2035)[4]

Solar energy, a good and abundant choice

Solar energy is available throughout the world as radiant light or heat from the sun, using technology such as photovoltaics, solar architecture, artificial photosynthesis, solar thermal power, solar heating and concentrated solar power.[6] The average intensity of total solar irradiance deposits on the surface of the Earth is 1362 watt/m^2 according to the last NASA satellite missions.[7] This value is higher than the actual demand and makes the sun energy the most abundant resource on earth.

The International Energy Agency (IEA) reported on September 2014, that the sun could be the largest source of electricity by 2050. According to the roadmaps, 16% of electrical energy generated by photovoltaics, and 11% generated by concentrating solar power plants, preventing the emission of more than 6 billion tons of carbon dioxide per year.[8]

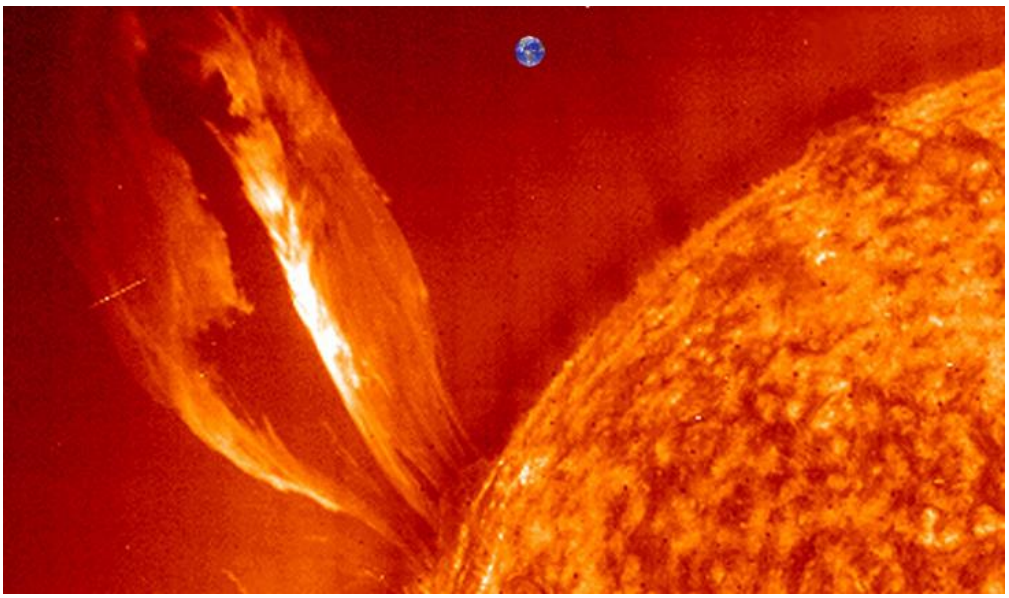

Figure 4. Approximate size of Earth compared to the Sun (Earth shown for size comparison), credit ESA and NASA[9]

Photovoltaics, source of electricity

Photovoltaic cells are electronics devices that converting solar energy directly into electricity by photovoltaic effect, enabling photons to “extract” the electrons out of a molecular lattice, leaving a free electron and a “hole” pair which diffuse into an electric field to separate contacts, generating direct current (DC) electricity. This technology does not emit greenhouse gases (GHG) or pollutants during operation.

Edmund Bequerel discovered the photovoltaic effect in 1839, when he observed that platinum covered with silver bromide or silver chloride electrodes illuminated in aqueous solution produced a photocurrent.[10] In 1905, Einstein described the nature of light and the photoelectric effect on which photovoltaic technology is based.[11] However, the first silicon solar cell was introduced in 1953 by Bell Laboratories,[12] from this research until now the innovation on this technology have been developed.

The operation of photovoltaics requires three basic steps for generation of electrical power via the absorption of incident sunlight:[13]

1. Absorption of photons by the photoactive material, generating electron and hole pairs (excitons).

2. Photoinduced charge separation and the generation of mobile carriers.

3. Collection of electrons at one electrode and holes at the opposite electrode (separation and extraction of carriers to an external circuit).

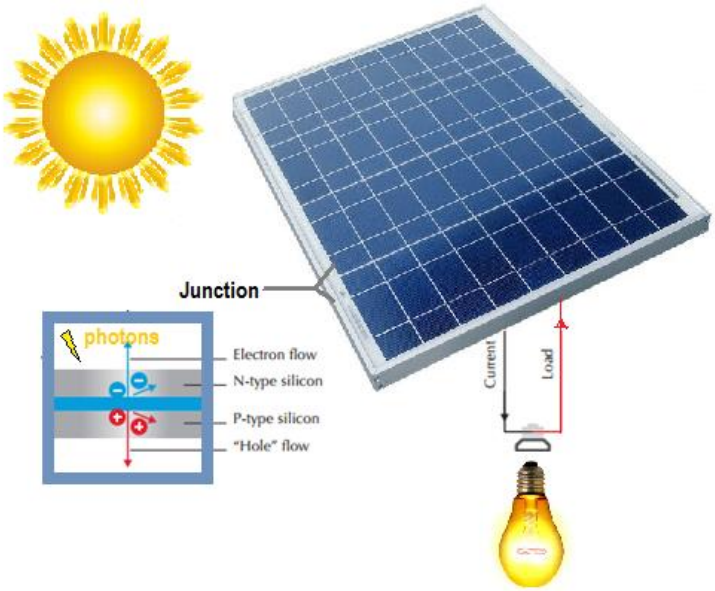

Figure 5. Solar cell and the photovoltaic effect

Solar photovoltaic cells are commercially available with a significant potential for growth. In the last years the photovoltaic capacity has increased to 150 gigawatts (GW). Since early 2014, the Republic of China has led the global market followed by Japan and the United States (Figure 6).[14]

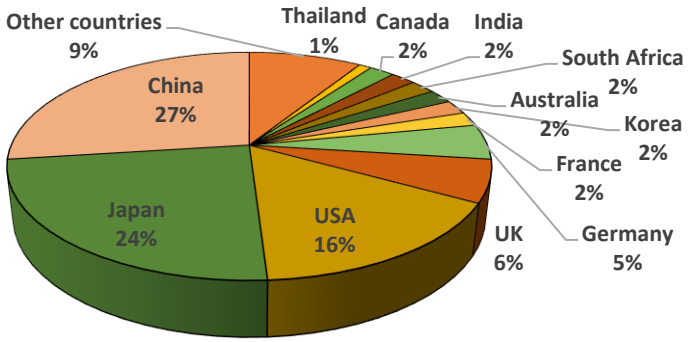

Figure 6. Global PV market in 2014[15]

Figure 7. Photograph of a photovoltaic device installed in a Guatemalan's house

The National Renewable Energy Laboratory (NREL) presents a graphic of highest confirmed conversion efficiencies for research cells from 1976 to 2015 (Figure 8). The best efficiency is around 46% by the multi-junction cells (four junctions or more concentrator), these devices can achieve a higher total conversion efficiency because they can convert more of the energy spectrum of light to electricity, using more than one band gap and more than one junction, to generate a voltage but these cells are expensive and their application is preferred in space applications.

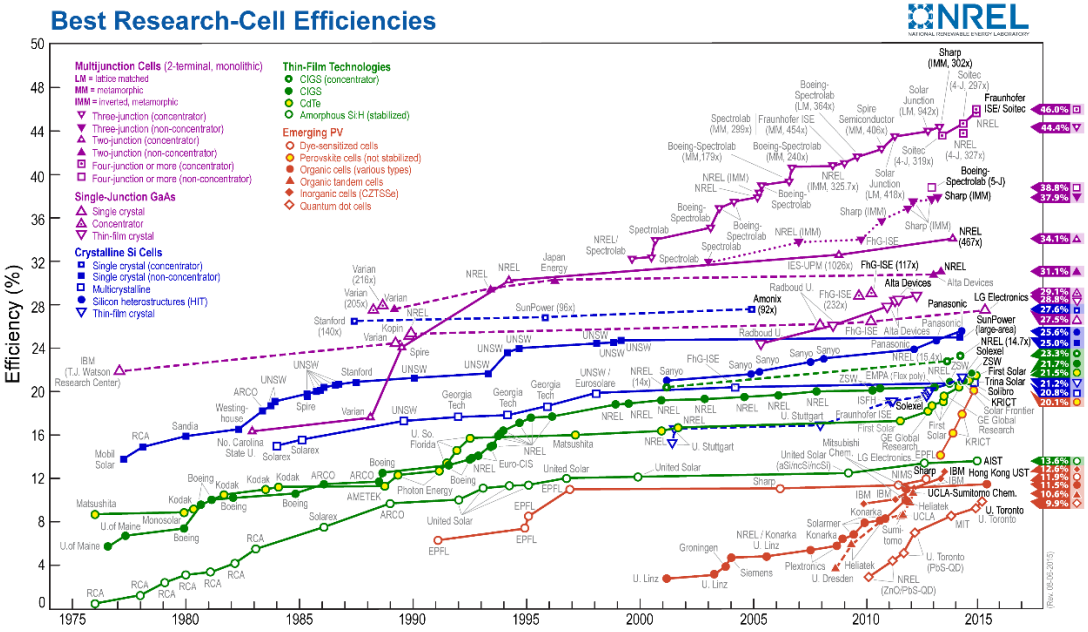

Figure 8. Best Research photovoltaic cells efficiencies[16]

The silicon dioxide panels have good efficiencies but are expensive and not environmental friendly; its construction involves some risks due to the quartz extracted from mines and then refined into elemental silicon, putting the miners in risk of lung disease silicosis. The process to turning metallurgical grade silicon into a purer form called polysilicon generates the toxic silicon tetrachloride. The thin film devices are usually made of cadmium, a heavy metal known to be carcinogenic and genotoxic.

The emerging solar cells have lower efficiencies but they have some advantage (cost, flexibility, lightness) in comparison to silicon photovoltaics. [17] Figure 8 shows the improvement of the efficiency in the last 24 years.

Emerging photovoltaic technologies

New generation of photovoltaics have been researched in the last years, the most promising for their remarkable progress are organic solar cells, hybrid dye sensitized solar cells, and perovskite solar cells.[18] In the next section, the first two will be widely described.

The emerging solar cells can provide an alternative and complementary approach for the exploitation of solar energy; offers low manufacture cost, they are flexible, light, and more environmental friendly. Organic semiconductors are a less expensive alternative to inorganic semiconductors like Si. In addition, organic molecules can be processed by techniques not available for crystalline inorganic semiconductors.[17]

Porphyrins, interesting molecules for solar cells

The term "porphyrin" comes from the Greek prophyros and means purple.[19] These molecules play a very important role in the metabolism of living organism: the chlorophylls of chloroplasts drive the photosynthesis allowing the plants and other organisms to convert light energy into chemical energy that can be released to fuel the organisms' activities. Other significant porphyrin is the Heme as a component of hemoglobin that transports oxygen to animal tissues and as the central unit of myoglobin ensuring the storage of oxygen.[20]

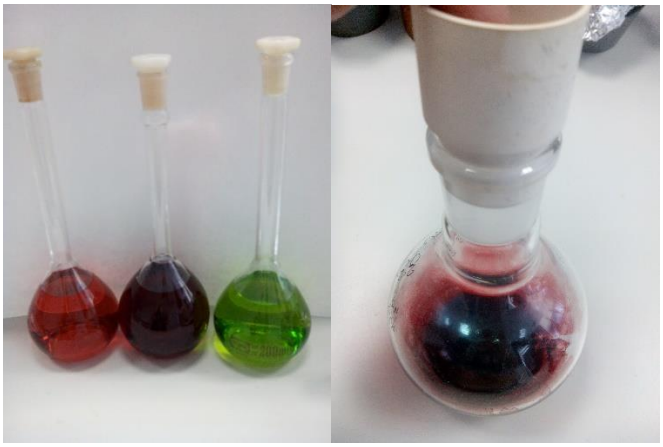

Figure 9. Three different porphyrins in solution in CH_2Cl_2 (left) and solid functionalized porphyrin (right)

Porphyrins have been explored in different disciplines due to their structural robustness, thermal stability, rich metal coordination chemistry, strong aromaticity, emission, electronic and magnetic properties. The structure of a porphyrin is a macrocycle that consist in four pyrroles and four methine carbons, having 18 π-electron being aromatic (Figure 10).

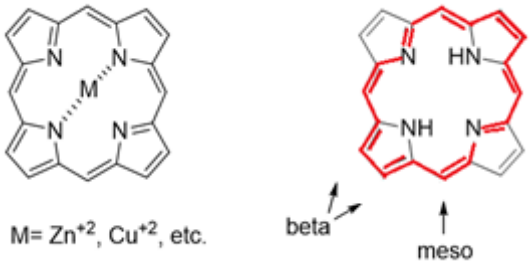

Figure 10. Porphyrin structure

The NH protons inside the ring of porphyrins possess acidic character and hence can be deprotonated yielding porphyrinato ions. These dianion species, with their electronically sensitive planar framework and central cavity with more or less rigid size, exhibit remarkable ligation characteristic towards metal ions. A crucial factor to form stable metalloporphyrins seems to be the compatibility of porphyrin ring size with the ionic radical of the metal cations. Stable complexes result when these two sizes match while their instability tends to increase when the size of the cation is too big or too small with very few exceptions. The minimum coordination number of the metal ion possible in metalloporphyrin is four, and the dianion porphyrinato is ideally suited to act as a tetradenate ligand with metal ions.[21]

Synthesis of the porphyrin macrocycle is not easy; in 1986 Lindsey described a method of synthesis of meso-substituted porphyrins in gram scale by reaction of pyrrole with the corresponding aldehyde under acid catalysis and an oxidizing agent. It is important to control the concentration of reagents to find a balance between porphyrin formation and possible products of polymerization of pyrrole with the aldehyde to give high molecular weight polymers. Different methods of synthesis of both symmetric and asymmetric substituted porphyrins in the meso positions have been described.[22]

Porphyrins show strong visible light absorption bands due to the π-π^* electron transition of the macrocycle. The UV-Vis absorption spectrum of porphyrin exhibits characteristic Soret and Q bands. Optical transitions from the closely spaced HOMO and HOMO+1 to the LUMO, interact strongly to generate a high energy S_2 excited state with a large oscillator strength in the blue of the visible spectrum (Soret band) located between 390 and 430 nm. A lower energy S_1 excited state with diminished oscillator strength in the red of the spectrum (Q band) around 480 and 700 nm.[23] The Q bands are consequent to the vibronic transitions to S_1 excited state.[24] The electrons of the central substituents has a lower impact in the optical Q absorptions, and the spectra of free-base porphyrins changes from four banded to a two banded spectrum after the metalation, due to the symmetry of the free-base porphyrin.[25]

The photoluminescence spectra of the porphyrins displays small Stokes shifts (difference between position of the maxima absorption band and emission spectra being of the same electronic transition).[26,27] Two peaks appear due to the transition from the S_1 state back to different vibronic levels of S_o ground state. Zinc porphyrins show dual fluorescence, the emission of S_2 and S_1 due to the large energy gap between both excited states, causes slow internal conversion. For metalloporphyrins the single excited state lifetimes are near to 1 ps from the S_2 and ~2 ns from S_1.[28,29] The fluorescence bands for metalloporphyrin are around 600 nm and the phosphorescence bands are near 700 nm.

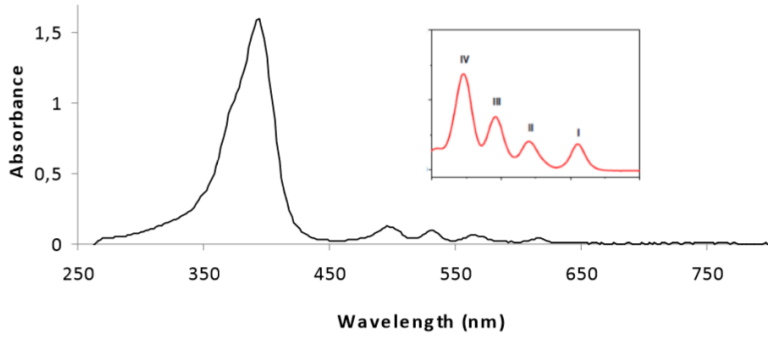

Figure 11. Characteristic absorption bands of porphyrins

Recently, the application of this type of molecules in photovoltaics has received great attention,[30] due to the high absorptivity (extinction coefficient ε > 10^4 $M^{-1}cm^{-1}$) over the spectral range corresponding to the solar irradiance spectrum at the earth's surface. The solar irradiance spectrum air mass (AM) 1.5, is the most intense measure of the sun's energy to reach earth's surface (>0.75 $W \cdot m^{-2}nm^{-1}$) between 375 and 900 nm. Porphyrins containing redox inactive metals usually shows two one electron oxidation and two one electron processes reductions (reversible).[31] Porphyrins donate electrons to the acceptor as consequence of the absorbing sunlight and to the low first oxidation potential, donating electrons to the acceptor group.

Oligothienylenevinylenes (*n*TVs) as π conjugated linkers

The unique electronic properties of linear π-conjugated systems (conjugated polymers and oligomers) originated from the delocalization of π-electrons over a number of recurrent monomer units, allowing their application as advanced materials in electronic and photonic areas.[32]

The oligothienylenevinylenes (*n*TV's) belong to the second generation of conjugated oligomers and have been studied as linkers between electroactive moieties,[33] due to their stability and their high electron delocalization, working as rigid wire to provide a stable distance and reproducible behavior between the donor and the acceptor groups or anchoring group.[34]

These electron-rich molecules are formed by repetitive number of monomer units and based on an aromatic structure of thiophenes linked through positions 2 and 5 by vinylene fragments (Figure 12), β positions, 3 and 4, may remain free or can be used to modify its physical properties. Adding alkyl chains to the β position of *n*TVs increase their solubility and produce a bathochromic effect.

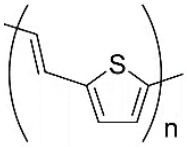

Figure 12. *n*TV's structure

The planarity of oligothienylenevinylenes causes further electron delocalization and a decrease in the energetic HOMO-LUMO difference.[35] The presence of double bonds of the configuration produces at the same time a decrease of the overall aromatic character of the linear conjugated system and hence of π-electron localization and the suppression of the rotational disorder.[32]

New oligormers and co-oligormers based in thiophene have been studied at the Institute of Nanoscience, Nanotechnology and Molecular Materiales (INAMOL), UCLM. Novel synthetic procedures that allow the achievement of lengths of oligomers near to the effective conjugation length and their electronic and optical properties have been studied in a wide number of Donor-Bridge-Acceptor, Donor-Bridge-Donor and Acceptor-Bridge-Acceptor systems. The effect of the introduction of vinylenes or ethynylene linkers between monomers is also taken into account. The performance of the bridges is addressed by the functionalization of the edges with electron donors or electron acceptors, to study the delocalization of charges through the bridges. The photophysical studies of oligomers and co-oligomes acting as bridges are elucidated in collaboration with other international research groups related with the field of nanoscience and nanotechnology, the next paragraphs include some of the most relevant studies.

A set of novel oligo-thienylenevinylene organic molecules have been synthesized and characterized for use as electron donor moieties in bulk-heterojunction solution-processed organic solar cells combined with $PC_{71}BM$ as an electron acceptor[36]. The results show a broad range of solar-to-electrical conversion efficiencies, with values up to 4.9% achieved, although it was demonstrated that all device performances were mainly limited by lower mobility, which limited the fabrication of the solar cells to very thin active layers. An increase in the number of thiophene units and the use of alkyl chains broaden the absorption spectra to the red region and allow higher FF, nevertheless an increase in charge recombination was also observed in these cases.

Molecular architectures formed by zinc porphyrins (ZnP), and fullerenes linked by various bridging groups have been the subject of numerous studies in recent years. Although C_{60}–*n*TV dyads have been investigated in which *n*TVs act as electron donors. The small damping factor (β=0.016) for the charge separation via ZnP suggests the high effectiveness

of *n*TV as molecular wire.[37] Novel donor–bridge–acceptor arrays covalently connected by oligo(thienylenevinylene) (*n*TV) molecular wires (*n* = 3 and 8), show the influence of the *n*TV-length on the electrochemical and electronic properties of the ZnP–*n*TV–C_{60} triads. The fluorescence measurements on the intensity quenching and lifetime shortening have been revealed through the direct communication between the excited state of ZnP and remote C_{60} over the *n*TV bridge.[38]

New dyes based on conjugated thienylenevinylene units and electron-donating triphenylamine unit (TPA) have been synthesized and used as efficient light-harvesting materials in molecular photovoltaic devices. These dyes show efficient electron injection into the TiO_2 conduction band and slow back electron transfer to the oxidized dye.[34b]

In this thesis, *n*TVs have been used as connectors for its good behavior as molecular wires, allowing an extending π conjugation of the porphyrin systems.

References

[1] CAIT World Resources Institute (WRI) Home Page. http:// www.cait.wri.org (accessed Jul 4, 2015).

[2] International Energy Agency (IEA), Energy and Climate Change, World Energy Outlook Special Report 2015, http://www.worldenergyoutlook.org/energyclimate/ (accessed Jul 5, 2015).

[3] European Environmental Agency (EEA) Home Page. http://www.eea.europa.eu (accessed Jul 5, 2015).

[4] BP. Energy Outlook 2035, 2015. http://www.bp.com/energyoutlook (accessed Jul 5, 2015).

[5] European Commission. Energy: Renewable Energy Directive. http://www.ec.europa.eu/energy/en/ (accessed Jul 5 2015).

[6] Royal Society of Chemistry (RSC). Campaigning & Outreach, Tackling Global Challenges: Energy. http://www.rsc.org/campaigning-outreach/global-challenges/energy (accessed Jul 5 2015).

[7] National Aeronautics and Space Administration (NASA). Solar Dynamic Observatory (SDO): Solar Irradiance. http://sdo.gsfc.nasa.gov/ (accessed Jul 5 2015).

[8] International Energy Agency (IEA). Press Releases: How solar energy could be the largest source of electricity [Online] September 2014, Paris. http://www.iea.org/ (accessed Jul 5 2015).

[9] National Aeronautics and Space Administration (NASA). The Sun. http://www.nasa.gov/sun (accessed Jul 5 2015).

[10] Becquerel, E. *C. R. Acad. Sci.* **1839**, *9*, 561.

[11] Einstein, A. *Ann. Phys.* **1905**, *322*, 891.

[12] Chapin, D. M.; Fuller, C. S.; Pearson, G. L. *J. Appl. Phys*. **1954**, *25*, 676.

[13] Heeger, A. J. *Adv. Mater*. **2014**, *26*, 10.

[14] International Energy Agency (IEA). Technology Roadmap: Solar Photovoltaic Energy [Online] September 2014. http://www.iea.org/ (accessed Jul 5, 2015).

[15] International Energy Agency (IEA). Photovoltaic Power Systems Programme 2014 Snapshot of Global PV Markets 2014. http://www.iea-pvps.org (accessed Sep 5, 2015).

[16] National Renewable Energy Laboratory (NREL). Golden: CO. http://www.nrel.gov/ (accessed Jul 1, 2015).

[17] Spanggard, H.; Krebs, F. C. *Sol. Energ. Mat. Sol. Cells.* **2004**, *83*, 125.

[18] Ragoussi, M. E.; Torres, T. *Chem. Commun.* **2015**, *51*, 3957.

[19] The Online Etymology Dictionary. Porphyria (n.). http://www.etymonline.com/ (accessed Jul 1, 2015).

[20] Wöhrle, D. *Book Review: The colors of life: an introduction to the Chemistry of Porphyrins and Related Compounds*. L. R. Milgrom. Oxford University Press, Oxford, 1997, 249, *J. Porphyrins Phthalocyanines* **1997**, *1*, 395.

[21] Osuka, A.; Saito, S. *Angew. Chem. Int. Ed.* **2011**, *50*, 4342.

[22] Rao, P. D.; Dhanelalekshmi, S.; Littler, B. J.; Lindsey, J. S. *J. Org. Chem.* **2000**, *65*, 7323.

[23] Gouterman, M. *The Porphyrins* (Vol.III) Ed.; D. Dolphin; Academic Pess Inc.: New York, **1978**, Vol.3, 1.

[24] Huang, X.; Nakanishi, K.; X.; Berova, N. *Chirality*, **2000**, *12*, 237.

[25] Gouterman, M. *J. Molec. Spectrosc.* **1961**, *6*, 138.

[26] Best, S.; Gispert, J.R. *Coordination Chemistry*; Wiley-VCH: 2008; *Appl. Organometal. Chem*. **2009**, *23*, 482.

[27] Kitai, A. H. *Principles of Luminescence, in Luminescent Materials and Applications*; John Wiley and Sons: Ltd, Chichester, UK, **2008**.

[28] Uttamlal, M.; Holmes-Smith, A. S. *Chem. Phys. Lett.* **2008**, *454*, 223.

[29] Karolczak, J.; Kowalska, D.; Lukaszewicz, A.; Maciejewski, A.; and Steer, R. P. *J. Phys. Chem. A.* **2004**, *108*, 4570.

[30] Kesters, J.; Verstappen, P.; Kelchtermans, M.; Lutsen, L.; Vanderzande, D.; Maes, W. *Adv. Energy Mater.* **2015**, *5,* 1500218.

[31] Hodge, J.; Michael G.; Hill, M. G.; Harry, B.; Gray, H. B. *Inorg. Chem.*, **1995**, *34*, 809.

[32] Roncali, J. *Acc. Chem*. *Res*. **2000**, *33*, 147.

[33] Jestin, I.; Frère, P.; Mercier, N.; Levillain, E.; Stievenard, D.; Roncali J. *J. Am. Chem. Soc*. **1998**, *120*, 8150.

[34] [a] Caballero, R.; Barea, E. M.; Fabregat-Santiago, F.; de la Cruz, P.; Márquez, L.; Langa, F.; Bisquert J. *J. Phys. Chem. C*. **2008**, *112*, 18623.[b] Casado, J.; González, S. R.; Moreno-

Oliva, M.; López-Navarrete, J. T.; Caballero, R.; de la Cruz, P.; Langa, F. *Chem. Eur. J.* **2009**, *15*, 2548. [c] Clifford, J. N.; Forneli, A.; López-Arroyo, L.; Caballero, R.; de la Cruz, P.; Langa, F.; Palomares, E. *ChemSusChem.* **2009**, *2*, 344. [d] Aljarilla, A.; López-Arroyo, L.; de la Cruz, P.; Oswald, F.; Meyer, T.; Langa, F. *Org. Lett.* **2012**, *14*, 5732.

[35] [a]Jestin, I.; Frère, P.; Blanchard, P.; Roncali, *J. Angew. Chem.* **1998**, *37*, 942. [b] Elandaloussi, E. H.; Frère, P.; Roncali, *J. Chem. Commun*, **1997**, 301.

[36] Montcada, N. F.; Domínguez, R.; Pelado, B.; de la Cruz, P.; Viterisi, A.; Palomares, E.; Langa, F. *J. Mater. Chem. A,* **2015**, *3*, 11340.

[37] Oswald, F.; Islam, D.M. S.; Araki, Y.; Troiani, V.; Caballero, R.; de la Cruz, P.; Ito, O.; Langa, F. *Chem. Commun.* **2007**, 4498.

[38] Oswald, F.; Islam, D.M. S.; Araki, Y.; Troiani, V.; Caballero, R.; de la Cruz, P.; Ito, O.; Langa, F. *Phys. Chem. Chem. Phys.* **2014**, 16, 2443.

CHAPTER 1

Porphyrins for Bulk Heterojunction Solar Cells (BHJSC)

1. Porphyrins for Bulk Heterojunction Solar Cells (BHJSC)

1.1 Organic photovoltaics (OPV)

Organic semiconductors have the ability of transporting charge carriers and are appealing for their properties and their improvements in performance of photonic applications, such as organic light-emitting diodes (OLED), organic field-effect transistors (OFET), organic solar cells (OSC), sensors, liquids crystals and others optoelectronic applications.[1,2] The advances in synthetic organic chemistry have allowed to prepare a wide variety of conjugated systems with good optoelectronic properties to be a part of organic devices.[3]

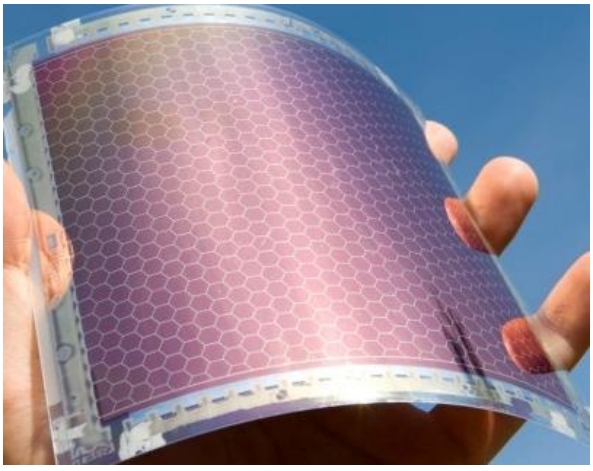

Figure 13. Photography of organic solar cell[4]

The first organic photovoltaic cell came in 1959 when an anthracene single crystal was studied; this cell exhibited a photovoltage of 200 mV with an extremely low efficiency.[5]

Usually, organic solar cells comprise a *p*-type, organic semiconductor (electron donor, polymeric or small molecules) and *n*-type (electron acceptor).[6] High optical absorption coefficients of these materials offer the possibility of the production of very thin solar cells, flexible devices that can be fabricated using high throughput: a low temperature approach that employs well established printing techniques.[7,8,9,10]

The absorption of a solar photon creates an exciton, which diffuse to the D/A interface, where they are dissociated into free holes and electrons. Opposite polarity carriers (holes and electrons) transport through the donor and acceptor channels to anodes and cathodes respectively, subsequently charges are collected at the electrodes and resulting in the generation of electrical power.[6]

According to Mishra and Bäuerle fundamental steps occurring in these devices are:[3]

1. The photoexcitation of the donor to produce an exciton (electron and hole pair bound by Coulumb interactions).

2. Subsequent diffusion of the exciton in the donor-acceptor interface (longer diffusion length).

3. Dissociation of bound excitons at the D/A interface to form an electron-hole pair (increased charge separation requires optimal energy offset between LUMO of the donor and LUMO of the acceptor).

4. Free charge carrier transport and collection at the external electrodes.

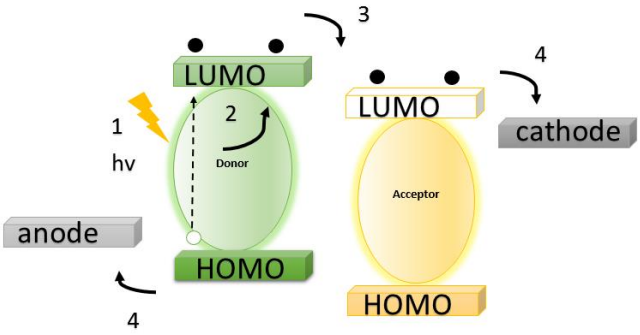

Figure 14. Fundamental steps in OPV

There are two principal types of architectures for donor-acceptor interphase of OPV:

- Planar heterojunction cells (PHJ), formed by two successive deposited donor and acceptor layers.

- Bulk heterojunction (BHJ), these are devices containing heterogeneous mixtures of unstructured donor-acceptors, producing a higher internal interface. The composite materials of donor and acceptor have a phase separation of nanoscale size.[3]

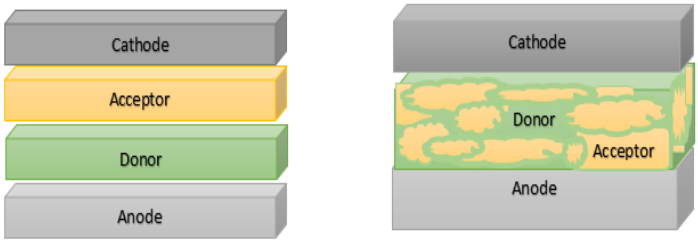

Figure 15. Planar heterojuction (left) and bulk heterojuction (right)

The two principal processing techniques for the fabrication of OPV devices are: vacuum deposition and solution processing. The bilayer heterojunction is fabricated by vacuum deposition due to difficulty finding suitable solvents for donor layer and acceptor layer without destroying the donor-acceptor interface.[3] The solution processes (spin-coating, dip-coating,

inkjet printing, and spray technique) for BHJ, allow large-scale production by printing techniques.[11] The morphology and phase separation of the active layer is related to the nature of the material and can be optimized by controlling the manufacturing conditions.

Fullerenes derivatives are the most successful acceptors in the OPVs due to their ability and high electron affinity.[6] Typically C_{60} and C_{70} are used as acceptors in vacuum deposited OPVs, while $PC_{61}BM$ and $PC_{71}BM$ (Figure 16), are used in solution processed OPVs as acceptors.[3] $PC_{61}BM$ has a limited absorption in the visible region, which limits its contribution to the J_{SC} of the device. $PC_{71}BM$ is less symmetric, giving rise to optical transitions, therefore extending its absorption spectrum into the visible region, so it can often provide a complimentary absorption profile to the donor materials, and increase the overall J_{SC}.

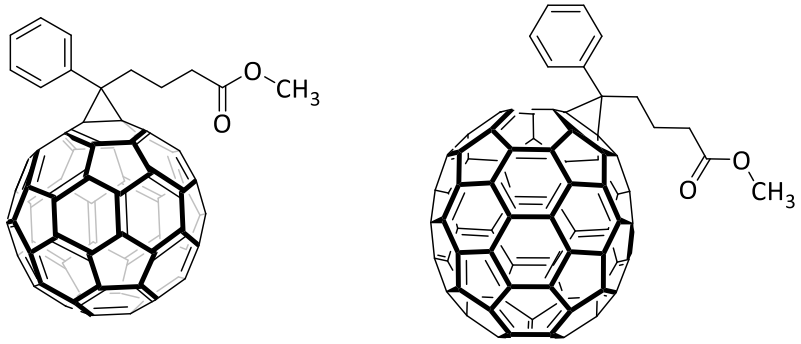

Figure 16. $PC_{61}BM$ (left) and $PC_{71}BM$ (right)

Other fullerene derivatives have been used as acceptor in recent years.[3] Among others, $PC_{61}BM$ analogues where the phenyl ring replaced by thiophene, fluorene, or triphenylamine units and bis-adducts of PCBM have been successfully synthesized.[12,13]

Recently, it has been demonstrated that π-conjugated systems substituted with electron-withdrawing moieties, generally exhibit lower LUMO energy levels and therefore facilitate electron injection, leading to an increased *n*-type character.[3] Over the last years, nonfullerene based *n*-type materials have been tested as acceptors:[14] diketopyrrolopyrrols,[15] derivates of pentacene, [16] derivate of imides, [17, 18, 19] chlorinatedSubPc, [20] anthradithiophene, [21] oligothiophene,[22,23] benzothiadiazole derivates,[24] dicyano-substituted derivatives,[25,26] among others.[27] However, compared to fullerenes and their derivatives, non-fullerene acceptors have shown lower performance in OPV devices, especially in solution processed BHJ OPVs.[6] The main limitations most often arise from blend morphology and charge transport issues, nevertheless the non-fullerene acceptor, still being investigated to get the best results.

The charge transport depends on the ability of carriers to move the charge from one molecule to another and it depends on the energy gap between the highest occupied molecular orbital (HOMO) of the donor and the lowest unoccupied molecular orbital (LUMO) of the acceptor. Optical measurements provide essential information about the electronic properties,

presenting evidence of electronic transfer of these materials. In addition, the energy levels of HOMO and LUMO are important with respect to the electron acceptor, the exciton and transport layers in organic solar cells, these levels can be determined by cyclic voltammetry.[3]

The electrochemical band gap is calculated by the difference of HOMO and LUMO energy levels, allowing the selection of the best candidates for their use in the fabrication of efficient photovoltaic cells. Conductors must cover the visible and infrared spectrum for better absorption and light gathering. Most π conjugated systems only cover the visible region of the spectrum; therefore electron donor fragments can be attached to oligomers and polymers, to act as electron deficient units, and to reduce the band gap.

It is necessary to ensure efficient exciton diffusion in the donor-acceptor interface, it can be achieved by a minimal displacement of approximately 0.3-0.4 eV between the LUMO of the donor and LUMO of the acceptor.[28] The HOMO energy level can be increased by a strong donor, and by reducing the bandgap, but this can decreases the V_{OC}. Therefore, it is important to optimize the energy level positions between the donor and acceptor, to enable efficient charge separation without losing the photovoltage of the solar cell. The operation of a solar cell is estimated according to the following parameters:[3]

- **The power conversion efficiency (η or PCE)**

The power conversion efficiency of a cell is determined by the ratio between the maximum output power (P_{out}) and the power of the incident light (P_{in}).The incident light power is usually standardized to be equivalent to AM 1.5 solar spectrum.

$$\eta = \frac{V_{OC*}J_{SC}FF}{P_{in}}$$

Equation 1.

Where:

η= power conversion efficiency

J_{SC}= short-circuit current

V_{OC}= open-circuit voltage

FF= Fill Factor

It must be remarked that the efficiency of a solar cell is a parameter of the device, and not an intrinsic property of the material. The efficiency of the device depends on the preparation and processing.

- **Short circuit Current (J_{SC})**

J_{SC} represents the maximum photocurrent reachable from the solar cell and it depends on the surface area of the photoactive layer, its thickness and the number of photons absorbed by

the solar cell, as long as no saturation effects occur. The quantum efficiency for charge separation and the transport of the charge carriers through the material are important. A broad absorption spectrum is advantageous, as it is important to harvest a fraction as large as possible of the photons from the broad spectrum of the sun.

- **Open Circuit Voltage (V_{OC})**

V_{OC} represents the maximum measured photovoltage delivered by the solar cell, when the current is zero. This factor is determined by the difference in the quasi-Fermi levels of the phase separated donor and acceptor domains.[13]

$$V_{oc} \sim E_{\ fullerene}\,(LUMO) + E_{\ semiconductor\ p}(HOMO) \frac{K_B}{e\left[ln\left(\frac{n_e n_h}{Nc^2}\right)\right]}$$

Equation 2.

Where:
n_e= electron density
n_h= hole density
Nc= density of states
K_B= Boltzman constant

This equation was initially verified by correlating the difference between the HOMO of the donor and the LUMO of the acceptor in BHJ solar cells fabricated with 26 different donor polymers.[28] This excellent correlation required the addition of an additional 0.3 eV of unknown origin.

V_{OC} can be increased by the difference in work functions of the anode and cathode. However, the use of interlayers (electron transport/hole blocking and hole transport/electron blocking) tends to decouple the open circuit voltage from the difference in the anode and cathode work functions.[28] This can also be influenced by recombination processes, resulting in a decrease of the maximum value of V_{OC}.[29]

- **Fill Factor (FF)**

FF describes the quality of the solar cell and determines the photogeneration of charge carriers and the carrier fraction that reaches the electrodes. The maximum area of the current-voltage curve determines the fill factor. The FF is the result of competition between the processes of recombination of charge carriers and transport process (see Figure 17).

The molar absorption coefficient of the molecule must be increased for higher external quantum efficiencies (EQE) and the HOMO and LUMO energy levels should be adjusted to increase the V_{OC} and FF.

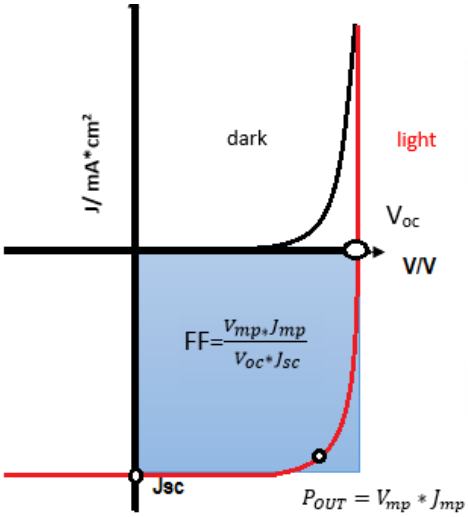

Figure 17. Current-voltage (J-V) characteristics of a typical solar cell

1.2 Small Molecule bulk heterojuction solar cells (SMBHJSC)

SMBHJSC are defined as active layer of unstructured, heterogeneous mixtures of donor and acceptor organic semiconductors with discrete molecular structures (non polymeric).[11] Traditionally, organic photovoltaics used a polymeric material with long chained molecular systems as P3HT, as electron donors, but currently tends to been studied discrete molecules or more commonly known as small molecules. Small molecular semiconductors for OPVs have advantages over polymer cells, including well-defined molecular structure and molecular weight, high purity without batch to batch variations.

In BHJSC high efficiency has been achieved as result of innovations of small molecular materials and device fabrication. The highest PCE for solution-processed BHJ architecture reported has been achieved with **B0** (Figure 18), this molecule has an acceptor-donor-acceptor structure with oligothiophene showing a certified PCE of 10%.[30] In porphyrins the highest efficiency in SMBHJSC is obtained by **B31** in 8% PCE[31] (see Figure 18).

In order to improve the device performance it is necessary understand the relationships between chemical structures and optical, electronic and device properties.[6]

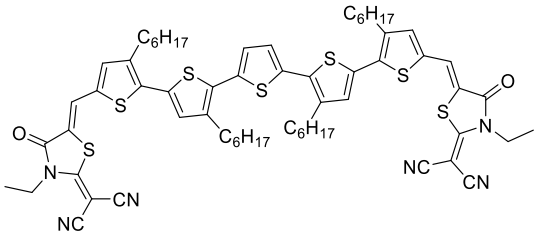

$PC_{71}BM$ 10.08 %

B0

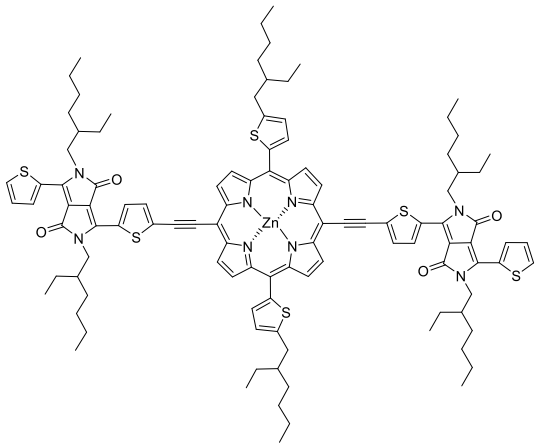

$PC_{61}BM$ 8.08 %

B31

Figure 18. Molecules with high efficiency solar cells for BHJ

Some basic requirements of specific intrinsic properties for an ideal small molecule are:[3]

- Broad absorption in the visible, red and near infrared regime, having a high molar extinction coefficient to capture more photons, corresponding with a low optical bandgap.
- Effective migration of excitons D/A interface, by a long exciton diffusion lengths.
- High mobility of hole and electron mobility for accelerating charge transport, which allows a thicker active layer required for increased light harvesting, and reduces charge recombination and series resistance.
- Suitable HOMO/LUMO energy levels to ensure a large V_{OC} and a downhill energy offset for exciton dissociation.
- High crystallinity of the active materials may be beneficial to improve the device performance. Moderate crystallinity of materials can improve charge carrier mobility, but high crystallinity will cause large phase separation scale and low PCE of devices.

Easy sublimation, relatively low molecular weight, and excellent thermal stability are necessary for vacuum deposited materials; good film-forming property and sufficient solubility are also necessary for solution processed materials.

A variety of methods can be used to study the nanomorphology of the donor-acceptor blend being the most significant:[13] Atomic force microscopy (AFM), grazing-incidence wide-angle X-ray scattering (GWAX) and by transmission electron microscopy (TEM). AFM provides detailed and useful information about the nanostructure of the surface of the BHJ film, the GWAX provides detailed information on the structure and crystallinity, and TEM probes the internal structure that determines the length scale of the phase separation and the connectivity of the phase separated networks.

It should be remarked that the morphology and the scale of the phase separation in BHJ film is not only related to the nature of materials, but can also be optimized by carefully controlling the device fabrication conditions.

The following parameters influence on the nanoscale morphology of the BHJ blends:

- Donor and fullerene ratio in the BHJ film.
- Solvent used in the BHJ composite.
- Chemical additives to improve solubility and FF. Additives can reduce the domain size in BHJ layer allowing cell efficiency in the device. A significant increase of the efficiency has been achieved by using 1,8-diioctane (DIO), with a PCE record of 6.7% (without DIO 4.52%).[32]
- Thermal or solvent annealing to control the phase: enabling the crystallization and diffusion of one or both components in the blend leading to mixing and coarsening of the phase separation. Annealing at high temperatures improves the crystallinity within the phase separated donor and acceptor networks, facilitates charge transport to the electrodes and increases the power conversion efficiency. This remarkable thermal stability of the nano-scale interpenetrating donor-acceptor networks suggests that long lifetimes might be possible with BHJ solar cells.
- Molecular structure of the materials: the conducting molecules and fullerene structures determine their solubility and miscibility in organic solvents in solution. The solvent influences the drying time during film formation. For solution processing, the use of long alkyl or alkoxy side chains has been a common approach. The side chain nature affects the solubility, the configuration and intermolecular interaction of the molecules, and affects the absorption, energy levels and charge transport properties. The side chain affects morphology of blend films. For instance, increasing the content of alkyl side chains, relative to the conjugated main chain in the molecule, may result in deterioration

in charge transport. It is of crucial importance for the fine-tuning of the structures and properties relationship, that the molecules be balanced in suitable solubilizing groups at an appropriate location.

- The absorption characteristics: energy levels and charge carrier mobility can be controlled by the careful design of the molecule with the desired optoelectronic properties. It has also been observed that the small molecules tend to have a higher V_{OC}, while J_{SC} and FF tend to be lower compared to the polymers values, so enhancing and extending the absorption of active materials to match solar radiation is one of the main ways to improve J_{SC} and efficiencies of OPV devices.

For energy conversion efficiencies exceeding 10%, the donor must have a bandgap lower than 1.74 eV and a LUMO level lower than -3.92 eV, maintaining the FF and the average EQE at least equal to 0.65. The V_{OC} of devices have a direct relationship to the difference between the HOMO level of the donor and the LUMO level of the acceptor. A lower HOMO of a donor and a higher LUMO of an acceptor would help achieve a higher V_{OC}. The charge-carrier mobility of electrons and holes in the donor acceptor blend must be high enough to allow efficient charge extraction and FF of 0.65.[28]

To prevent losses in the photocurrent in the absence of second order recombination is an important parameter, carrier mobilities of $\sim 10^{-3}$ $cm^2V^{-1}s^{-1}$ for devices with an active layer thickness of several hundred nanometers. The highest energy conversion efficiencies derived above are in the range of 10% for single-bulk-heterojunction solar cell. To go beyond 10% efficiency, it is necessary to increase the external quantum efficiency of the device by improving light management and/or improving FF through the optimization of the electrical design.[28]

1.3 Porphyrins for Bulk Heterojunction Solar Cells, brief review

Improvements have been made in the molecular design of porphyrins as small molecules for BHJSC and the devices have been optimized to enhance the power conversion efficiency, therefore these cells have developed high J_{SC} and high V_{OC}. Figure 19, Figure 20 and Table 1 shows all the porphyrin based SMBHJSC described up to July 2015.

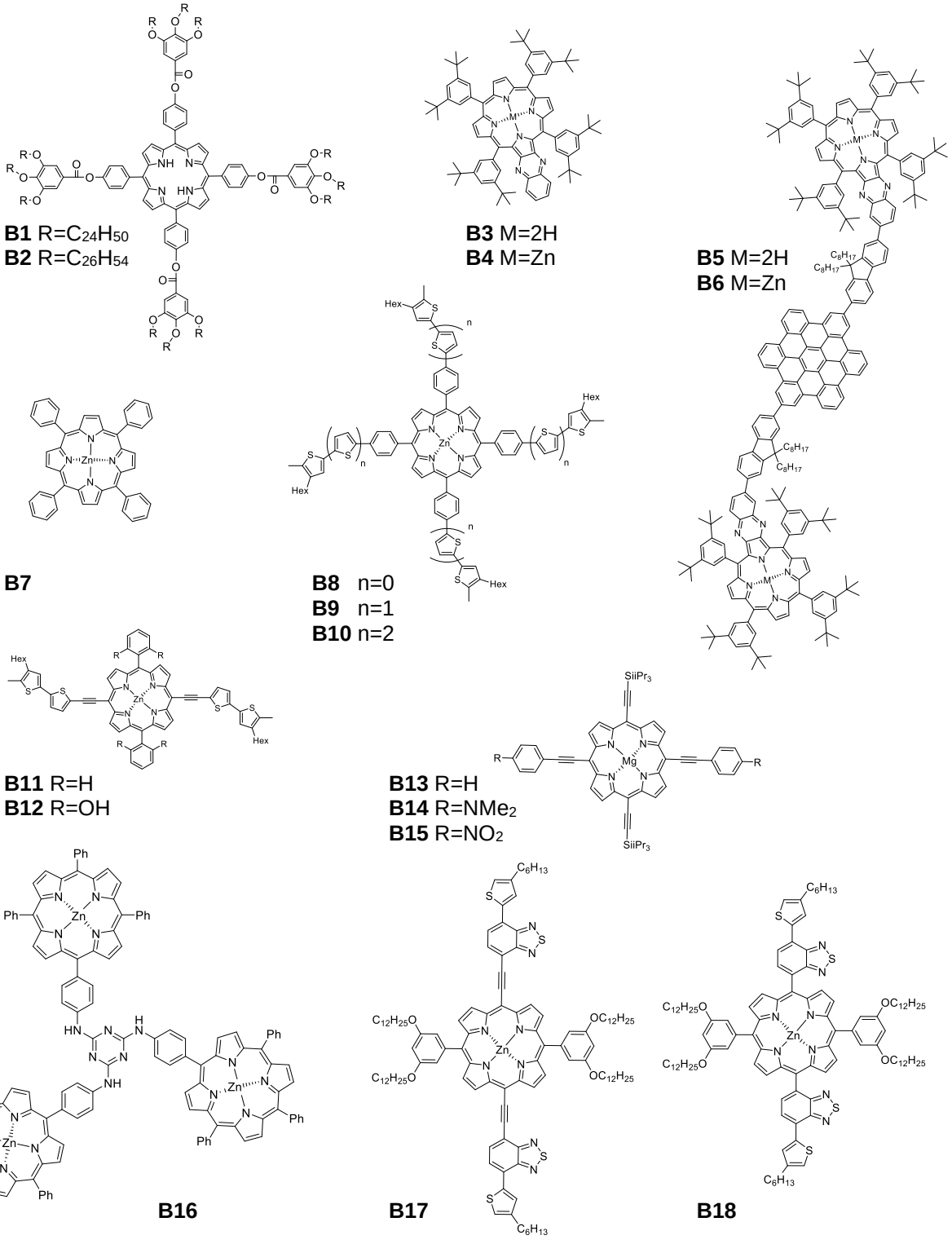

Figure 19. Porphyrins as small molecules for BHJSC (I)

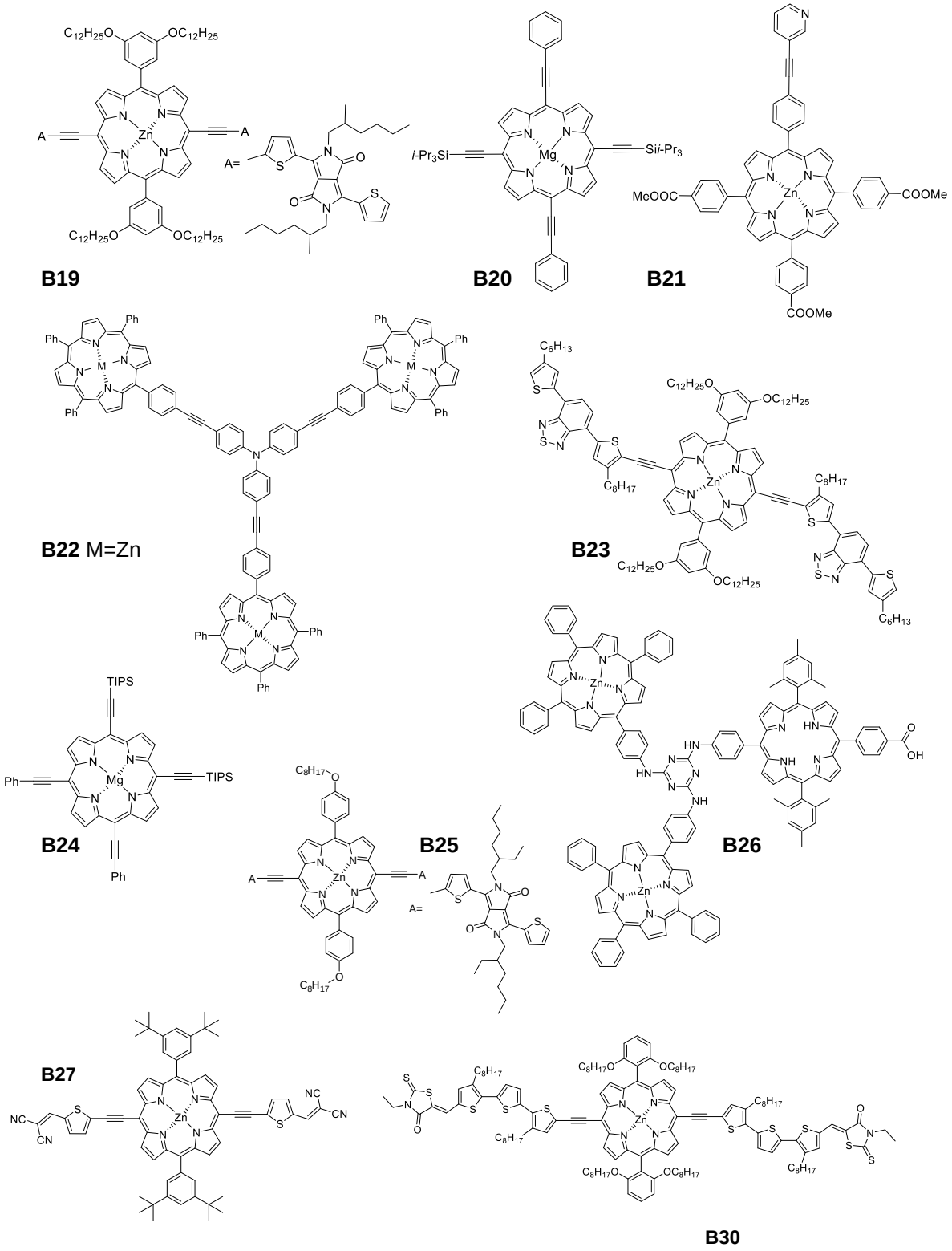

Figure 20. Porphyrins as small molecules for BHJSC (II)

Table 1. Photovoltaic parameters for devices comprising porphyrins as small molecules in BHJSC

Molecule	*ACEPTOR*	*Ratio (D:A)*	*Solvent*	*Additive*	*Hole mobility[a] $cm^{-2}V^{-1}s^{-1}$*	*Thickness (nm)*	*V_{OC} (V)*	*J_{SC} ($mA.cm^{-2}$)*	*FF*	*PCE[b] (n,%)*	*Reference*
B1	$PC_{61}BM$[c]	1:1	CB	----------	----------	230-250	--	3.99	--	0.71	[33]
B2	$PC_{61}BM$[c]	1:1	CB	----------	----------	230-250	--	5.02	--	0.78	[33]
B3	$PC_{61}BM$	1:2	CB	----------	----------	60-70	0.83	2.70	0.37	0.83	[34]
B4	$PC_{61}BM$	1:2	CB	----------	----------	60-70	0.76	2.03	0.34	0.53	[34]
B5	$PC_{61}BM$	1:2	CB	----------	----------	60-70	0.94	2.91	0.44	1.20	[34]
B6	$PC_{61}BM$	1:2	CB	----------	----------	60-70	0.80	2.89	0.38	0.87	[34]
B7	$PC_{61}BM$	1:9	ODCB	----------	----------	65	0.41	1.55	0.38	0.24	[35]
B8	$PC_{61}BM$	1:3.5	DCB	THF (10:1)	----------	-----	0.68	2.14	-----	0.45	[36]
B9	$PC_{61}BM$	1:3.5	DCB	THF (10:1)	----------	-----	0.66	1.95	-----	0.36	[36]
B10	$PC_{61}BM$	1:3.5	DCB	THF (10:1)	----------	-----	0.65	1.85	-----	0.32	[36]
B11	$PC_{61}BM$	1:3.5	DCB	THF (10:1)	----------	-----	0.56	5.28	0.32	1.00	[36]
B12	$PC_{61}BM$	1:3.5	DCB	THF (10:1)	----------	-----	0.62	4.13	0.30	0.76	[36]
B13	$PC_{61}BM$[d]	1:4	CB	----------	$2.3*10^{-5}$		0.92	6.4	0.41	2.5	[37]
B14	$PC_{61}BM$[d]	1:4	CB	----------	$3.7*10^{-5}$		0.55	3.3	0.31	0.57	[37]
B15	$PC_{61}BM$[d]	1:4	THF/TOL (1:1)	----------			0.97	1.6	0.16	0.25	[37]
B16	$PC_{61}BM$	1:10	CB	----		150	0.6	2.25	0.32	0.5	[38]
B17	$PC_{71}BM$	1: 3	CB/DCB	1% Py			0.85	9.46	0.50	4.02	[39]
B18	$PC_{71}BM$	1:3	CB/DCB	1% Py			0.88	2.81	0.28	0.71	[39]
B19	$PC_{61}BM$	1:1	CB/DCB	3% Py	$1.6*10^{-4}$		0.80	11.88	0.50	4.78	[40]
B20	$PC_{61}BM$[e]	1:5	CB		$8.4*10^{-6}$	40	0.90	4.6	0.39	1.6	[41]
B21	$PC_{71}BM$[c]	1:1	THF	------	---	90-95	0.86	8.44	0.56	4.06	[42]
B22	$PC_{61}BM$	1:6	CB	------	---	70	0.6	2.06	0.31	0.4	[43]
B23	$PC_{71}BM$	1:2	CB	0.25 Eq Bipy	-----		0.84	8.34	0.40	2.81	[44]
B24	$PC_{61}BM$[d]	1:3	CB	----	------		0.83	4.5	0.39	1.5	[45]
B25	$PC_{61}BM$	1:1.2	CB	4% DIO	$4.68*10^{-4}$		0.71	16.00	0.64	7.23 (6.83)	[46]
B26	$PC_{71}BM$	1:1	THF	5% CN	-----	-----	0.92	8.06	0.53	3.93	[47]
B27	$PC_{71}BM$	1:1	THF	4% Py	$8.34*10^{-5}$	-----	0.88	10.64	0.56	5.24	[48]
B30	$PC_{71}BM$	1:1	THF	Py 4%	$8.45*10^{-5}$	90	0.76	11.67	0.62	5.50	[49]
B31	$PC_{61}BM$	1:1.2	CB	Py		125	0.78	16.76	0.61	8.08 (8.04)	[50]

[a]Active layer; [b]Best efficiencies (averages indicated in parenthesis); [c]Thermally annealed; [d]Heated at 65˚C for 10 min; [e]Inverted device structure.

Figure 21 shows the tendency per year of the best efficiencies of devices comprising porphyrins as small molecules in BHJSC.

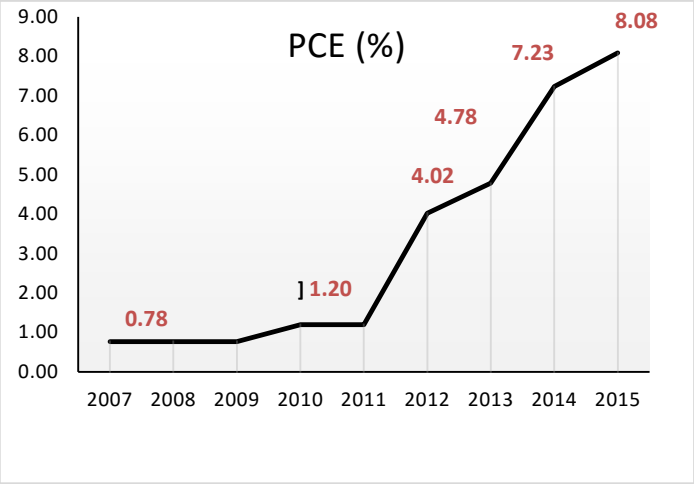

Figure 21. PCE (%) of devices comprising porphyrins as small molecule in BHJSC per year

1.3.1 Improvement of SMBHJSC based on Porphyrins

Novel designs of porphyrin systems as small molecule in BHJSC, can be improved to obtain best efficiencies in the devices, but a good design in the molecule is not enough to obtain best results. The devices can be improved by the morphology of the donor-acceptor active layer, where they should contain domains of mixtures of donor-acceptor, with larger interfacial layers to dissociate photo-generated exactions and keep a network to transport charge carriers to the electrodes.[51,52] The morphology of the active layer and the light absorption can be improved by optimization of concentration, ratios of donor:acceptor, thickness layer, thermal annealing,[53,54] solvent additives,[55,56,57] and solvent mixtures.[58,59,60]

1.3.1.1 Molecular engineering of the porphyrin structures

Different molecules based on porphyrin skeleton have been studied as small molecules (*p*-type semiconductor) for BHJSC. The ethynyl group has been studied as connector coplanar group,[61] extending the π conjugation of the system, allowing best absorption efficiency and improving the crystallinity of the active layer blend, promoting the exciton generation and improving the photocurrent for the solar cell.

By incorporating acceptor units, a push-pull effect is achieved, diminishing the LUMO and consequently the band gap. As a result, the light absorption is extended to the red, which increases the current.

Analysis of the efficiency of **B8**-**12**, shows how to design a planar system can improves the efficiency, the first three molecules have a phenyl linker and different units of thiophene moieties. The devices prepared with **B8**-**10** show a J_{SC} of 2.14, 1.95 and 1.85 mA/cm^2 respectively and PCE of 0.45%, 0.36% and 0.32%, decreasing with the number of thiophene moieties and the distortion of phenyl linkers with respect to the porphyrin core interference with the extension of the conjugation. In the other hand, molecules **B11-12** have ethynil linkers at 5, 15 positions, these linkers extend the π conjugation of the system and enhance the optical

absorption efficiency. Other characteristic of these linkers is that as consequence of the higher planarity, the film crystallinity, the exciton generation efficiency and the photocurrent for the solar cells are improved. The molecules **B11-12** show PCE of 1% and 0.76% respectively. The decrease of PCE value in **B12** is due to the presence of the alkyl chains molecule, decreasing the crystallinity of films and inducing more disordered states in the active layer, having a negative effect on the carrier mobility.[36]

The molecules **B13**-**15** show high solubility and strong intermolecular interaction, these molecules have aliphatic and aromatic groups connected to the porphyrin core via ethynyl linkers in order to expand the π conjugated systems and obtain a planar structure. **B15** has a poor PCE efficiency of 0.25%, due to the rough surface morphology of the active layer, observed in AFM images, the lower solubility is due to the strong intermolecular π-π interaction between porphyrin and nitro substituted phenyl group moieties, nevertheless **B13** has the best PCE with 2.5%, this molecule has a good balance of hole and electron mobility and favorable film morphology, hole mobility $2.3*10^{-5}$ $cm^{-2}V^{-1}s^{-1}$ and electron mobility $9.1*10^{-4}$ $cm^{-2}V^{-1}s^{-1}$.[37]

The molecules **B17**-**18** with ethynylene links between 2,1,3-benzothiadiazole and porphyrin, also allow the delocalization of π electrons through the molecule. **B18** have a moderate hole mobility of $7.4*10^{-6}$ $cm^2V^{-1}s^{-1}$ higher than **B17** with $2.5*10^{-9}$ $cm^2V^{-1}s^{-1}$, **B18** has a PCE of 4.02% in comparison to **B17** the molecule is more planar and the ethyl bridge improve the efficiency.[39]

1.3.1.2 Thickness of the active layer in porphyrins based SMBHJSC

The thickness of the active layer must be controlled and optimized, as a thicker layer increases the charge recombination and a thinner layer decreases the photo absorption. [62] The thickness depends in the solvent, the speed, time and acceleration of the spin coated active layer. The thickness of the devices using porphyrin with good efficiency is between 90 and 125 nm (Table 1).

The influence of the thickness onto the efficiency for 5,10,15,20-tetraphenyl-21H,23H-porphine zinc **B7**, was studied from 50 to 93 nm,[35] obtaining at 68 nm the best value of efficiency (0.24%), and IPCE maximum (19.2%) at 445 nm. Nevertheless, the low efficiency of the dispositive was attributed to the low hole mobility of ~10^{-10} $cm^2V^{-1}s^{-1}$.[63,64,65]

1.3.1.3 Porphyrin:PCBM ratio

The donor: acceptor ratio has a strong influence in the photovoltaic performance. In general when the amount of the acceptor material is too low in the active layer the electron transporting ability decreases and a higher amount of acceptor, decrease the absorbance and the hole transport ability.

1.3.1.4 Thermal annealing in porphyrins as small molecules for BHJSC

Thermal annealing in materials science, is a heat treatment that alters the physical and sometimes chemical properties of a material. It involves heating a material beyond its recrystallization temperature, maintaining a suitable temperature, and then cooling. Under annealing, atoms migrate in the crystal lattice and the number of dislocations decreases, leading to the change in morphology of the material. In bulk heterojunction solar cells thermal annealing enhance the light absorption properties, the charge transport to the electrodes and decrease the resistance allowing higher J_{SC}, FF and PCE.[10]

Thermal annealing in the devices comprising $PC_{61}BM$ as acceptor and as donor the liquid crystalline porphyrins **B1-2** improve the PCE, show a J_{SC} of 1.34 mA/cm^2 and 1.14 mA/cm^2 respectively and after the treatment increase to 3.99 mA/cm^2 and 5.02 mA/cm^2, leading in a higher PCE of 0.71% and 0.78%.[33,66] Before the annealing the data indicated similar phase sequence in both porphyrins, of isotropic, hexagonal LC phase, ordered hexagonal LC phase and crystallinity. Presumably the thermal annealing induced the homeotropic alignment, in this state a rod-like liquid crystalline molecule aligns perpendicularly to the substrate, providing an efficient hole conduction along the columnar axis, and optimize the light harvesting.

1.3.1.5 Additives in the devices

The addition of chemical additives in the active layer can reduce the domain size, allowing a better efficiency in the device.[67] Moderate crystallinity of materials can improve charge carrier mobility, but high crystallinity will cause large phase separation scale and low PCE of devices. Pyridine has been successfully used as additive in porphyrin based BHJSC. The lone electron pair on the nitrogen atom of pyridine could coordinate with the Zn atom in the porphyrin core, therefore this additive improve the efficiency, disrupting the intramolecular π stacking by coordination to Zn, improving at the same time the J_{SC} and consequently, the efficiency.

Porphyrin **B19** having diketopyrrolopyrrole as acceptor unit, exhibit broad intense absorption in the visible and near to the IR region, after the addition of 3% of pyridine the dispositive with $PC_{61}BM$ has a PCE of 4.78%.[40] Likewise the maximum external quantum efficiency (EQE) of the device processed with pyridine presented an increment, from 34% to 43% at 570 nm, in comparison with the devices without pyridine. The AFM imaging indicates smaller domains for the film with pyridine, improving the morphology of the active layer, for efficient exciton dissociation and charge transport. The phase topography of the pristine film exhibit microscale phase separation and the root-mean-square roughness value is 2.45 nm, and the films with pyridine shows smaller phase separation domains, and the roughness value is 1.68 nm, the surface is smoother and has more grains, suggesting better morphological features for efficient exciton dissociation and charge transporting, suggesting an increase of J_{SC}.

The conjugated acceptor-donor-acceptor with zinc porphyrin core and dicyanovinyl substituted thiophene **B27** was designed,[48] highest values of IPCE were obtained for the device processed with pyridine, in comparison with the device without pyridine, leading in an increase of the values of J_{SC} and FF, therefore devices with $PC_{71}BM$, exhibit a PCE of 3.65%, after the addition of 4% of pyridine the device exhibit a PCE of 5.24%.The film of THF shows a smooth surface with a root mean square roughness of 3.45 nm, and domain size of 40-50 nm, and with pyridine the domain size reduce to 15-20 nm and the roughness to 1.45 nm. This reduced domain size allows increasing the donor-acceptor interfacial area for exciton dissociation to charge transfer efficiency and charge collection efficiency, resulting in enhanced J_{SC} and best PCE.

The active layer of $PC_{71}BM$ and the porphyrin **B30**, A-π-D-π-A, (with ethyl rhodanine as electron withdrawing and linked octyl thiophene-ethynylene bridge), was improved by THF, pyridine and thermal annealing, increasing the PCE from 2.95% to 5.50%.[49] The symmetrical structure expected to enhance π-π stacking interactions which could be beneficial for high mobility. In the same way, the highest value of IPCE was obtained for the device processed with pyridine, in comparison with the device without pyridine.

The actual record porphyrin in SMBHJSC, meets the parameters of a plannar design with a porphyrin ring linked to two diketopyrrolopyrrole units by ethynylene bridges **B31**. The devices fabricated without solvent additive and without thermal annealing had a PCE of 5.89%, J_{SC} of 12.72 mA/cm^2 and FF of 55.76%. In the presence of 1% pyridine and thermal annealing at 120 °C, for 10 minutes, show a PCE of 8.08%, J_{SC} of 16.76 mA/cm^2 and FF of 61.8%. Moreover, adding pyridine to the device improved the EQE from 45% to 65%. The GIXD and the absorption shows that pyridine additive enhance the crystallinity. The π-π stacking direction transformed from a *J*-type to a less *H*-type aggregation. The large aromatic surface offers a higher contact area and more relative positions of stacked porphyrins that could performance as channels for carrier transport. The TEM showed the blend with additive, with a finer phase separation with an approximate size of 30 nm in comparison with the 100 nm of the blend without additive and thermal annealing. The sharp reduction in length scale led to a 35% increase of the current.[50] The energy loss (E_{loss}) is the difference between the band gap and the open circuit voltage (V_{OC}), the minimum 0.6 eV, is suggested to enhance the energy efficiency by which photons are converted into collectable charges, the molecule **B31** shows a 0.59 E_{loss} value.

Porphyrin **B25**, porphyrin-5,15-bis(2,5-bis-(2-ethyl-hexyl)-3,6-di-thyenyl-2-yl-2,5-dihydro-pyrrolo-[3,4-c]pyrrole-1,4-dione-5'-yl-ethynyl)-10,20-bis-(4-octyloxy phenyl)-porphyrin zinc was designed with 4-octyloxy-phenyl groups used in place of the 3,5-di(dodecyloxy)-phenyl groups of **B19** to diminish the long chains and therefore suppressed the intermolecular π-π stacking. The device shows a PCE up to 5.83%, V_{OC} of 0.74 V, J_{SC} of 14.7 mA/cm^2, FF of 0.53. 1,8-diiodooctane (DIO) was employed, as additive and the performance was enhanced with values

of PCE up to 7.23%, V_{OC} of 0.71 V, J_{SC} of 16 mA/cm^2 and FF of 0.64. Besides, by adding DIO the EQE increased up to 5%. The morphologies of the blends by AFM shows phase images with no apparent crystalline domains. The root-mean-square (RMS) roughness of blends without additive is 0.857 nm and with DIO 0.345 nm, the lower roughness shows better miscibility between the donor and the acceptor in the active layer, and may form a finer interpenetrating network to facilitate exciton separation and charge transfer. TEM images confirm that blend films with DIO, are more continuous interpenetrating network.

The only example of chloronophtalene as additive for porphyrin based SM BHJSC is the **B26**,[47] this porphyrin has two zinc-metalated porphyrin units and one free base porphyrin unit covalently linked by amino phenyl groups to a central s-triazine unit. The addition of 5% chloronaphtalene in the THF solution of the processed BHJSC, improve the efficiency from 2.85% to 3.93%, due to the enhancement of the short circuit current J_{SC} of the solar cell from 6.45 mA/cm^{-1} to 8.06 mA/cm^{-1}. Besides, the device processed with chloronophtalene as additive showed broader IPCE, than the device processed only with THF. This improvement is responsible of a highest J_{SC}. The device shows a stronger incident photon current efficiency, and a higher degree of crystallinity of the active layer of the latter solar cell, resulting in faster charge transfer process and more efficient exciton dissociation.

1.4 General objective

The main objective of this work is the design, synthesis and characterization of new families of discrete porphyrins (small molecules) with the configuration A-π-D-π-A, to analyze their performance in Bulk Heterojunction Solar Cells (BHJSCs), and the effect in the performance devices, changing the porphyrin core, the acceptor and the π conjugation linker of the structures.

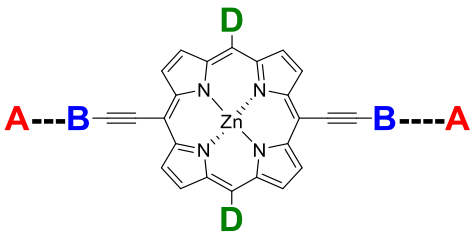

A) Study the effect of change the linked moiety to the porphyrin core at meso position (**D**) for a mesityl, 2,6-bishexyloxybenzene or hexylthiophene:

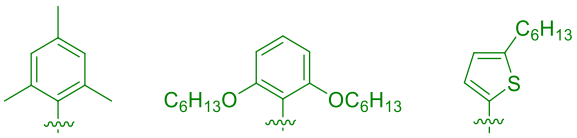

Mesityl **2,6-bishexyloxybenzene** **3-hexylthiophene**

B) Study the effect of change the **B** bridge between porphyrin core and the acceptor for 3,4-dihexylthiophene, *(E)*-1,2-bis(3,4-dihexylthiophen-2-yl)ethylene) or 4,4-dihexyl-4H-cyclopenta[2,1-b:3,4-b']dithiophene.

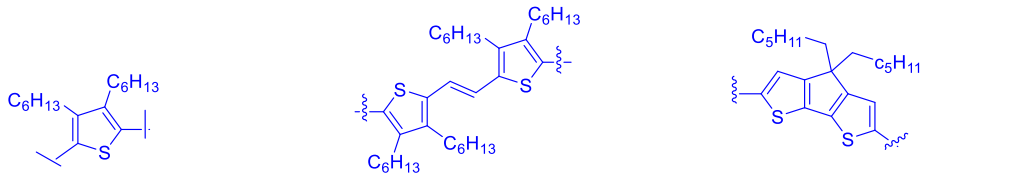

3,4-dihexylthiophene **(E)-1,2-bis(3,4-dihexylthiophen-2-yl)ethylene)** **4,4-dihexyl-4H-cyclopenta[2,1-b:3,4-b']dithiophene**

C) Study the effect of change **A** acceptor for 3-ethylrhodanine or dicyanovinylene group.

3 ethylrhodanine **dicyanovinylene**

1.4.1 Specific objectives

I. Design, synthesis and characterization of **SA1**-**2** to analyze the difference between two π conjugation linkers (3,4-dihexylthiophene and *(E)*-1,2-bis(3,4-dihexylthiophen-2-yl)ethylene), and their performance in BHJSC, with dicyanovinylene as electro withdrawing moiety.

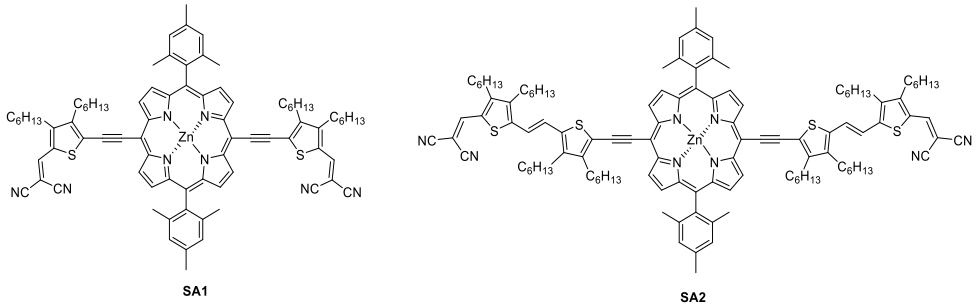

Figure 22. Molecules **SA1**-**2**

II. Design, synthesis and characterization of **SA3**-**4** to analyze 3-ethylrhodanine as electro withdrawing moiety with 3,4-dihexylthiophene and *(E)*-1,2-bis(3,4-dihexylthiophen-2-yl)ethylene as π conjugation linkers, to comparing the difference with **SA1**-**2** in the performance of BHJSC.

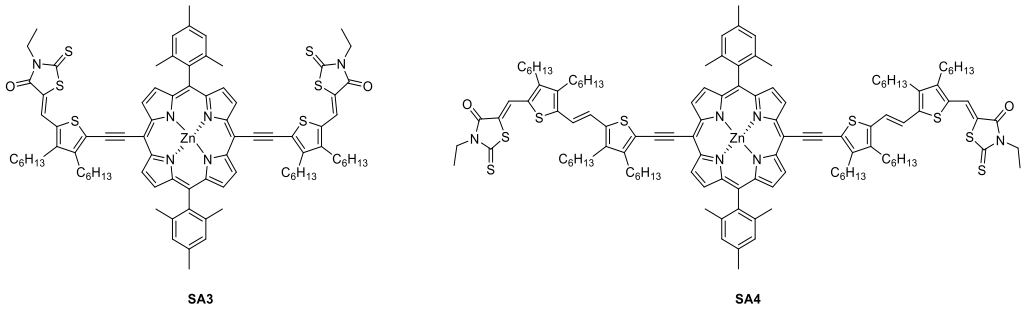

Figure 23. Molecules **SA3**-**4**

III. Design, synthesis and characterization of **SA5**-**6** to analyze the difference between dicyanovinylene and 3-ethylrhodanine as electro withdrawing, using 4,4-dihexyl-4H-cyclopenta[2,1-b:3,4-b′]dithiophene as bridge in the performance of BHJSC.

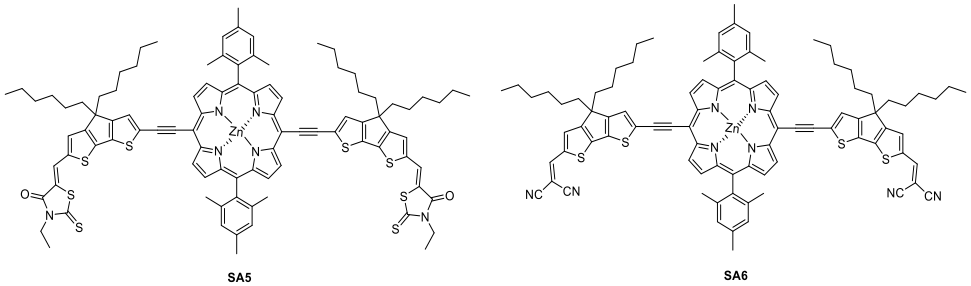

Figure 24. Molecules **SA5**-**6**

IV. Design, synthesis and characterization of bulky porphyrins to study the performance of BHJSC. **SA7**-**10** to analyze the influence of *(E)*-1,2-bis(3,4-dihexylthiophen-2-yl)ethylene and 4,4-dihexyl-4H-cyclopenta[2,1-b:3,4-b']dithiophene as conjugated linkers, with different acceptors, 3-ethylrhodanine and dicyanovinylene, in the performance of BHJSC.

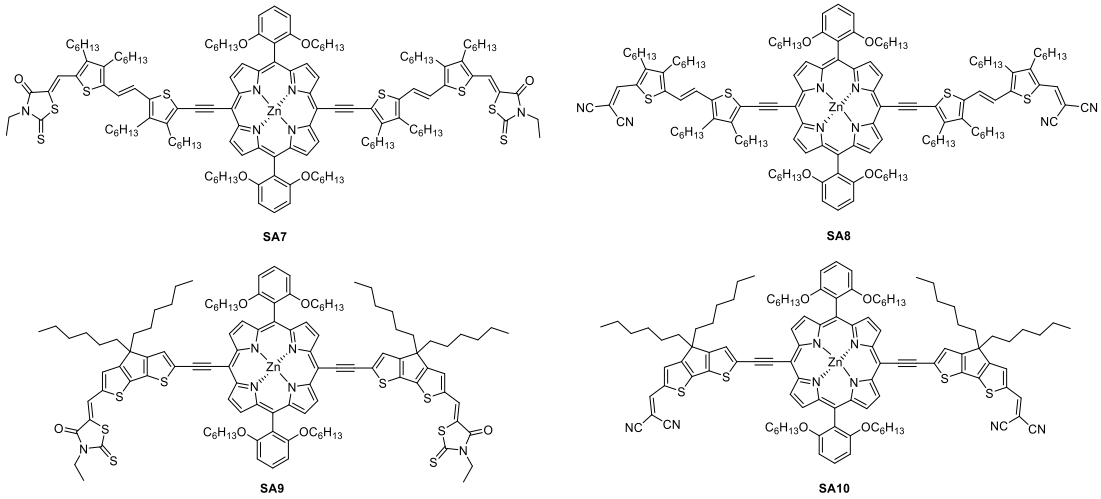

Figure 25. Molecules **SA7-10**

V. Design, synthesis and characterization of **SA11-12** to analyze a planar core with hexylthiophene moiety, and the difference between 3,4-dihexylthiophene and *(E)*-1,2-bis(3,4-dihexylthiophen-2-yl)ethylene as π conjugation linkers and 3-ethyl rhodanine as acceptor in the performance of BHJSC.

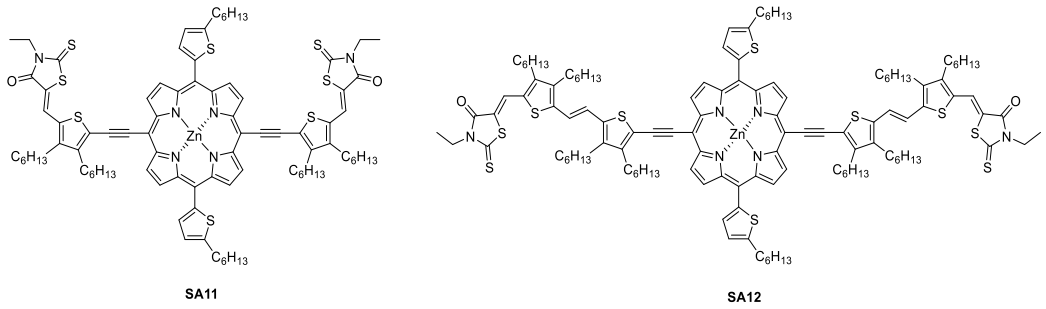

Figure 26. Molecules **SA11-12**

1.5 SA1 and SA2

1.5.1 Synthesis and characterization of SA1 and SA2

A modification of Roncali and Col[68] procedure was employed to synthesize, 3,4-dihexyl-5-iodothiophene-2-carbaldehyde (**C1**) and *(E)*-5-(2-(3,4-dihexyl-5-iodothiophen-2-yl)vinyl)-3,4-dihexylthiophene-2-carbaldehyde (**C2**), starting from 3,4-dihexylthiophene (**1TV**) (see Scheme 1).

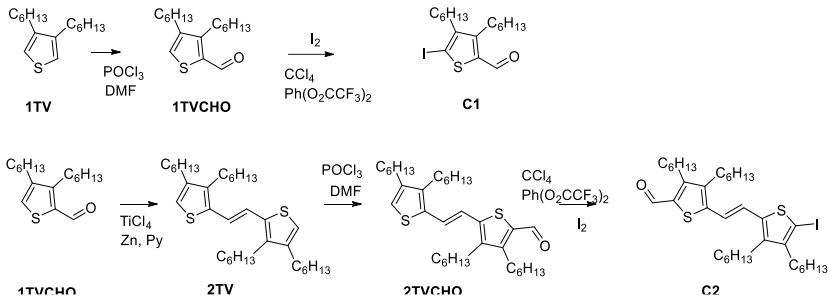

Scheme 1. Synthesis of **C1** and **C2**

3,4-Dihexylthiophene-2-carbaldehyde (**1TVCHO**) was obtained in 98% yield, starting from 3,4-dihexylthiophene (**1TV**) in the presence of *N*,*N*-Dimethylformamide (DMF) and phosphoryl chloride ($POCl_3$), the mixture was refluxed one night, according to the Vilsmeier formylation conditions. Then, following the McMurry [69] coupling procedure, 3,4-dihexylthiophene-2-carbaldehyde (**1TVCHO**), in anhydrous tetrahydrofuran (THF) and pyridine, reacted with Ti (0), formed from the reduction of titanium tetrachloride ($TiCl_4$) with zinc (Zn). The dimer *(E)*-1,2-bis(3,4-dihexylthiophen-2-yl)ethylene (**2TV**) was obtained in 88% yield. Then the Vilsmeier formylation (DMF and $POCl_3$) of the dimer allowed obtaining the monoformylation product **2TVCHO**, in 70% yield (controlling the reaction conditions to reduce the formation of bisaldehyde). In some cases *(E)*-5-(2-(3,4-dihexylthiophen-2-yl)vinyl)-3,4-dihexylthiophene-2-carbaldehyde (**2TVCHO**) is observed as isomers *Z* and *E* mixture, treated by molecular iodine and toluene refluxed 3 days to transform *Z* isomer in *E*. [70]

Iodoaldehydes **C1** and **C2** were prepared by the reaction of the aldehydes **1TVCHO** and **2TVCHO** with molecular iodine (I_2), and bistrifluoroacetoxiiodobenzene ($PhI(OCOCF_3)_2$) in 84% and 62% yield.[71] ^{1}H-NMR spectrum of **C1** shows the corresponding signal of the aldehyde at 9.90 ppm, (view experimental part Figure 138). The IR spectrum of **C1** shows the characteristic carbonyl band (C=0) at 1654 cm^{-1}, and shows the characteristics bands of the hexyl groups of *n*TV´s at 2923 and 2854 cm^{-1} and the corresponding C-I band at 674 cm^{-1} (view experimental part Figure 139). In the ^{1}H-NMR spectrum of **C2**, the signal at 6.85 ppm is observed, corresponding to the proton linked to the thiophene ring (see experimental part Figure 140). In the Infrared spectrum of **C2** the characteristic carbonyl band at 1654 cm^{-1}, and the

corresponding bands of the hexyl groups of *n*TV´s at 2923 and 2854 cm^{-1} and appears the characteristic C-I band at 698 cm^{-1} (see the experimental part Figure 141).

Molecule [5,15-bis-(trimethylsilyl)ethynyl)-10,20-dimesitylporphyrinato]zinc (II) (**P1**) was synthesized following the procedure of Scheme 2.

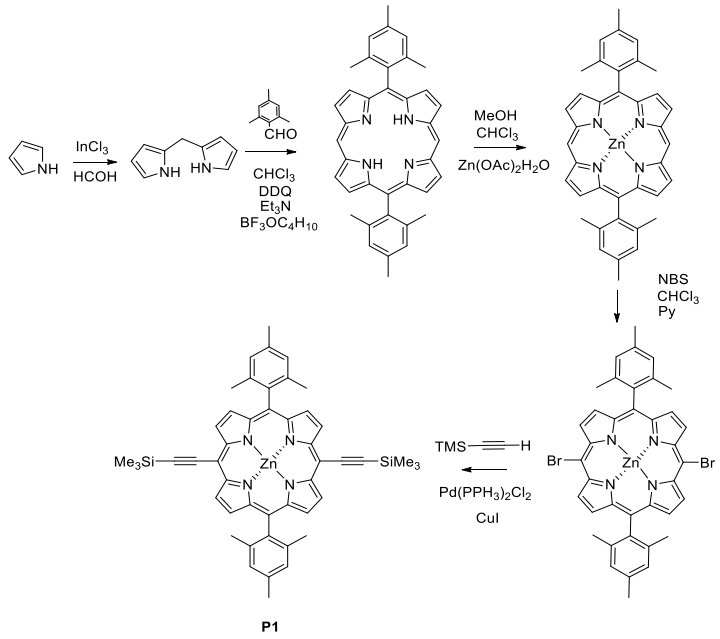

Scheme 2. Synthesis of **P1**

The synthesis to the porphyrin A_2B_2, 5,15-bis-(2,4,6-trimethylphenyl)porphyrin was initiated by the preparation of the dipyrromethane by reaction of pyrrole and paraformaldehyde, catalyzed by indium trichloride ($InCl_3$), in 72% yield.[72]

At room temperature in Ar atmosphere, 2,4,6-trimethylbenzaldehyde was added to a solution of dypirromethane and chloroform (stabilized with ethanol), before boron trifluoride diethyl etherate $BF_3O(C_2H_5)_2$ was added to produce the porphyrinogen, then this is oxidized with 2,3-dichloro-5,6-dicyano-*p*-benzoquinone (DDQ); next, trimethylamine is added to neutralize traces of nucleophilic acid. The free base porphyrin was purified through a column chromatography (silica gel and hexane:$CHCl_3$, (1:1)). 5,15-bis-(2,4,6-trimethylphenyl)porphyrin is obtained in 35% yield.[73] The ^{1}H-NMR spectrum of 5,15-bis-(2,4,6-trimethylphenyl)porphyrin shows the signals at -3.04 ppm, corresponding to two protons linked with the nitrogen rings of the free base; signals at 10.25 ppm corresponding to the two protons at the meso position of the porphyrin ring, and signals at 9.35 and 8.91 ppm corresponding to the protons at the beta position of the heterocycle ring (see in the experimental part the Figure 142).

Then, the porphyrin is treated at room temperature in $CHCl_3$ with zinc acetate dehydrated ($(ZnOAc)_2$ x$2H_2O$). The metal carrier dissociates producing an unsaturated species, combined with the dianion produced by the deprotonation of the free base of the porphyrin. [5,15-

Dimesitylporphyrinato] zinc (II) is obtained in quantitative yield.[74] The ^{1}H-NMR spectrum of [5,15-dimesitylporphyrinato] zinc does not show the signals in -3.04 ppm, corresponding to two protons linked with the nitrogen rings of the free base (see in the experimental part the Figure 143).

[5,15-dibromo-10,20-dimesitylporphyrinato] zinc (II) is obtained in 98% yield, by the treatment of the porphyrin with *N*-bromosuccinimide (NBS) in presence of catalytic quantities of pyridine. The ^{1}H-NMR spectrum of (5,15-dibromo-10,20-dimesitylporphyrinato) zinc (II) confirm the bromination, as it does not show the signals at 10.27 ppm corresponding to the protons linked to the carbons at meso position of the porphyrin ring (see in the experimental part Figure 144).

The [5,15-bis-(trimethylsilyl)ethynyl)-10,20-dimesitylporphyrinato] zinc (II) (**P1**) was synthesized by Sonogashira (cross-coupling reaction) [75] with trimethylsylilacetylene, using bis(triphenylphosphine)palladium(II) chloride ($Pd(PPh_3)_2Cl_2$), and cupper iodine (CuI) as catalyzes, to form a carbon-carbon bond between the terminal alkyne of the trimethylsylilacetylene and the porphyrin, it requires absolute inert atmosphere conditions and was reacted overnight at room temperature to obtain **P1** in 97% yield.[76] The ^{1}H-NMR spectrum of **P1** shows the presence of the signal at 0.62 ppm, these protons represent the two trimethylsylil groups incorporated to the molecule (see experimental part Figure 145). The infrared spectrum of **P1** shows the characteristic band of the triple bond C-C at 2136 cm^{-1}. The ^{13}C-NMR spectrum of **P1** shows a signal at 0.34 ppm corresponding to the carbons of the trimethylsylil groups linked to the molecule and shows at 100.63 and 101.50 ppm corresponding to the two quaternaries carbons of the triple bond (see experimental part Figure 146).

Scheme 3 illustrates the synthetic route used to obtain organic semiconducting compounds **SA1**-**2**, starting from **P1**. The trimethylsilyl group was quantitatively removed by hydrolysis with TBAF, then water was added to quench the reaction and a liquid-liquid extraction with $CHCl_3$ was realized. The solvent was evaporated affording the product without further purification. The product and the iodoaldehyde **C1** and **C2** were reacted under Sonogashira coupling with $Pd(PPh_3)_2Cl_2$ and CuI, nevertheless the yield was under 20%, and another method was tried. In this new methodology, the product reacted under Ar atmosphere with the corresponding iodoaldehyde **C1** and **C2** under Pd-catalyzed copper-free Sonogashira coupling[77] conditions, employing the air stable dative ligand triphenylarsine, which, in spite of its toxicity, has allowed the copper-free Sonogashira coupling combined with tris(dibenzylideneacetone) dipalladium(0), ($Pd_2(dba)_3$), to afford the bisaldehydes **A1-2** in 81% and 71% yields, respectively.

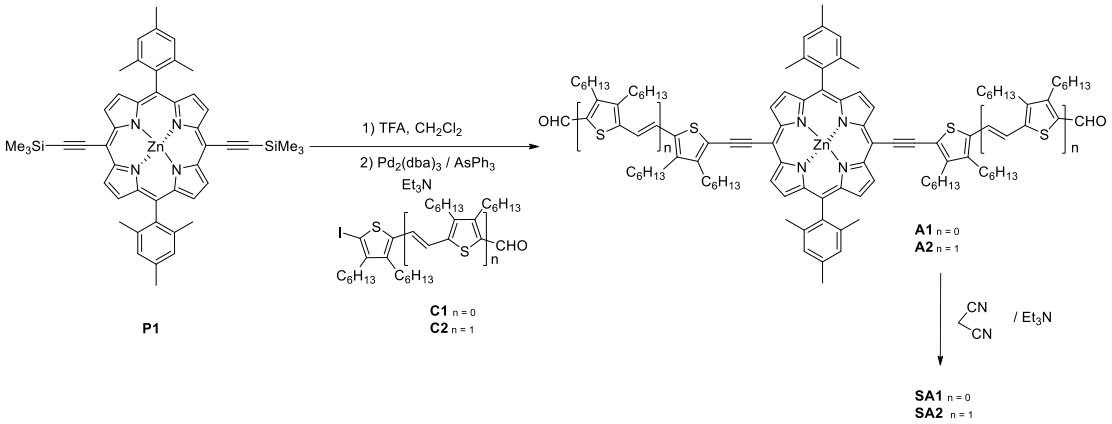

Scheme 3. Synthetic route to chromophores **SA1-2**

The ^{1}H-NMR spectra of **A1-2** show the expected signals corresponding to the aldehyde protons at 9.16 ppm and 9.56 ppm, respectively. Compound **A2**, show the *trans* configuration of the double bond, which was confirmed by a coupling constant of 15.5 Hz (see experimental part, Figure 147 and Figure 148). ^{13}C-NMR spectra of **A1-2** does not show the signals at 0.34 ppm corresponding to the two trimethylsilyl groups, substituted by the fragments of *n*TV, and show the signal at 181.24 and 181.73 ppm respectively of the carbon of the aldehyde and at 89.54 and 90.67 ppm respectively, corresponding to the triple bond carbon linked to the porphyrin and the *n*TV, the aliphatic signals appear between 32.33 and 14.02 ppm to **A1**, and 32.25 and 14.02 ppm to **A2** (see experimental part, Figure 27, Figure 149 and Figure 150).

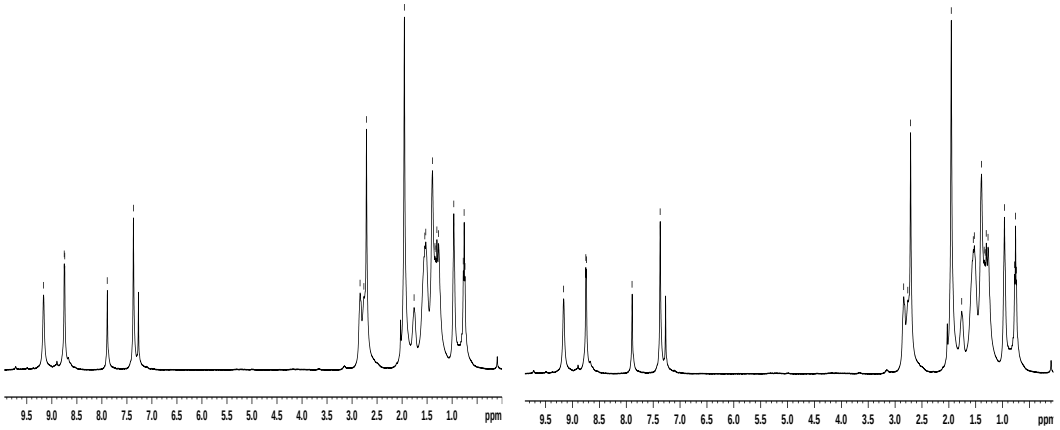

Figure 27. ^{1}H-NMR spectra (400 MHz, $CDCl_3$) of **A1** (right) A**2** (left)

The infrared spectrum of **A1** show the band at 1650 cm^{-1}, corresponding to the carbonyl group and the band C-H at 2919 and 2854 cm^{-1} corresponding to the alkyl chains of the oligomers *n*TV´s. The band at 2173 cm^{-1} is assigned to the triple bond (see experimental part Figure 155). The infrared spectrum of **A2** show the 1650 cm^{-1} band corresponding to the

carbonyl group of the aldehyde and the bands C-H at 2919 y 2854 cm^{-1} corresponding to the alkyl chain of the *n*TV´s (see experimental part Figure 155).

Finally, the target compounds **SA1** and **SA2** were obtained by Knoevenagel condensation[78] of **A1** and **A2** with malononitrile, in the presence of trimethylamine, in 81% and 79% yields, respectively. In the ^{1}H-NMR spectra of **SA1** and **SA2**, the aldehyde proton signals are not observed and new vinylic protons signals were observed at 7.89 ppm and 7.69 ppm, respectively, indicating the successful condensation (Figure 27, Figure 151, Figure 152).

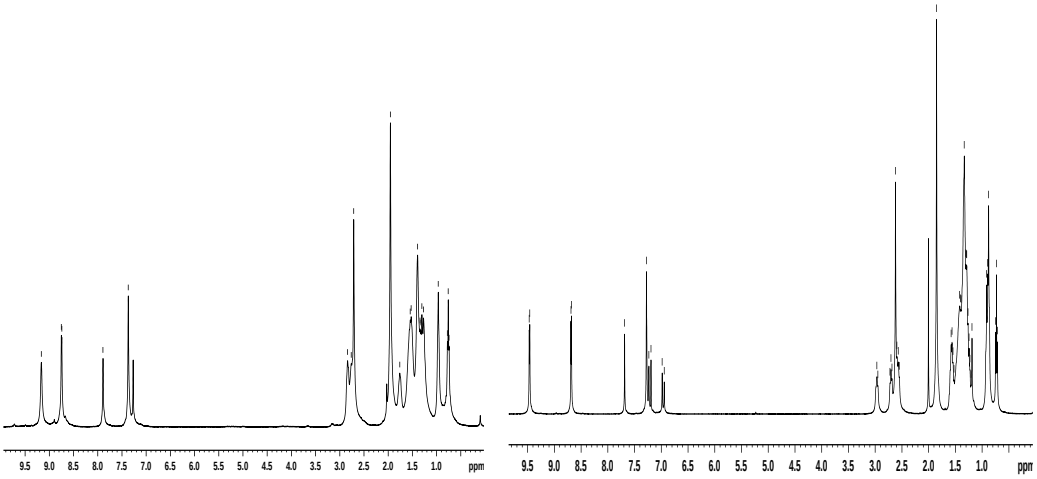

Figure 28. ^{1}H-NMR spectra (400 MHz, $CDCl_3$) of **SA1** (left) and **SA2** (right)

^{13}C-NMR spectra of **SA1**-**SA2** not show the signal at 181.24 and 181.73 ppm respectively corresponding to the precursor aldehydes, and new signals at 115.07, 113.87 and 75.19 ppm of **SA1**, and 115.59, 114.17 and 73.14 ppm of **SA2**, corresponding to the dicyanovinylene moieties, are observed (Figure 29, Figure 153, Figure 154).

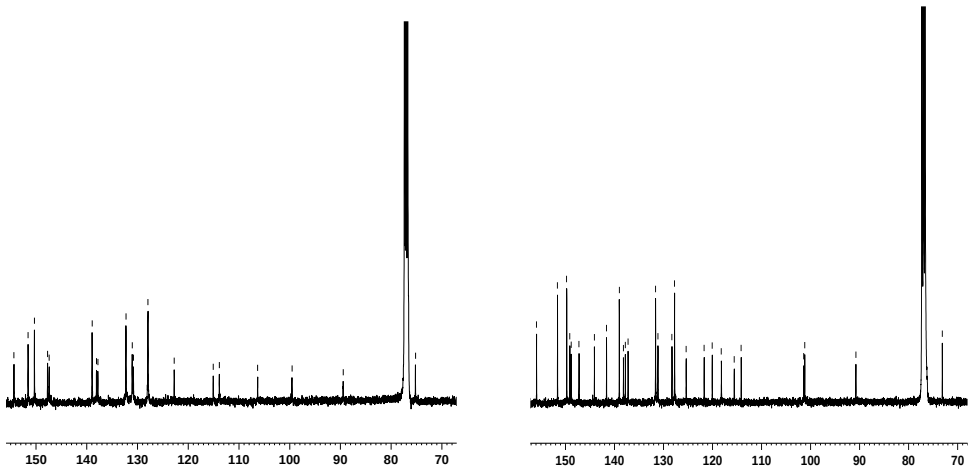

Figure 29. 70-160 ppm ^{13}C-NMR spectra (100 MHz, $CDCl_3$) of **SA1** (left) and **SA2** (right)

The infrared spectrum of **SA1** does not show the band at 1650 cm^{-1} corresponding to the precursor carbonyl of the aldehyde and a new signal is observed at 2223 cm^{-1}, corresponding to the dicyanovinyl group (Figure 30).

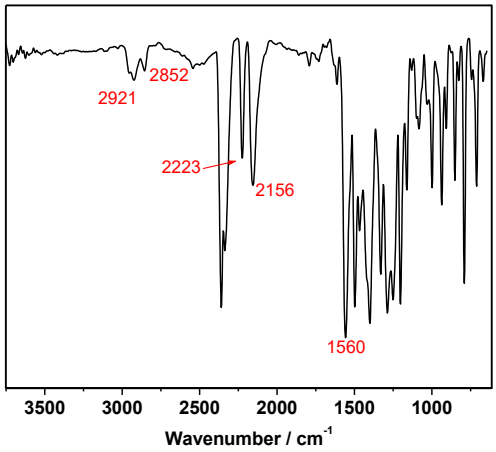

Figure 30. FT-IR spectrum of compound **SA1**

The infrared spectrum of **SA2** does not show the band at 1650 cm^{-1} corresponding to the precursor aldehyde and shows a new band at 2217 cm^{-1} assigned to the triple bond (Figure 31).

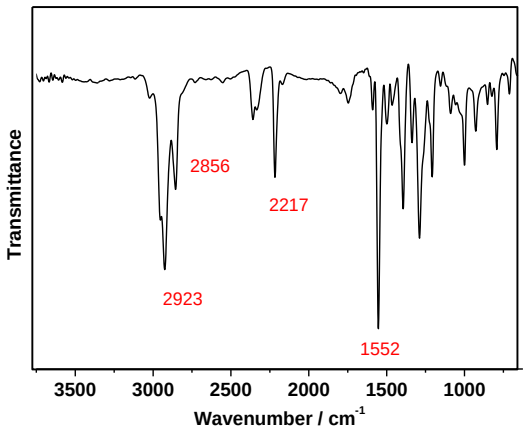

Figure 31. FT-IR spectrum of compound **SA2**

The mass spectrometry is currently the most suitable ionization technique for determining the molecular weight of compounds. The mass spectrum of compound **SA1** shows the molecular ion peak at *m/z* 1308.56 amu, (experimental part, Figure 156) and compound **SA2** exhibited the molecular ion peak at *m/z* 1861.94 amu (see experimental part, Figure 157), both values were according to the predicted exact mass.

The thermal stabilities of compounds **SA1** and **SA2** were evaluated by thermogravimetric analysis (TGA) under nitrogen with a heating rate of 10 °C/min. Compounds **SA1-SA2** display excellent thermal stabilities up to 300 ºC with decomposition temperature (Td) of 369 ºC and 374 ºC for **SA1** and **SA2**, respectively (Figure 32). **SA1-2** have thermal stabilities appropriate for photovoltaic applications.

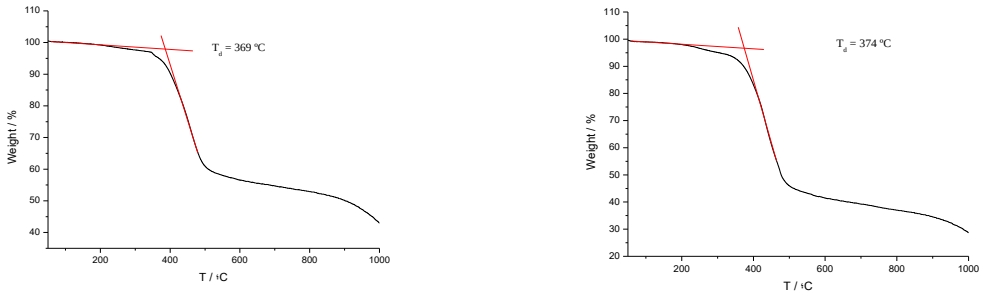

Figure 32. Thermogravimetric analysis of **SA1** (left) and **SA2** (right)

1.5.2 Optical Properties of SA1 and SA2

The UV-Vis absorption spectra of the precursor aldehydes (**A1-A2**) and those of the final compounds **SA1-2** in dichloromethane solution exhibit a panchromatic absorption in the visible region. These spectra show the Soret band (λ_{max} = 465 nm and 499 nm respectively) bathochromically shifted, with respect to the Soret band in the precursor porphyrin **P1** (λ_{max} = 435 nm). New intense broad bands are observed (at λ_{max} = 668 nm for **A1** and 698 nm for **A2**), assigned to intramolecular charge transfer (ICT) (Figure 33 and Figure 34). In solution, **SA1**-**2** show absorption ranges from 400 nm to 750 nm with a valley centered at 600 nm. The introduction of the dicyanovinyl fragments (**SA1-SA2**) lead to a bathochromic shift of both bands (λ_{max} = 497 (ε=5.26) and 705 (log ε = 5.04) for **SA1** and 542 (log ε = 5.17) and 705 nm (ε=5.24) for **SA2**) with respect to the corresponding aldehydes (**A1-A2**) as a consequence of the extension of the conjugation and due to the strong electron-withdrawing properties of the dicyanomethylene moiety **SA2** shows a higher π conjugation and a wider absorbance as result of increase thienylenevinylene length (Figure 35).

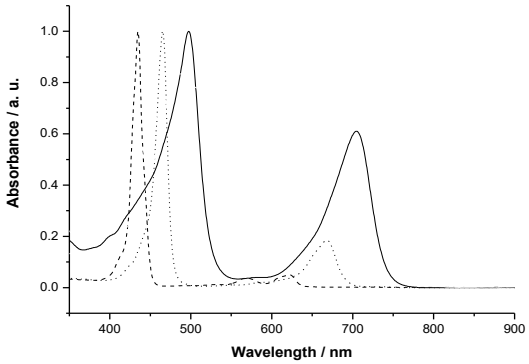

Figure 33. Normalized UV-Vis absorption spectra of **SA1** (solid line) and precursors **P1** (dashed line) and **A1** (dotted line) in dichloromethane solution (10^{-6} M)

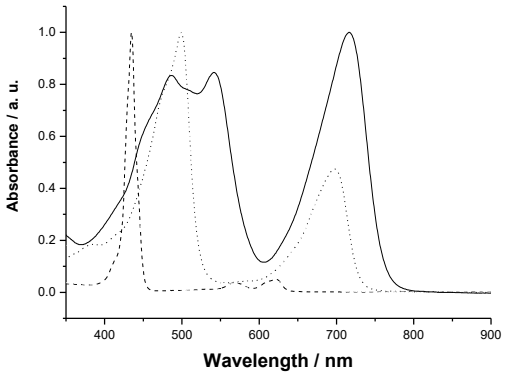

Figure 34. Normalized UV-Vis absorption spectra of **SA2** (solid line) and precursors **P1** (dashed line) and **A2** (dotted line) in dichloromethane solution (10^{-6} M)

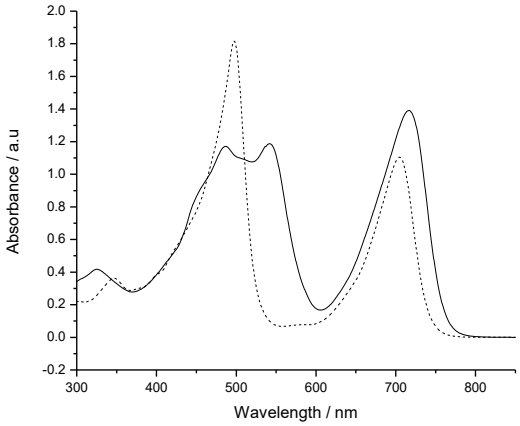

Figure 35. Absorption spectra of **SA1** (dashed line) and **SA2** (solid line) in dichloromethane solution (10^{-5} M)

Exciting **SA1** at λ_{exc} = 497 nm and **SA2** at λ_{exc} = 542 nm in dichloromethane as solvent, the fluorescence spectra display a red-shift around 30.2 nm of the emission band for compound **SA2** in comparison to **SA1**, due to the increased conjugation by one more thienylenevinylene unit. If the emission spectra of compounds **SA1** and **SA2** are compared with those of the precursor aldehydes **A1-A2**, a significant quenching of the emission is observed, attributed to more efficient electron transfer processes (see experimental part, Figure *158*).

In thin film, the absorption maximum for **SA1** is bathocromically shifted relative to those in solution, by 13 nm. **SA2** shows a pronounced absorbance between of 400-850 nm, with a red-shifted maximum of 33 nm (764 nm). These results suggest that the extended backbone in **SA2** results in stronger intermolecular π-π stacking interactions than in **SA1** (Figure 36).

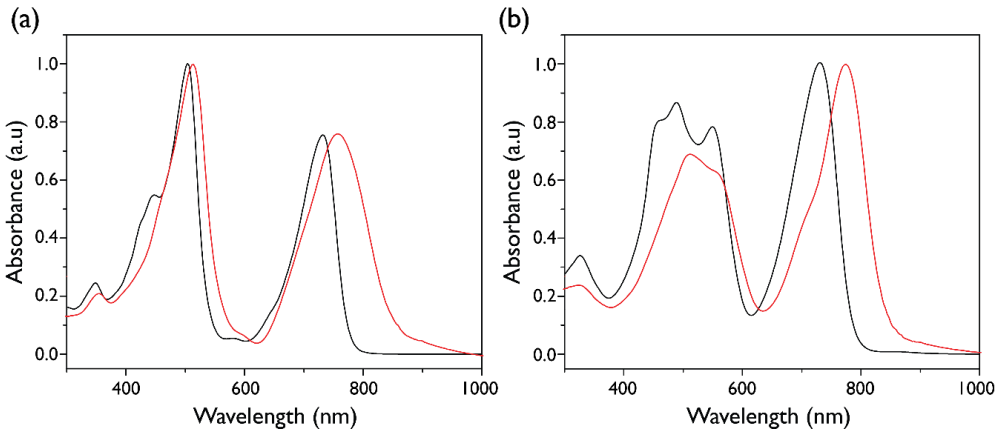

Figure 36. Normalized UV-Vis spectra of **SA1** (a) and **SA2** (b) in CH_2Cl_2 solution (black line) and in thin films (red line)

The optical properties of **SA1-2** in CH_2Cl_2 solutions as well as of their thin-films are shown in Figure 36 and the characteristics of semiconductors **SA1-2** are collected in Table 2.

Table 2. UV-Vis Absorption, Fluorescence Emission[a] and OSWV[b] data for compounds **SA1**-**2**.

	λ_{max} *soln* (nm)	*Log* (ε)	λ_{max} *film* (nm)	λ_{em} (nm)	E^1_{ox}[b, c] (V)	E^1_{red} (V)	E_{HOMO}[d] (eV)	E_{LUMO}[e] (eV)	E_g[f] (eV)
SA1	497	5.26	516	717	0.40	-1.34	-5.50	-3.76	1.74
	705	5.04							
SA2	542	5.17	734	747	0.26	-1.44	-5.36	-3.66	1.70
	731	5.24							

[a] 10^{-5} M, in dichloromethane; [b] 10^{-3} M in ODCB-acetonitrile (4:1) versus Fc/Fc^+ (E_{ox} = 0.04 V) glassy carbon, Pt counter electrode, 20 ºC, 0.1 M Bu_4NClO_4, scan rate = 100 mV s^{-1}; [c] Nonreversible processes; [d] calculated with respect to ferrocene, E_{HOMO}: –5.1 eV;[40] [e] estimated from E^1_{red}; [f] Eg= E_{HOMO} – E_{LUMO}.

1.5.3 Electrochemical Properties

The electrochemical properties of **SA1** and **SA2** were investigated using Cyclic Voltammetry (CV) and Osteryoung Square Wave Voltammetry (OSWV) in *o*-DCB-acetonitrile (4:1) (Figure 37 and Figure 38). In the anodic scan, both compounds show a first reversible one-electron oxidation wave at 0.40 V for **SA1** and 0.26 V for **SA2** (vs Fc/Fc^+ in all cases) which correspond to the first oxidation of the porphyrin. For **SA2**, the extended conjugation gives rise to a decrease of the E_{ox} value by 14 mV with respect to **SA1**. A second reversible oxidation wave is observed at 0.78 V for **SA1** and at 0.62 V for **SA2**. Compound **SA2** shows two more non reversible oxidation waves at 0.93 and 1.02 V attributed to the oxidation of the thienylenevinylene moieties. The estimated E_{HOMO} values were calculated with respect to ferrocene as reference (E_{HOMO}: -5.1 eV)[79] and were determined to be -5.50 eV for **SA1** and -5.36 eV for **SA2**, in good agreement with the oxidation potentials. Low-lying HOMO levels should result in high open-circuit voltages (V_{OC}) and are, therefore, desired.[80]

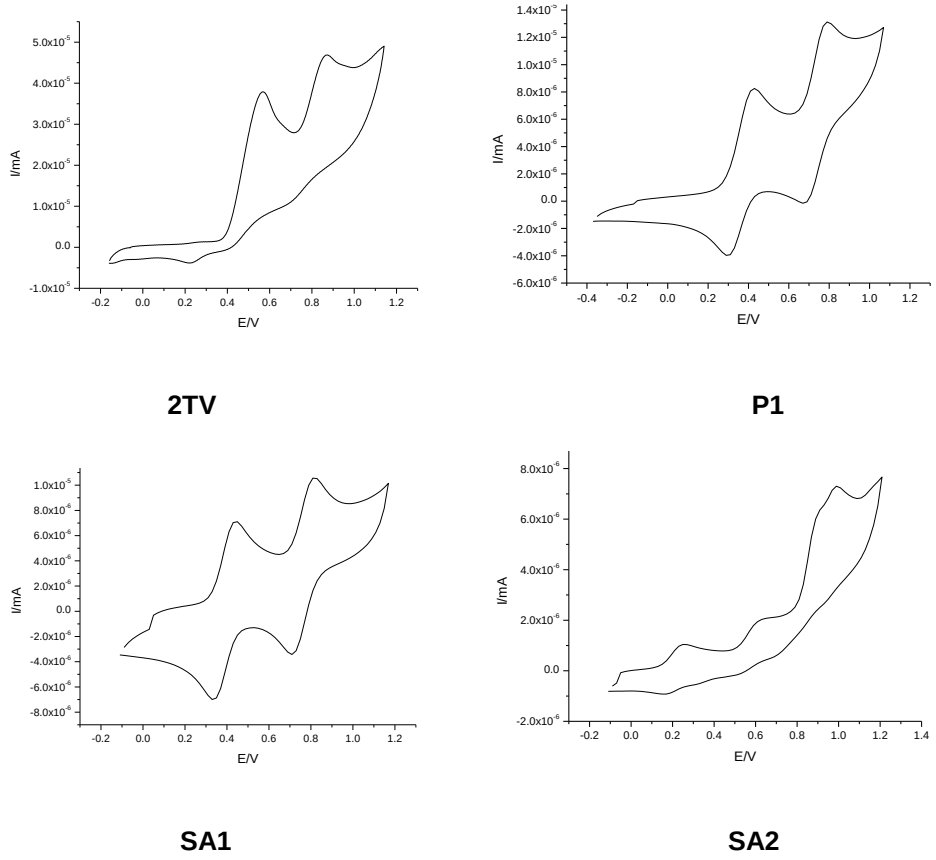

Figure 37. CV plot of compounds **SA1**-**2** and precursors **P1** and **2TV** (anodic window)

Additionally **SA1-2** show a first reduction potential at -1.34 and -1.44 V respectively. Therefore E_{LUMOs} of **SA1-2** (calculated by electrochemical), are higher than E_{LUMO} of PCBM (-3.9 eV), with values of -3.76 and -3.66 eV for **SA1** and **SA2**, respectively. The HOMO-LUMO gaps, electrochemical determined, are as narrow as 1.74 and 1.70 eV for **SA1** and **SA2**, respectively. Hence, the LUMO energy levels of these small-molecules match quite well the LUMO energy of

$PC_{61}BM$ (-3.9 eV) and $PC_{71}BM$ (-4.0 eV), which suggest an energetically favorable electron transfer from **SA1** and **SA2** to the acceptor moiety that should in turn favor the exciton dissociation.

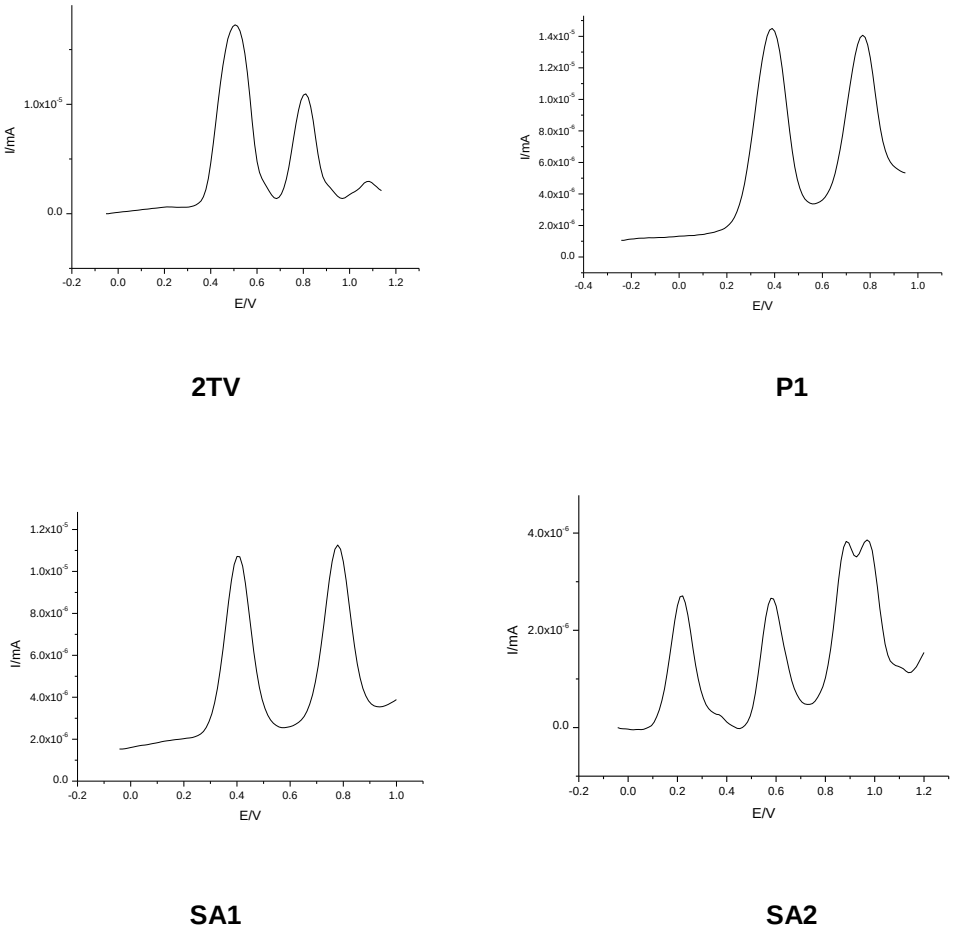

Figure 38. OSWV of compounds **SA1**-**2** and the precursors **2TV** and **P1** (anodic window)

1.5.4 Theoretical Calculations

Theoretical calculations were carried out by density functional (DFT) at the B3LYP 6-31G* level.

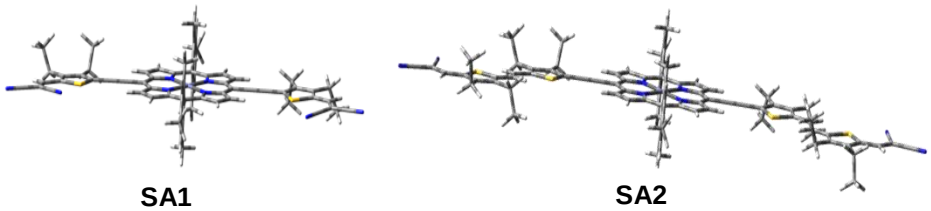

Figure 39. Optimized geometries of **SA1**-**2**

The optimized structure of both **SA1-2**, show that the core is almost perfectly flat, with the aryl groups bounded to the porphyrin core being perpendicular to the macrocycle (dihedral

angle of 90º), while the thienylenevinylene fragments are almost in the same plane with respect to the porphyrin rings with a dihedral angle around 0.5º. This planarity allows an extension of the conjugation between the porphyrin and the dicyanovinylene fragments. The bond lengths of the π-conjugated bridge between the porphyrin and the acceptor units are around 1.40 Å, both for single and double bonds, revealing a quinoid character. This fact suggests some zwitterionic contribution to the ground state.

The distribution of the orbital coefficients of the HOMO and LUMO states (Figure 40) show that the charge density of the HOMO of **SA1-2** is delocalized over the whole conjugated system, the porphyrin and thienylenevinylene moieties. Similar to the HOMO, the LUMO spreads over the π-conjugated system. Since both orbitals, HOMO and LUMO (Figure 40) are somewhat overlapped, this favors the HOMO to LUMO electronic transitions.

The theoretical HOMO-LUMO gaps are similar for both dyes, being slightly lower for compound **SA2** (ΔE = 1.72 eV) than for **SA1** (ΔE = 1.87 eV). This fact is mainly due to the more extended conjugation, increasing the HOMO level in **SA2** and is related to the bathochromic shift of the maximum absorption wavelength of compound **SA2** with respect to that of dye **SA1** (according with the experimental data), which improves the light harvesting behaviour. Finally, the offset between the LUMO of the donor (**SA1** or **SA2**) and the LUMO of the acceptor ($PC_{61}BM$ or $PC_{71}BM$),[81] from 0.54 eV to 1.01 eV, ensures efficient exciton dissociation at the D/A interface.

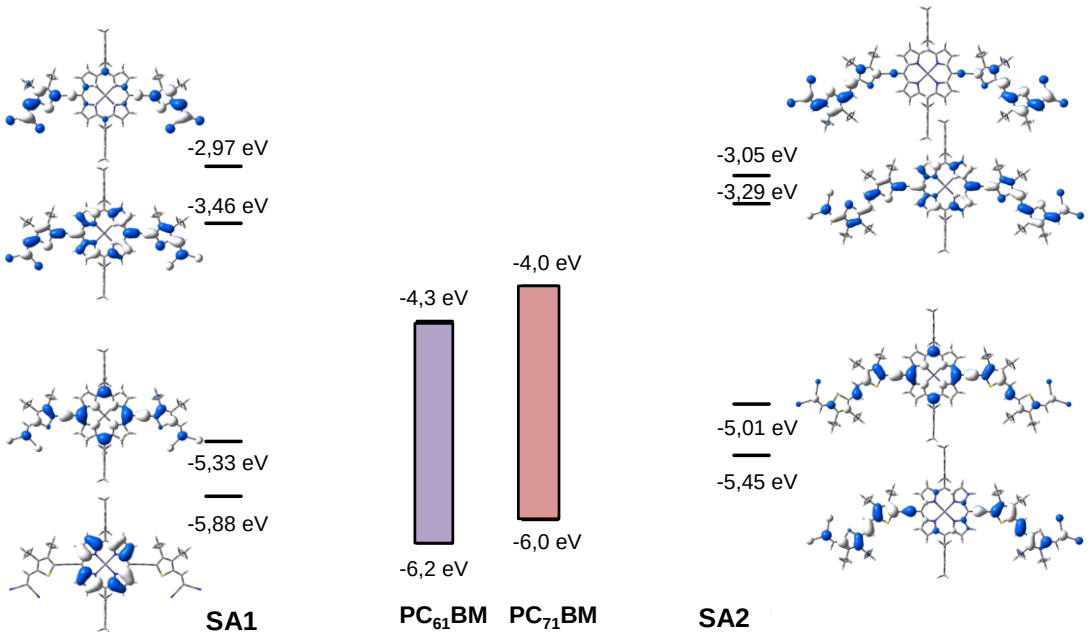

Figure 40. Electronic density contours and energy levels for HOMO-1, HOMO, LUMO, and LUMO+1 calculated at the B3LYP/6-31G** level for dyes **SA1** and **SA2** compared with the energy levels of the $PC_{61}BM$ and $PC_{71}BM$ frontier orbitals

1.5.5 Photovoltaic properties

Thanks to the collaboration with Professor Luis Echegoyen, the solar cells were optimized at the University of Texas, at El Paso, $PC_{61}BM$ and $PC_{71}BM$ were purchased from American Dye Source and used as received. The ITO-coated glasses (Delta technologies, 5-15 Ω) were pre-cleaned stepwise by ultracentrifugation 15 minutes in detergent, deionized water, methanol, acetone and iso-propanol and then by a 30 minutes UV-ozone treatment. A thin layer of PEDOT:PSS (Clevios P VP AI 4083, 5000 rpm, 30 seconds, ≈ 30 nm) was spin-coated onto the ITO and baked at 150 ºC for 15 minutes in air. Subsequently, the active layer (**SA1/SA2**:$PC_{61}BM$, 30 mg/mL) with varying weight ratios (1:4, 1:2 and 1:1) was spin-coated at 1500 rpm from chlorobenzene solutions. **SA1** or **SA2**, **SA1/SA2**:$PC_{71}BM$ (1:2, 30 mg/mL) was spin-coated at 1500 rpm. Then the devices were transferred to a N_2 filled glove box (<0.1 ppm O_2 and < 0.1 ppm H_2O) for further processing. The photoactive layer was annealed at 80 ºC for 10 minutes followed by thermal evaporation of 20 nm of calcium and 80 nm of aluminum (1×10^{-6} mbar) with a shadow mask of 0.4 cm^2. The photovoltaic properties were measured under 1 sun, AM1.5G (air mass 1.5 global) spectrum from a solar simulator (Photo Emission Tech CT100) at 100 mW/cm^2. The J_{SC}–V_{OC} characteristics were recorded with a Keithley 2420 source unit.

To explore the potential photovoltaic (PV) properties of **SA1** and **SA2**, solar cells were fabricated using the conventional sandwich structure of ITO/poly(3,4-ethylenedioxythiophene):polystyrenesulfonate (PEDOT:PSS)/small molecule: acceptor/Ca/Al. The active layer was spin-coated from chlorobenzene solutions. The ratio of **SA1** and **SA2** to $PC_{61}BM$ was adjusted, ranging from 1:1 to 1:4 (w/w), and the optimized value was found to be 1:2 for both of them. The optimized ratio was employed in a blend of **SA1** and **SA2** with $PC_{71}BM$. The current density-voltage (*J-V)* characteristics and the external quantum efficiency (EQE) for the conventional device are shown in Figure 41 a-d and the performance parameters are summarized in Table 3 as a function of the weight ratios of Donor:$PC_{61}BM$.

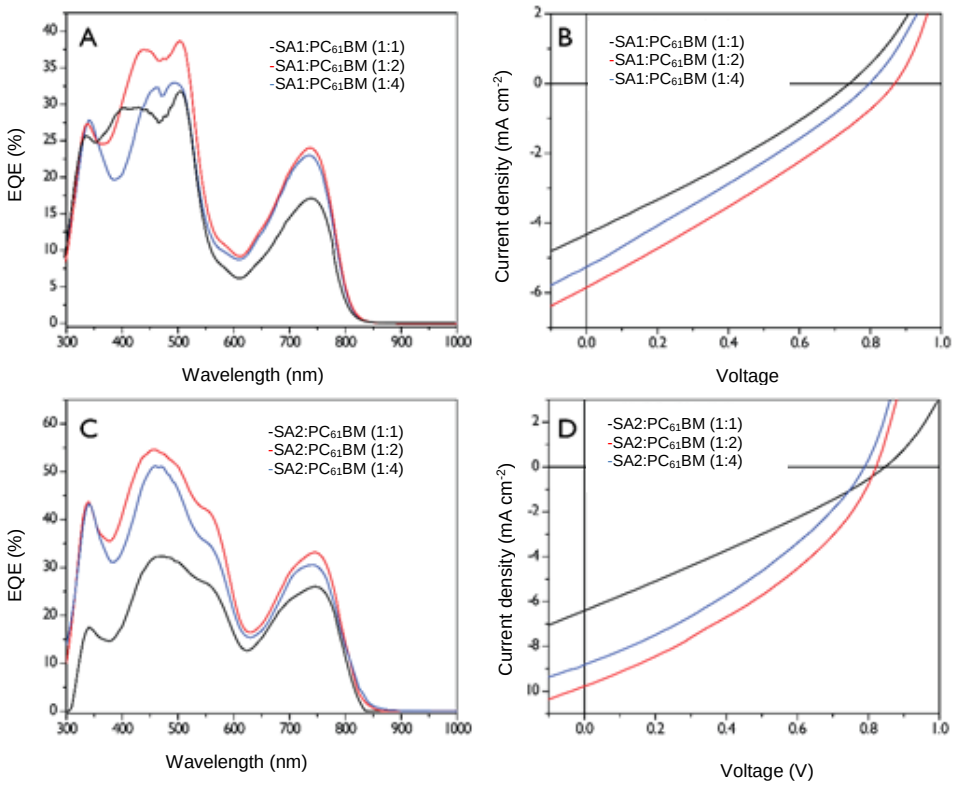

Figure 41. EQE and *J-V* characteristics of the SMBHJ for **SA1** and **SA2** blending with $PC_{61}BM$ at different ratios

Figure 41 b and Figure 41 d illustrate the best photovoltaic performances at varying D/A ratios. Photovoltaic devices containing **SA1**:$PC_{61}BM$ exhibited high V_{OC} (0.86 V) at the optimized blend ratio of 1:2 w/w, with a short circuit current (J_{SC}) of 5.72 mA cm^{-2}, and a fill factor (FF) of 28.4% for an average PCE of 1.45%. Increasing as well as decreasing the amount of $PC_{61}BM$ resulted in a lower PCE. In contrast, photovoltaic devices incorporating a blend of **SA2** and $PC_{61}BM$ exhibited an average PCE of 2.70%, with a V_{OC} of 0.82 V, FF of 35.2% and a noteworthy J_{SC} of 9.79 mA cm^{-2}, as consequence of efficient light absorbing properties of **SA2**. Average values were taken from 12 devices. The high values observed for the V_{oc} using **SA1** are in agreement with the deeper HOMO level of **SA1** (-5.50 eV) *vs* **SA2** (-5.36 eV). The electron acceptor ($PC_{61}BM$) was replaced by $PC_{71}BM$ due to the broader absorbance and the higher extinction coefficient of the latter in the visible range. SMBHJ devices were fabricated with an architecture of ITO/PEDOT:PSS/**SA2** or **SA1**:$PC_{71}BM$ (1:2 w/w)/Ca/Al. Photovoltaic devices based on **SA2** and $PC_{71}BM$ yielded an increased PCE of 3.21%, a remarkable 14% improvement, with an average J_{SC} of 10.83 mA cm^{-2}, V_{OC} of 0.82 V and a slightly improved FF (Figure 42). Surprisingly, no improvement was observed employing **SA1**:$PC_{71}BM$ (1:2 w/w) as the photoactive layer (Figure 43). In order to support the performances of the above devices, incident photo-to-current efficiency (IPCE) measurements were also conducted. As shown in Figure 41 b, the IPCE response of **SA1** with $PC_{61}BM$ covers the visible spectrum ranging, from 300 nm to 800 nm, which matches the absorption spectra. The devices incorporating **SA2** exhibited more efficient photoconversion efficiency than those based on **SA1**, due to broader

and higher IPCE response in the 300-600 nm range. Therefore, the addition of an extra unit of thienylenevinylene leads to a stronger light-harvesting which results in a significant improvement in the power conversion efficiency. In addition, the IPCE values were further improved for a **SA2**:$PC_{71}BM$ blend with a remarkable IPCE of 60% at 427 nm (Figure 42). The theoretical J_{SC} values integrated from the EQEs are in good agreement with those experimentally observed in all cases (± 5% mismatch).

Table 3. Summary of the photovoltaic performance of **SA1** and **SA2** blended with $PC_{61}BM$ and $PC_{71}BM$ under the illumination of AM1.5G, 100 mW/cm^2.

Active layer	*V_{OC} (V)*	*J_{SC} (mA cm^{-2})*	*FF (%)*	*PCE [Highest] (%)*
***SA1**:$PC_{61}BM$ (1:4)*	0.78±0.03	5.38±0.33	27.8±0.27	1.16±0.1[1.26]
***SA1**:$PC_{61}BM$ (1:2)*	0.86±0.01	5.67±0.12	28.1±0.22	1.36±0.1[1.48]
***SA1**:$PC_{61}BM$ (1:1)*	0.63±0.02	4.62±0.13	29.1±0.21	0.84±0.1[0.91]
***SA2**:$PC_{61}BM$ (1:4)*	0.79±0.03	8.41±0.21	33.2±0.29	2.21±0.1[2.34]
***SA2**:$PC_{61}BM$ (1:2)*	0.82±0.02	9.44±0.26	35.0±0.22	2.70±0.1 [2.82]
***SA2**:$PC_{61}BM$ (1:1)*	0.84±0.02	5.84±0.30	27.3±0.21	1.35±0.1[1.48]
***SA1**:$PC_{71}BM$ (1:2)*	0.84±0.01	5.56±0.12	26.4±0.20	1.24±0.1[1.34]
***SA2**:$PC_{71}BM$ (1:2)*	0.82±0.01	10.83±0.24	35.7±0.24	3.16±0.1 [3.21]

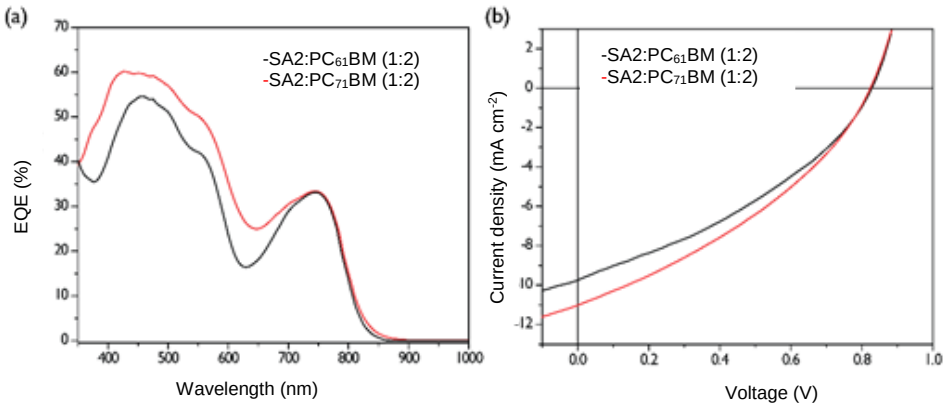

Figure 42. EQE (a) and *J-V* (b) characteristics of the SMBHJ for **SA2** blending with $PC_{61}BM$ and $PC_{71}BM$ in a 1:2 ratio

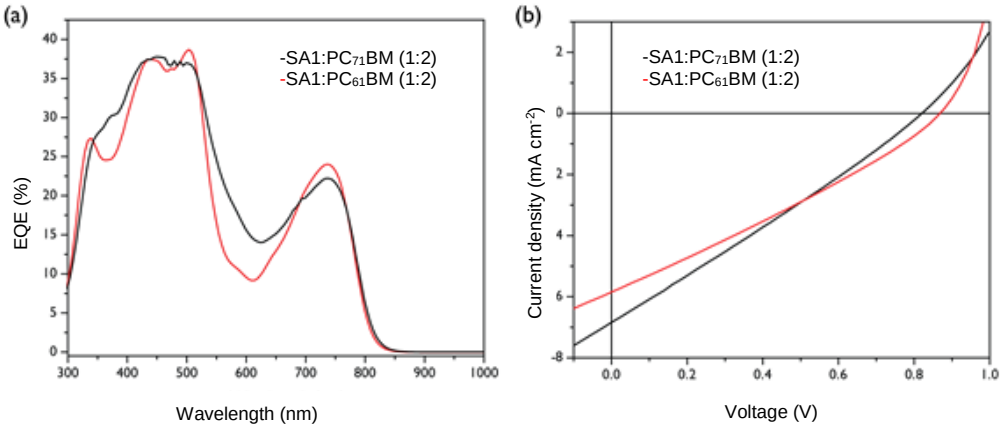

Figure 43. EQE (a) and *J-V* (b) characteristics of the SMBHJ for **SA1** blending with PC61BM and $PC_{71}BM$ in a 1:2 ratio

Inspecting the morphology of the photoactive layers by atomic force microscopy using the tapping mode (AFM) provided some explanation for lower power conversion efficiencies obtained for the photovoltaic devices[82] incorporating **SA1** and **SA2** when blended with $PC_{61}BM$ and $PC_{71}BM$ (Figure 44). The topography images for $PC_{61}BM$ and $PC_{71}BM$ reveal the formation of coarse morphologies with faceted islands features showing a root-mean-square roughness (rms) of 1.9 and 1.7 nm, respectively. Large aggregates of several hundred nanometers were observed which limit the exciton dissociation efficiencies and the charge transport, explaining the lower FF and J_{SC} values measured for these devices. On the other hand, the surface morphology of devices containing **SA2**:$PC_{61}BM$ and **SA2**:$PC_{71}BM$ exhibit a smoother surface topography (rms of 1.0 and 0.9 nm, respectively) with smaller aggregate sizes indicating better morphological features for exciton dissociation at the donor-acceptor interfaces, which correlate with the higher FF and J_{SC} and higher power conversion efficiencies observed.

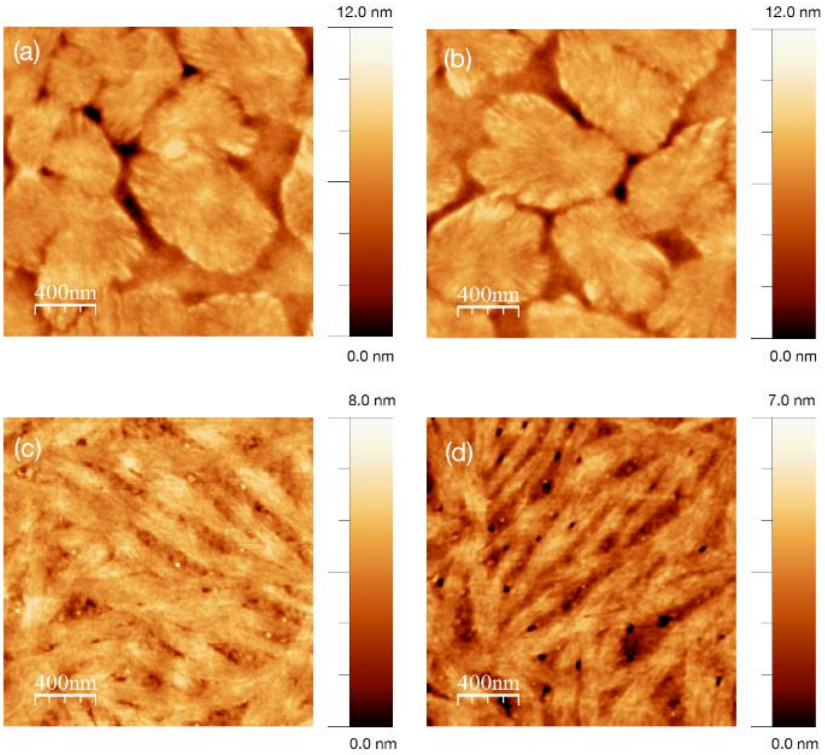

Figure 44. Tapping mode AFM height images (2 μm x 2 μm) of **SA1** films spin-coated from chlorobenzene blended with (a) PC61BM and (b) PC71BM; Tapping mode AFM height images (2 μm x 2 μm) of **SA2** films spin-coated from chlorobenzene blended with (c) $PC_{61}BM$ and (d) $PC_{71}BM$

1.6 SA3 and SA4

1.6.1 Synthesis and characterization of SA3 and SA4

Scheme 4 illustrates the synthetic route used to obtain organic semiconductor compounds **SA3** and **SA4**, starting from the previously reported molecules **A1-2** (see chapter 1 section 1.5.1). The compounds **SA3-4** were obtained by Knoevenagel condensation. Next, 3-ethylrhodanine was added to a solution of **A1**-**2** in $CHCl_3$, then two drops of piperidine were added and the solution was refluxed overnight. The solvent was evaporated and the product was purified by chromatography column with silica gel eluted with hexane and dichloromethane (1:1), and then was recrystallized using CH_2Cl_2: MeOH to afford the products **SA3-4** in 82% and 45% yields, respectively. All compounds were satisfactorily characterized by ^{1}H and ^{13}C-NMR, FT-IR spectroscopies and MALDI-MS spectrometry (see the experimental section).

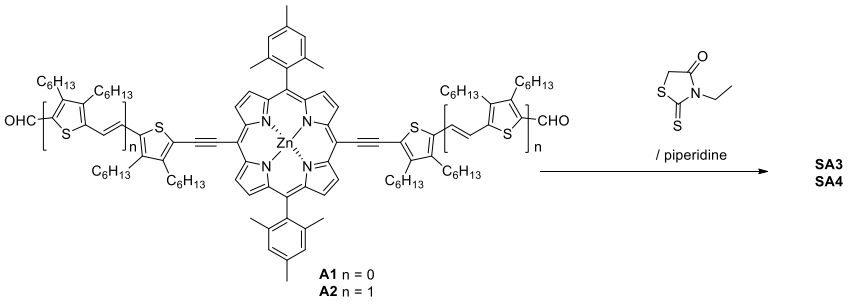

Scheme 4. Synthetic route to molecules **SA3**-**4**

^{1}H-NMR spectra of **SA3** and **SA4**, show the successful condensation with the new vinyl protons signals at 8.00 ppm and 7.95 ppm, respectively (Figure 45).

The mass spectrum of compound **SA3** showed the molecular ion peak at *m/z* 1498.77 amu, and the compound **SA4** exhibited the molecular ion peak at *m/z* 2051.69 amu, (Figure 165 and Figure 166). In the infrared spectra of **SA3** and **SA4** do not appear the carbonyl band at 1650 cm^{-1} (corresponding to the precursor) and have been observed new bands at 1230 cm^{-1} and 1700 cm^{-1} in **SA4** and 1700 cm^{-1} and 1203 cm^{-1} in **SA3**. These bands correspond to the thiocarbonyl and to the amide groups, respectively, in 3-ethylrhodanine (see in the experimental part, Figure 164).

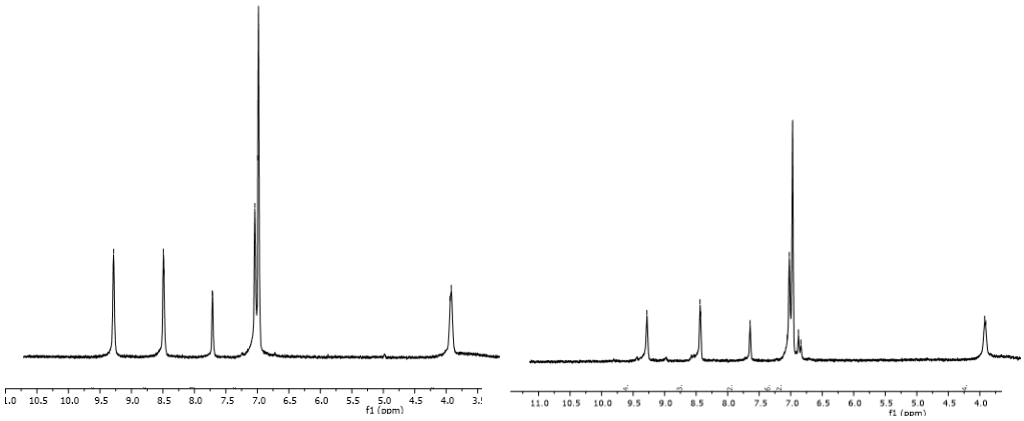

Figure 45. 3 to 11 ppm ^{1}H-NMR spectra (400 MHz, $CDCl_3$) of **SA3** (left) and **SA4** (right)

TGA measures were done and provided information about the good thermal stabilities of **SA3** and **SA4** with decomposition temperatures of 377 ºC and 355 ºC respectively (Figure 46).

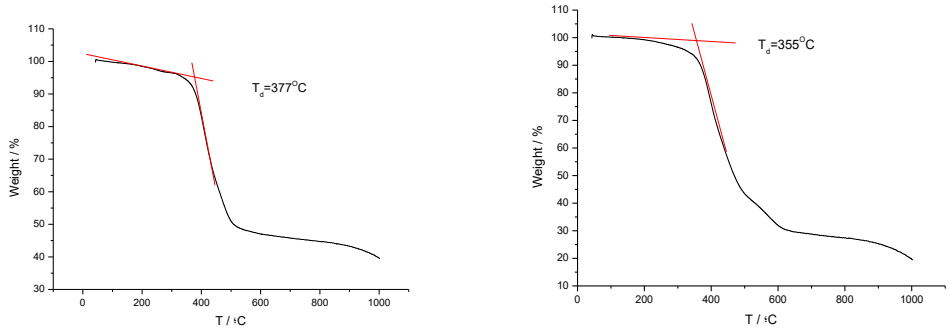

Figure 46. Thermogravimetric analysis of **SA3** (left) and **SA4** (right)

1.6.2 Optical Properties

Optical properties of **SA3** and **SA4** in CH_2Cl_2 solution (Figure 49), as well as in thin-films are collected in Table 4.

The UV-Visible spectrum of **SA3** in CH_2Cl_2 exhibited the characteristic absorption pattern of a Zn-chelated porphyrin having an intense Soret band at 507 nm (log ε =5.27), red shifted 42 nm in comparison to the precursor aldehyde **A1**; and **SA3** show as well an intermolecular charge transfer (ITC) intense band at 709 nm (log ε =5.09), (Figure 47).

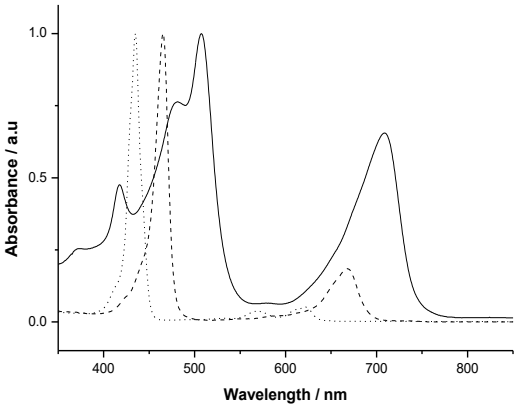

Figure 47. Normalized UV-Vis absorption spectra of compounds **SA3** (solid line) and precursors **P1** (dotted line), **A1** (dashed line) dichloromethane

The extension of the conjugation on the bridge by introduction of a new thienylenevinylene unit show a significant impact on the absorption spectrum of **SA4** leading to a red-shifted of the Soret band to 547 nm (log ε =5.02), this value is shifted 48 nm in comparison to the precursor **A2**; and **SA4** spectrum shows an ITC band lightly red shifted respecting to **SA3** with maximum at 716 nm (log ε =5.02), (Figure 48).

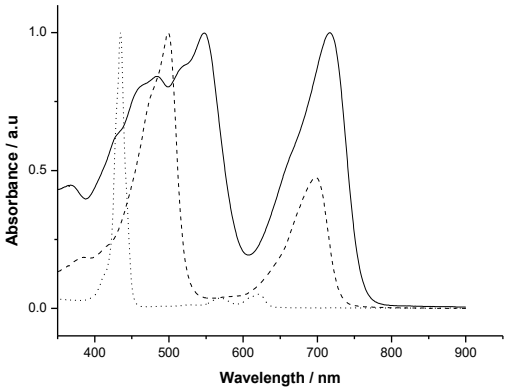

Figure 48. Normalized UV-Vis absorption spectra of compounds **SA4** (solid line) and precursors **P1** (dotted line), **A2** (dashed line) dichloromethane

The intense broad ITC band **SA3-4** is also red-shifted, 41 and 20 nm respectively to their precursors **A1-2**. In solution, **SA3** and **SA4** show absorption ranges from 300 nm near to 800 nm with a valley between 558-601 nm for **SA3** and at 608 nm for **SA4**. The introduction of the 3-ethylrhodanine fragments (**SA3-SA4**) lead to a bathochromic shift and broad absorption as a consequence of the extension of the conjugation.

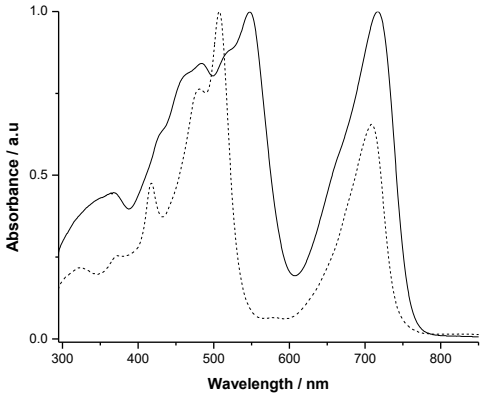

Figure 49. Normalized absorption spectra of **SA3** (dashed line) and **SA4** (solid line) in dichloromethane solution (10^{-5} M)

In the solid state, the absorption maximum of **SA3** and **SA4** is shifted to the red side of the spectra, relative to those in CH_2Cl_2 solution, by 59 and 48 nm respectively, as consequence of the π-π stacking in solid state.

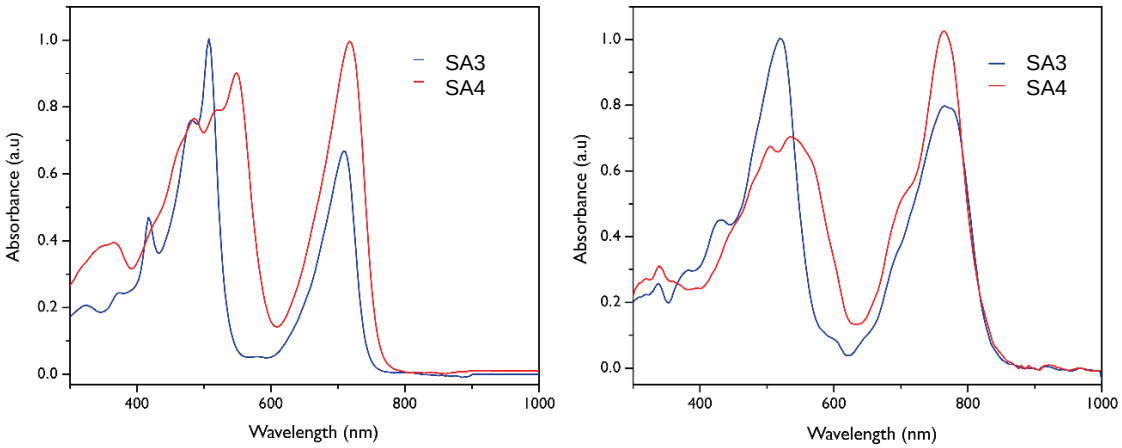

Figure 50. Normalized UV-Vis spectra in CH_2Cl_2 solution (left) and thin films (right) **SA3** (blue line) and **SA4** (red line)

The fluorescence spectra in dichloromethane display a red-shift of the emission band for compound **SA4** (λ_{exc}= 483 nm) in comparison to that for **SA3** (λ_{exc}= 417), around 19 nm, due to the increased conjugation by the new thienylenevinylene unit (Figure 51).

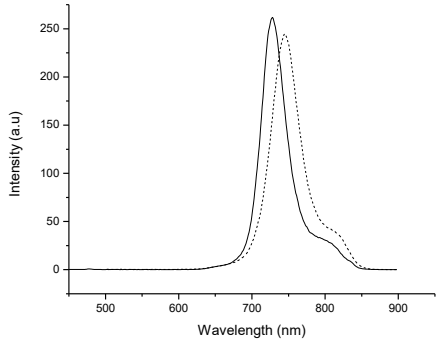

Figure 51. Fluorescence spectra were recorded in CH_2Cl_2 (λ_{exc}= 417 nm for **SA3**, and λ_{exc}= 483 nm for **SA4**)

Table 4. UV-Vis Absorption, Fluorescence Emission[a] and OSWV[b] data for compounds **SA3** and **SA4**.

	λ_{max} *soln* (nm)	*log* (ε)	λ_{max} *film* (nm)	λ_{em} (nm)	E^1_{ox}[b, c] (V)	E^1_{red}	E_{HOMO}[d] (eV)	E_{LUMO}[e] (eV)	E_g[f] (eV)
SA3	481	5.16	429	727	0.26	-1.52	-5.36	-3.58	1.78
	507	5.27	519						
	709	5.09	765						
SA4	482	4.95	504	746	0.14	-1.60	-5.24	-3.50	1.74
	547	5.02	534						
	716	5.02	765						

[a] 10^{-5} M, in dichloromethane; [b] 10^{-3} M in ODCB-acetonitrile (4:1) versus Fc/Fc^+ (E_{ox} = 0.04 V) glassy carbon, Pt counter electrode, 20 ºC, 0.1 M Bu_4NClO_4, scan rate = 100 mV s^{-1}; [c] reversible processes; [d] calculated with respect to ferrocene, E_{HOMO}: –5.1 eV; [e] estimated from E^1_{red}; [f] Eg= E_{HOMO} – E_{LUMO}.

1.6.3 Electrochemical Properties

Electrochemical measures of **SA3** and **SA4** were done in *o*-DCB-acetonitrile (4:1), then HOMO-LUMO orbitals were calculated based on the reduction and oxidation potentials (Table 4, Figure 52 and Figure 53). **SA3-4** show a first reversible oxidation wave at 0.25 V and 0.13 V respectively, which are assigned to the first oxidation of the porphyrin. Following a similar pattern that in **SA1-2,** for **SA4** the extended conjugation gives rise to a decrease of the E_{ox} value by 12 mV with respect to **SA3**. A second reversible oxidation wave is observed at 0.65 V for **SA3** and at 0.42 V for **SA4**. Compound **SA4** shows two more non reversible oxidation waves at 0.63 and 0.88 V attributed to the oxidation of the thienylenevinylene moieties. The estimated E_{HOMO} values were calculated with respect to ferrocene as reference (E_{HOMO}: -5.1 eV) and were determined to be -5.36 eV for **SA3** and -5.24 eV for **SA4**.

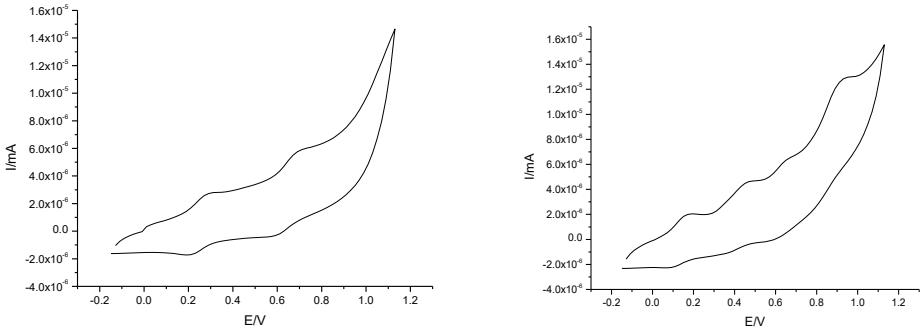

Figure 52. CV of compounds **SA3** (right) and **SA4** (left) (anodic window)

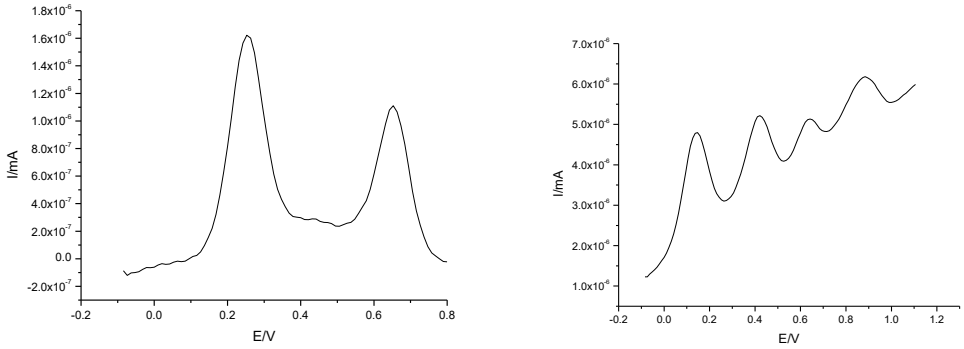

Figure 53. OSWV of compounds **SA3** (right) and **SA4** (left) (anodic window)

Approximate LUMO energies of both compounds were calculated from the first reduction potential, and these values are higher than that E_{LUMO} of $PC_{71}BM$ (-4.0 eV), with values of -3.58 and -3.50 eV for **SA3** and **SA4** respectively, which suggest an energetically electron favorable transfer from **SA3**-**SA4** to the acceptor molecule that should turn to the exciton dissociation. The HOMO-LUMO gaps, electrochemical determined, are as narrow as 1.78 and 1.74 eV for **SA3** and **SA4**, respectively.

1.6.4 Theoretical Calculations

In order to go inside into the structure and the electronic properties, theoretical studies were done by performing density functional theory (DFT) calculations at the B3LYP 6-31G* level in vacuo using Gaussian 03W.

The best geometry obtained of **SA3** and **SA4**, show that π conjugated system, porphyrin macrocycle and bounded thienylenvinylene monomers are planar. The dihedral angles of this system are around 4º. The calculated dihedral angle of the *N*-ethylrhodanine with the thiophene ring is $\theta \approx 1.5$º. The planarity of the whole π-conjugated system is liable for the extension of the

conjugation and this fact is consistent with the calculated wave functions of the frontier molecular orbital.

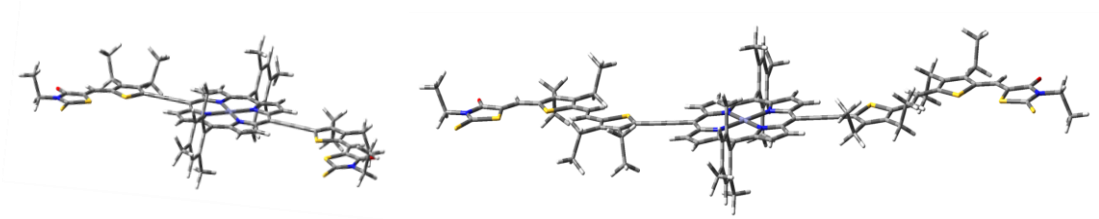

Figure 54. Optimized geometries of **SA3**-**4**

The HOMO and LUMO states are spread all over the porphyrin and the corresponding thienylenvinylene system. These orbitals are overlapped, promoting HOMO to LUMO electronic transitions (Figure 55).

The theoretical HOMO-LUMO gaps are similar for both dyes, being slightly lower for compound **SA4** (ΔE = 1.72 eV) than for **SA3** (ΔE = 1.85 eV), these values are in the same order of those obtained by the electrochemical measurements. The higher extension of the conjugation in **SA4** results an increase in the HOMO energy level, and, because of that a bathochromic shift of the maximum absorption wavelength improving the light harvesting behavior.

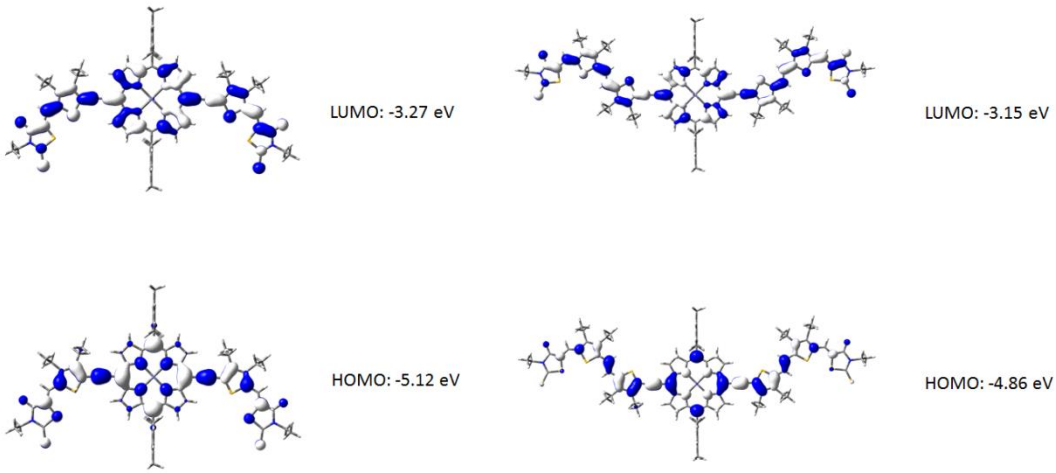

Figure 55. Electronic density contours and energy levels for HOMO and LUMO calculated at the B3LYP/6-31G** level for **SA3** and **SA4**

1.6.5 Photovoltaic properties

The devices were performed by Agustin Molina, from Luis Echegoyen group at the University of Texas, at El Paso, USA.

Bulk heterojunction solar cells of **SA3** and **SA4**, were fabricated, using the same conventional sandwich structure that in **SA1-2** (see chapter 1 section 1.5.5). The ratio of **SA3** and **SA4** to $PC_{71}BM$ was adjusted, ranging from 1:2 to 1:4 (w/w), and the optimized value was found to be 1:4 for **SA4** and 1:2 for **SA3**. The optimized ratio was employed in a blend of **SA3** and **SA4** with $PC_{71}BM$. The photovoltaic devices were measured under an ambient atmosphere employing AM 1.5G simulated illumination at an intensity of 100 mW/cm^2.

The Figure 56 and Figure 57 exhibit the best photovoltaic performances at varying D/A ratios. Photovoltaic devices containing **SA3**:$PC_{71}BM$ exhibited high V_{OC} (0.85 V) at the optimized blend ratio of 1:2 w/w, with a J_{SC} of 11.36 mA cm^{-2}, and FF of 30.8 for an average PCE of 3.01%. Photovoltaic devices incorporating a blend of **SA4**:$PC_{71}BM$ exhibited an average PCE of 4.24%, with a V_{OC} of 0.80 V, FF of 40.1% and an amazing J_{SC} of 13.20 mA cm^{-2}. The high values observed for the V_{OC} using **SA3** are in agreement with the deeper HOMO level of **SA3** (-5.36 eV) *vs* **SA4** (-5.24 eV). Figure 56 and Figure 57, the IPCE response of **SA3** with $PC_{71}BM$ covers the visible spectrum ranging, from 300 nm to 800 nm, which matches the absorption spectra. The devices incorporating **SA4** exhibited more efficient photoconversion efficiency than those based on **SA3**, due to broader and higher IPCE response in the 300-850 nm range. Therefore, the addition of rhodanine as acceptor, leads to a significant improvement in the power conversion efficiency. In addition, the IPCE values were further improved for a **SA4**:$PC_{71}BM$ blend with a remarkable IPCE of 80% at 417 nm.

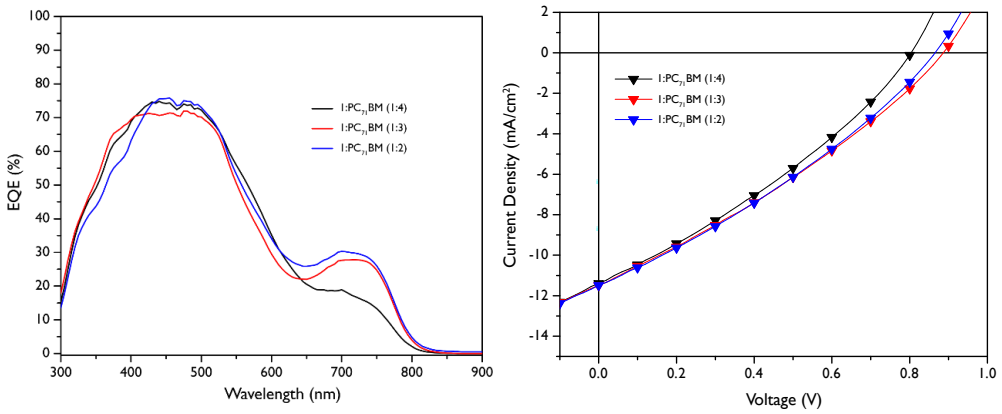

Figure 56. EQE (a) and *J*-*V* (b) characteristics of the SMBHJ for **SA3** blending with $PC_{61}BM$ and $PC_{71}BM$ in a 1:2 ratio

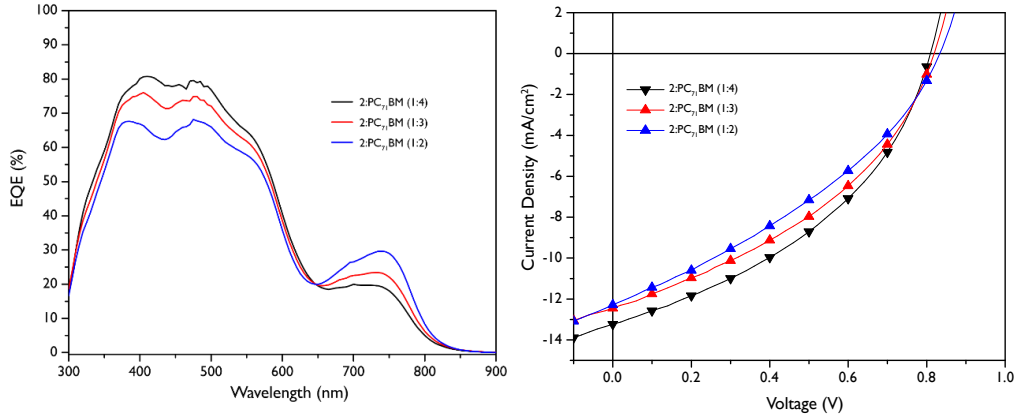

Figure 57. EQE (a) and *J-V* (b) characteristics of the SMBHJ for **SA4** blending with $PC_{61}BM$ and $PC_{71}BM$ in a 1:2 ratio

Table 5. Summary of the photovoltaic performance of **SA3** and **SA4** blended with $PC_{71}BM$ under the illumination of AM1.5G, 100 mW/cm2.

Active layer	*V_{OC} (V)*	*J_{SC} (mA cm^{-2})*	*FF (%)*	*PCE [Highest](%)*
***SA3:**PC$_{71}$BM (1:4)*	0.79±0.04	11.03±0.31	31.4±0.2	2.73 ±0.2[2.86]
***SA3:**PC$_{71}$BM (1:3)*	0.87±0.01	11.48±0.25	30.2±0.1	3.01 ±0.1[3.04]
***SA3:**PC$_{71}$BM (1:2)*	0.85±0.01	11.36±0.21	30.8±0.3	3.01±0.1[3.05]
***SA4:**PC$_{71}$BM (1:4)*	0.80±0.04	13.2 ±0.21	40.1±0.29	4.24±0.1[4.35]
***SA4:**PC$_{71}$BM (1:3)*	0.82±0.02	12.45±0.24	38.5±0.24	3.91 ±0.1 [3.98]
***SA4:**PC$_{71}$BM (1:2)*	0.84±0.03	12.12±0.37	34.7±0.26	3.55 ± 0.1 [3.63]

1.6.6 Hole mobility

The hole mobility was measured by Nuria Fernández Montcada, from Emilio Palomares Group at the Institut Catalá d'Investigació Química, (ICIQ), Tarragona, Spain; using the Space Charge Limited Current method (SCLC). The hole mobility of these devices is one of the critical conditions to determine the most optimal fabrication method as the final thickness of the devices are strongly limited by this characteristic of the donor molecule.

The mobility average for **SA3** and **SA4** molecules is $1.25 \cdot 10^{-5}$ $Vcm^{-2}s^{-1}$ and $1.56 \cdot 10^{-5}$ $Vcm^{-2}s^{-1}$ respectively. When the donor group used in the molecular framework is very strong, as happens using porphyrins, the effect of the side chains on mobility becomes less critical and the porphyrin governs the hole mobility. Moreover, they do not present a higher mobility in this case.

In addition, to understand the difference of the electrical performance between both devices, charge extraction and the transient photovoltage were measured. The geometric contribution of total extracted charges is indicated with a straight line and calculated to be 80 and 64 $nFcm^{-2}$ for

SA3-4 respectively (see experimental part Figure 167). Figure 58 shows charge corresponding to the chemical capacitance in order to count only the charges that can be stored inside the bulk of the device. **SA3** device has a right-shift in agreement with the increase in V_{oc} observed in IV characterization. Moreover, the system is capable to store more charges and then efficiently extracted in **SA4**.

SA4 present longer life-times than **SA3**, this agrees with the hypothesis about a better and proper aggregation of **SA4** and $PC_{71}BM$; that could explain also the differences observed in the EQE and could be one reason for the higher efficiency of **SA4**. All these results points out that the stacking is optimized for **SA4**; as consequence of a better interaction between the sulphure units that increase the possibility of electron hopping towards the donor/fullerene interface, the FF is slightly enhanced and, hence, as the amount of fullerene could be increased the charges are transferred more efficiently retarding the recombination.

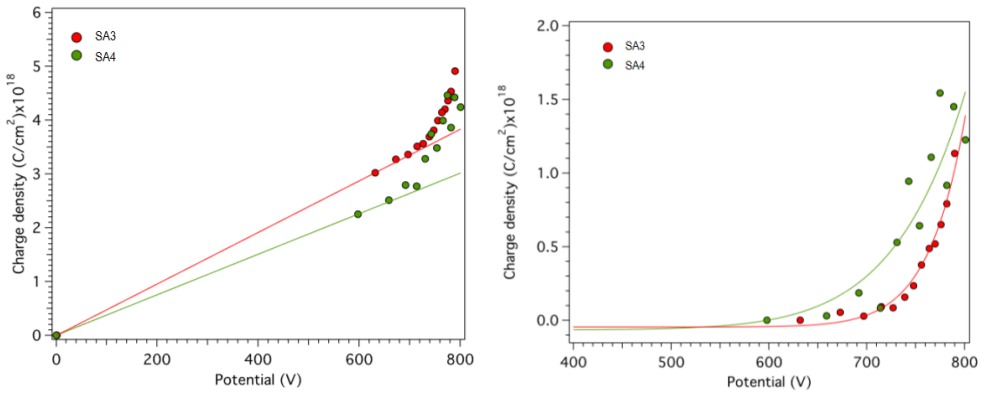

Figure 58. Charge density at different applied potentials of **SA3** and **SA4**. A) CE including all the capacitance contribution b) the same CE excluding the geometric capacitance

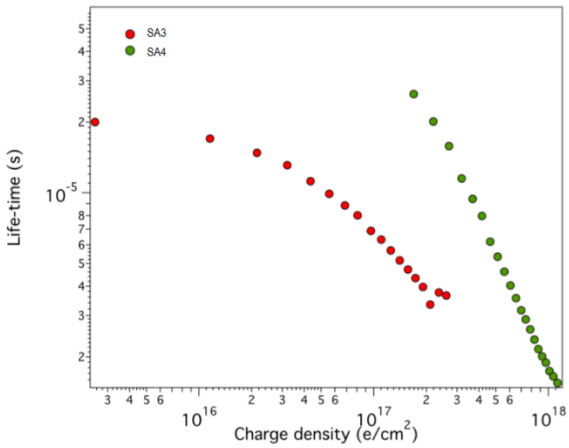

Figure 59. Charge life-time of **SA3** and **SA4**

1.7 SA5 and SA6

1.7.1 Synthesis and characterization of SA5 and SA6

Scheme 5 illustrates the synthetic route to the connector **C3** starting from 4,4-dihexyl-4H-cyclopenta[2,1-b:3,4-b′]dithiophene (**BTC**); the formylating agent, also known as the Vilsmeyer-Haack Reagent, is formed *in situ* from *N,N*-Dimethylformamide (DMF) and phosphoryl chloride ($POCl_3$), an electrophilic aromatic substitution leads to α-chloro amines, which are rapidly hydrolyzed during work up to give the aldehyde, affording 4,4-dihexyl-4H-cyclopenta[2,1-b:3,4-b′]dithiophene-2-carboxaldehyde (**BTCCHO**) in 83% yield.

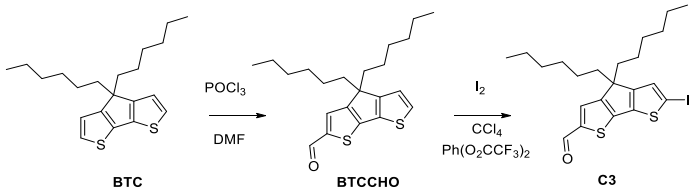

Scheme 5. Synthetic route to **C3**

^{1}H-NMR spectrum of **BTCCHO**, shows one singlet at 7.58 ppm corresponding to the β position to the sulfur atom, near to the aldehyde, and one singlet at 9.84 ppm assigned to the proton of the formyl group. Also is observed two duplets at 7.40 ppm and 6.99 ppm, corresponding to β and α positions respectively in **BTC** ring (see experimental part Figure 169).

Then, iodoaldehyde **C3** was prepared by reaction of the aldehyde **BTCCHO** with molecular iodine (I_2), and bistrifluoroacetoxiiodobenzene ($PhI(OCOCF_3)_2$) in CCl_4 at room temperature one night, in 92% yield (see more synthesis details at the end of this chapter).[71]

In the ^{1}H-NMR spectrum of **C3**, the duplet at 7.40 ppm corresponding to the α position in **BTC** have disappeared, indicating the successful iodation, and shows two singlets at 7.57 and 7.17 ppm assigned to the β positions to the sulfur atoms; the characteristic signal at 9.84 ppm corresponding to the formyl group is also observed (see experimental part Figure 170).

Scheme 6 shows the synthetic route used to obtain compounds **SA5** and **SA6**, this synthesis began from *bis*-trimethylsilyl porphyrin **P1**. The trimethylsilyl group was quantitatively removed by hydrolysis with TBAF, and then water was added to quench the reaction, then the product was extracted with $CHCl_3$ and the solvent was evaporated. The product, without further purification was reacted with **C3** under Pd-catalyzed Sonogashira coupling conditions, one night at reflux of anhydrous THF, to afford the bisaldehyde **A3** in 70% yield.

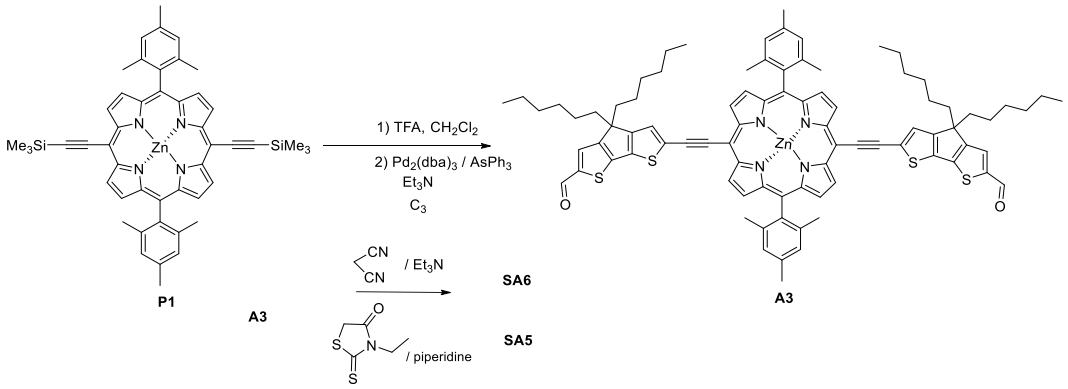

Scheme 6. Synthetic route to molecules **SA5** and **SA6**

The ^{1}H-NMR spectrum of **A3** shows all the expected signals for the porphyrin macrocycle at 9.64 and 8.78 ppm and the aldehyde proton is observed at 9.79 ppm, (see experimental part Figure 171).^{13}C-NMR spectrum of **A3** shows the signal at 182.75 ppm, corresponding to the carbons of the formyl groups and at 91.13 and 99.74 ppm the signals of the triple bond carbons linked to the porphyrin and the **BTC**, the aliphatic signals are between 38.00 and 14.27 ppm. The spectrum does not show the signal at 0.34 ppm corresponding to the two trimethylsylil groups, substituted by the fragments of **BTCCHO** (see experimental part Figure 172).

The target compound **SA6** was obtained by Knoevenagel condensation of **A3** with malononitrile in the presence of triethylamine in 86% yield and **SA5** by reaction of **A3** with 3-ethylrhodanine in the presence of piperidine in 91% yield.

^{1}H-NMR spectrum of **SA5** shows a signal at 8.01 ppm, indicating the successful condensation, also shows signals corresponding to the methyl of rhodanine at 4.18 ppm (Figure 60). ^{1}H-NMR spectrum of **SA6** shows signal at 7.72 ppm assigned to the successful condensation and consequently for both compounds the aldehyde signals at 9.79 ppm are not observed.

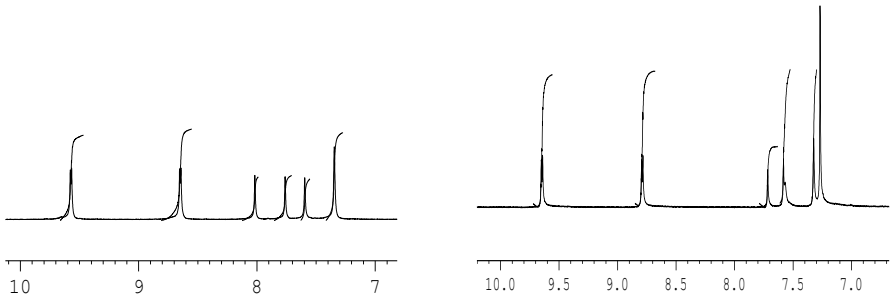

Figure 60. 7 to 10 ppm region of the ^{1}H-NMR spectra (400 MHz, $CDCl_3$) of **SA5** (left) and **SA6** (right)

^{13}C-NMR spectrum of **SA5** shows signals at 192.53, 167.68 and 40.61 ppm (see Figure 173, experimental section), corresponding to the carbon atoms of the rhodanine groups. In **SA6** new signals at 115.12, 114.37 and 72.51 ppm corresponding to the dicyanovinylene groups are observed, and for both compounds the signals corresponding to the carbons of the aldehyde are not observed at 182.75 ppm (see experimental part Figure 174).

The mass spectra, match with the expected values of compounds **SA5** and **SA6**. The mass spectrum of **SA5** showed the molecular ion peak at *m/z* 1687.05 amu, while compound **SA6** exhibited the molecular ion peak at *m/z* 1497.23 amu (see experimental part, Figure 175 and Figure 176).

The stability of compounds **SA5** and **SA6** at high temperature were estimated by TGA, using the same conditions of **SA1-2**. Compounds **SA5** and **SA6** show decomposition at 387ºC and 400 ºC, respectively (see Figure 61).

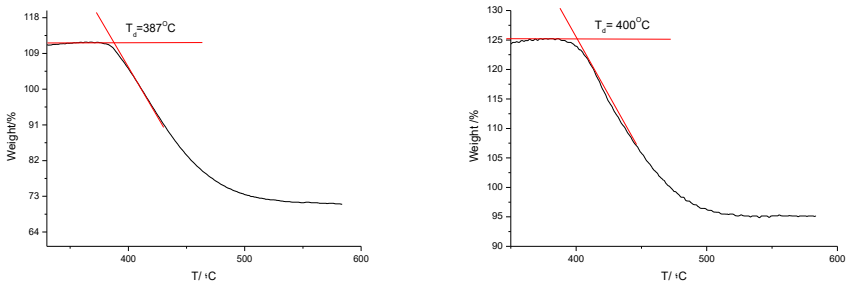

Figure 61. TGA of **SA5** (left) and **SA6** (right)

1.7.2 Optical Properties

The UV-Vis absorption spectra, in CH_2Cl_2 solution, of the precursor aldehyde **A3** and those of the final compounds **SA5**, **SA6** exhibit a broad absorption in the visible region. The spectrum of **A3** shows the Soret band (λ_{max} = 489 nm) red-shifted, with respect to the Soret band in the precursor porphyrin **P1** (λ_{max} = 435 nm). **A3** shows a new band at λ_{max} = 693 nm, assigned to intramolecular charge transfer (ICT). In **SA5-6** ITC band is more intense that **A3**, as consequence of the introduction of the fragments 3-ethyl-rhodanine in **SA5**, (Figure 62), and dicyanovinylene in **SA6** (Figure 178), showing a higher charge transference.

Similar absorption were found for **SA5**-**6** spectra in solution of CH_2Cl_2, showing absorption ranges from 362 nm to 797 nm with a valley centered at 602 nm, matching with the solar spectrum, making this compounds functional for solar cells (Figure 63).

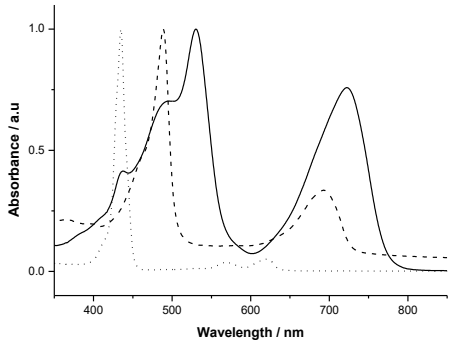

Figure 62. Normalized UV-Vis absorption spectra of compounds **SA5** (solid line) and precursors **A3** (dashed line) and **P1** (dotted line)

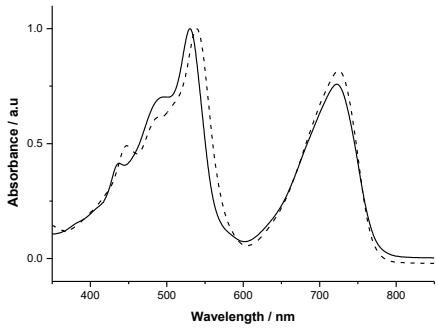

Figure 63. Normalized UV-Vis absorption spectra of **SA5** (solid line) and **SA6** (dashed line) in CH_2Cl_2 solution (10^{-5} M)

Table 6. UV-Vis Absorption, Fluorescence Emission[a] and OSWV[b] data for compounds **SA5-6**.

	λ_{max} *soln* (nm)	*Log* (ε)	λ_{em} (nm)	E^1_{ox}[b, c] (V)	E^1_{red} (V)	E_{HOMO}[d] (eV)	E_{LUMO}[e] (eV)	E_g[f] (eV)
SA5	437	4.69	752	0.20	-1.53	-5.30	-3.57	1.73
	488	4.92						
	530	5.08						
	722	4.96						
SA6	448	5.25	750	0.26	-1.42	-5.36	-3.68	1.68
	489	5.34						
	539	5.55						
	725	5.47						

[a] 10^{-5} M, in dichloromethane; [b] 10^{-3} M in ODCB-acetonitrile (4:1) versus Fc/Fc^+ (E_{ox} = 0.04 V) glassy carbon, Pt counter electrode, 20 °C, 0.1 M Bu_4NClO_4, scan rate = 100 mV s^{-1}; [c] reversible processes; [d] calculated with respect to ferrocene, E_{HOMO}: –5.1 eV; [e] estimated from E^1_{red}; [f] Eg= E_{HOMO} – E_{LUMO}.

The fluorescence spectra for **SA5** (λ_{exc} = 530 nm) and **SA6** (λ_{exc} = 539 nm) in CH_2Cl_2, show an emission band at 750 and 748 nm respectively, nevertheless, **SA6** shows a low emission intensity attributed to more efficient electron transfer processes (see experimental section Figure 178).

1.7.3 Electrochemical Properties

Electrochemical potentials of **SA5** and **SA6** were measured by Cyclic Voltammetry (CV) and Osteryoung Square Wave Voltammetry (OSWV) in *o*-DCB-acetonitrile (4:1), then, E_{HOMO} and E_{LUMO} were calculated (Table 6, Figure 64 and Figure 179). **SA5-6** show a first reversible one-electron oxidation wave at 0.26 V for **SA6** and 0.20 V for **SA5** (vs Fc/Fc^+ in all cases) which correspond to the first oxidation of the porphyrin. For **SA6**, the electron withdrawing properties of the rhodanine, decrease the E_{ox} value by 6 mV with respect to **SA5**. A second reversible oxidation wave is observed at 0.48 V for **SA5** and at 0.65 V for **SA6**. Compound **SA6** shows another non reversible oxidation wave at 1.08 V and **SA5** shows two non reversible oxidation wave at 0.76 V and 1.02 V. The estimated E_{HOMO} values were calculated with respect to ferrocene as reference (E_{HOMO}: -5.1 eV) and were determined to be -5.30 eV for **SA5** and -5.36 eV for **SA6**. The HOMO-LUMO gaps determined by electrochemical are as narrow as 1.73 and 1.68 eV for **SA5** and **SA6**, respectively. The E_{LUMO} calculated with the first reduction potential; for both compounds are higher than that E_{LUMO} of $PC_{71}BM$, with values of -3.57 and -3.68 eV for **SA5** and **SA6**, respectively, which help to an energetically favorable electron transfer from **SA5**-**SA6** to the acceptor moiety that should in turn favor the exciton dissociation.

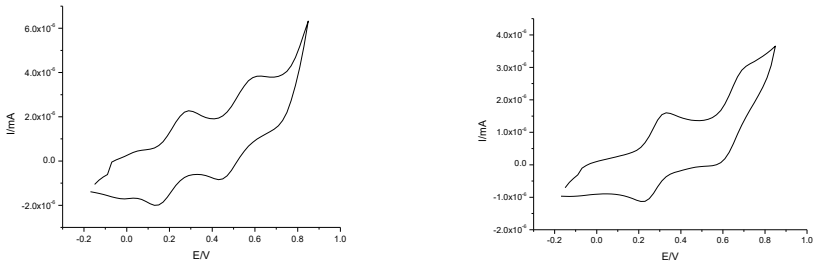

SA5 **SA6**

Figure 64. CV of compounds **SA5** and **SA6** (anodic window)

1.7.4 Theoretical Calculations

Theoretical energy levels and geometrical structures of **SA5-6**, were calculated by Gaussian 03W (Figure 65 and Figure 66). The optimized structure of **SA5-6**, show the meso-substituted aryl groups bounded to the porphyrin core being perpendicular to the porphyrin core (θ~90º), the macrocycle is almost coplanar, while the **BTC** fragments are almost in the same plane with respect to the porphyrin ring.

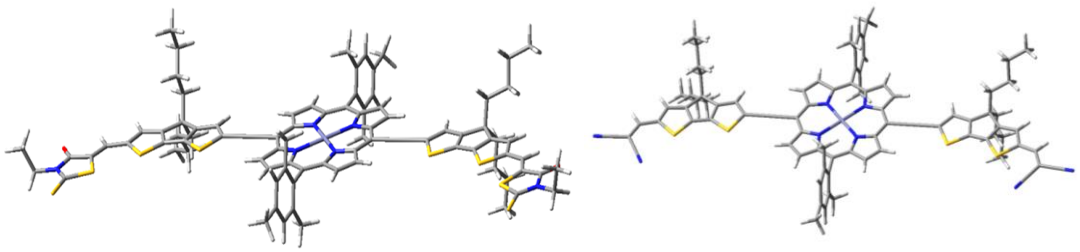

Figure 65. Stable geometries for **SA5-6**

The electron density at the HOMO is fully delocalized over all the conjugated system and the LUMO moves away from the acceptor group, towards the electron-acceptor part. The HOMO and LUMO state shows that the charge density of the HOMO of **SA5**-**6** is delocalized over the whole conjugated system, as same as in the last molecules. The theoretical HOMO-LUMO gaps are similar for both dyes, being slightly higher for compound **SA5** (Δ*E* = 1.79 eV) than for **SA6** (Δ*E* = 1.77 eV).

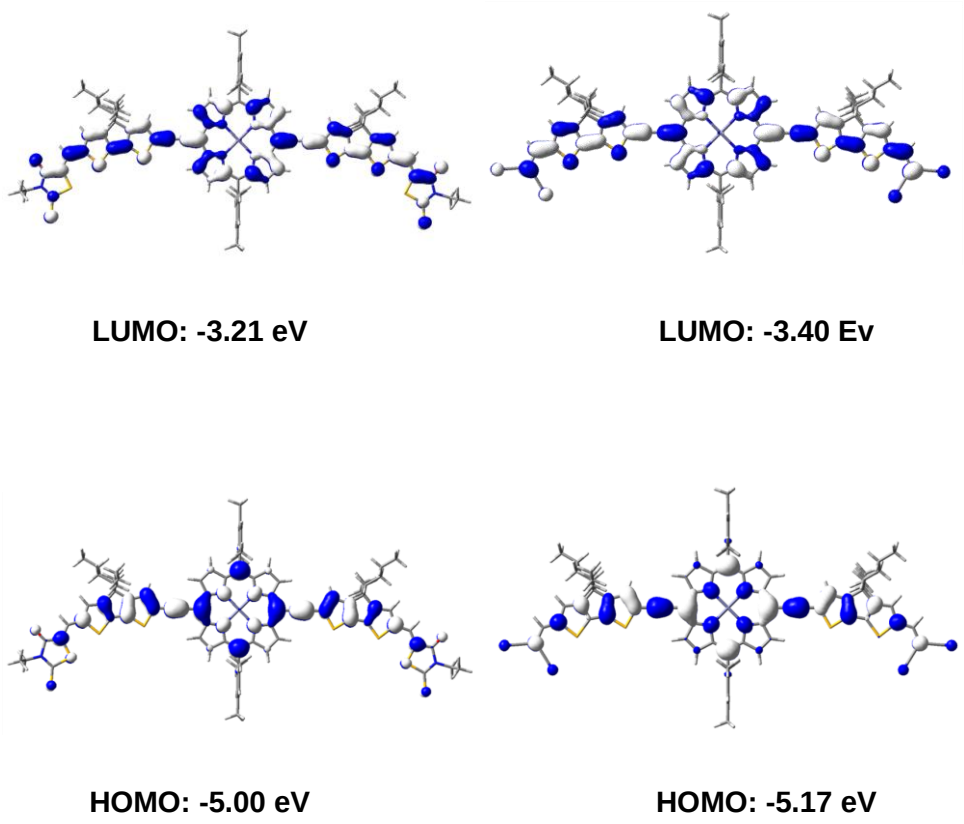

Figure 66. Electronic density contours and energy levels for HOMO and LUMO calculated for **SA5** (left) and **SA6** (right)

1.7.5 Photovoltaic properties

To study the application of **SA5** and **SA6** in the photovoltaic devices, preliminary measures were performed at the Institute of Chemical Research of Catalonia ICIQ, Tarragona, Spain, thanks to a visit to Professor Emilio Palomares's group (these values are not optimized).

SA5 and **SA6** solutions were prepared in chlorobenzene (20 mg/mL) with $PC_{71}BM$ (using different weight ratios) and left under stirring overnight. Substrates coated with a PEDOT:PSS solution was spin-coated over the ITO to form a film (~ 25 nm). The spinning was carried out for 30 seconds at 4500 rpm followed by 30 seconds more at 3500 rpm. PEDOT was annealed at 120ºC for 15 minutes inside the glove box. Next, solution was spin coated over the PEDOT layer at 2000 rpm (2 acc). Finally thin layers of LiF (0.6 nm) and Al (90 nm) were deposited for normal devices, using a high vacuum thermal evaporator (see Scheme 7).

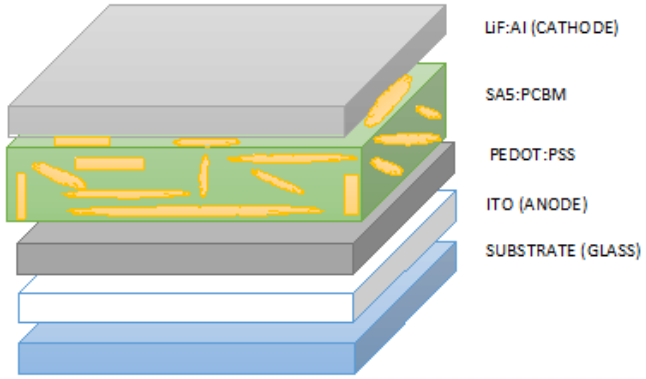

Scheme 7. General structure of BHJSC

Table 7. Summary of the photovoltaic performance of **SA5** blended with $PC_{71}BM$ with different ratios under the illumination of AM1.5G, 100 mW/cm^2.

Active layer [a]	V_{OC} *(V)*	J_{SC} *(mA cm^{-2})*	*FF (%)*	*PCE [Highest](%)*
***SA5**:PC$_{71}$BM (1:2)*	0.73	7.29	32.96	1.50
***SA5**:PC$_{71}$BM (1:3)*	0.79	9.57	33.25	2.56
***SA5**:PC$_{71}$BM (1:4)*	0.78	9.85	34.06	2.61
***SA5**:PC$_{71}$BM (1:5)*	0.69	8.74	31.43	1.89
***SA5**:PC$_{71}$BM (1:4)*[b]	0.80	11.72	41.08	3.87
***SA6**:PC$_{71}$BM (1:4)*[b]	0.80	9.78	35.48	2.77

[a] Not optimized devices; [b] Solutions prepared with 1% of pyridine

Different strategies, such as donor:acceptor ratio controlling, thermal annealing, solvent annealing, adding additives, and others; have been used to get BHJSC layers with ideal morphological properties, like appropriate phase separation, suitable domain size and favorable molecular orientation of both donor phase and acceptor phase.[83] The donor:acceptor ratio is

one of the most important parameters in the fabrication process of photovoltaic devices. The balanced hole and electron transport property is necessary to avoid accumulation of charge, to facilitate charge transport process during the photoelectric conversion. Different weight ratios of **SA5** and PCBM were studied, the ratio 1:5 afford a lower $V_{OC,}$ nevertheless the FF decrease in comparison to ratio 1:4 which has higher J_{SC} and FF in comparison to the other devices, therefore, although V_{OC} is higher, the integration of the others parameters allow the highest PCE (2.61%).

SA5 devices were optimized by adding pyridine,[84] without additive V_{OC} of **SA5** (1:4) is slightly lower (0.78 V) than with pyridine (0.80 V), moreover, the current increase from 8.74 mA cm^{-2} without additive to 11.72 mA cm^{-2} with 1% of pyridine. **SA5** without additive has a PCE of 2.61% and 1% of pyridine afford a PCE of 3.87%. Photovoltaic devices incorporating a blend of **SA6**:$PC_{71}BM$ with 1% of pyridine exhibited a PCE of 2.77% (see Figure 67).

SA5 and **SA6** exhibit good V_{OC} values (~0.80 V). Additionally **SA5** shows a J_{SC}, similar to reported porphyrin devices with higher PCE (5%). Nevertheless, FFs of **SA5-6** are too low to enhance this efficiency (see Table 1). The performance in **SA5-SA6** devices can be optimized by enhancing the FF. Moreover, the preliminary results show both compounds as good materials for photovoltaic devices.

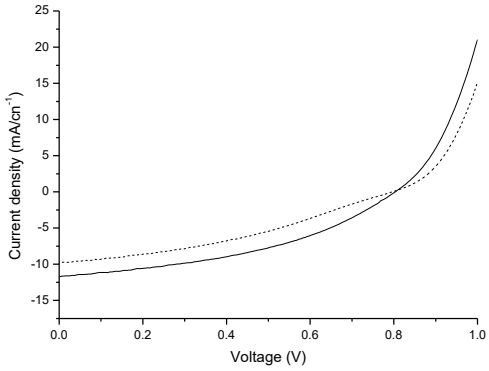

Figure 67. *J-V* characteristics of the SMBHJ for **SA5** (solid line) and **SA6** (dash line) blending with $PC_{71}BM$ in a 1:4 ratio, using 1% of pyridine

1.8 SA7, SA8, SA9 and SA10

1.8.1 Synthesis and characterization of S7-10

Scheme 8 shows the synthetic route for the preparation of precursor porphyrin **P2S**, starting from resorcinol and 1-bromohexane in presence of K_2CO_3, this solution was refluxed in dry THF affording 1,3-dihexyloxybenzene (99% yield). Next, tetramethylethylenediamine (TMEDA) was added to a solution of 1,3-dihexyloxybenzene in dry THF at 0 °C, then n-BuLi was added dropwise, the mixture was stirred at 0 °C during 30 minutes, and then DMF was added and stirred during 1 hour at room temperature. The mixture was poured into a hydrochloric acid solution to obtain 2,6-dihexyloxybenzenaldehyde in 71% yield. In the ^{1}H-NMR spectrum of 2,6-dihexyloxybenzenaldehyde, the signal at 10.55 ppm corresponding to the aldehyde, was observed (see Figure 181 and Figure 182 in the experimental part).

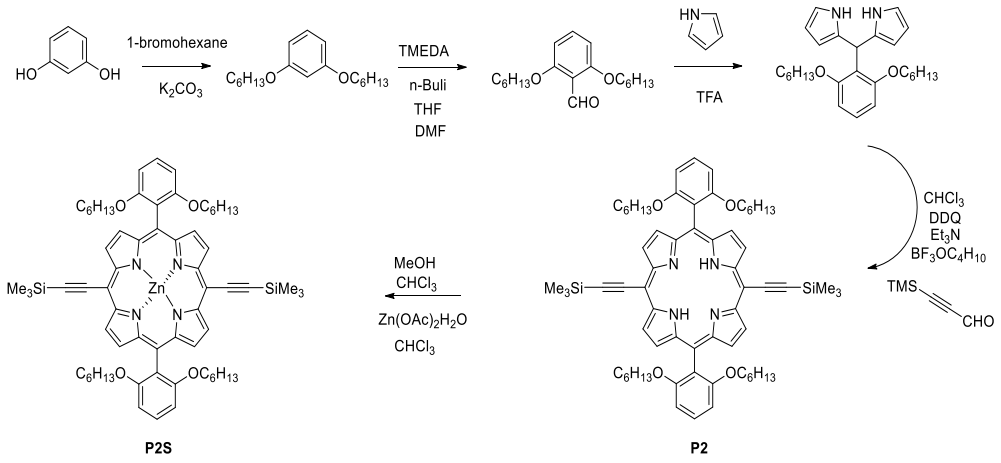

Scheme 8. Synthesis of **P2S**

A solution of 2,6-dihexyloxybenzenaldehyde in pyrrole was stirred, then was added trifluoroacetic acid and the reaction was quenched with a saturated solution of hydroxide sodium, affording the product 5-(2,6-dihexyloxybenzyl)dypirromethane in 65% yield.

Under Ar atmosphere, 3-(trimethylsilyl)-2-propynal was added to a solution of 5-(2,6-dihexyloxybenzyl)dypirromethane in chloroform and $BF_3(Et_2O)_2$ to form the porphyrinogen and this was oxidized with DDQ, and after 1 hour Et_3N was added, to obtain 5,15-bis-(trimethylsilyl)ethynyl)-10,20-(2,6-dihexyloxybenzyl)lporphyryn (II), **P2**, in 19% yield.[85] The characterization of all new molecules was performed by using ^{1}H-NMR, ^{13}C-NMR, FT-IR spectroscopies and MALDI-TOF mass spectrometry.

Zinc acetate dihydrated ($(ZnOAc)_2$ x$2H_2O$) was added to a solution of porphyrin in $CHCl_3$, affording in [5,15-bis-(trimethylsilyl)ethynyl)-10,20-(2,6-dihexyloxybenzyl)lporphyrinato] zinc (II), (**P2S**) in quantitative yield. The ^{1}H-NMR spectrum of **P2S** shows the protons corresponding to the porphyrin core at 9.6 ppm and 8.80 ppm and the signals at 3.8 ppm assigned to the four

protons next to oxygen in the hexyloxy chains; and does not show the signal at -2.07 ppm, corresponding to the protons of the nitrogen into the porphyrin core, indicating the successful metalation of the porphyrin core (see supporting information, Figure 183 and Figure 184).

Scheme 9 illustrates the synthetic route for preparation of **SA7** and **SA8**, starting from **P2S**.

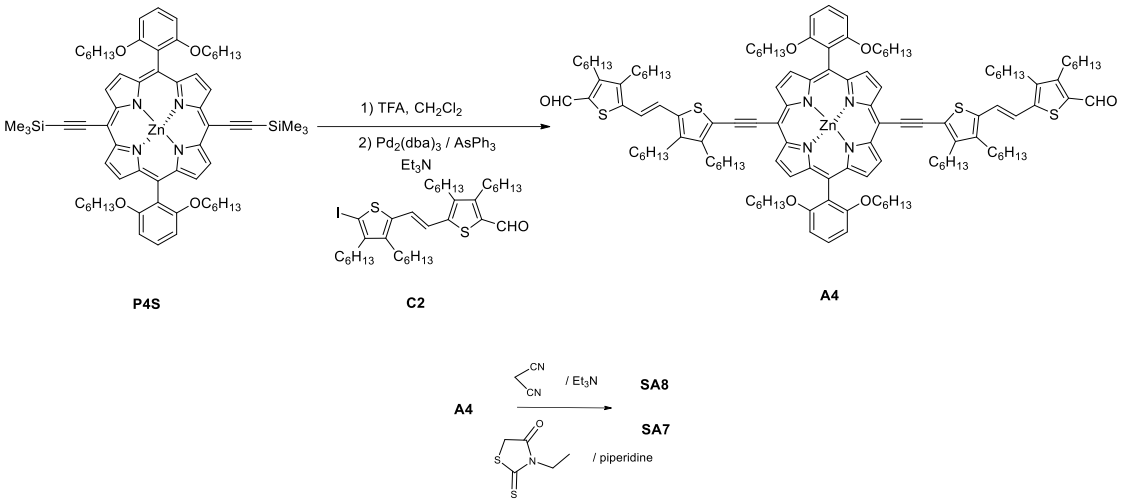

Scheme 9. Synthetic route to chromophores **SA7** and **SA8**

The trimethylsilyl group was quantitatively removed by hydrolysis with TBAF and water was added to quench the reaction, then the product was extracted with $CHCl_3$. The solvent was evaporated and the product, without further purification, reacted with the corresponding iodoaldehyde **C2** under Pd-catalyzed copper-free Sonogashira coupling conditions, using triphenylarsine and $Pd_2(dba)_3$ to afford bisaldehyde **A4** in 51% yields.

The ^{1}H-NMR spectrum of **A4** shows the expected signals of the porphyrin at 9.60 and 8.85 ppm and shows at 9.95 ppm signals corresponding to aldehyde protons and also shows the *trans* configuration of the double bond of **2TV** at 7.38 and 7.12 ppm with a 15.5 Hz coupling constant (see experimental part Figure 185). ^{13}C-NMR spectrum of **A4** shows a signal at 181.91 ppm assigned to the carbon of the aldehyde group and shows aliphatic signals corresponding to the alkyl chains of *n*TV between 32.32 and 13.50 ppm (see experimental part Figure 186). The infrared spectrum of **A4** shows the characteristics band at 1652 cm^{-1} corresponding to the carbonyl of the aldehyde (C=O). From 2854 to 2952 cm^{-1} bands corresponding to the alkyl chains of *n*TV´s are observed (see experimental part Figure 187).

The target compound **SA7** was obtained by Knoevenagel condensations of **A4** with 3-ethyl-rhodanine and piperidine as base in 59% yields and **SA8** was obtained by condensation of **A4** with malononitrile in presence of triethylamine in 73% yield. ^{1}H-NMR spectrum of **SA7** shows new vinylic signals at 7.97 ppm, indicating a successful condensation, it also shows signals at 4.24 ppm, corresponding to the ethyl near to the rhodanine and does not show signals corresponding to aldehyde protons at 9.95 ppm of the precursor. ^{1}H-NMR spectrum of **SA8**

shows new vinylic signals at 7.80 ppm assigned to a successful condensation and does not show signals corresponding to aldehyde protons of the precursors at 9.95 ppm (see Figure 68).

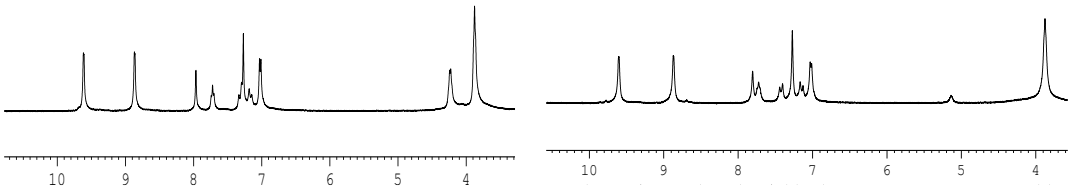

Figure 68. 11 to 3 ppm ^{1}H-NMR spectra (400 MHz, $CDCl_3$) of **SA7** (left) and **SA8** (right)

^{13}C-NMR spectrum of **SA7** shows signals at 192.68, 167.72 and 40.12 ppm (Figure 69), corresponding to the carbon atoms of the rhodanine groups. ^{13}C-NMR spectrum of **SA8** shows signals at 115.68, 114.27 and 73.09 ppm corresponding to dicyanovinylene moiety. In both spectra do not appear signals at 181.91 ppm corresponding to the aldehydes.

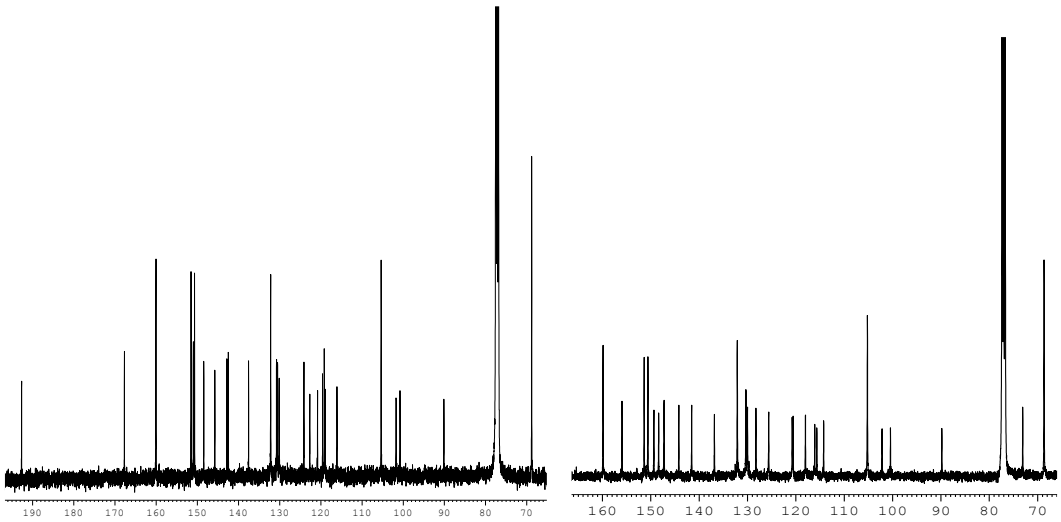

Figure 69. 70-160 ppm ^{13}C-NMR spectra (100 MHz, $CDCl_3$) of **SA7** (left) and **SA8** (right)

Infrared spectrum of **SA7** shows new bands at 1234 cm^{-1} and 1702 cm^{-1}, corresponding to the thiocarbonyl and amide respectively in 3-ethylrhodanine, and does not show the carbonyl band at 1652 cm^{-1} (Figure 70).

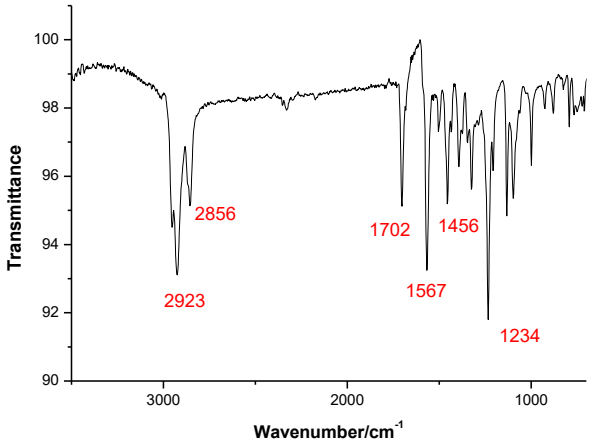

Figure 70. FT-IR Infrared spectrum of **SA7**

Infrared spectrum of **SA8** shows new bands at 2217 cm^{-1} corresponding to dicyanovinylene, and does not show the characteristic band at 1652 cm^{-1} corresponding to the carbonyl of the aldehyde (Figure 71).

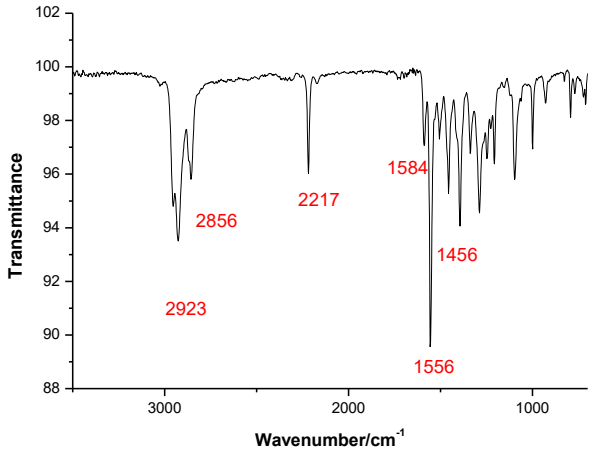

Figure 71. FT-IR Infrared spectrum of **SA8**

Scheme 10 illustrates the synthetic route to **SA9**-**10**, starting from **P4S**. The trimethylsilyl group was quantitatively removed by hydrolysis with TBAF and, without further purification, reacted with the corresponding iodoaldehyde **C3** under Pd-catalyzed copper-free Sonogashira coupling conditions to afford bisaldehyde **A5** in 44% yields. The target compound **SA9** was obtained by Knoevenagel condensations of **A5** with malononitrile in the presence of triethylamine in 59% yield, and **SA10** was obtained with 45% yields by condensation with 3-ethyl-rhodanine.

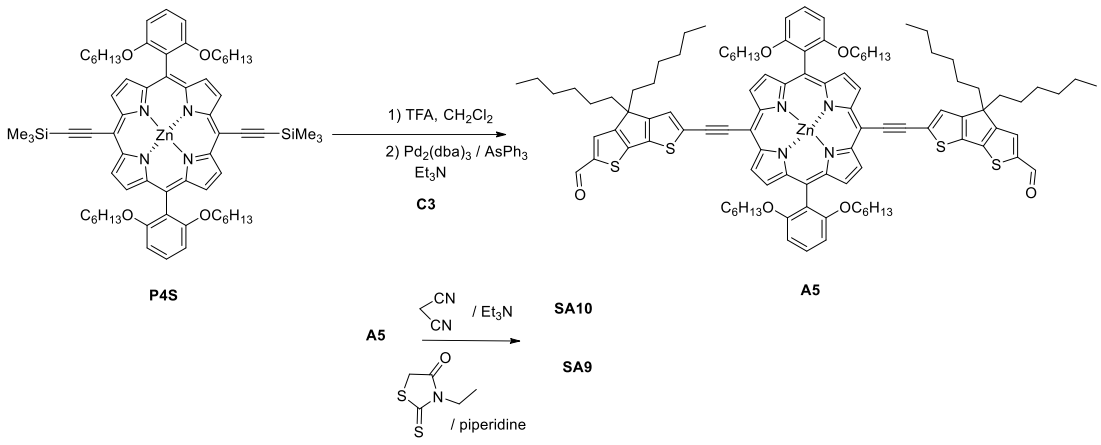

Scheme 10. Synthetic route to chromophores **SA9** and **SA10**

^{1}H-NMR spectrum of **A5** shows expected signals corresponding to the porphyrin macrocycle at 9.61 and 8.89 ppm and shows signals at 9.86 corresponding to aldehyde protons, also shows at 7.64 and 7.55 ppm protons corresponding to the thiophene rings (see experimental part Figure 194). ^{13}C-NMR spectrum of **A5** shows at 182.64 ppm a signal corresponding to the carbon of the aldehyde group and aliphatic signals appear between 37.85 and 13.53 ppm (see experimental part Figure 195). The infrared spectrum of **A5** shows the characteristic band at 1656 cm^{-1} corresponding to the carbonyl of the aldehyde (see experimental part Figure 196).

^{1}H-NMR spectrum of **SA9** shows new signal at 7.77 ppm, assigned to the vinyl protons, indicating a successful condensation, and also shows protons corresponding to the ethyl of the ethylrhodanine at 3.91 ppm. ^{1}H-NMR spectrum of **SA10** shows new signals at 7.80 ppm, confirming the successful condensation. Both spectra do not show signals at 9.86 ppm corresponding to the formyl group (Figure 72, Figure 188 and Figure 190).

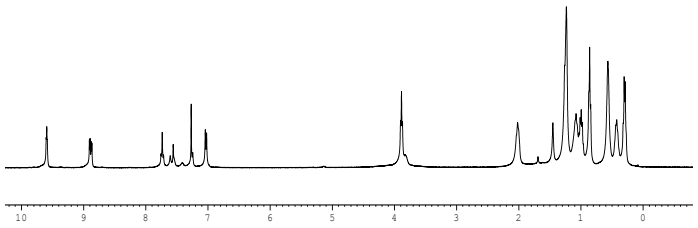

Figure 72. ^{1}H-NMR spectrum (400 MHz, $CDCl_3$) of **SA9**

^{13}C-NMR spectrum of **SA9** shows signals at 191.52, 167.04 and 39.89 ppm, corresponding to the carbons of the rhodanine groups. ^{13}C-NMR spectrum of **SA10** shows new signals at

128.26 and 68.63 ppm, assigned to the dicyanovinyl groups (Figure 198 and Figure 201). Both spectra do not show signals at 182.64 ppm, corresponding to the precursor aldehyde.

Infrared spectrum of **SA9** shows new bands at 1238 cm^{-1} and 1697 cm^{-1} assigned to thiocarbonyl and amide respectively, present in 3-ethylrhodanine, which has been sucesfully coupled to the molecule (Figure 70).

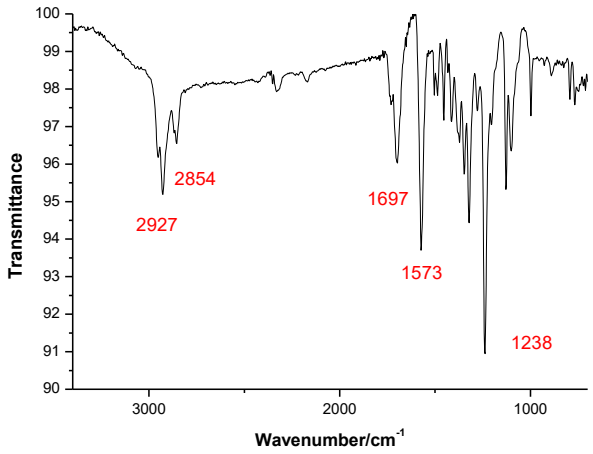

Figure 73. FT-IR Infrared spectrum of **SA9**

The infrared spectrum of **SA10** does not showed the band at 1652 cm^{-1} corresponding to the carbonyl of the aldehyde and a new band at 2217 cm^{-1} of dicyanovinylene group is observed (Figure 74).

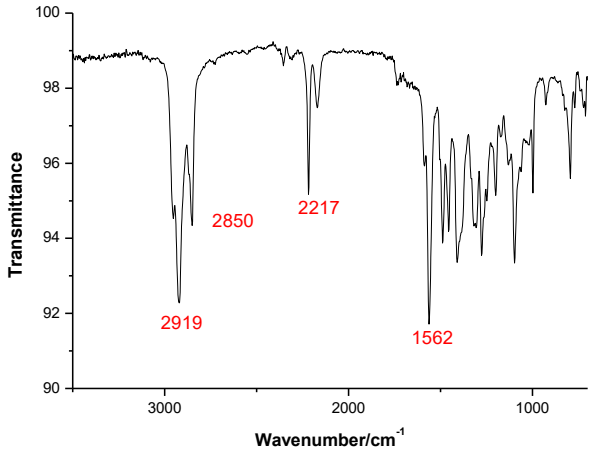

Figure 74. FT-IR Infrared spectrum of **SA10**

The mass spectra of compounds **SA7-10** show the molecular ion peak at *m/z* 2367.15, 2177.19, 2002.73 and 1812.80 amu respectively, according to the exact mass forecasted (see experimental part Figure 192, Figure 193, Figure 203 and Figure 204).

TGA studies of **SA7**, **SA8**, **SA9** and **SA10** show decomposition temperatures of 372, 387, 349, and 358 ºC respectively, which agree with the expected properties in materials for solar cells (Figure 75).

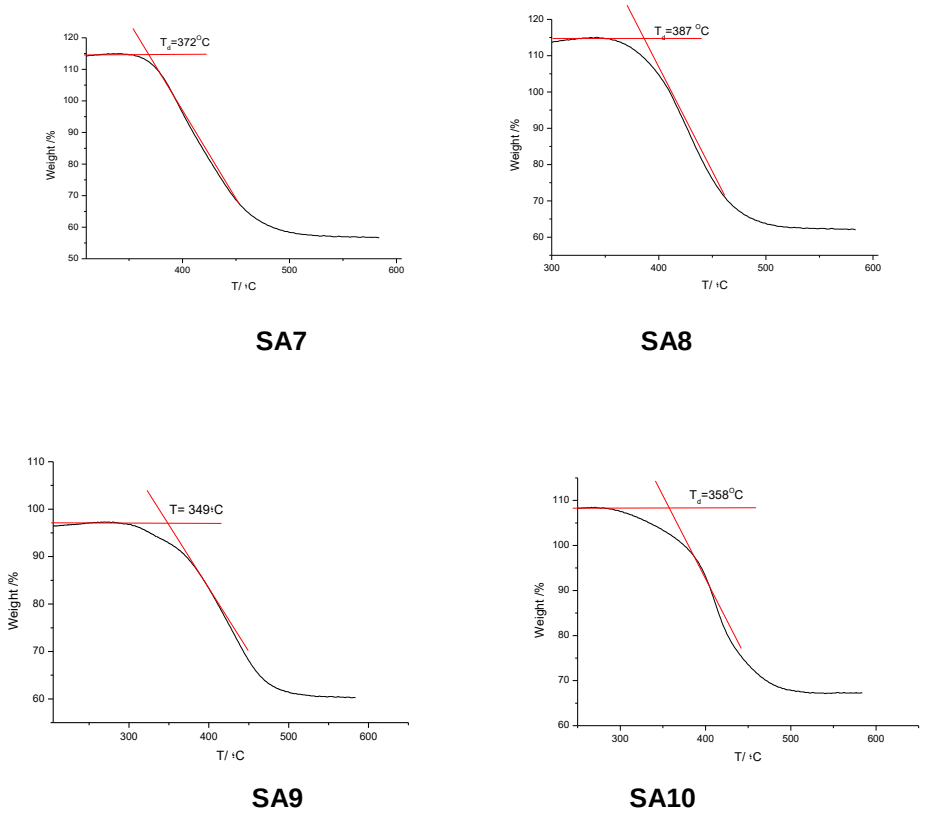

SA7 **SA8**

SA9 **SA10**

Figure 75. Thermogravimetric analysis of **SA7-10**

1.8.2 Optical Properties

The UV-Vis spectra of the precursor aldehydes **A4** and **A5**, in solution of CH_2Cl_2 show the Soret band at λ_{max} = 492 nm and $\lambda_{max=}$ 502 nm, respectively. Both Soret bands are bathochromically shifted, with respect to the Soret band in the precursor porphyrin **P2S** at λ_{max} = 442 nm. Both aldehydes show a new intense band at λ_{max} = 686 nm and λ_{max} = 694 nm, respectively, corresponding to intramolecular charge transfer (ICT), (Figure 76).

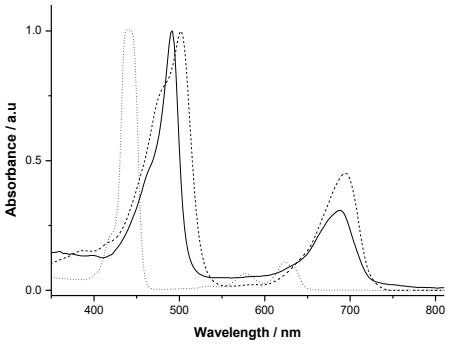

Figure 76. Normalized absorption spectra of **P2S** (dotted line), **A4** (dashed line) and **A5** (solid line) in dichloromethane solution (10^{-5} M)

UV-Vis spectra of **SA7-10** in CH_2Cl_2 solution exhibit an absorption that covers a wide range of wavelengths within the solar emission spectrum (300-760 nm), having high values of log(ε) (see Table 8). **SA7-10** spectra present a red-shift of the absorption bands in comparison with the precursor aldehydes and have intense ITC band, as consequence of the push-pull effect with the addition of an electron acceptor moiety as 3-ethylrhodanine or dicyanovynil, therefore **SA7** absorption spectrum shows a wider absorption ranges, from 302 nm to 768 nm with a valley centered at 612 nm, with maximum bands at λ_{max} = 714 nm, 552 nm and 484 nm. The absorption spectrum of **SA9** shows ranges from 372 nm to 768 nm with a valley centered at 604 nm, with maximum bands at λ_{max} = 716 nm, 538 nm. However, **SA7** shows wider absorbance that **SA9** due to the higher conjugation of **2TV** in comparison with **BTC**. Similarity, **SA8** shows absorption ranges from 304 nm to 788 nm with a valley centered at 608 nm, with maximum bands at λ_{max} = 714 nm, 546 nm and 488 nm, **SA10** shows ranges from 358 nm to 794 nm with a valley centered at 604 nm, with maximum bands at λ_{max} = 722 nm, 536 nm to **SA10** (Figure 78). The fluorescence spectra of **SA7-10** show strong emissions at 741, 754, 755 and 751 nm respectively.

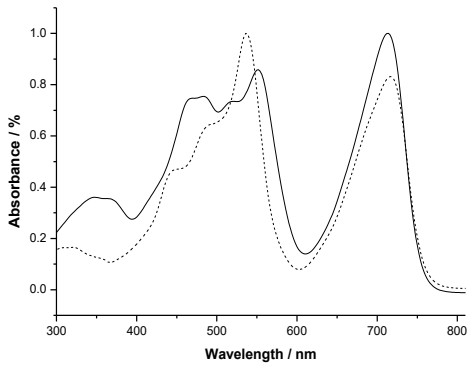

Figure 77. Normalized absorption spectra of **SA7** (solid line) and **SA9** (dash line) in CH_2Cl_2 solution (10^{-5} M)

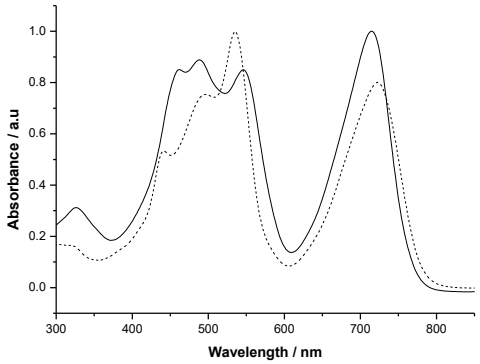

Figure 78. Normalized UV-Vis absorption spectra of compounds to **SA8** (solid line) and **SA10** (dash line) in dichloromethane solution (10^{-5} M)

Table 8. UV-Vis Absorption, Fluorescence Emission and OSWV data for compounds **SA7-10**

	λ_{max} soln (nm)	log (ε)	λ_{em} (nm)	E^1_{ox} [b, c] (V)	E^1_{red} (V)	E_{HOMO} [d] (eV)	E_{LUMO} [e] (eV)	E_g [f] (eV)
SA7	484	5.05	741	0.44	-1.40	-5.54	-3.70	1.84
	552	5.11						
	714	5.17						
SA8	488	4.96	754	0.15	-1.45	-5.25	-3.65	1.60
	546	4.94						
	714	5.01						
SA9	538	5.13	755	0.18	-1.35	-5.28	-3.75	1.53
	716	5.21						
SA10	536	5.20	751	0.21	-1.43	-5.31	-3.67	1.64
	722	5.12						

[a] 10^{-5} M, in dichloromethane; [b] 10^{-3} M in ODCB-acetonitrile (4:1) versus Fc/Fc^+ (E_{ox} = 0.04 V) glassy carbon, Pt counter electrode, 20 °C, 0.1 M Bu_4NClO_4, scan rate = 100 mV s^{-1}; [c] reversible processes; [d] calculated with respect to ferrocene, E_{HOMO}: –5.1 eV; [e] estimated from E^1_{red}; [f] Eg= E_{HOMO} – E_{LUMO}.

1.8.3 Electrochemical Properties

Redox and oxidation potentials of **SA7-SA10** were measured using Cyclic Voltammetry (CV) and Osteryoung Square Wave Voltammetry (OSWV) in *o*-DCB-acetonitrile (4:1), before HOMO and LUMO levels were calculated (Figure 79 and Figure 202).

All compounds show a first reversible one-electron oxidation wave at 0.44 V for **SA7,** 0.15 V for **SA8**, 0.18 V for **SA9** and 0.21 V for **SA10** (vs Fc/Fc^+ in all cases) which correspond to the first oxidation of the porphyrin. Moreover E_{HOMO} of all compounds was calculated from the first oxidation potential, were determined to be -5.54 eV for **SA7**, -5.21 eV for **SA8**, -5.28 eV for **SA9**

and -5.31 eV for **SA10**. Others reversible oxidation waves are observed at 0.79 and 1.00 V for **SA7,** 0.57 and 0.87 V for **SA8,** 0.48, 0.68 and 0.75 V for **SA9**, 0.61 and 1.05 V for **SA10**. Some compounds show others non reversible oxidation wave at 1.2 V for **SA7**, 0.95 V for **SA8**, 1.01 V for **SA9**. The HOMO-LUMO gaps, optically determined, are 1.70 for **SA7** and 1.69 eV for **SA8**, **SA9** and **SA10** and 1.68 eV for **SA5** and **SA6**, respectively.

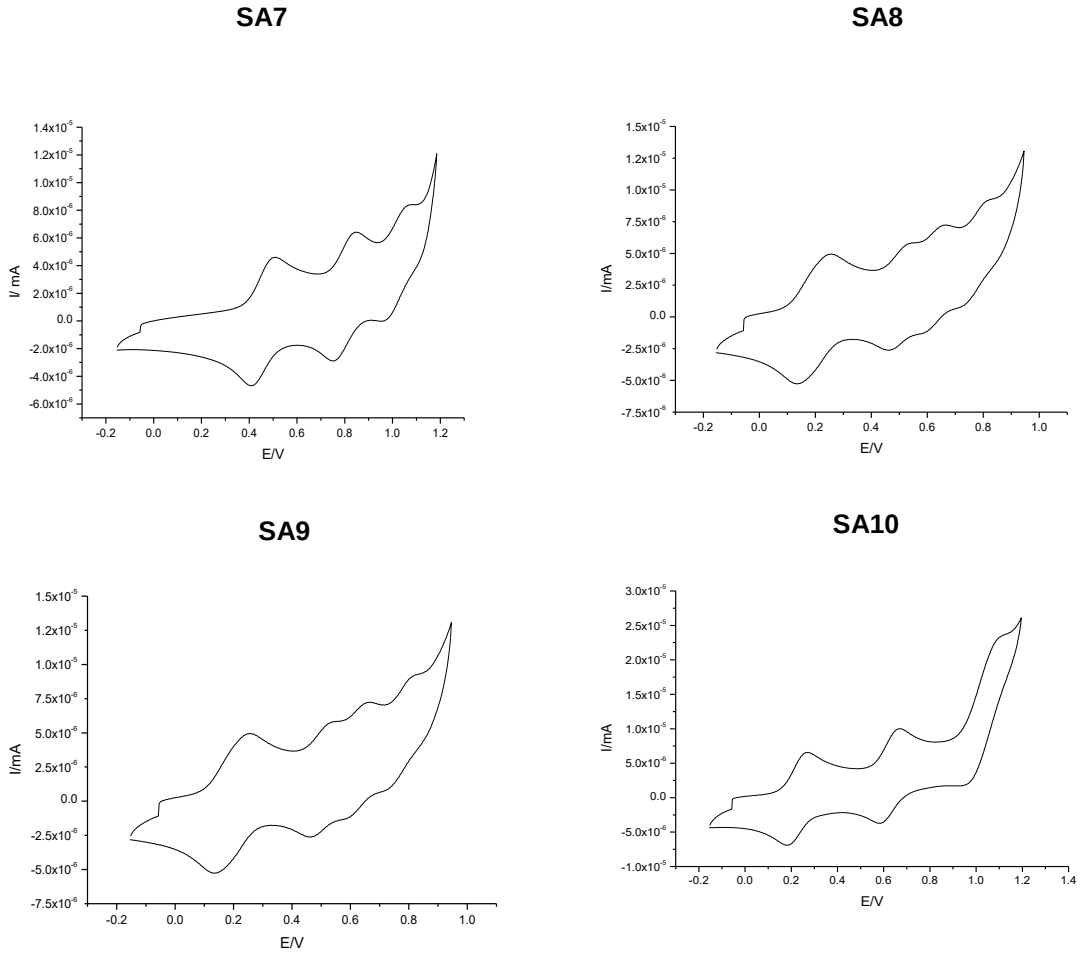

Figure 79. CV plot of **SA7**-**SA10** (anodic window)

The reduction potential is associated with electron affinity and indicates an approximate value of E_{LUMO} level. The calculated values of -3.84 for **SA7** -3.56 for **SA8** -3.59 for **SA9** and -3.62 eV for **SA10**, are appropriate to an energetically favorable electron transfer to the acceptor moiety that should in turn favor the exciton dissociation (see experimental part Figure 202). The HOMO-LUMO gaps, optically determined, are 1.70 for **SA7** and 1.69 eV for **SA8**, **SA9** and **SA10** and 1.68 eV for **SA5** and **SA6**, respectively.

1.8.4 Theoretical Calculations

The most stable geometries and theoretical HOMO and LUMO energy levels of **SA7-10** were carried out by theoretical calculations, using Gaussian 03W (Figure 80 and Figure 81).

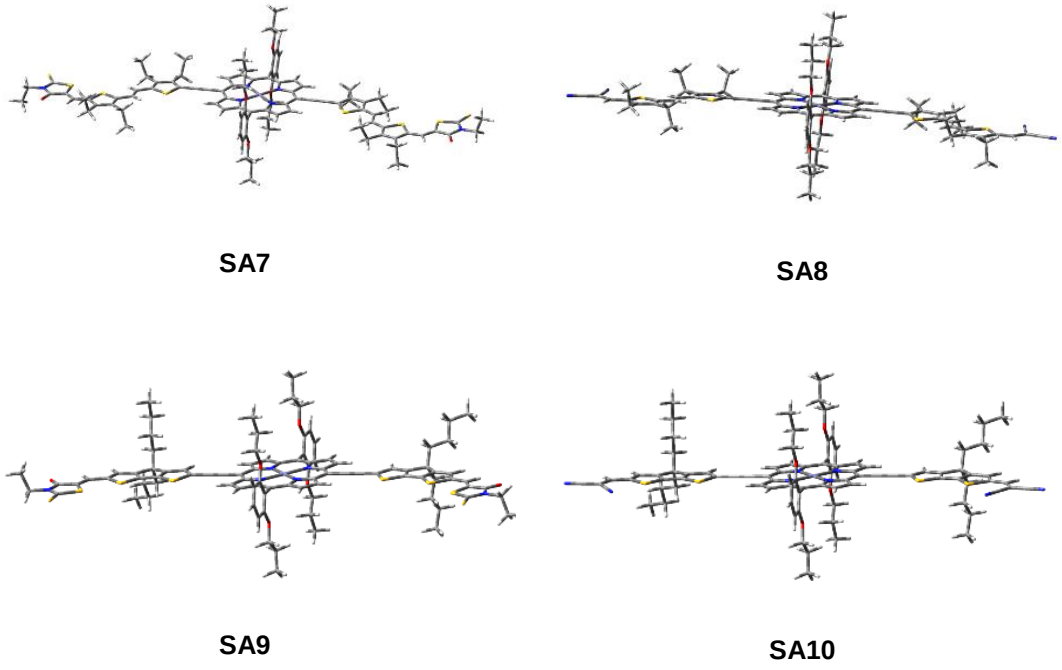

Figure 80. Geometric structures of **SA7**-**10**

The optimized structures **SA7-10** show the porphyrin macrocycle almost coplanar with the conjugated linker **2TV** or **BTC**, and phenyl rings in all molecules have a perpendicular angle with respect to the porphyrin core. The planarity allows an extension of the conjugation between the porphyrin and the conjugated linker.

The distribution of the orbital coefficients of the HOMO and LUMO states, show an overlapping between the HOMO and LUMO, in all the molecules, allowing the HOMO to LUMO electronic transitions. The HOMO charge density of compounds **SA7-10** are delocalized over the porphyrin and connector fragments. The theoretical HOMO-LUMO gaps in **SA7-10** are 1.66, 1.66, 1.71, 1.74 eV, being slightly lower compounds with **2TV** as conjugated linker.

SA8

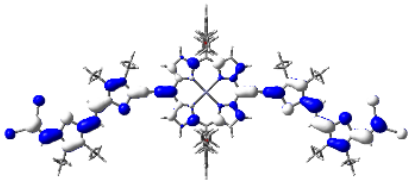

LUMO: -3,13 eV

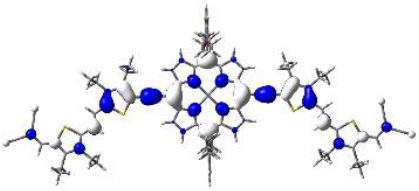

HOMO: -4,79 eV

SA7

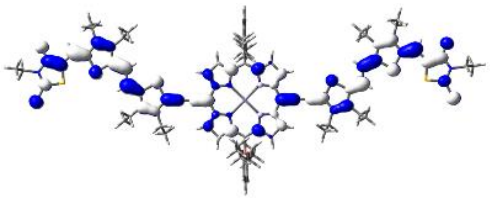

LUMO:-2,99 Ev

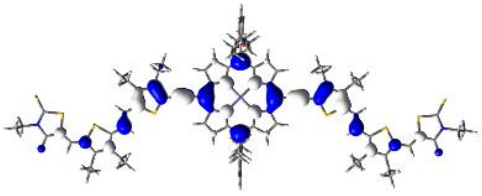

HOMO: -4,65 eV

SA10

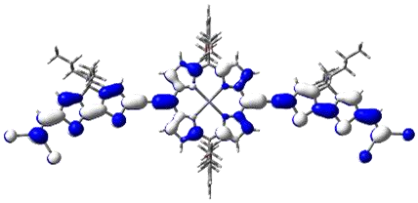

LUMO:-3,21 eV

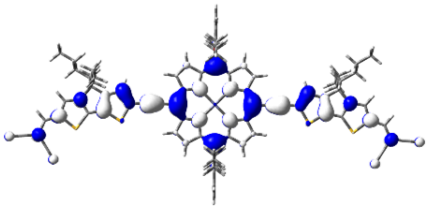

HOMO: -4,95 eV

SA9

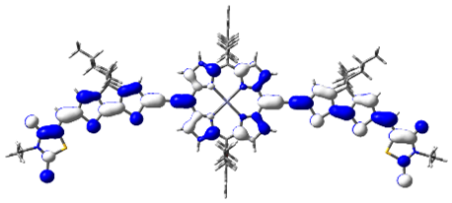

LUMO:-3,05 eV

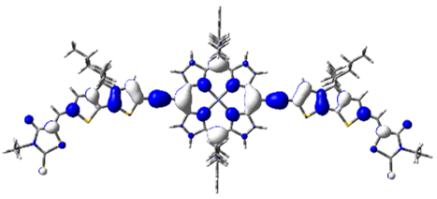

HOMO: -4,76 eV

Figure 81. Electronic density contours and energy levels for HOMO and LUMO calculated for **SA7-10**

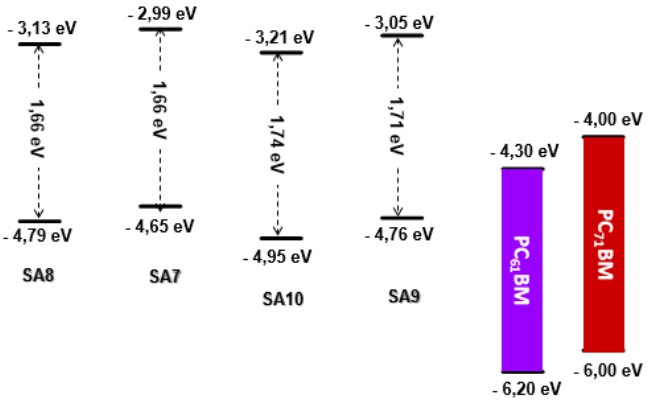

Figure 82. HOMO-LUMO of **SA7-10** and PCBM

1.8.5 Photovoltaic properties

The photovoltaic performance of **SA7-10**, were studied at the Institute of Chemical Research of Catalonia (ICIQ), Tarragona, Spain (preliminary measures).

SA7-10 devices were prepared in chlorobenzene (20 mg/mL) with $PCBM_{71}$ (ratio 1:4 w/w), using the same methodology that **SA5-6** devices; moreover, all new devices were prepared with 1% of pyridine. **SA7-10** show lower J_{SC} probably as consequence of the alcoxy chains, this bulky morphology interrupt π-π conjugation, decreasing the current. However, **SA9** shows a higher J_{SC} of 9.28 mA/cm^{-1} affording best PCE (2.20%) in relation with the other devices, probably as consequence of a better optimization. The devices incorporating 3-ethylrhodanine as acceptor, lead to a significant improvement in the power conversion efficiency with higher FF that compounds with dicyanovinylene. Nevertheless all FFs are too low to develop devices with higher PCE. Moreover V_{OC} of devices with dicyanovinylene **SA8** and **SA10** are lower that devices with rhodanine **SA7** and **SA10**. In addition, probably the widely variation of V_{OC} and J_{SC} values in similar structures **SA7-10**, is a consequence of the poor optimization of the devices, with only one batch measured for **SA7**, **SA8** and **SA10**.

Table 9 shows a summary of the photovoltaic performance of **SA7**-**SA10** blended with $PC_{71}BM$ (1:4) under the illumination of AM1.5G, 100 mW/cm^2.

Table 9. Photovoltaic performance of **SA7** to **SA10**

ACTIVE LAYER	*V_{OC} (V)*	*J_{SC} (mA cm^{-2})*	*FF (%)*	*PCE [Highest](%)*
SA7:$PC_{71}BM$ (1:4)[a B]	0.74	4.67	43.86	1.51
SA8:$PC_{71}BM$ (1:4) [a b]	0.60	4.67	25.44	0.14
SA9:$PC_{71}BM$ (1:4) [a b]	0.76	9.28	31.05	2.20
SA10:$PC_{71}BM$ (1:4) [a b]	0.43	2.61	29.80	0.33

[a] 1% of pyridine; [b] Not optimazed values

1.9 SA11 and SA12

1.9.1 Synthesis and characterization of SA11 and SA12

Synthesis of **SA11-2** was performed thanks to the collaboration of Gabriela Moran. Scheme 11 shows the synthetic route of precursor **P3**, starting from 2-hexylthiophene, DMF and $POCl_3$, according to the Vilsmeier formylation conditions, affording 5-hexylthiophene-2-carbaldehyde (**HTCHO**), in 94% yield. **HTCHO** reacted with pyrrole, via a modification of Lindsey's TFA acid catalyzed condensation, [86] affording 2,2'-((5-hexylthiophen-2-yl)methylene)bis(1H-pyrrole) in 77.5% yield.

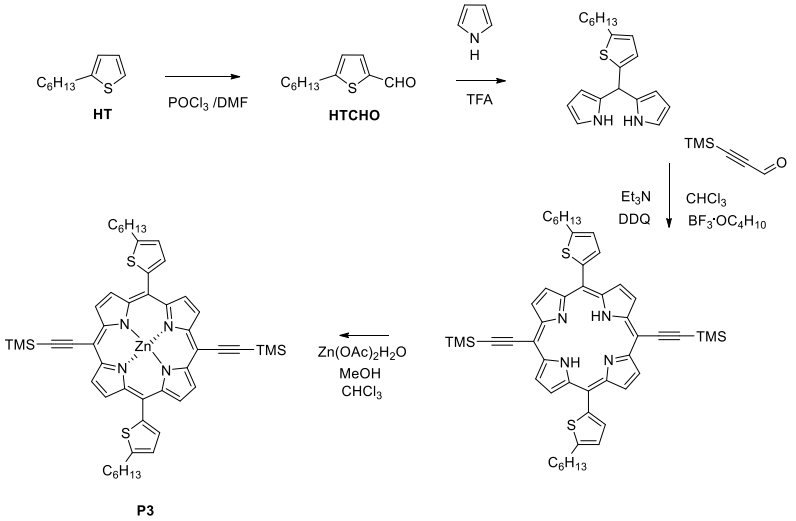

Scheme 11. Synthesis of **P3**

Finally, under Ar atmosphere, 3-(trimethylsilyl)-2-propynal was added to a solution of 2,2'-((5-hexylthiophen-2-yl)methylene)bis(1H-pyrrole) in $CHCl_3$ and $BF_3O(C_2H_5)_2$ was added to produce the porphyrinogen and this was oxidized with DDQ, after 1 hour Et_3N was added, affording 5,15-bis(5-hexylthiopen-2-yl)-10,20-bis((trimethylsilyl) ethynyl) porphyrin in 7.3% yield.[87] Porphyrin was treated with zinc acetate in $CHCl_3$ at room temperature during one night and [5,15-bis(5-hexylthiopen-2-yl)-10,20-bis((trimethylsilyl) ethynyl) porphyrinato] zinc (**P3**) was obtained in quantitative yield.[88] ^{1}H-NMR spectrum of **P3** shows all the expected signals, and in particular a signal at 0.62 ppm corresponding to the protons of the two trimethylsilyl groups (Figure 206).

Scheme 12 illustrates the synthetic route of **SA11-2**. The first step of the synthesis, was the preparation of 5,15-bis(5-hexylthiopen-2-yl)-10,20-bisethynyl porphyrinato zinc (**P3S**) was made by a double deprotection of the terminal triple bond by treatment of **P3** with TBAF, then was extracted with $CHCl_3$, the solvent was evaporated and the product was used directly in the following reaction. Aldehydes **A6-7** were obtained by double copper-free Sonogashira coupling

of **P3S** and the iodine aldehydes **C1-2**, using as $Pd_2(dba)_3$ and triphenylarsine, in presence of Et_3N refluxing for 18 hours, affording both aldehydes **A6-7** in 60% yield.

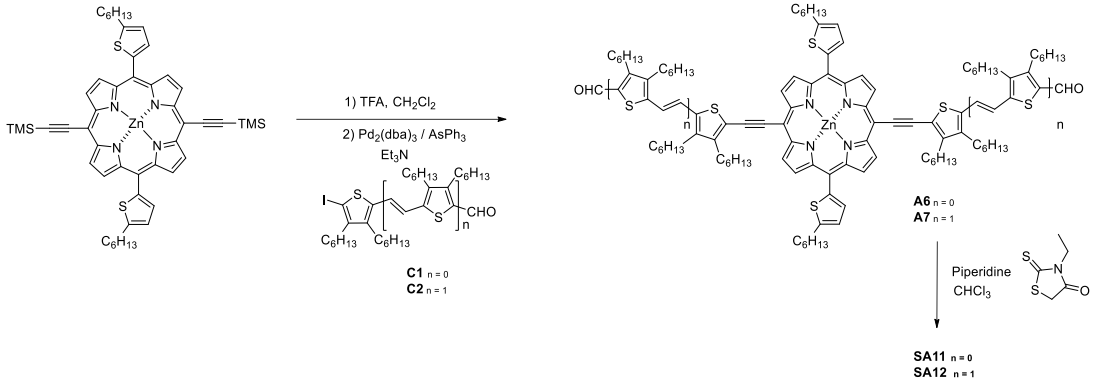

Scheme 12. Synthetic route to **SA11-12**

Compounds **SA11**-**12** were obtained by a double Knoevenagel condensation of **A6**-**7** with 3-ethylrhodanine and piperdine, affording final molecules in 95% and 34% yield respectively. ^{1}H-NMR spectrum of **SA11** shows a new signal at 6.64 ppm and **SA12** at 7.79 ppm; in both compounds these signals confirm the successful condensation (Figure 83) and additionally **SA12** show signals at 7.05 and 6.76 ppm assigned to the protons of **2TV** double bond, with a coupling constant of 16 Hz, therefore confirming the *trans* configuration. Additionally, both spectra do not show signals at 9.56 ppm corresponding to the protons of the two aldehyde groups.

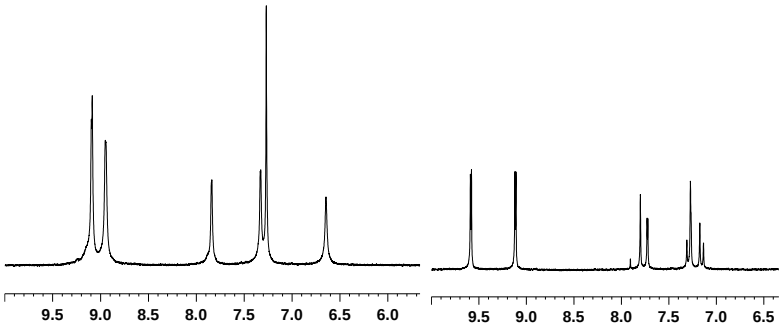

Figure 83. 7-10 ppm ^{1}H-NMR spectra of **SA11-12**

^{13}C-NMR spectrum of **SA11** shows signals at 191.66, 166.77 and 39.50 ppm and **SA12** at 191.95, 166.59 and 39.47 ppm, in both spectra these signals are assigned to the carbons of the rhodanine groups (Figure 84).

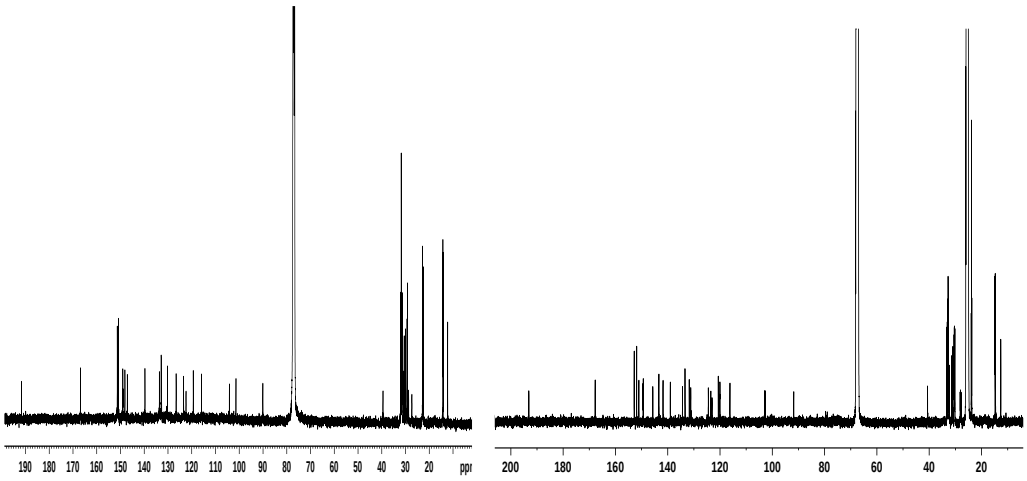

Figure 84. ^{13}C-NMR spectra of **SA11-12**

Infrared spectra of **SA11-12** show new bands assigned to ethylrhodanine moieties, at 1230 and 1240 cm^{-1} assigned to the thiocarbonyl respectively, and at 1680 and 1700 cm^{-1} respectively, corresponding to the amide. Also both spectra show bands between 2840 and 2920 cm^{-1} corresponding to the alkyl chains of *n*TV´s and hexylthiophene. Additionally both spectra do not show carbonyl band at 1650 cm^{-1} (Figure 85 and Figure 86).

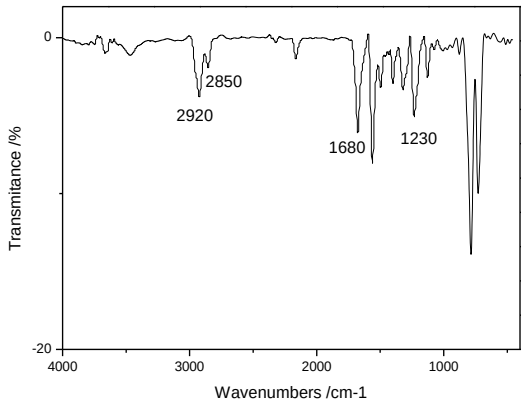

Figure 85. Infrared spectrum of **SA11**

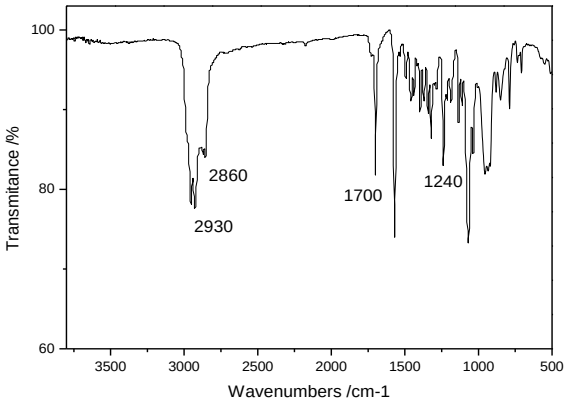

Figure 86. Infrared spectrum of **SA12**

MALDI-TOF mass spectrometry of **SA11-12** confirmed the molecular mass and showed the molecular ion *m/z* at 1597.27 and 2148.16 amu respectively (see experimental part Figure 211).

TGA investigations where done for **SA11-12**, and both compounds exhibit good thermal stabilities, with Td of 364ºC for **SA11** and 365 ºC for **SA12** (Figure 87).

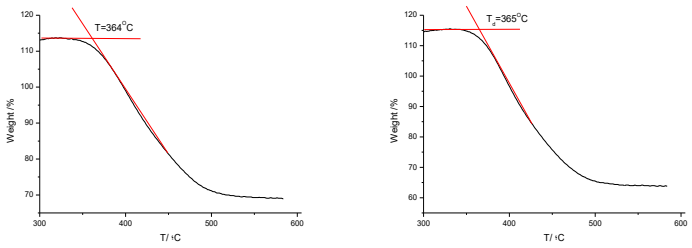

Figure 87. Thermogravimetric analysis of **SA11** (left) and **SA12** (right)

1.9.2 Optical properties

The UV-Vis spectra of **SA11-12** in solution are similar to those previously described. **A6-7** spectra show the Soret band λ_{max} at 472 nm and 503 nm respectively. The introduction of the rhodanine fragments lead to a bathochromic shift, of **SA11-12** bands as consequence of the extension of the conjugation. **SA11** has a strong absorption in the visible region with a maximum of 716 nm (log ε = 4.95), 511 nm (log ε = 5.21), 421 (log ε = 4.66), a high molar extinction coefficient that improves the light collection and allows current photogeneration. Increasing the π conjugation upon increasing the length of the thienylenevinylene in **SA12** results in a wider absorbance. **SA11** show the maximum absorption band of the spectrum at 510 nm, and **SA12** at 716 nm.

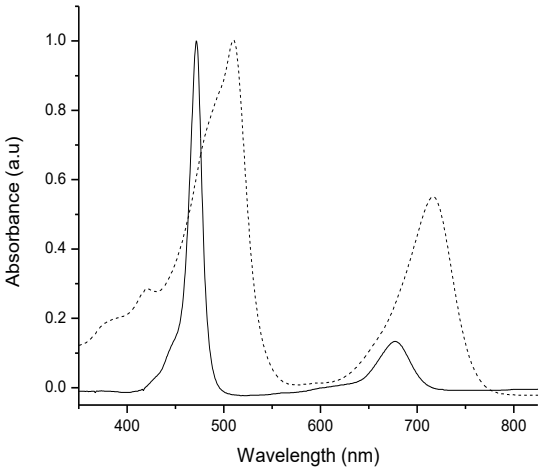

Figure 88. Normalized UV-Vis absorption spectra of **SA11** (dashed line) and precursor **A6** (solid line) in THF

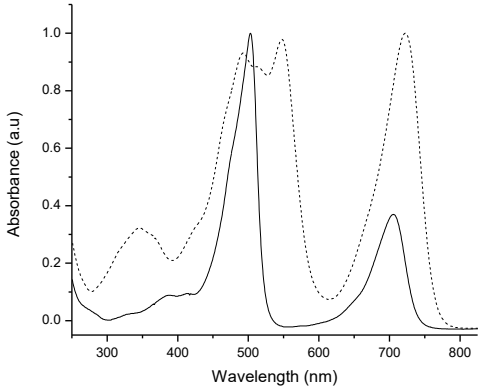

Figure 89. Normalized UV-Vis absorption spectra of **SA12** (dashed line) and precursor **A7** (solid line) in THF

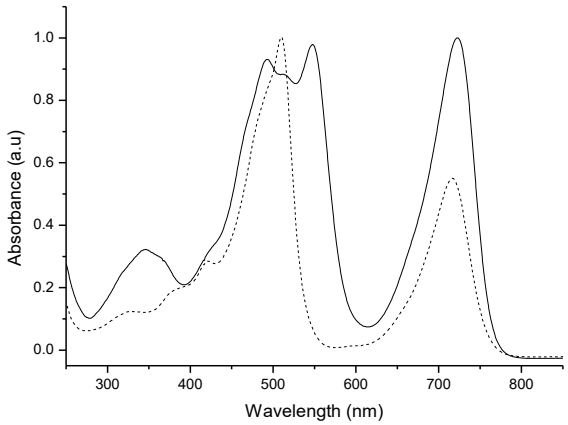

Figure 90. Normalized UV-Vis absorption spectra of **SA11-12**

Table 10. UV-Vis Absorption, Fluorescence Emission[a] and OSWV[b] data for compounds **SA11-12**

	λ_{max} soln (nm)	log (ε)	λ_{em} (nm)	E^1_{ox}[b, c] (V)	E^1_{red} (V)	E_{HOMO}[d] (eV)	E_{LUMO}[e] (eV)	E_g[f] (eV)
SA11	421	4.66	748	0.32	-1.48	-5.42	-3.62	1.80
	511	5.21						
	716	4.95						
SA12	346	4.71	750	0.20	-1.54	-5.30	-3.56	1.74
	493	5.17						
	510	5.15						
	548	5.19						
	723	5.20						

[a] 10^{-5} M, in THF; [b] 10^{-3} M in ODCB-acetonitrile (4:1) versus Fc/Fc^+ (E_{ox} = 0.04 V) glassy carbon, Pt counter electrode, 20 ºC, 0.1 M Bu_4NClO_4, scan rate = 100 mV s^{-1}; [c] Nonreversible processes; [d] calculated with respect to ferrocene, E_{HOMO}: –5.1 eV; [e] estimated from E^1_{red}; [f] Eg= E_{HOMO} – E_{LUMO}.

1.9.3 Electrochemical properties of SA11 and SA12

Electrochemical techniques were employed to measure oxidation and reduction potentials of **SA11-12** by Cyclic Voltammetry (CV) and Osteryoung Square Wave Voltammetry (OSWV) in *o*-DCB/acetonitrile (4:1) and tetrabutylammonium perchlorate as supporting electrolyte. The oxidation waves were measured at 0.32, 0.69 and 1.17 V for **SA11**, where the first one is reversible and the last two non-reversible, and 0.20, 0.48, 0.67 and 0.90 V for **SA12**, where the first three are reversible and the last one non-reversible (see Table 10, Figure 91, Figure 213 and experimental part Figure 212).

The extended conjugation of **SA12** decreased the E_{ox} value by 12 mV with respect to **SA11**. The estimated E_{HOMO} values were determined to be -5.42 eV for **SA11** and -5.30 eV for **SA11**.

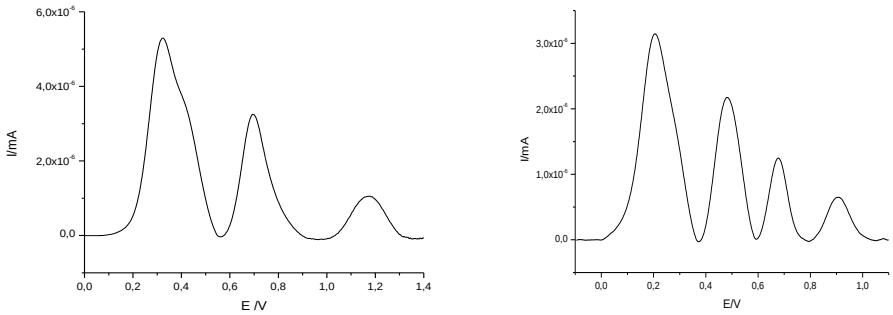

Figure 91. OSWV **SA11** (left) and **SA12** (right), (anodic window)

E_{LUMO} is related to the first reduction potential (-1.48 V and -1.54 V for **SA11-12** respectively); for both compounds E_{LUMO} values (-3.62 and -3.56 eV for **SA11** and **SA12**, respectively), match quite well the LUMO energy of $PC_{61}BM$ (-3.9 eV) and $PC_{71}BM$ (-4.0 eV), which suggest an energetically favorable electron transfer from **SA11** and **SA12** to the acceptor moiety that should favor the exciton dissociation.

Comparing with $PC_{71}BM$ as reference, the energy difference between the HOMO level of porphyrin compounds **SA11** and **SA12**, and the between $PC_{71}BM$ LUMO level, is 1.42 eV for compound **SA11** and 1.30 eV to **SA12**, values which in principle allow high open circuit voltages. The HOMO-LUMO gaps, electrochemical determined, are as narrow as 1.80 and 1.74 eV for **SA11** and **SA12**, respectively

1.9.4 Theoretical Calculations

Theoretical geometry and HOMO-LUMO properties of **SA11-12** were measured by (DFT) at the B3LYP 6-31G* (d, p) level, in gas phase, using Gaussian 03W. The most stables geometries of **SA11-12** are shown in Figure 92. Thienylenevinylene fragments are almost coplanar with the plane described by the porphyrin ring and the triple bond, with dihedral angle of 2.84° to **SA11** and 5.29° to **SA12**. This planarity allows an extension of the conjugation between the porphyrin and the rhodanine fragments. The hexylthiophene rings are attached to the porphyrin system to this plane with dihedral angle of 69.5°.

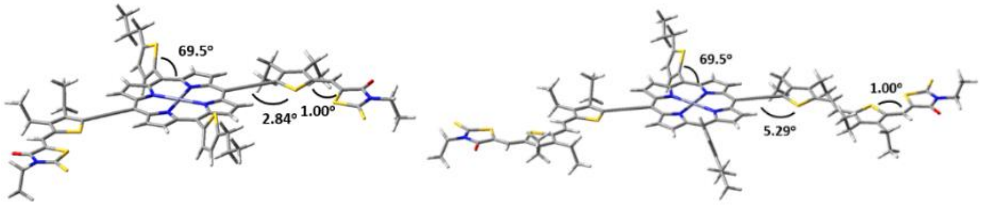

Figure 92. Geometric structure of **SA11-12**

The theoretical distributions of the orbital coefficients of the HOMO and LUMO states, shows that there exists overlapping between the HOMO and LUMO, in both molecules, favoring the HOMO to LUMO electronic transitions. The charge density of the HOMO of **SA11** and **SA12** is delocalized over the porphyrin and thienylenevinylene fragments. The theoretical difference of HOMO-LUMO gap is lower in the case of compound **SA12**, and agrees with the values obtained experimentally, 1.87 eV and 1.74 for **SA11-12** respectively, probably as consequence of the extended conjugation, increasing the HOMO level in **SA12**, with respect to **SA11**.

Theoretical energy difference between HOMO level and LUMO of $PC_{71}BM$ was calculated, showing 1.11 eV for compound **SA11** and 0.87 eV for compound **SA12**, what ensures efficient exciton dissociation at the D/A interface. (Figure 93).

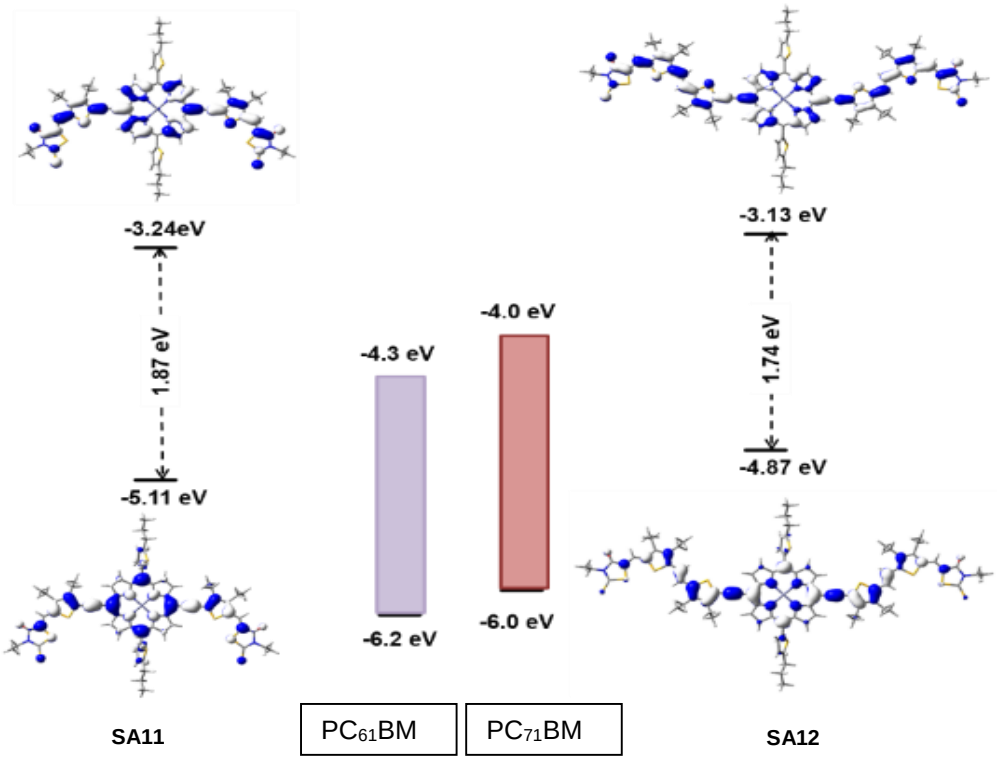

Figure 93. Electronic density contours and energy levels for HOMO and LUMO calculated for **SA11** and **SA12**

1.9.5 Photovoltaic properties

The preliminary results of the **SA11-12** photovoltaic parameters have been performed at the Institute of Chemical Research of Catalonia ICIQ, Tarragona, Spain, thanks to a collaboration with Professor Emilio Palomares.

First, **SA11**:$PC_{71}BM$ ratios were optimized, showing 1:3 ratio to be the best performance. Then, inside of the glovebox **SA11** devices were tested in different additive concentrations showing 1% pyridine devices a better performance (see Table 4). The last optimization was

measured with 1% pyridine, different ratios and thermal annealing. The best results were obtained with a 1:1 ratio and a thermal annealing of 110°C during 10 minutes with a 2.64% PCE and 9.01 mA/cm^{-2} J_{SC} (see *Table 11*).

Table 11. Photovoltaic performance of **SA11** (not optimized values)

ACTIVE LAYER	*V_{OC} (V)*	*J_{SC} (mA cm^{-2})*	*FF (%)*	*PCE [Highest](%)*
SA11:$PC_{71}BM$ (1:3)	0.73	2.51	28.50	0.52
SA11:$PC_{71}BM$ (1:3)[a]	0.74	9.33	33.90	2.36
SA11:$PC_{71}BM$ (1:3)[b]	0.51	6.26	32.60	1.05
SA11:$PC_{71}BM$ (1:1)[ac]	0.80	9.01	36.50	2.64

[a] 1% of pyridine; [b] 3% of pyridine; [c] thermal annealing (110ºC, 10 min); [d] thermal annealing (110ºC, 25 min)

SA12 devices were measured with 1% pyridine, a ratio 1:3, and different annealing times. 10 minutes of annealing showed a 9.73 mA/cm^{-2} current and 2.57% PCE, with only one optimization **SA12** shows to be a promising device to allow a higher PCE.

Table 12. Photovoltaic performance of **SA12** (with 1% pyridine, not optimized values)

ACTIVE LAYER	*V_{OC} (V)*	*J_{SC} (mA cm^{-2})*	*FF (%)*	*PCE [Highest](%)*
SA12:$PC_{71}BM$ (1:3)	0.68	9.59	33.50	2.18
SA12:$PC_{71}BM$ (1:3) [a]	0.74	9.73	35.40	2.57
SA12:$PC_{71}BM$ (1:3) [b]	0.65	10.40	32.00	2.19

[a] thermal annealing (110ºC, 10 min); [b] thermal annealing (110ºC, 25 min)

1.10 Chapter 1. Summary

Twelve new A_2B_2 porphyrins with the configuration A-π-D-π-A were synthesized and characterized by ^{1}H and ^{13}C-NMR, FT-IR spectroscopies and MALDI-MS spectrometry. Additionally, thermal analysis was evaluated.

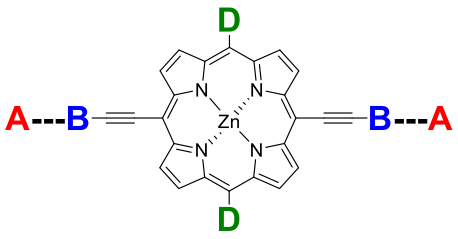

D

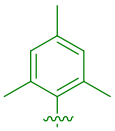

Mesityl

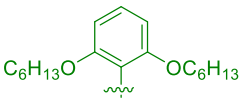

2,6-bishexyloxybenzene

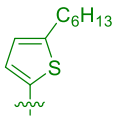

3-hexylthiophene

B

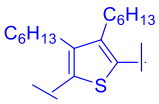

3,4 hexylthiophene

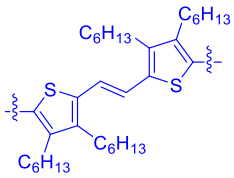

(E)-1,2-bis(3,4-dihexylthiophen-2-yl)ethylene)

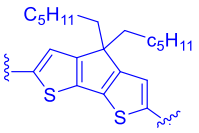

4,4-dihexyl-4H-cyclopenta[2,1-b:3,4-b']dithiophene

A

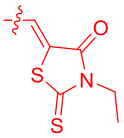

3-ethylrhodanine

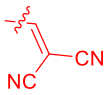

dicyanovinylene

Table 13. Donor, bridge and acceptor moieties of **SA1-12** porphyrins

D	B	A	Molecule
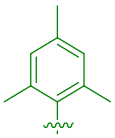	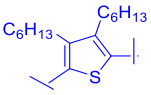		**SA1**
		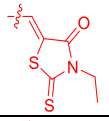	**SA3**
	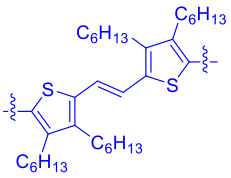		**SA2**
		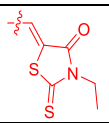	**SA4**
	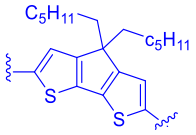	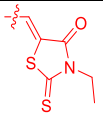	**SA5**
		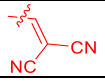	**SA6**
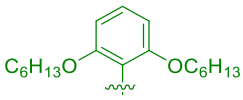	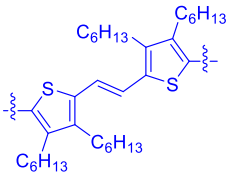	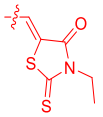	**SA7**
			**SA8**
	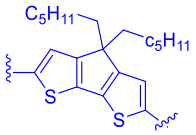	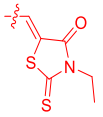	**SA9**
		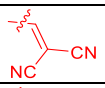	**SA10**
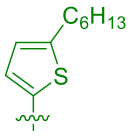	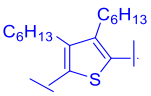	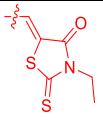	**SA11**
	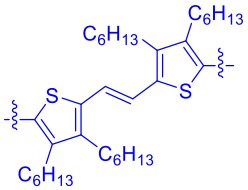	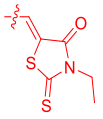	**SA12**

All new porphyrins showed similar absorption spectra, with an intense and broad Soret band and a second intense red-shifted band, attributed to intermolecular charge transfer. In addition, electrochemical properties were measured and HOMOs and LUMOs for all compounds were calculated, which agreed with the desirable values for p-type semiconductors. Next, photovoltaic devices were tested; in general, the optimized devices showed similar values of V_{OC} and FF, and devices with higher J_{SC} afforded higher PCE, depicted in Table 14.

Table 14. Photovoltaic parameters of **SA1-SA12**

ACTIVE LAYER[a]	V_{OC} *(V)*	J_{SC} *(mA cm^{-2})*	*FF (%)*	*PCE [Highest](%)*
SA1:$PC_{61}BM$ (1:2)	0.86	5.67	28.1	1.36
SA2:$PC_{71}BM$ (1:2)	0.82	10.83	35.7	3.16
SA3:$PC_{71}BM$ (1:3)	0.87	11.48	30.2	3.01
SA4:$PC_{71}BM$ (1:4)	0.80	13.20	40.1	4.24
SA5:$PC_{71}BM$ (1:4)[b]	0.80	11.72	41.1	3.87
SA6:$PC_{71}BM$ (1:4)[b]	0.80	9.78	35.5	2.77
SA7:$PC_{71}BM$ (1:4)[b]	0.74	4.67	43.9	1.51
SA8:$PC_{71}BM$ (1:4)[b]	0.60	2.67	25.4	0.14
SA9:$PC_{71}BM$ (1:4)[b]	0.76	9.28	31.1	2.20
SA10:$PC_{71}BM$ (1:4)[b]	0.43	2.61	29.8	0.33
SA11:$PC_{71}BM$ (1:1)[b]	0.80	2.64	36.5	2.64
SA12:$PC_{71}BM$ (1:3)[bc]	0.74	2.57	35.4	2.57

[a] Solvent: chlorobenzene; [b] Not optimized, 1% pyridine; [c] Thermal annealing.

In the former sections a detail analysis for each molecule was done. However, to understand the general behavior of these porphyrins different trends for porphyrin groups were analyzed. First, the behavior of **B** bridge was studied, employing the same **D** moiety and **A** acceptor (see Table 15).

Absorption of mesityl porphyrins with different bridges were analyzed (

Figure 94). The spectra showed a general tendency; porphyrins with *(E)*-1,2-bis(3,4-dihexylthiophen-2-yl)ethylene, exhibited a broader absorption than porphyrins with 4,4-dihexyl-4H-cyclopenta[2,1-b:3,4-b′]dithiophene and porphyrins with 3,4-dihexylthiophene, which corresponded with the expected values. The Soret band of porphyrin with 3,4-dihexylthiophene in both series was blue shifted (~44 nm) in comparison to *E)*-1,2-bis(3,4-dihexylthiophen-2-yl)ethylene porphyrin.

Table 15. Porphyrins with different **B** bridges and same donor and acceptor

D	A	B	Molecules
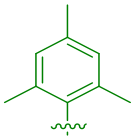	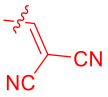	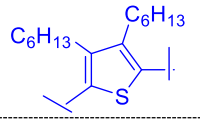	**SA1**
		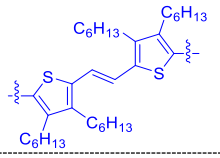	**SA2**
		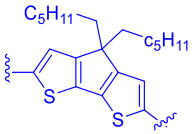	**SA6**
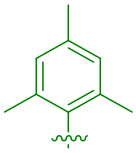	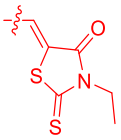	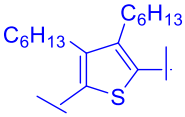	**SA3**
		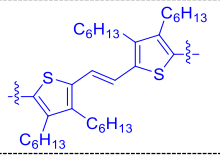	**SA4**
		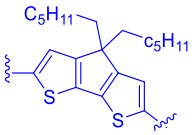	**SA5**

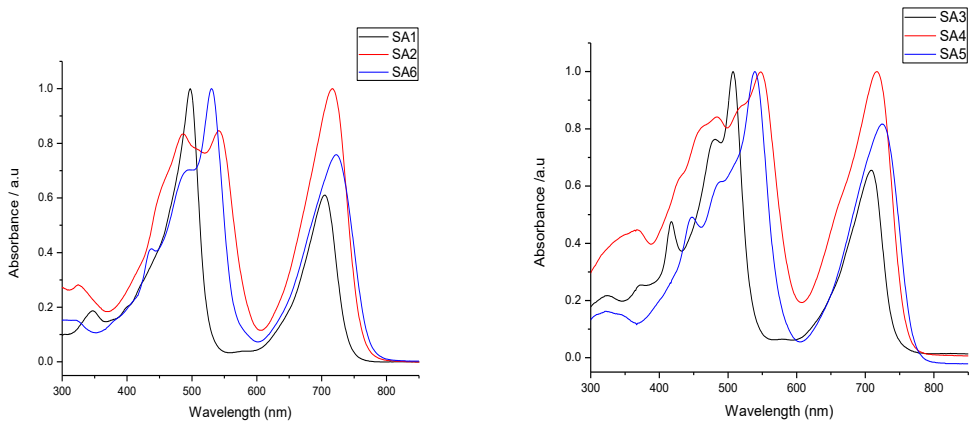

Figure 94. Normalized spectra of mesityl porphyrins with dicyanovinyl moieties and different bridges (left) and mesityl porphyrins with rhodanine moieties and different bridges (right). Bridges: 3,4-dihexylthiophene (black), 4,4-dihexyl-4H-cyclopenta[2,1-b:3,4-b′]dithiophene (blue) and *(E)*-1,2-bis(3,4-dihexylthiophen-2-yl)ethylene (red).

HOMO levels of porphyrins with different bridges were analyzed. Porphyrins with 3,4-dihexylthiophene showed a higher HOMO than 4,4-dihexyl-4H-cyclopenta[2,1-b:3,4-b′]dithiophene porphyrins and *E)*-1,2-bis(3,4-dihexylthiophen-2-yl)ethylene porphyrins, as was expected (Table 16).

Table 16. HOMO level and photovoltaic parameters of mesityl porphyrins with different bridges

Molecule	*HOMO**	*V_{OC} (V)*	*J_{SC} (mA cm^{-2})*	*FF (%)*	*PCE [Highest](%)*
SA1[a]	-5.50	0.86	5.67	28.1	1.36
SA6[b]	-5.36	0.80	9.78	35.5	2.77
SA2[c]	-5.36	0.82	10.83	35.7	3.16
SA3[a]	-5.36	0.87	11.48	30.2	3.01
SA5[b]	-5.30	0.80	11.72	41.1	3.87
SA4[c]	-5.24	0.80	13.20	40.1	4.24

*calculated by E_{HOMO}: –5.1 eV- $E^{1}_{ox;}$ Bridges: [a]3,4-dihexylthiophene; [b]4,4-dihexyl-4H-cyclopenta[2,1-b:3,4-b′]dithiophene; [c] *(E)*-1,2-bis(3,4-dihexylthiophen-2-yl)ethylene.

In order to understand the photovoltaic performance, the same two series were analyzed. Nevertheless, the devices were tested in different conditions, therefore this comparison is only a general reference to study the behavior of different porphyrin moieties. Moreover, studies of morphology, mobilities and other devices parameters are still in progress.

According to the calculated V_{OC}, porphyrins with 3,4-dihexylthiophene exhibited a higher value than porphyrins with other bridges, and these results agreed with the determinated experimental $V_{OC.}$ The calculated V_{OC} of 4,4-dihexyl-4H-cyclopenta[2,1-b:3,4-b′]dithiophene porphyrins was lower than *(E)*-1,2-bis(3,4-dihexylthiophen-2-yl)ethylene porphyrins. Nevertheless, for mesityl porphyrins with dicyanovinyl, (*E)*-1,2-bis(3,4-dihexylthiophen-2-yl)ethylene porphyrins exhibited an experimental V_{OC} 0.02 V higher than 4,4-dihexyl-4H-cyclopenta[2,1-b:3,4-b′]dithiophene porphyrins, and for mesityl porphyrins with rhodanine exhibited the same $V_{OC.}$

Next, J_{SC} in mesityl porphyrins with dicianovynil groups showed a significant difference between the different bridges. (*E)*-1,2-bis(3,4-dihexylthiophen-2-yl)ethylene showed the highest value (10.83 mAcm^{-2}); followed by 4,4-dihexyl-4H-cyclopenta[2,1-b:3,4-b′]dithiophene (9.78 mAcm^{-2}) and 3,4-dihexylthiophene (5.67 mAcm^{-2}). Mesityl porphyrins with rhodanine groups showed the same trending; moreover, the difference between each bridge is $\pm$ 2 mAcm^{-2}. Then, FF showed low values for 3,4-dihexylthiophene porphyrins and similar for the other two bridges. To finish this analysis, PCE was analyzed and as consequence of the difference in $J_{SC,}$ *(E)*-1,2-

bis(3,4-dihexylthiophen-2-yl)ethylene porphyrins showed the highest PCE, followed by 4,4-dihexyl-4H-cyclopenta[2,1-b:3,4-b']dithiophene, and 3,4-dihexylthiophene.

Then the behavior of rhodanine and dicyanovinyl groups, as acceptor, was analyzed with the same **D** moiety and same **B** bridge (see Table 17).

Table 17. Porphyrins with the same donor and bridge**,** and different **C** acceptor

D	B	A	Molecules
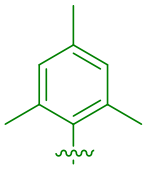	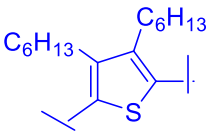	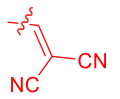	**SA1**
		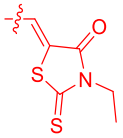	**SA3**
	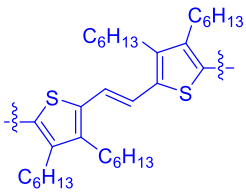	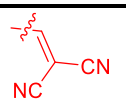	**SA2**
		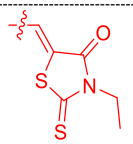	**SA4**
	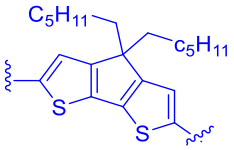	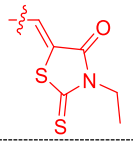	**SA5**
		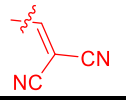	**SA6**
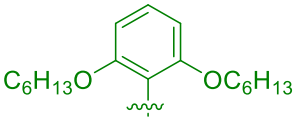	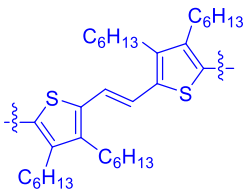	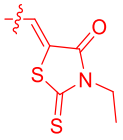	**SA7**
		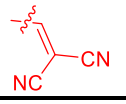	**SA8**
	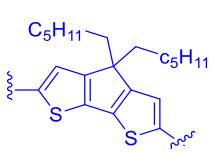	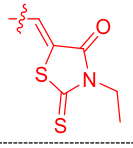	**SA9**
		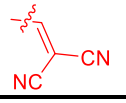	**SA10**

HOMO levels of the two acceptors were analyzed, those porphyrins with rhodanine as acceptor moiety were easier to oxidize and their HOMO was lower, as was expected; as consequence of the stronger acceptor properties of dicyanovinyl groups (see Table *18*).

Table 18. HOMO level and photovoltaic parameters of mesityl porphyrins with different acceptors

Molecule	*HOMO*	*V_{OC} (V)*	*J_{SC} ($mA\ cm^{-2}$)*	*FF (%)*	*PCE [Highest](%)*
SA1[a]	-5.50	0.86	5.67	28.1	1.36
SA3[b]	-5.36	0.87	11.48	30.2	3.01
SA2[a]	-5.36	0.82	10.83	35.7	3.16
SA4[b]	-5.24	0.80	13.20	40.1	4.24
SA6[a]	-5.36	0.80	9.78	35.5	2.77
SA5[b]	-5.30	0.80	11.72	41.1	3.87
SA9[a]	-5.31	0.76	9.28	31.1	2.20
SA10[b]	-5.28	0.43	2.61	29.8	0.33

Acceptor: [a] dicyanovinyl group; [b] rhodanine group

The photovoltaic performance of **SA1-SA4** have been already optimized; **SA5-10** devices still in process of optimization and only preliminary results are presented. As was indicated before, dicyanovinyl based porphyrins must be higher than those porphyrins having rhodanine as acceptor group. Nevertheless, experimental V_{OC} is similar for both with a difference of $\pm$ 0.01 V (see Table ***18***). **SA9-10** showed a different behavior, probably because with this devices only one measured was done. According to the tendency, **SA9-10** can be optimized to afford best V_{OC}, J_{SC} and PCE. In addition, J_{SC} and PCE can also be optimized for **SA5-6**. However, for optimized devices FF and J_{SC} is higher for rhodanine based porphyrins than for dicyanovinyl based porphyrins, affording higher PCE for these devices.

1.11 Conclusions

I. Twelve new small molecules based on porphyrin with structure A-π-D-π-A were designed, synthesized and fully characterized

II. The performance of all new porphyrin based systems in BHJSC was evaluated.

III. Mesityl porphyrin with *(E)*-1,2-bis(3,4-dihexylthiophen-2-yl)ethylene as bridge and rhodanine as acceptor (**SA4**), showed a higher J_{SC} (13 mA/cm^{-1}), allowing a higher PCE (4.24%) in comparison to the other optimized devices.

IV. Porphyrins with 3,4-dihexylthiophene as bridge showed a higher V_{OC}, (0.86 V for **SA1** and 0.87 for **SA3**) than the other optimized porphyrin based devices (0.82 V for **SA2**, 0.80 for **SA4**).

V. Porphyrins with rhodanine moiety as acceptor reached higher J_{SC} than porphyrins with dicyanovynil as terminal end, affording a better PCE.

VI. Porphyrins with (*E)*-1,2-bis(3,4-dihexylthiophen-2-yl)ethylene as bridge showed higher J_{SC} than porphyrins with other bridges, leading to higher PCE.

VII. FFs of all devices are low (~30%) and need to be optimized to enhance the efficiency.

1.12 General experimental details

1.12.1 Synthetic work condition details

Synthetic procedures were carried out under inert argon atmosphere, in dry solvent unless otherwise noted. All reagents and solvents were reagent grade and were used without further purification. Chromatographic purifications were performed using silica gel 60 SDS (particle size 0.04-0.06 mm) for flash chromatography (230-400 mesh ASTM) and silica gel 60, (particle size 0.06-0.2 mm) for column chromatography (70-230 mesh ASTM). Analytical thin-layer chromatography was performed using Merck TLC silica gel 60 F254.

1.12.1.1 Spectroscopy Characterization

^{1}H-NMR spectra were obtained on Bruker TopSpin AV-400 (400 MHz) spectrometer. Chemical shifts are reported in parts per million (ppm) relative to the solvent residual peak ($CDCl_3$, 7.27 ppm), (THF-d_8 1.73, 3.58 ppm).^{13}C-NMR chemical shifts (δ) are reported relative to the solvent residual peak ($CDCl_3$, 77.0 ppm), (THF, 25.5 ppm).

UV-Vis measurements were carried out on a Shimadzu UV 3600 spectrophotometer. For extinction coefficient determination, solutions of different concentration were prepared in CH2Cl2 (HPLC grade) with absorption between 0.1-1 of absorbance using a 1 cm UV cuvette. The emission measurements were carried out on Cary Eclipse fluorescence spectrophotometer.

Mass spectra (MALDI-TOF) were recorded on a VOYAGER DETM STR mass spectrometer using dithranol as matrix. Melting points are uncorrected.

Fourier transform infrared spectrophotometer FT-IR Thermo Nicolet AVATAR 370 incorporating an ATR (attenuated total reflectance), software EZ OMNIC, version 6.2. In each case the most characteristic bands are indicated for each compound. Measurements were made with liquid samples, some solids with KBr and the oils with ATR accessory.

1.12.1.2 Density Functional Theory (DFT) calculations

The molecular geometries and frontier molecular orbitals of these new dyes have been optimized by density functional theory (DFT) calculations at the B3LYP/6-31G* level.[89]

1.12.1.3 Electrochemistry

Cyclic voltammetry was performed in ODCB-acetonitrile (4:1) solutions. Tetrabutylammonium perchlorate (0.1 M as supporting electrolyte) were purchased from Acros and used without purification. Solutions were deoxygenated by argon bubbling prior to each experiment which was run under argon atmosphere. Experiments were done in a one-compartment cell equipped with a platinum working microelectrode ($\varnothing$ = 2 mm) and a platinum

Gwire counter electrode. An $Ag/AgNO_3$ (0.01 M in CH_3CN) electrode was used as reference and checked against the ferrocene/ferrocenium couple (Fc/Fc^+) before and after each experiment.

1.12.1.4 Thermal stability

The thermal stability was evaluated by TGA on a Mettler Toledo TGA/DSC Start System under nitrogen, with a heating rate of 10 ºC/min. Heating of crystalline samples leads to melting of the solids, but no recrystallization was observed.

1.12.2 Experimental details in the synthesis of SA1 and SA2

General procedure to Vilsmeier formilation

At room temperature to a solution of the interested compound (1eq) in 1,2-dichloroethane (1,2 DCE, dryed over $MgSO_4$ anh) was added dimethylformamide (DMF,1.8 eq), then was added drop to drop of phosphorus trichloruride, ($POCl_3$, 1.6 eq) the mixture was stirred during 18 hours at reflux temperature. The reaction was quenched with a saturated solution of sodium acetate (NaOAc, sat.) while stirring for 1 hour until reach neutral pH, and extracted with CH_2Cl_2. The combined organic phases were dried over anhydrous $MgSO_4$ and filtered. The solvent was removed by rotary evaporation.

Synthesis of 3,4-dihexyl-2-thiophencarboxaldehyde [90]

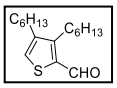

Following the general procedure to Vilsmeier formilation, to a solution of 3,4-dihexylthiophene (15.9 mmol, 4.00 g) in 48 mL of 1,2-DCE (3 mL/mmol) was added DMF (28.6 mmol, 2.2 mL), then was added drop to drop of $POCl_3$ (25.4 mmol, 2.3 mL). The product was purified by column chromatography (silica gel, hexane:$CHCl_3$, 1:1). The compound was obtained as a yellow oil (15.58 mmol, 4.40 g, 98% yield). ^{1}H-NMR (400 MHz, $CDCl_3$) δ/ppm: 10.02 (s, 1H), 7.35 (s, 1H), 2.89 (t, 2H, *J* = 5.9 Hz), 2.54 (t, 2H, *J* = 5.9 Hz), 1.64-1.57 (m, 4H), 1.39-1.31 (m, 12H), 0.92-0.88 (m, 6H).

Synthesis of *(E)*-1,2bis(2-(3,4-dihexyl-2-yl)ethylene [90]

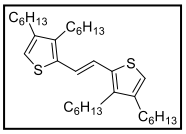

To a solution of powder zinc (Zn, 3 eq, 41.9 mmol, 2.74 g) in 94 mL of THF (6.8 mL/mmol), was added titanium tetrachloride ($TiCl_4$, 1.5 eq, 21.0 mmol, 2.3 mL) The mixture was stirred at reflux temperature during 1 hour. The reaction was cold to room temperature and was added a solution of 3,4-dihexyl-2-thiophencarboxaldehyde (1 eq, 14.0 mmol, 3.91 g) and pyridine (py, 2 eq, 27.9 mmol, 2.3 mL). The reaction was stirred 18 hours at reflux temperature. The reaction was quenched with water and extracted with $CHCl_3$ (3 x 100 mL). The combined organic extract was dried over anhydrous $MgSO_4$ and filtered. The solvent was removed by rotary evaporation. The product was purified by column chromatography (silica gel, hexane). The compound was obtained as oil (6.16 mmol, 1.72 g, 88% yield). ^{1}H-NMR (400 MHz, $CDCl_3$) δ/ppm: 7.00 (s, 2H), 6.75 (s, 2H), 2.60 (t, 4H, *J* = 7.8 Hz), 2.49 (t, 4H, *J* = 7.8 Hz), 1.63 (q, 4H, *J* = 7.7 Hz), 1.50 (q, 4H, *J* = 7.7 Hz), 1.40 (m, 8H), 1.35-1.33 (m, 16H), 0.93-0.90 (m, 12H).

Synthesis of *(E)*-5-(2-(3,4-dihexylthiophen-2-yl)vinyl)-3,4-dihexylthiophene-2-carbaldehyde [90]

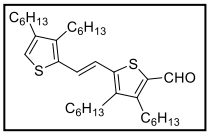

Using the general procedure to Vilsmeier formilation, DMF (6.2 mmol, 0.5 mL) was added to a solution of *(E)*-1,2bis(2-(3,4-dihexyl-2-thienyl) (4 mmol, 2.16 g) in 135 mL of 1,2-DCE (33 mL/mmol). Then $POCl_3$ (5.2 mmol, 0.5 mL) was added

dropwise. The crude was purified by chromatography column (silica gel, hexane:$CHCl_3$, 3:2). The final product was yellow oil (2.68 mmol, 1.5 g, 67% yield). ^{1}H-NMR (400 MHz, $CDCl_3$) δ/ppm: 9.97 (s, 1H), 7.27 (d, 1H, *J* = 15.5 Hz), 6.96 (d, 1H, *J* = 15.5 Hz), 6.85 (s, 1H), 2.85 (t, 2H, *J* = 8.0 Hz), 2.64-2.57 (m, 4H), 2.49 (t, 2H, *J* = 7.8 Hz), 1.67-1.27 (m, 32H), 0.93-0.85 (m, 12H).

General synthetic procedure for iodation reactions

To a solution of the connector aldehydes (**C1-3**) (1 eq) in carbon tetrachloride (CCl_4, 1.25 mL/mmol) was added $PhI(OCOCF_3)_2$ (0.55 eq) and molecular iodine (I_2, 0.5 eq). The mixture was stirred at room temperature. The reaction was quenched with a saturated solution of sodium thiosulfate (Na_2SO_3 sat.) while stirring for 15 min and extracted with CH_2Cl_2. The combined organic phases were dried over anhydrous $MgSO_4$ and filtered. The solvent was removed by rotary evaporation.

Synthesis of 5-iodo-3,4-dihexyl-2-thiophencarboxaldehyde (C1) [71]

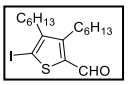

Using the general procedure previously described, 3,4-dihexyl-2-thiophencarboxaldehyde (1.8 mmol, 500 mg) was reacted with $PhI(OCOCF_3)_2$ (1.0 mmol, 416 mg) and I_2 (0.9 mmol, 226 mg) in 2.2 mL of CCl_4. The product was purified by column chromatography (silica gel, hexane:$CHCl_3$, 7:3). **C1** was obtained as yellow oil (1.51 mmol, 610 mg, 84% yield**).** ^{1}H-NMR (400 MHz, $CDCl_3$) δ/ppm: 9.90 (s, 1H), 2.94-2.90 (m, 2H), 2.57-2.53 (m, 2H), 1.64-1.57 (m, 4H), 1.39-1.31 (m, 12H), 0.93-0.88 (m, 6H). ^{13}C-NMR (100 MHz, $CDCl_3$) δ/ppm: 181.21, 150.46, 148.40, 143.02, 89.74, 32.33, 31.49, 31.46, 30.56, 29.69, 29.30, 29.26, 27.80, 22.57, 22.52, 14.06, 14.03. MALDI-TOF MS (*m/z*): calculated for $C_{17}H_{27}IOS$: 406.08; found: 406.08 (M+). FT-IR (ATR) υ/cm^{-1}: 2923, 2854, 1654, 1523, 1461, 1427, 1365, 1222, 1126, 1079, 721, 674.

Synthesis of *(E)*-1-(5-Formyl-3,4-dihexyl-2-thienyl)-2-(5-iodo-3',4'-dihexyl-2'-thienyl)ethylene (C2)

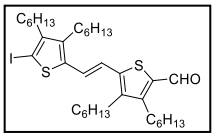

Using the general procedure previously described to iodation, E-(5-Formyl-3,4-dihexyl-2-thienyl)-2-(3',4'-dihexyl-2'-thienyl)ethylene (0.6 mmol, 338 mg) was reacted with $PhI(OCOCF_3)_2$ (0.3 mmol, 142 mg), I_2 (0.3 mmol, 77 mg) in 0.75 mL of CCl_4. The product was purified by column chromatography (silica gel, hexane:$CHCl_3$, 3:2). **C2** was obtained as yellow oil (0.37 mmol, 255 mg, 62% yield). ^{1}H-NMR (400 MHz, $CDCl_3$) δ/ppm: 9.98 (s, 1H), 7.19 (d, 1H, *J* = 15.5 Hz), 6.97 (d, 1H, *J* = 15.5 Hz), 2.84 (t, 2H, *J* = 7.7 Hz), 2.64 (t, 2H, *J* = 7.7 Hz), 2.58 (t, 2H, *J* = 7.7 Hz), 2.49 (t, 2H, *J* = 7.7 Hz), 1.50-1.27 (m, 32H), 0.94-0.88 (m, 12H). ^{13}C-NMR (100 MHz, $CDCl_3$) δ/ppm: 181.92, 152.97, 147.73, 146.57, 141.79, 141.79, 141.57, 141.00, 134.77, 123.09, 118.77, 75.46, 32.26, 31.56, 31.54, 31.52, 31.13, 31.00, 29.76, 29.32, 27.91, 27.11, 26.40, 22.60, 22.54, 14.09, 14.05.

MALDI-TOF MS (*m/z*): calculated for $C_{35}H_{55}IOS_2$: 682.27; found: 683.49 (M+). FT-IR (ATR) u/cm^{-1}: 2923, 2850, 1654, 1600, 1523, 1461, 1403, 1375, 1249, 1211, 933, 725, 678, 663.

Synthesis of dipyrromethane [91]

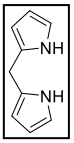

At room temperature to a solution of pyrrole (100 eq, 7.2 mol, 482 mL, previously filtered by neutral aluminum oxide) was added paraformaldehyde (1 eq, 71.7 mmol, 2.16 g), and indium trichloride ($InCl_3$, 0.1 eq, 7.2 mmol, 1.59 g), the mixture was stirred 150 minutes at 55°C, then was cooled to room temperature. Before was added sodium hydroxide (NaOH, 3 eq, 215.1 mmol, 8.60 g) and stirred by night. The crude was filtered and reduced the excess of pyrrole by distillation. The product was purified by cromatography column (silica gel, hexane:$CHCl_3$, 9:1), the compound was obtained as white solid (0.04 mol, 7.10 g, 72% yield). ^{1}H-NMR (400 MHz, $CDCl_3$) δ/ppm: 7.59 (s, 2H), 6.61 (d, 2H), 6.21 (d, 2H), 6.09 (s, 2H).

Synthesis of 5,15-dimesitylporphyrin [92]

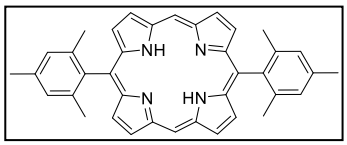

In completely anaerobic conditions, a solution of the corresponding dipyrromethane (2 eq, 14.4 mmol, 2.10 g) and 2,4,6-trimethylbenzaldehyde (2 eq, 14.4 mmol, 2.1 mL) in 1.40 L of $CHCl_3$ (97 mL/mmol) was treated with boron trifluoride diethyl etherate ($BF_3O(C_4H_{10})$, 3.3mM, 4.7 mmol, 0.6 mL). The mixture was stirred for 3 h. Before 2,3-dichloro-5,6-dicyano-p-benzoquinone (DDQ, 3 eq, 21.5 mmol, 4.9 g) was added and the reaction mixture and was stirred for 1 h. Then 2 mL of Et_3N, was added and stirred during 30 min. The solvent was removed by rotary evaporation and the solid was purified by column chromatography (silica gel, hexane:$CHCl_3$, 1:1). 5,15-Dimesitylporphyrin was obtained as a purple solid (2.56 mmol, 1400 mg, 35% yield). ^{1}H-NMR (400 MHz, $CDCl_3$) δ/ppm: 10.25 (s, 2H), 9.35 (d, 4H, *J* = 4.5 Hz), 8.91 (d, 4H, *J* = 4.5 Hz), 7.35 (s, 4H), 2.69 (s, 6H), 1.87 (s, 12H), -3.04 (s, 2H). ^{13}C-NMR (100 MHz, $CDCl_3$) δ/ppm: 146.77, 145.37, 139.49, 137.85, 137.63, 131.80, 130.00, 127.85, 117.29, 104.57, 21.72, 21.52. MALDI-TOF MS (*m/z*): calculated for $C_{38}H_{34}N_4$: 546.09; found: 546.28 (M+). FT-IR (ATR) u/cm^{-1}: 3305, 1828, 1604, 1411, 1373, 1319, 1234, 1052, 950, 852, 782, 736, 694, 617.

Synthesis of [5,15-dimesitylporphyrinato] zinc (II)[92]

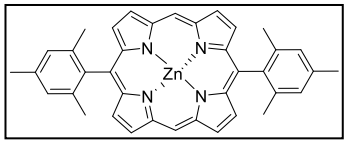

To a solution of 5,15-dimesitylporphyrin (1 eq, 2.5 mmol, 1.35 g) in 209 mL of $CHCl_3$, was added a solution of $Zn(OAc)_2{\cdot}2H_2O$ (5eq, 12.5 mmol, 2.26 g) in 6.2 mL of MeOH. The mixture was stirred 18 hours. The reaction was quenched with water and extracted with $CHCl_3$ (3 x 100 mL). The combined organic extract was dried over anhydrous $MgSO_4$ and filtered. The solvent was removed by rotary evaporation. The product was purified by column chromatography (silica gel, hexane:$CHCl_3$, 1:1). The product [5,15-dimesitylporphyrinato] zinc

(II), was obtained as a purple solid (2.47 mmol, 1510 mg, 99% yield). ^{1}H-NMR (400 MHz, $CDCl_3$) δ/ppm: 10.27 (s, 2H), 9.41 (d, 4H, *J* = 4.4 Hz), 9.00 (d, 4H, *J* = 4.4 Hz), 7.35 (s, 4H), 2.69 (s, 6H), 1.85 (s, 12H). ^{13}C-NMR (100 MHz, $CDCl_3$) δ/ppm: 149.83, 149.41, 139.32, 138.78, 135.70, 132.11, 131.26, 127.68, 118.23, 105.50, 21.66, 21.49. MALDI-TOF MS (*m/z*): calculated for $C_{38}H_{32}N_4Zn$: 608.57; found: 608.19 (M+). FT-IR (ATR) υ/cm^{-1}: 1816, 1608, 1438, 1388, 1318, 1211, 1052, 856, 786, 728, 701, 617.

Synthesis of [5,15-dibromo-10,20-dimesitylporphyrinato] zinc (II)

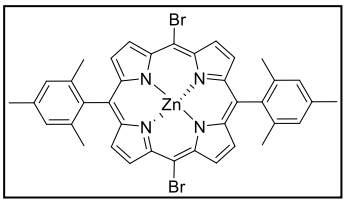

To a solution of [5,15-dimesitylporphyrinato] zinc (II) (1 eq, 1.5 mmol, 920 mg) in 80 mL of $CHCl_3$, *N*-bromosuccinimide (NBS) (2 eq, 3.0 mmol, 536 mg) and 1 mL of pyridine were added. The mixture was stirred 30 minutes and quenched with acetone. The solvent was removed by rotary evaporation and the solid was purified by column chromatography (silica gel, hexane:$CHCl_3$, 7:3). The product [5,15-dibromo-10,20-dimesitylporphinato] zinc (II) was obtained as a purple solid (1.45 mmol, 1117 mg, 98% yield). ^{1}H-NMR (400 MHz, $CDCl_3$) δ/ppm: 9.59 (d, 4H, *J* = 4.6 Hz), 8.71 (d, 4H, *J* = 4.6 Hz), 7.80 (s, 4H), 2.65 (s, 6H), 1.80 (s, 12H). ^{13}C-NMR (100 MHz, $CDCl_3$) δ/ppm: 150.48, 149.93, 139.10, 138.84, 137.55, 133.33, 131.96, 127.66, 122.33, 120.12, 104.09, 55.43, 21.64, 21.45. MALDI-TOF MS (*m/z*): calculated for $C_{38}H_{30}Br_2N_4Zn$: 766.73; found: 766.01 (M+). FT-IR (ATR) υ/cm^{-1}: 1808, 1604, 1423, 1373, 1315, 1203, 1072, 995, 860, 786, 740, 694, 628, 609.

Synthesis of [5,15-bis-(trimethylsilyl)ethynyl)-10,20-dimesitylporphyrinato] zinc (II) (P1)

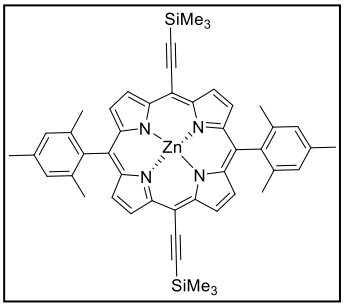

In a schlenk tube under an argon (Ar) atmosphere, a solution of [5,15-dibromo-10,20-dimesitylporphyrinato] zinc (II) (1 eq, 1.4 mmol, 1.10 g) in 62 mL of THF and 3 mL of Et_3N was added over a mixture of $Pd(PPh_3)_2Cl_2$ (0.1 eq, 0.1 mmol, 54 mg) and CuI (0.05 eq, 0.07 mmol, 13 mg). Afterwards, trimehylsilylacethylene (5.4 mmol, 0.8 mL) was added. The mixture was stirred 18 h. The solvent was removed by rotary evaporation and the solid was purified by column chromatography (silica gel, hexane:$CHCl_3$, 7:3) and recrystallized from CH_2Cl_2/MeOH. **P1** was obtained as a purple solid (1.35 mmol, 1.07 g, 97% yield). ^{1}H-NMR (400 MHz, $CDCl_3$) δ/ppm: 9.68 (d, 4H, *J* = 4.6 Hz), 8.79 (d, 4H, *J* = 4.6 Hz), 7.33 (s, 4H), 2.68 (s, 6H), 1.86 (s, 12H), 0.62 (s, 18H). ^{13}C-NMR (100 MHz, $CDCl_3$) δ/ppm: 152.09, 149.94, 139.04, 138.35, 137.64, 131.87, 131.67, 131.45, 127.72, 120.91, 107.36, 101.49, 100.63, 21.51, 21.48, 0.34. MALDI-TOF MS (*m/z*): calculated for $C_{48}H_{48}N_4Si_2Zn$: 800.58; found: 800.27 (M+). FT-IR (ATR) υ/cm^{-1}: 2136, 1808, 1604, 1438, 1380, 1334, 1203, 1072, 995, 860, 786, 736, 694, 617.

Synthesis of [5,15-bis-(ethynyl)-10,20-dimesitylporphyrinato] zinc (II) (P1S)

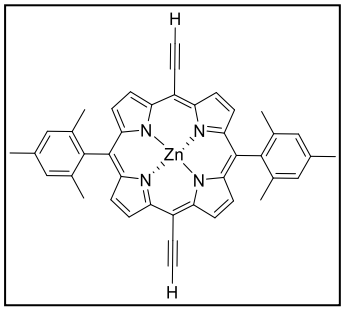

To a solution of **P1** (0.7 mmol, 550 mg) in 150 mL of CH_2Cl_2, was added TBAF 1 M in THF (1.65 mmol, 1.65 mL). The solution was stirred at room temperature for 2 h and treated with $CaCl_2$ (8.2 mmol, 912 mg). The reaction was hydrolyzed with water and extracted with $CHCl_3$ (3 x 150 mL). The combined organic extract was dried over anhydrous $MgSO_4$ and filtered; finally, the solvent was removed by rotary evaporation. The deprotected product was quantitatively obtained and it was used in the next synthetic step without further purification.

General Procedure for the Sonogashira coupling

Under completely anaerobic conditions, by cycles of vacuum and argon atmosphere, a solution of the porphyrin (**P1S**, **P2S**, **P3S**, **P4S**) (1 eq), the corresponding connector (**C1**, **C2**, **C3**, **C4**, **C5**) (3 eq) and freshly distilled Et_3N (45 mL/mmol) in dryed and degasified THF (230 mL/mmol) was added over a mixture of $Pd_2(dba)_3$ (0.6 eq) and $AsPh_3$ (3.8 eq). The reaction mixture was refluxed for 18 h. The solvent was removed by rotary evaporation.

Synthesis of A1

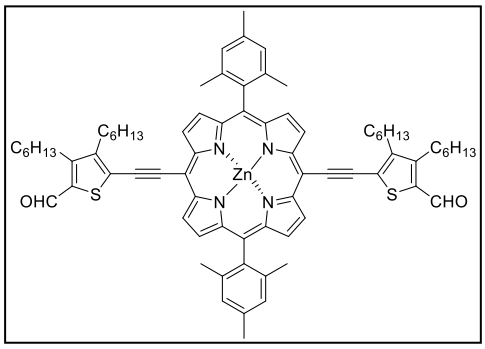

Using the general procedure previously described, [5,15-bis-(ethynyl)-10,20-dimesitylporphyrinato] zinc (II) (0.34 mmol, 658 mg), 5-Iodo-3,4-dihexyl-2-thiophencarboxaldehyde (1.02 mmol, 417 mg), 15 mL of Et_3N in 79 mL of THF were allowed to react. The product was purified by column chromatography (silica gel, hexane:CH_2Cl_2, 7:3) followed by recrystallization from CH_2Cl_2:MeOH. **A1** was obtained as a green solid (0.22 mmol, 337 mg, 81% yield). ^{1}H-NMR (400 MHz, $CDCl_3$) δ/ppm: 9.49 (d, 4H, *J* = 4.4 Hz), 9.16 (s, 2H), 8.75 (d, 4H, *J* = 4.4 Hz), 7.33 (s, 4H), 2.99 (t, 4H, *J* = 7.6 Hz), 2.80 (t, 4H, *J* = 7.6 Hz), 2.69 (s, 6H), 1.89 (s, 12H), 1.60 (t, 4H, *J* = 7.2 Hz), 1.54 (t, 4H, *J* = 7.2 Hz), 1.43-1.22 (m, 24H), 0.93 (t, 6H, *J* = 6.4 Hz), 0.77 (t, 6H, *J* = 7.0 Hz). ^{13}C-NMR (100 MHz, $CDCl_3$) δ/ppm: 207.23, 181.21, 151.69, 151.66, 150.08, 148.21, 139.99, 138.11, 137.87, 137.32, 131.89, 131.18, 129.36, 127.83, 122.00, 103.12, 100.09, 89.53, 32.32, 31.76, 31.58, 30.91, 30.88, 29.67, 29.41, 28.66, 27.46, 22.65, 22.62, 21.59, 21.51, 14.12, 14.01. MALDI-TOF MS (*m/z*): calculated for $C_{76}H_{84}N_4O_2S_2Zn$: 1212.53; found: 1212.53 (M+). FT-IR (ATR) υ/cm^{-1}: 2919, 2854, 2175, 2053, 1650, 1612, 1489, 1438, 1403, 1330, 1284, 1207, 1150, 995, 937, 848, 790, 709.

Synthesis of A2

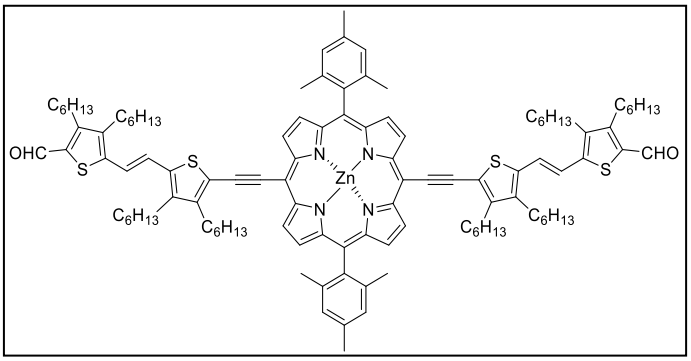

Using the general procedure previously described, [5,15-bis-(ethynyl)-10,20-dimesitylporphyrinato] zinc (II) (0.34 mmol, 658 mg), *(E)*-1-(5-Formyl-3,4-dihexyl-2-thienyl)-2-(5-iodo-3',4'-dihexyl-2'-thienyl)ethylene (1.02 mmol, 702 mg), 15 mL of Et_3N in 79 mL of THF. **A2** was obtained as a green solid (0.14 mmol, 246 mg, 71%). ^{1}H-NMR (400 MHz, CDCl3) δ/ppm: 9.56 (s, 1H), 9.55 (d, 4H, *J* = 4.6 Hz), 8.73 (d, 4H, *J* = 4.6 Hz), 7.32 (s, 4H), 7.32 (d, 2H, *J* = 15.5 Hz), 7.08 (d, 2H, *J* = 15.5 Hz), 3.05 (t, 4H, *J* = 7.9 Hz), 2.79 (t, 4H, *J* = 7.9 Hz), 2.75 (t, 4H, *J* = 8.3 Hz), 2.68 (s, 6H), 2.66 (t, 4H, *J* = 7.2 Hz), 1.91 (t, 4H, *J* = 7.2 Hz), 1.89 (s, 12H), 1.67-1.31 (m, 60H), 1.00-0.91 (m, 18H), 0.80 (t, 6H, *J* = 7.2 Hz). ^{13}C-NMR (100 MHz, CDCl3) δ/ppm: 181.73, 153.15, 151.59, 149.68, 148.48, 146.94, 142.74, 141.94, 139.03, 138.32, 137.67, 137.28, 134.58, 131.47, 131. 05, 127.71, 123.46, 121.51, 118.95, 118.91, 101.16, 100.84, 90.67, 32.25, 31.80, 31.66, 31.59, 31.54, 31.19, 30.94, 29.70, 29.45, 29.34, 29.26, 27.49, 27.11, 26.44, 22.66, 22.57, 21.53, 21.47, 14.17, 14.12. MALDI-TOF MS (*m/z*): calculated for $C_{112}H_{140}N_4O_2S_4Zn$: 1764.92; found (M+): 1765.07. FT-IR (ATR) υ/cm-1: 2919, 2854, 2175, 1646, 1592, 1500, 1454, 1388, 1338, 1292, 1207, 1095, 998, 929, 852, 790, 709.

General procedure for the Knoevenagel condensations with malonitrile

To a solution of **A1-2** (1 eq) in 25 mL/mmol of CH_2Cl_2, malonitrile (3 eq) and 3 drops of Et_3N were added. The reaction mixture was stirred for 18 h and quenched by the addition of water and extracted with $CHCl_3$ (3 x 150 mL). The combined organic extract was dried over anhydrous $MgSO_4$ and filtered. The solvent was removed by rotary evaporation. The product was purified by column chromatography (silica gel, hexane:CH_2Cl_2, 1:1) and recrystallized with CH_2Cl_2: MeOH.

Synthesis of SA1

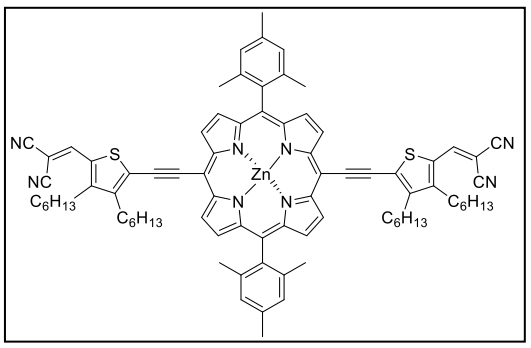

Using the general procedure previously described, **A1** (0.08 mmol, 100 mg) in 2 mL of CH_2Cl_2 were allowed to react with malonitrile (0.25 mmol, 16 mg). **SA1** was obtained as a green solid (0.06 mmol, 87 mg, 81% yield). ^{1}H-NMR (400 MHz, $CDCl_3$) δ/ppm: 9.16 (s, 4H), 8.75 (d, 4H, *J* = 4.2 Hz), 7.89 (s, 2H), 7.37 (s, 4H), 3.84 (m, 4H),

2.76 (m, 4H), 2.71 (s, 6H), 1.96 (s, 12H), 1.76 (m, 4H), 1.64-1.74 (m, 12H), 1.27-1.22 (m, 16H), 0.97 (m, 6H), 0.76 (t, 6H, *J* = 6.7 Hz). ^{13}C-NMR (100 MHz, $CDCl_3$) δ/ppm: 154.35, 151.57, 150.32, 147.73, 147.40, 138.92, 138.06, 137.79, 132.25, 131.02, 130.78, 127.93, 122.76, 115.07, 113.87, 106.31, 99.53, 89.43, 75.19, 32.34, 31.71, 31.55, 31.46, 30.90, 30.71, 30.15, 29.73, 29.55, 29.14, 28.71, 22.61, 21.65, 21.54, 14.11, 13.98. MP: > 300°C. MALDI-TOF MS (*m/z*): calculated for $C_{82}H_{84}N_8S_2Zn$: 1308.53; found: 1308.56 (M+). FT-IR (ATR) υ/cm^{-1}: 2923, 2854, 2225, 2154, 2053, 1612, 1489, 1465, 1403, 1330, 1288, 1249, 1203, 1083, 998, 937, 850, 790, 711.

Synthesis of SA2

Using the general procedure previously described, **A2** (0.2 mmol, 295 mg) in 3 mL of CH_2Cl_2, malonitrile (0.5 mmol, 33 mg). **SA2** was obtained as a green solid (0.06 mmol, 246 mg, 79% yield).

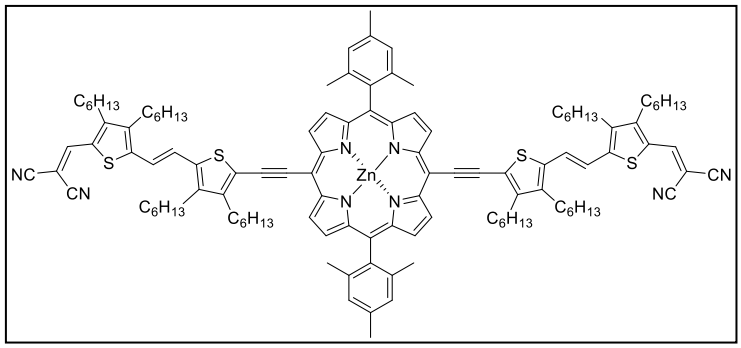

^{1}H-NMR (400 MHz, $CDCl_3$) δ/ppm: 9.46 (d, 4H, *J* = 4.4 Hz), 8.68 (d, 4H, *J* = 4.4 Hz), 7.69 (s, 2H), 7.28 (s, 4H), 7.21 (d, 2H, *J* = 15.6 Hz), 6.96 (d, 2H, *J* = 15.6 Hz), 2.96 (t, 4H, *J* = 7.7 Hz), 2.70 (t, 4H, *J* = 7.7 Hz), 2.62 (s, 6H), 2.57 (m, 8H), 1.85 (s, 12H), 1.60-1.54 (m, 8H), 1.49-1.26 (m, 56H), 0.94-0.56 (m, 18H), 0.73 (t, 6H, *J* = 7.0 Hz). ^{13}C-NMR (100 MHz, $CDCl_3$) δ/ppm: 155.91, 151.63, 149.76, 149.12, 148.83, 147.24, 144.08, 141.61, 139.00, 138.16, 137.78, 137.22, 131.61, 131.12, 128.29, 127.76, 125.39, 121.72, 120.07, 118.21, 115.59, 114.17, 101.40, 101.19, 90.76, 73.13, 32.17, 31.79, 31.60, 31.55, 31.49, 31.00, 29.73, 29.45, 29.31, 29.28, 27.82, 27.47, 26.81, 22.66, 22.63, 22.62, 22.56. MP: > 300°C. MALDI-TOF MS (*m/z*): $[M]^+$ calculated for $C_{118}H_{140}N_8S_4Zn$: 1860.94; found: 1861.94. FT-IR (ATR) υ/cm^{-1}: 2928, 2856, 2217, 2171, 1552, 1500, 1457, 1399, 1336, 1288, 1209, 1091, 998, 929, 854, 794, 711.

1.12.3 Experimental details in the synthesis of SA3 and SA4

General procedure for the knoevenagel condensations with 3-ethyl rhodanine

To a solution of **A1-2** (1 eq) in 75 mL/mmol of $CHCl_3$. 3-ethylrhodanine (10 eq) and 3 drops of piperidine were added. The reaction mixture was refluxed and stirred for 12 h and quenched by the addition of water and extracted with $CHCl_3$ (3 x 150 mL). The combined organic extract was dried over anhydrous $MgSO_4$ and filtered. The solvent was removed by rotary evaporation. The product was purified by column chromatography (silica gel, $CHCl_3$) and recrystallized with CH_2Cl_2: MeOH**.**

Synthesis of SA3

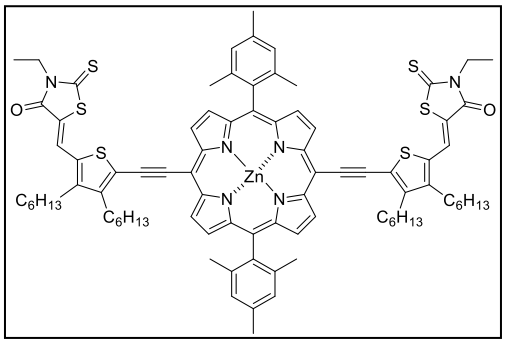

Using the general procedure previously described, **A1** (0.06 mmol, 80 mg) in 5 mL of $CHCl_3$, 3-ethylrhodanine (0.65 mmol, 110 mg)**. SA3** was obtained as a green solid (0.05 mmol, 81 mg, 82% yield). ^{1}H-NMR (400 MHz, $CDCl_3$) δ/ppm: 9.57 (d, 4H, *J* = 4.8 Hz), 8.78 (d, 4H, *J* = 4.4 Hz), 8.00(s, 2H), 7.33(s, 4H), 4.22 (d,4H, J=5.7 Hz), 3.11 (m, 4H), 2.88 (m, 4H), 2.67 (s, 6H), 1.88 (s, 12 H), 1.65 (m, 8H), 1.54-1.52 (m, 12H), 1.39-1.30 (m, 18), 0.95(m, 6H),0.81- 0.77 (m, 6H). ^{13}C-NMR (100 MHz, $CDCl_3$) δ/ppm: 192.50, 167.65, 151.79, 150.20, 149.22, 148.40, 139.17, 138.02, 133.72, 132.08, 131.30, 128.00, 127.76, 123.64, 122.30, 120.72, 40.16, 32.04, 31.95, 31.79, 31.07, 29.91, 29.65, 29.44, 28.14, 22.84, 21.74, 21.67, 14.29, 14.19, 12.52. MP: > 300°C. MALDI-TOF MS (*m/z*): calculated for $C_{88}H_{94}N_6S_6O_2Zn$: 1498.51; found: 1498.75 (M+). FT-IR (ATR) υ/cm^{-1}: 2924, 2855, 1700, 1677, 1565, 1500, 1400, 1322, 1234, 1203, 1130, 998, 883, 794, 709.

Synthesis of SA4

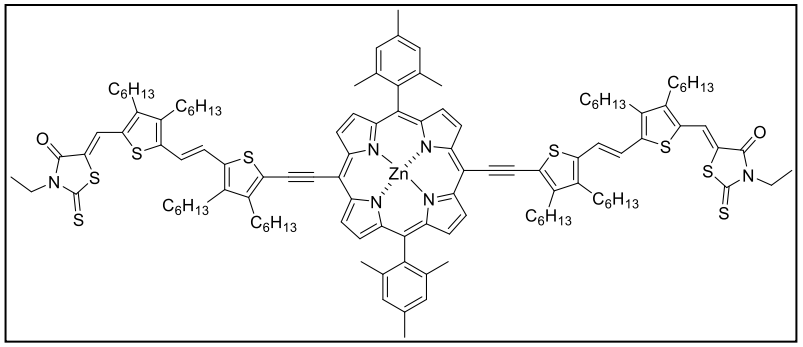

Using the general procedure previously described, **A2** (0.04 mmol, 80 mg) in 4 mL of $CHCl_3$, 3-ethylrhodanine (0.45 mmol, 72 mg). **SA4** was obtained as a green solid (0.05 mmol, 42 mg, 45% yield). ^{1}H-NMR (400 MHz, $CDCl_3$) δ/ppm: 9.58 (d, 4H, *J* = 4.1Hz), 8.74 (d, 4H, *J* = 3.45 Hz), 7.95 (s, 2H), 7.36 (d, 2H), 7.32 (s, 4H), 7.18 (d, 2H, *J* = 15.4 Hz), 4.22(d, 4H, J=6.76 Hz), 3.35, (m, 2H), 3.08 (t,4H, J=6.8Hz), 2.82-2.67(s,14H), 2.18 (s,12H), 1.95-1.85 (m,14H), 1.67(t,4H, *J* = 5.79 Hz), 1.55 (s,12H), 1.43-1.26 (m,30H), 0.97-0.80 (m, 18H), 0.08 (t, 18H, *J* = 4.3 Hz). ^{13}C-NMR (100 MHz, $CDCl_3$) δ/ppm: 192.74, 167.79, 151.93, 151.04, 149.99, 149.05, 145.70, 142.89, 142.70, 139.33, 138.13, 137.86, 131.82, 131.43, 130.99, 128.05, 121.88, 119.38, 101.65, 101.14, 40.22, 32.12, 31.95, 31.91, 31.87, 31.75, 31.50, 31.25, 30.05, 29.70, 29.61, 27.72, 22.97, 22.90, 21.82, 14.52, 14.49, 14.38, 14.33, 12.63. MP > 300°C. MALDI-TOF MS (*m/z*): calculated for $C_{122}H_{150}N_6O_2S_8Zn$: 2050.89; found: 2051.69 (M+). FT-IR (ATR) υ/cm^{-1}: 2958, 2919, 2850, 1700, 1565, 1496, 1457, 1434, 1392,1322, 1261,1230, 1130, 1091, 998, 925, 883, 794, 736.

1.12.4 Experimental details in the synthesis of SA5-SA6

Synthesis of 4,4-dihexyl-4H-cyclopenta[2,1-b:3,4-b′]dithiophene-2-carbaldehyde

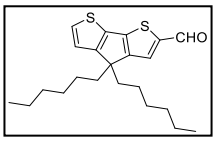

Following the Vilsmeier formilation procedure, at room temperature to a solution of 4,4-dihexyl-4H-cyclopenta[2,1-b:3,4-b′]dithiophene (1.44 mmol, 500 mg) in 18 mL of 1,2 DCE was added DMF (2.59 mmol, 0.19 mL), then was added drop to drop of $POCl_3$, (2.59 mmol, 0.24 mL). The product was purified by column chromatography (silica gel, hexane:$CHCl_3$, 1:1). The compound was obtained as a yellow oil (450 mg, 1.20 mmol, 83% yield). ^{1}H-NMR (400 MHz, $CDCl_3$) δ/ppm: 9.84 (s,1H), 7.59 (s, 1H), 7.40 (d, 1H, *J* = 4.86 Hz), 6.99 (d,2H, *J* = 4.86 Hz), 1.86 (m,4H), 1.28, (m, 2H), 1.73 (m, 10H), 0.93(m, 4H), 0.81 (m, 6H).

Synthesis of 4,4-dihexyl-6-iodo-4H-cyclopenta[2,1-b:3,4-b′]dithiophene-2-carbaldehyde

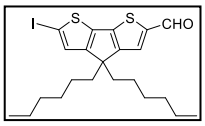

Using the general procedure previously described to iodation, 4,4-dihexyl-4H-cyclopenta[2,1-b:3,4-b′]dithiophene-2-carbaldehyde, (1.2 mmol, 450 mg) was reacted with $PhI(OCOCF_3)_2$ (0.65 mmol, 280 mg) and I_2 (0.59 mmol, 152 mg) in 1.5 mL of CCl_4. The product was purified by column chromatography (silica gel, hexane:$CHCl_3$, 7:3). **C3** was obtained as yellow oil (450 mg, 1.11 mmol, 92% yield)**.** ^{1}H-NMR (400 MHz, $CDCl_3$) δ/ppm: 9.84 (s, 1H), 7.57 (s, 1H), 7.17 (s, 1H), 1.84 (m, 4H), 1.14, (m, 12H), 0.92 (m, 4H), 0.82 (m, 6H). ^{13}C-NMR (100 MHz, $CDCl_3$) δ/ppm: 182.49, 161.02, 157.09, 146.70, 143.45, 135.85, 129.80, 124.88, 124.30, 116.79, 54.55, 37.40, 31.55, 29.17, 24.43, 22.49, 13.90.

Synthesis of A3

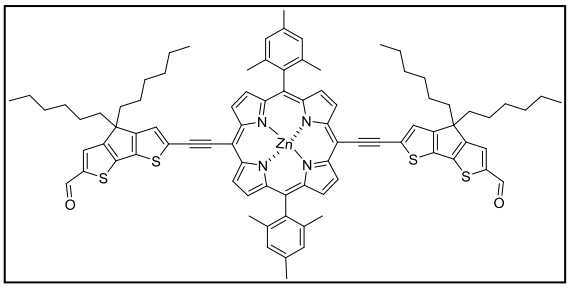

Using the general procedure of sonogashira coupling previously described, porphyrin 5,15-bis-(ethynyl)-10,20-dimesitylporphinato zinc (II) (0.35 mmol, 230 mg), **C3** (1.05 mmol, 525 mg), 15 mL of Et_3N in 80 mL of THF was added over a mixture of $Pd_2(dba)_3$ (0.21 mmol, 192 mg) and $AsPh_3$ (1.4 mmol, 428mg). **A3** was obtained as green solid (0.28 mmol, 404 mg, 82%). **¹**H-NMR (400 MHz, $CDCl_3$) δ/ppm: 9.79 (s,2H), 9.64 (d, 4H, *J* = 4.5 Hz), 8.74(d, 4H, *J* = 4.5 Hz), 7.33 (s, 4H), 2.67 (m, 4H), 2.00 (t, 6H, *J* = 7.9 Hz), 1.87 (m, 13H), 1.53 (m, 10H), 1.25-1.22 (m, 22H), 1.08 (M, 6H), 0.89-0.83 (m, 9H). ^{13}C-NMR (100 MHz, $CDCl_3$) δ/ppm: 182.75, 162.31, 159.36, 151.84, 150.11, 147.40, 144.01, 139.24, 138.45, 138.01, 137.44, 131.92, 131.42, 130.11, 128.39, 128.03, 126.35, 121.95, 100.76, 99.74, 91.13, 54.52, 38.00, 32.15, 31.84, 29.92, 29.89, 29.59, 24.87, 22.92, 22.86, 21.77, 21.72, 14.35, 14.27. MALDI-TOF MS (*m/z*): calculated for $C_{86}H_{88}N_4O_2S_4Zn$: 1400.51;

found: 1401.40 (M+). FT-IR (ATR) υ/cm^{-1}: 2931, 2915, 2850, 2811, 2140, 2059, 1650, 1500, 1423, 1396, 1334, 1288, 1226, 1149, 1130, 1076, 998, 852, 802, 713.

Synthesis of SA5

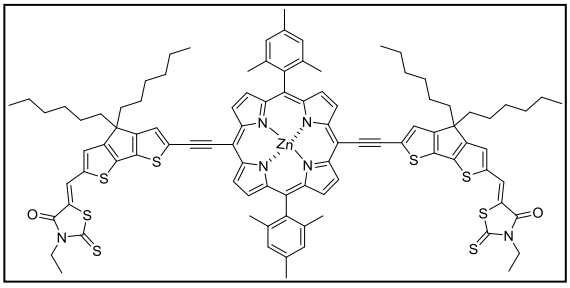

Using the general procedure to knoveanaguel condensation with 3-ethylrhodanine previously described, **A3** (0.10 mmol, 150 mg) in 5 mL of $CHCl_3$ were allowed to react with 3 ethyl-rhodanine (1.06 mmol, 172.32 mg). **SA5** was obtained as a green solid (137 mg, 0.09 mmol, 91% yield). ^{1}H-NMR (400 MHz, $THFd_8$) δ/ppm: 9.57 (d, 4H, *J* = 4.4 Hz), 8.65 (d, 4H, *J* = 4.4 Hz), 8.01 (s, 2H), 7.76 (s, 2H), 7.59 (s, 2H), 7.34 (s, 4H), 4.18 (m, 4H), 2.64 (m,6H), 2.51 (m, 9H), 2.09 (t, 6H, *J* = 7.67 Hz), 1.90 (m, 12H), 1.28-1.23 (m, 28H), 1.11 (m, 6H), 0.83 (m, 9H). ^{13}C-NMR (100 MHz, $CDCl_3$) δ/ppm: 192.53, 167.68, 162.02, 161.64, 152.55, 150.76, 146.62, 140.86, 140.02, 139.86, 138.81, 131.88, 129.48, 128.84, 127.40, 126.93, 122.34, 119.29, 101.07, 92.03, 55.42, 40.61, 38.88, 32.75, 30.82, 23.69, 22.05, 21.75, 14.55, 12.55. MP: >300°C. MALDI-TOF MS (*m/z*): calculated for $C_{96}H_{98}N_6O_2S_8Zn$: 1686.48; found: 1687.05 (M+). FT-IR (ATR) υ/cm^{-1}: 2931, 2854, 2368, 2321, 1700, 1577, 1504, 1488, 1415, 1373, 1315, 1234,1126, 1103, 998, 879, 829, 790, 732, 709

Synthesis of SA6

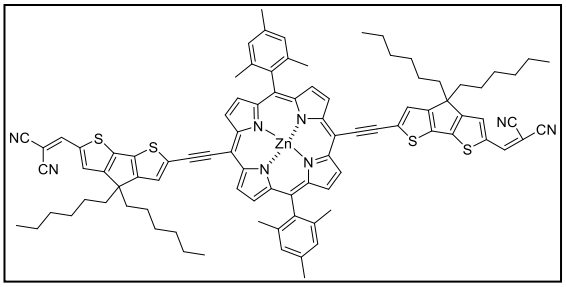

Using the general procedure to knoevenaguel condensation with malonitrile previously described, **A3** (0.03mmol, 50 mg) in 3 mL of $CHCl_3$, malonitrile (0.10 mmol, 7 mg)**. SA6** was obtained as a green solid (46 mg, 0.02 mmol, 88% yield)**.** ^{1}H-NMR (400 MHz, $CDCl_3$) δ/ppm: 9.65 (d, 4H, *J* = 4.5 Hz), 8.79(d, 4H, *J* = 4.5 Hz), 7.72 (s, 2H), 7.58 (s, 2H), 7.57 (s, 2H), 7.32 (s, 2H), 2.67 (m, 4H), 2.00 (t, 6H), 1.87 (m, 12H), 1.53 (m, 4H), 1.26-1.22 (m, 22H), 1.17-1.05 (m, 6H), 0.87-0.83 (m, 9H).^{13}C-NMR (100 MHz, $CDCl_3$) δ/ppm: 164.07, 160.09, 151.81, 150.90, 150.47, 150.19, 139.18, 138.29, 138.08, 136.84, 136.46, 132.08, 131.41, 130.83, 128.03, 126.29, 122.26, 115.12, 114.37, 101.37, 100.51, 91.14, 72.51, 54.67, 38.01, 31.78, 29.78, 24.85, 22.81, 21.73, 14.23. MP: > 300°C. MALDI-TOF MS (*m/z*): calculated for $C_{92}H_{88}N_8S_4Zn$: 1496.53; found: 1497.23 (M+). FT-IR (ATR) υ/cm^{-1}: 2919, 2850, 2360, 1727, 1562, 1,457, 1407, 1380, 1276, 1130, 1079, 968, 890, 794, 740, 717, 709.

1.12.5 Experimental details in the synthesis of SA7-10

1,3-dihexyloxybenzene

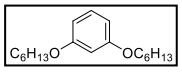

A mixture of resorcinol (1 eq, 10 g, 0.9 mol), 1-bromohexane (0.36 mol, 51 mLl) and K_2CO_3 (0.36 mol, 50 g) was refluxed for 4 days in dry THF (490 mL). The solvent was removed under reduced pressure and extracted with ethyl acetate (EtOAc, 3 × 100 mL). The combined extracts were washed with water and dried over anhydrous $MgSO_4$. After removal of solvent under reduced pressure, the product was purified by column chromatography eluting with hexane to give 1,3-di(hexyloxy)benzene (0.89 mol, 25.2 g, 99% yield). ^{1}H-NMR ($CDCl_3$, 400 MHz) δ/ppm: 7.16 (t, *J* = 8.3 Hz, 1H), 6.47 (m, 3H), 3.94 (t, *J* = 6.6 Hz, 4H), 1.77 (m, 4H), 1.45 (m, 4H), 1.34-1.36 (m, 8H), 0.91 (t, *J* = 6.6 Hz, 6H).

2,6-dihexyloxybenzaldehyde

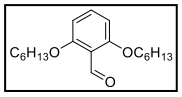

To a stirred solution of 1,3-dihexyloxybenzene (22.66 mmol, 6.31 g) in dry THF (35 mL) at 0 °C, was added tetramethylethylenediamine (TMEDA) (25.60 mmol, 3.83 mL), the solution was desgassed with argon and dropwise n-BuLi (27.19 mmol, 10.9 mL, 1.5 M in hexanes). The mixture was stirred at 0 °C for 30 min and then DMF (33.9 mmol, 2.63 mL) was added. After 1 h, the mixture was poured into a hydrochloric acid solution. The THF phase was separated and the water phase was extracted with ether (3 × 30 mL). The combined organic phase was dried over anhydride Mg_2SO_4. The product was purified by column chromatography with silica gel and hexane:$CHCl_3$,6:4. The product was obtained as colorless oil; yield, (16.08 mmol, 4.48 g, 71% yield). ^{1}H-NMR (CDCl3, 400 MHz) δ/ppm: 10.54 (s, 1H), 7.38 (t, *J* = 8.0 Hz, 1H), 6.53 (d, 2H), 4.03 (t, 4H), 1.83 (m, 4H), 1.47-1.34 (m, 12H), 0.90 (t, 6H).

5-(2,6-dihexyloxybenzyl) dypirromethane

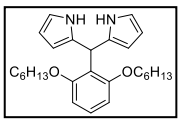

At room temperature a solution of 2,6-dihexyloxybenzaldehyde (1 eq, 5.92 mmol, 1.65 g) in pyrrole (25 eq 148 mmol, 10.28 mL, with previously filtered with neutral aluminum oxide) was stirred 15 minutes, then was added trifluoroacetic acid (TFA, 0.1 eq, 0.59 mmol, 67 mg) and was stirred 15 minutes. The reaction was quenched with a saturated solution of hydroxide sodium (NaOH, sat.), extracted with EtOAc (3 x 50 mL). The combined organic phases were dried over anhydrous $MgSO_4$ and filtered. The solvent was removed under reduced pressure. The crude was purified by chromatography column (silica gel, hexane:$CHCl_3$, 1:1). The final product was oil (48 mmol 20 g, 65% yield). ^{1}H-NMR (400 MHz, $CDCl_3$) δ/ppm: 8.57 (s, 2H), 7.13 (t, *J* = 8.2 Hz, 1H), 6.62 (d, 2H), 6.57 (d, 2H, *J* = 8.1 Hz), 6.0 (d, 2H), 5.89 (d ,2H), 3.88 (t, 4H), 1.29-127 (m, 10H), 0.92-0.89 (m, 12H).

Synthesis of 5,15-bis-(trimethylsilyl)ethynyl)-10,20-(2,6-dihexyloxybenzyl)lporphyryn (II)

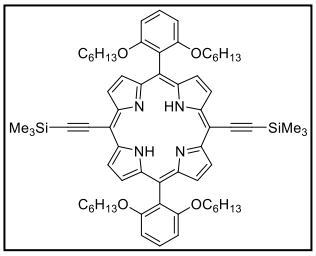

In Ar atmosphere, was added 3-(trimethylsilyl)-2-propynal (2 eq, 7.57 mmol, 1.12 mL) to a solution of 5-(2,6-dihexyloxybenzyl)dypirromethane (2 eq, 3.26 g, 7.5 mmol) in 757 mL of chloroform ($CHCl_3$, 100 mL/mmol) and $BF_3O(C_2H_5)_2$ (3.3mM, 2.49 mmol, 0.31 mL). The solution was stirred at room temperature for 60 minutes before adding DDQ (1.5 eq, 4.96 mmol, 1.13 g). The solution was stirred at room temperature for 1 hour before quenching with 1 mL of Et_3N. After 30 min the solvent was removed under reduced pressure. The crude was purified by chromatography column (silica gel, hexane:$CHCl_3$, 1:1.). The final product was a green-purple solid (0.72 mmol, 774 mg, 19% yield).). ^{1}H-NMR (400 MHz, $CDCl_3$) δ/ppm: 9.52 (d, 4H, *J* = 4.6 Hz), 8.78 (d, 4H, *J* = 4.6 Hz), 7.71 (t, 2H, *J* = 8.4 Hz), 7.00 (d, 4H, *J* = 8.5 Hz), 3.85 (t, 8H, *J* = 6.2 Hz), 1.50 (m, 2H), 1.31-1.28 (m, 6H), 0.97 (m, 9H), 0.63-0.56 (m, 30H), 0.45 (m, 6H), 0.30(m, 9H), -2.07 (s, 2H).

Synthesis of [5,15-bis-(trimethylsilyl)ethynyl)-10,20-(2,6-dihexyloxybenzyl)lporphyrinato] zinc (II) (P2)

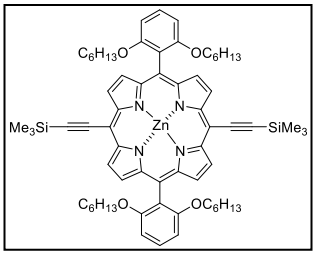

At room temperature $Zn(OAc)_2{*}2H_2O$ (5 eq, 3.39 mmol, 623 mg) was added to a solution of 5,15-bis-(trimethylsilyl)ethynyl)-10,20-(2,6-dihexyloxybenzyl)lporphyryn (II) (1 eq, 0.68 mmol, 717 mg) in 58 mL of $CHCl_3$ (85 mL/mmol), and 1.69 mL of methanol (2.5 mL/mmol). The solution was stirred at room temperature all night. The organic phase was extracted with chloroform ($CHCl_3$, 3 x 25mL). The resultant organic phase was dried with anhydrous magnesium sulfate ($MgSO_4$) and filtered. The solvent was removed under reduced pressure. The crude was purified by chromatography column (silica gel, hexane:$CHCl_3$, 1:1). The final product was a green-purple solid (0.67 mmol, 691 mg, 99.1 % yield). ^{1}H-NMR (400 MHz, $CDCl_3$) δ/ppm: 9.64 (d, 4H, *J* = 4.6 Hz), 8.89 (d, 4H, *J* = 4.6 Hz), 7.71 (t, 2H, *J* = 8.4 Hz), 7.01 (d, 4H, *J* = 8.4 Hz), 3.86 (t, 8H, *J* = 6.3 Hz), 1.37 (m, 2H), 1.32 (m, 2H) 1.29 (m, 2H), 0.97 (m, 9H, *J* = 7.29 Hz), 0.65-0.54 (m, 32H), 0.39 (m, 6H), 0.29 (m, 9H).

Synthesis of [5,15-bis-(ethynyl)-10,20-(2,6-dihexyloxybenzyl)lporphyrinato] zinc (II) (P2S)

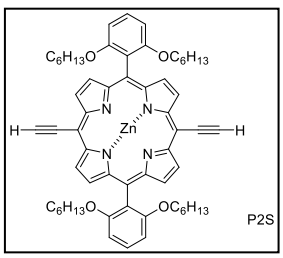

To a solution of **P2** (1 eq, 0.3 mmol, 337 mg) in 66 mL of $CHCl_3$ (220 mL/mmol), was added TBAF 1 M in THF (2.42 eq, 0.73 mmol, 0.73 mL). The solution was stirred at room temperature for 2 h and treated with $CaCl_2$ (12 eq, 3.60 mmol, 399 mg). The reaction was hydrolyzed with water and extracted with $CHCl_3$ (3 x 150 mL). The

combined organic extract was dried over anhydrous $MgSO_4$ and filtered; finally, the solvent was removed by rotary evaporation. The deprotected product was quantitatively obtained and it was used in the next synthetic step without further purification.

Synthesis of A4

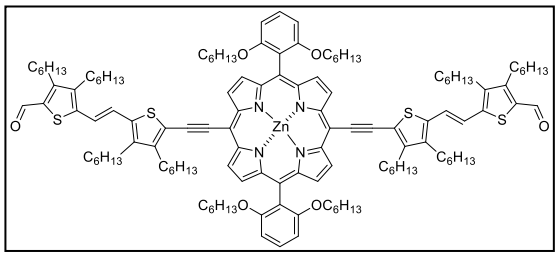

Using the general procedure for sonogashira coupling previously described, with a modification in **C2** equivalents, **P2S** (0.25 mmol, 243 mg), **C2** (2 eq, 0.5 mmol, 341 mg) in 11 mL of Et_3N in 58 mL of THF. **A4** was obtained as a green solid (0.13 mmol, 270 mg, 51%). ^{1}H-NMR (400 MHz, $CDCl_3$) δ/ppm: 9.94 (s, 2H), 9.60 (d, 4H, *J* = 4.5 Hz), 8.86 (d, 4H, *J* = 4.5 Hz), 7.71 (t, 2H, *J* = 8.49), 7.38 (d, 2H, *J* = 15.52), 7.12 (d, 2H, *J* = 15.52) 7.01 (d, 4H, *J* = 8.53 Hz), 3.87 (t, 8H, *J* = 6.14 Hz), 3.12 (t, 3H, *J* = 7.36 Hz), 2.88 (t, 3H, *J* = 7.32 Hz), 2.77 (t, 3H, *J* = 7.32 Hz), 2.69 (t, 3H, *J* = 7.32 Hz), 1.97 (m, 4H), 1.71-1.55 (m, 16H), 1.48-1.34 (m, 52H), 1.01-0.84 (m, 36H), 0.53 (m, 14H), 0.41 (m, 6H), 0.24 (m, 8H). ^{13}C-NMR (100 MHz, $CDCl_3$) δ/ppm: 181.91, 159.89, 153.09, 151.35, 150.52, 148.09, 146.97, 142.80, 141.93, 136.93, 134.79, 132.01, 130.33, 129.94, 123.58, 120.68, 119.55, 118.78, 115.88, 105.21, 101.46, 100.53, 89.78, 68.65, 32.32, 31.89, 31.71, 31.63, 31.58, 31.24, 31.04, 30.79, 29.80, 29.49, 29.39, 28.59, 27.56, 27.20, 26.52, 24.88, 22.75, 22.68, 22.60, 22.01, 14.19, 14.15, 14.11, 14.10, 13.50. MALDI-TOF MS (m/z): calculated for $C_{130}H_{176}N_4O_6S_4Zn$: 2081.18; found: 2082.29 (M+). FT-IR (ATR) υ/cm^{-1}: 2952, 2925, 2854, 2335, 2171, 1652, 1616, 1589, 1502, 1454, 1400, 1375, 1340, 1292, 1247, 1220, 1205, 1122, 1097, 1060, 997, 931, 823, 792, 765, 744, 723, 709.

Synthesis of SA7

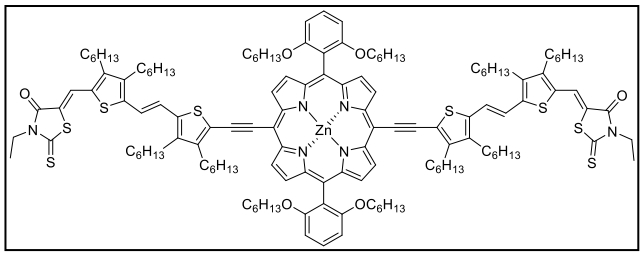

Using the general procedure for Knoevenagel with 3 ethylrhodanine previously described, **A4** (0.05 mmol, 110 mg) in 4 mL of $CHCl_3$, 3-ethylrhodanine (0.53 mmol, 85 mg)**. SA7** was obtained as a green solid (69 mg, 0.03 mmol, 59% yield). ^{1}H-NMR (400 MHz, $CDCl_3$) δ/ppm: 9.60 (d, 4H, *J* = 3.6 Hz), 8.86 (d, 4H, *J* = 3.6 Hz), 7.96 (s, 2H), 7.72 (t, 2H, *J* = 8.40), 7.31 (d, 2H, *J* =15.52), 7.17 (d, 2H, *J* =15.52), 7.02 (d, 4H, *J* = 8.08 Hz), 4.25 (d, 4H, *J* = 6.6 Hz), 3.87 (t, 8H, *J* = 6.21 Hz), 3.14 (m, 4H), 2.83-2.72 (m, 14H), 1.99 (m, 6H), 1.70-1.33, (m, 58H), 0.97-0.83 (m, 32H), 0.53-0.41 (m, 25H), 0.24 (m, 8H). ^{13}C-NMR (100 MHz, $CDCl_3$) δ/ppm: 192.68, 167.72, 160.05, 151.53, 150.98, 150.69, 148.44, 145.76, 142.84, 142.48, 137.56, 132.20, 130.78, 130.52, 130.12, 124.11, 122.69, 120.80, 119.17, 118.98, 116.10, 105.37, 101.74, 100.78, 90.12, 68.82, 40.12, 32.07, 31.97, 31.87, 31.80, 31.77, 31.68, 31.39, 31.24, 30.96, 30.01, 29.63, 29.51, 28.76, 27.87, 27.64,

27.32, 25.06, 22.94, 22.87, 22.80, 22.19, 14.42, 14.38, 14.30, 14.28, 13.67, 12.53. MP: >300°C. MALDI-TOF MS (m/z): calculated for $C_{141}H_{188}N_6O_6S_8Zn$: 2367.15; found: (M+) 2367.14. FT-IR (ATR) υ/cm^{-1}: 2951, 2923, 2856, 2331, 2173, 1702, 1567, 1504, 1456, 1392, 1324, 1234, 1205, 1130, 1095, 997, 923, 879, 827,792, 765, 721

Synthesis of SA8

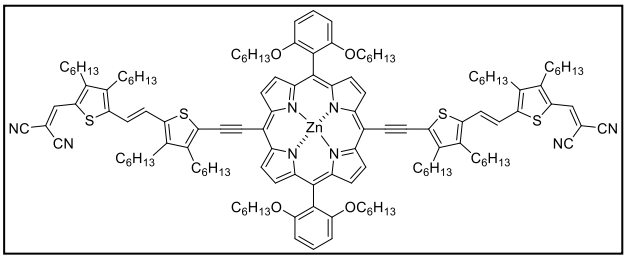

Using the general procedure to Knoevenaguel previously described, **A4** (0.05 mmol,110 mg) in 2 mL of $CHCl_3$ were allowed to react with malonitrile (0.15 mmol, 9.9 mg). **SA7** was obtained as a green solid (80 mg, 0.03 mmol, 73% yield). ^{1}H-NMR (400 MHz, $CDCl_3$) δ/ppm: 9.60 (d, 4H, *J* = 4.6 Hz), 8.87 (d, 4H, *J* = 4.6 Hz), 7.80 (s, 2H), 7.72 (t, 2H, *J* = 8.40), 7.42 (d, 2H, *J* =15.52), 7.15 (d, 2H, *J* =15.52) 7.02 (d, 4H, *J* = 8.53 Hz), 3.87 (t, 8H, *J* = 6.28 Hz), 3.13 (t, 3H), 2.82-2.71 (m, 9H), 2.05-1.98 (m, 6H), 1.68-1.26 (m, 68H), 0.96-0.86 (m, 32H), 0.53-0.41 (m, 22H), 0.24 (m, 8H). ^{13}C-NMR (100 MHz, $CDCl_3$) δ/ppm: 159.89, 155.97, 151.38, 150.61, 149.38, 148.39, 147.27, 144.22, 141.57, 136.86, 132.13, 130.34, 130.01, 128.28, 125.63, 120.77, 120.58, 118.03, 116.10, 115.68, 114.27, 105.22, 102.19, 100.45, 89.82, 73.09, 68.66, 31.89, 31.66, 31.61, 31.55, 31.04, 30.80, 29.49, 29.377, 28.61, 24.90, 22.76, 22.60, 22.02, 14.19, 14.12, 14.08, 13.40. MP: >300°C. MALDI-TOF MS (m/z): calculated for $C_{136}H_{176}N_8O_4S_4Zn$: 2177.20; found: (M+) 2177.19. FT-IR (ATR) υ/cm^{-1}: 2951, 2923, 2856, 2217, 2167, 1589, 1556, 1506, 1456, 1340, 1288, 1247, 1207, 1093, 998, 927, 827, 792, 721, 711.

Synthesis of A5

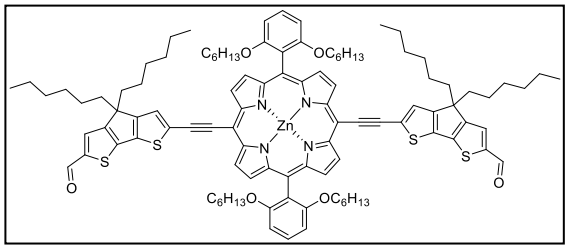

Using the general procedure to Sonogashira coupling previously described, with a modification in **C2** eq, P2S (0.30 mmol, 293 mg), **C3** (2 eq, 0.6 mmol, 330 mg) in 13 mL of Et_3N in 69 mL of THF. **A5** was obtained as a green solid (0.13 mmol, 227 mg, 44%). ^{1}H-NMR (400 MHz, $CDCl_3$) δ/ppm: 9.85 (s, 2H), 9.61 (d, 4H, *J* = 4.5 Hz), 8.89 (d, 4H, *J* = 4.5 Hz), 7.72 (t, 2H, *J* = 8.6), 7.64 (s, 2H), 7.55 (s, 2H), 7.02 (d, 4H, *J* = 8.34 Hz), 3.88 (t, 8H, *J* = 6.28 Hz), 2.0 (t, 6H, *J* = 8.24 Hz), 1.49 (m, 9H), 1.23 (m, 25H), 1.09 (m, 6H), 0.99 (m, 6H), 0.87-0.84 (m, 14H), 0.55 (m, 15H), 0.42 (m, 6H), 0.30-0.26 (m, 9H).^{13}C-NMR (100 MHz, $CDCl_3$) δ/ppm: 182.64, 162.11, 159.86, 159.05, 151.31, 150.70, 147.30, 143.81, 136.90, 132.25, 130.38, 130.05, 129.91, 128.69, 125.83, 120.48, 116.12, 105.20, 100.10, 99.81, 90.09, 68.61, 54.32, 53.44, 37.85, 31.64, 30.81, 29.69, 28.60, 24.91, 24.67, 22.66, 22.05, 14.06, 13.53. MALDI-TOF MS (m/z): calculated for $C_{104}H_{124}N_4O_6S_4Zn$: 1716.77; found: (M+) 1709.5. FT-IR (ATR) υ/cm^{-1}: 3725, 3620, 2950, 2927, 2856, 2370, 2354, 2171,

1656, 1618, 1585, 1498, 1454, 1419, 1394, 1336, 1322, 1305, 1278, 1245, 1224, 1203, 1128, 1097, 1062, 997, 929, 836, 792, 769, 711.

Synthesis of SA9

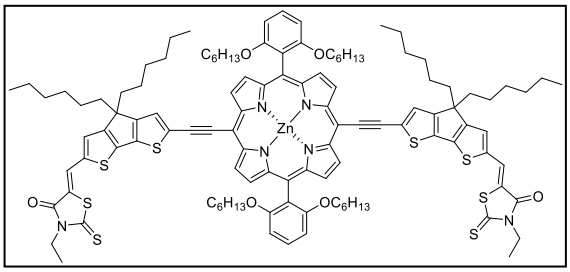

Using the general procedure previously described, **A5** (0.04 mmol, 80 mg) in 4 mL of $CHCl_3$, 3-ethylrhodanine (0.46 mmol, 74 mg)**. SA9** was obtained as a green solid (41 mg, 0.02 mmol, 45% yield). ^{1}H-NMR (400 MHz, $CDCl_3$) δ/ppm: 9.59 (d, 4H, *J* = 4.5 Hz), 8.89 (d, 4H, *J* = 4.5 Hz), 7.73 (t, 2H, *J* = 8.4), 7.61 (s, 2H), 7.55 (s, 2H), 7.41 (s, 2H), 7.03 (d, 4H, *J* = 8.4 Hz), 3.88 (t, 8H, *J* = 6.28 Hz), 2.01 (m, 8H), 1.45 (m, 4H), 1.23 (m, 27H), 1.07-0.84 (m, 21H), 0.85(m, 14H), 0.57 (m, 14H), 0.56 (m, 18H), 0.42 (m, 6H), 0.31 (m, 9H).^{13}C-NMR (100 MHz, $CDCl_3$) δ/ppm: 200.90, 191.52, 173.69, 167.04, 161.02, 160.49, 159.85, 151.28, 150.64, 146.15, 139.02, 137.26, 132.20, 130.33, 130.03, 128.82, 128.57, 128.32, 128.15, 127.85, 126.41, 125.74, 120.57, 117.64, 116.12, 105.21, 100.55, 99.85, 90.49, 68.59, 54.39, 39.89, 39.74, 37.94, 35.40, 31.64, 30.82, 29.68, 28.59, 24.89, 24.62, 22.66, 22.08, 14.07, 13.56, 12.16, 12.02. MP: >300°C. MALDI-TOF MS (m/z): calculated for $C_{114}H_{134}N_6O_6S_6Zn$: 2002.74; found: (M+) 2002.73. FT-IR (ATR) u/cm^{-1}: 2952, 2927, 2854, 2323, 2169, 1729, 1697, 1573, 1504, 1486, 1454, 1415, 1375, 1346, 1321, 1278, 1238, 1126, 1101, 997, 883, 791, 765, 721, 709.

Synthesis of SA10

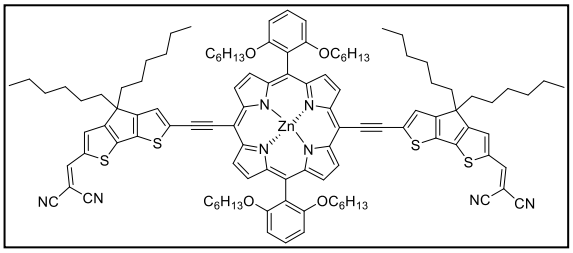

Using the general Knoevenaguel procedure previously described, **A5** (0.04 mmol, 80 mg) in 2 mL of $CHCl_3$ were allowed to react with malonitrile (0.13 mmol, 9.2 mg). **SA10** was obtained as a green solid (49 mg, 0.02 mmol, 59% yield). ^{1}H-NMR (400 MHz, $CDCl_3$) δ/ppm: 9.60 (d, 4H, *J* = 4.1 Hz), 8.87 (d, 4H, *J* = 4.1 Hz), 7.80 (s, 2H), 7.72 (t, 2H, *J* = 7.6), 7.42 (s, 2H), 7.16 (s, 2H), 7.02 (d, 4H, *J* = 8.25 Hz), 3.88 (m, 8H), 3.13 (m, 3H), 2.81-2.71 (m, 9H), 1.98 (m, 4H), 1.48-1.36 (m, 32H), 0.98-0.86 (m, 24H), 0.52-0.40 (m, 14H), 0.25 (m, 9H).^{13}C-NMR (100 MHz, $CDCl_3$) δ/ppm: 165.45, 159.86, 155.96, 151.36, 150.59, 149.37, 148.40, 141.56, 134.14, 133.70, 132.11, 131.02, 130.27, 130.00, 129.74, 128.26, 105.18, 68.63, 63.03, 32.20, 31.95, 31.87, 31.65, 31.59, 31.02, 30.78, 29.81, 29.72, 29.49, 29.36, 28.58, 24.89, 22.75, 22.72, 22.64, 22.59, 22.01, 14.15, 14.12, 14.08, 13.40. MP: >300°C. MALDI-TOF MS (m/z): calculated for $C_{110}H_{124}N_8O_4S_4Zn$: 1812.79; found: (M+)1812.80. FT-IR (ATR) u/cm^{-1}: 2956, 2919, 2850, 2356, 2316, 2217, 2165, 1577, 1562, 1486, 1454, 1405, 1317, 1274, 1247, 1197, 1130, 1090, 1062, 997, 927, 794, 769, 721, 709.

1.12.6 Experimental details in the synthesis of SA11 and SA12

Synthesis of 5-hexylthiophene-2-carbaldehyde

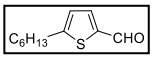

Following the Vilsmeier formilation procedure DMF (21.4 mmol, 1.6 mL) was added to a solution of 2-hexylthiophene (11.9 mmol, 2.00 g) in 35 mL of 1,2-DCE (3 mL/mmol), previously dried with anhydrous magnesium sulfate ($MgSO_4$). Then $POCl_3$, (19.0 mmol, 1.75 mL) was added dropwise. The crude was purified by chromatography column (silica gel, hexane:$CHCl_3$, 7:3). The final product was yellow oil (11.1 mmol, 2.2 g, 94% yield). ^{1}H-NMR (400 MHz, $CDCl_3$) δ/ppm: 9.81 (s, 1H), 7.61 (d, 1H, *J* = 3.73 Hz), 6.9 (d, 1H, *J* = 3.73 Hz), 2.87 (t, 2H, *J* = 7.72 Hz), 1.74-1.67 (m, 2H), 1.43-1.25 (m, 6H), 0.89 (t, 3H, *J* = 6.5 Hz). FT-IR (ATR) υ/cm^{-1}: 2930, 2850, 1670, 1460, 1220, 1040, 806, 760, 725, 671, 648.

Synthesis of 2,2'-((5-hexylthiophen-2-yl)methylene)bis(1H-pyrrole)

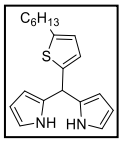

At room temperature under argon atmosphere, 0.08 mL of TFA (7.71 µL/mmol) was added to a solution of 5-hexylthiophene-2-carbaldehyde (2.00 g, 10.2 mmol, 1 eq) in 4.17 mL of pyrrol (60 mmol, 5.9 eq, with previously filtered with neutral aluminum oxide). The solution was stirred at room temperature for 30 min before quenching with trimethylamine (1 mL). The organic phase was extracted with chloroform ($CHCl_3$, 3x50mL). The resultant organic phase was dried with anhydrous magnesium sulfate ($MgSO_4$) and filtered. The solvent was removed under reduced pressure. The crude was purified by chromatography column (silica gel, hexane:$CHCl_3$, 1:1). The final product was a light brown oil (7.88 mmol, 2.46 g, 77.5% yield). ^{1}H-NMR (400 MHz, $CDCl_3$) δ/ppm: 7.93 (s, 2H), 6.7 (d, 4H, *J* = 2.62 Hz), 6.21-6.20 (m, 2H), 6.09 (s, 2H), 5.66 (s, 1H), 2.79 (t, 2H, *J* = 7.6 Hz), 1.73-1.65 (m, 2H), 1.43-1.35 (m, 6H), 0.95 (t, 3H, *J* = 6.5 Hz). FT-IR (ATR) υ/cm^{-1}: 3390, 2920, 2850, 1690, 1560, 1460, 1430, 1250, 1110, 1090, 1030, 968, 883, 760, 714.

Synthesis of 5,15-bis(5-hexylthiopen-2-yl)-10,20-bis((trimethylsilyl)ethynyl) porphyrin

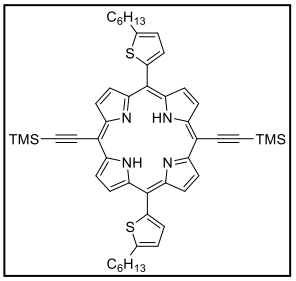

In completely anaerobic conditions, a solution of 2,2'-((5-hexylthiophen-2-yl)methylene)bis(1H-pyrrole) (2.00 g, 6.6 mmol, 2 eq) in 660 mL of $CHCl_3$, (100 mL/mmol) was added in a 1 L flask. It was added to the solution 3-(trimethylsilyl)-2-propynal (0.98 mL, 6.62 mmol, 2 eq) and boron trifluoride diethyl etherate ($BF_3OC_4H_{10}$, 3.3 mM, 0.27 mL, 2.18 mmol), The solution was stirred at room temperature for 45 min before adding DDQ (1.13 g, 4.96 mmol, 1.5 eq). The solution was stirred at room temperature for 1 hour before quenching with 1.3 mL of Et_3N (0.4 mL/mmol). After 30 min the solvent was removed under reduced pressure. The crude was purified by chromatography column (silica gel, hexane:$CHCl_3$:toluene, 7:2.8:0.2). The final product was a green-purple solid (0.23 mmol, 200 mg, 7.3% yield). ^{1}H-NMR (400 MHz, $CDCl_3$) δ/ppm: 9.6 (d, 4H, *J* = 4.6 Hz), 9.11 (d, 4H, *J* = 4.6 Hz), 7.69 (d, 2H, *J* = 3.2 Hz), 7.19 (d, 2H, *J* = 3.2 Hz), 3.14

(t, 4H, *J* = 7.54 Hz), 2.01-1.93 (m, 4H), 1.6-1.58 (m, 6H), 1.48-1.46 (m, 8H), 1.00 (t, 4H, *J* = 6.9 Hz), 0.62 (s, 18H), -2.13 (m, 2H). MALDI-TOF MS (m/z): calculated for $C_{50}H_{58}N_4S_2Si_2$: 834.36; found: 835.60 (M+). FT-IR (ATR) u/cm^{-1}: 3310, 2950, 2920, 2850, 2140, 1550, 1470, 1370, 1340, 1250, 1140, 1060, 984, 949, 837, 795, 756, 698, 617.

Synthesis of P3

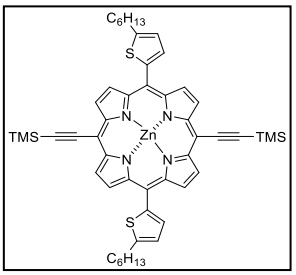

A solution of 5,15-bis(5-hexylthiopen-2-yl)-10,20-bis((trimethylsilyl)ethynyl) porphyrin (1 eq, 0.18 mmol, 150 mg) in 15 mL of $CHCl_3$ (85 mL/mmol), and 0.5 mL of MeOH (2.5 mL/mmol) was added to a 25 mL flask. It was added to the solution, zinc acetate ($Zn(OAc)_2$, 165 mg, 0.9 mmol, 5 eq). The solution was stirred at room temperature for 4 hours. The organic phase was extracted with $CHCl_3$ (3 x 25mL). The resultant organic phase was dried with anhydrous $MgSO_4$ and filtered. The solvent was removed under reduced pressure. The crude was purified by chromatography column (silica gel, hexane:$CHCl_3$, 1:1). The final product was a green-purple solid (0.17 mmol, 160 mg, 99.1 % yield). ^{1}H-NMR (400 MHz, $CDCl_3$) δ/ppm: 9.6 (d, 4H, *J* = 4.6 Hz), 9.18 (d, 4H, *J* = 4.6 Hz), 7.69 (d, 2H, *J* = 3.2 Hz), 7.19 (d, 2H, *J* = 3.2 Hz), 3.14 (t, 4H, *J* = 7.54 Hz), 2.01-1.93 (m, 4H), 1.64-1.60 (m, 6H), 1.48-1.47 (m, 8H), 1.00 (t, 4H, *J* = 6.9 Hz), 0.62 (s, 18H). MALDI-TOF MS (m/z): calculated for $C_{50}H_{56}N_4S_2Si_2Zn$: 896.28; found: 898.63 (M+). FT-IR (ATR) u/cm^{-1}: 2920, 2850, 2140, 1490, 1460, 1340, 1300, 1250, 1210, 1160, 1060, 1000, 972, 837, 791, 756, 710, 621.

Synthesis of P3S

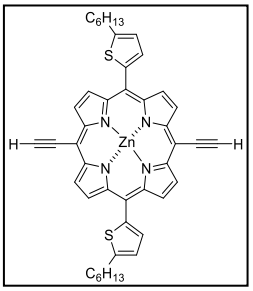

At room temperature under argon atmosphere, a solution of **P3** (150 mg, 0.16 mmol, 1 eq) in 35 mL of chloroform ($CHCl_3$, 220 mL/mmol), was added to a 100 mL flask. It was added to the solution TBAF (1M in THF, 0.4 mL, 0.4 mmol, 2.42 eq). The solution was stirred at room temperature for 3 hours, after that $CaCl_2$ (222 mg, 2 mmol, 12 eq) was added. After 30 min the organic phase was extracted with $CHCl_3$, (3 x 50mL). The resultant organic phase was dried with anhydrous $MgSO_4$ and filtered. The solvent was removed under reduced pressure. The final product was a blue-green solid, and it was used directly in the next synthetic step.

Synthesis of A6

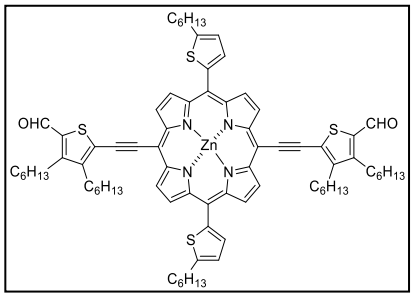

Using the general procedure for Sonogashira condensation previously described, to a solution of **P3S** (200 mg, 0.27 mmol), **C1** (337 mg, 0.8 mmol), 40 mL of THF and 7.5 mL of Et_3N, was added to a mixture of $Pd_2(dba)_3$ (152 mg, 0.16 mmol) and $AsPh_3$, (340 mg, 1.1 mmol). The crude was purified by chromatography column (silica gel, hexane:$CHCl_3$, 2:3) and recrystallized with CH_2Cl_2:MeOH. The final product was a turquoise solid (0.16 mmol, 218 mg, 60 % yield). ^{1}H-NMR (400 MHz, $CDCl_3$) δ/ppm: 9.56 (s, 2H), 9.07 (d, 4H, *J* = 4.6 Hz), 8.91 (d, 4H, *J* = 4.6 Hz), 7.76 (d, 2H, *J* = 3.2 Hz), 7.28 (d, 2H, *J* = 3.2 Hz), 3.23 (t, 4H, *J* = 7.6 Hz), 2.47 (s, 2H), 2.30 (s, 2H), 2.10-2.03 (m, 4H), 1.74-1.66 (m, 4H), 1.6-1.52 (m, 20H), 1.38-1.33 (m, 12H), 1.30-1.26 (m, 8H), 1.07-1.03 (t, 4H, *J* = 6.9 Hz), 0.92-0.87 (m, 18H). MALDI-TOF MS (m/z): calculated for $C_{78}H_{92}N_4O_2S_4Zn$: 1308.54; found: 1311.02 (M+). FT-IR (ATR) u/cm^{-1}: 2920, 2850, 2180, 1650, 1610, 1490, 1450, 1410, 1290, 1210, 976, 791, 733, 710, 667.

Synthesis of SA11

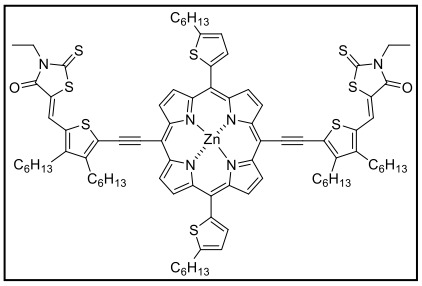

Using the general procedure for Knoevenaguel reaction with 3-ethylrhodanine with a modification of temperature and times of the reaction, 3-ethylrhodanine (36 mg, 228 µmol, 3 eq) and 4 drops of piperidine were added to a solution of **A6** (100 mg, 0.07 mmol) in 10 mL of $CHCl_3$.The solution was stirred at room temperature for 2 nights. The final product was a green-red solid (0.06mmol, 115mg, 95.5 % yield). ^{1}H-NMR (400 MHz, $CDCl_3$) δ/ppm: 9.09 (d, 4H, *J* = 3.9 Hz), 8.95 (d, 4H, *J* = 3.9 Hz), 7.83 (d, 2H, *J* = 1.9 Hz), 7.33 (d, 2H, *J* = 1.9 Hz), 6.64 (s, 2H), 3.73 (d, 4H, *J* = 5.8 Hz), 3.28 (t, 4H, *J* = 7.6 Hz), 2.3 (s, 2H), 2.12 (t, 4H, *J* = 7.28 Hz), 1.95 (s, 2H), 1.75 (s, 6H), 1.58 (s, 16H), 1.45 (s, 12H), 1.23-1.19 (m, 16H), 1.10 (d, 14H, *J* = 3.95 Hz), 0.97 (s, 4H), 0.85 (t, 4H, *J* = 6.9 Hz. ^{13}C-NMR (100 MHz, $CDCl_3$) δ/ppm: 192.00, 167.12, 151.68, 151.18, 149.32, 148.50, 147.50, 140.06, 134.01, 133.24, 133.03, 130.58, 126.94, 123.79, 122.77, 119.73, 116.27, 104.54, 101.75, 90.42, 39.86, 32.46, 32.18, 31.86, 31.73, 31.12, 30.95, 30.30, 29.73, 29.60, 29.04, 27.69, 23.24, 23.17, 22.92, 14.63, 14.57, 12.61. MP: >300°C. MALDI-TOF MS (m/z): calculated for $C_{88}H_{102}N_6O_2S_8Zn$: 1594.51; found: 1597.27 (M+). FT-IR (ATR) u/cm^{-1}: 3670, 3470, 2920, 2850, 2160, 1680, 1560, 1500, 1400, 1320, 1230, 1130, 1010, 877, 785, 729.

Synthesis of A7

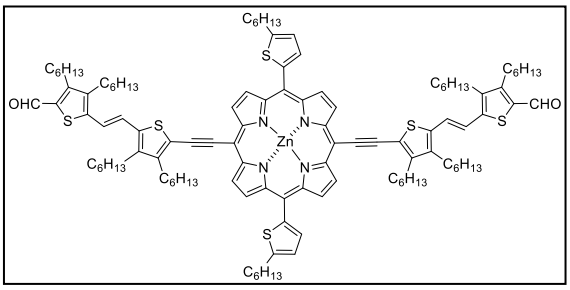

Using the general procedure for Sonogashira condensation previously described, to a solution of **P3** (125 mg, 0.17 mmol), **C2** (300 mg, 0.5 mmol), 40 mL of THF (230 mL/mmol) and 7.5 mL of Et_3N (45 mL/mmol), was added to a mixture of $Pd_2(dba)_3$ (92 mg, 0.1 mmol) and $AsPh_3$, (205 mg, 0.7 mmol). The crude was purified by chromatography column (silica gel, hexane:$CHCl_3$, 2:3) and recrystallized with CH_2Cl_2:MeOH. The final product was a turquoise solid (0.10 mmol, 374 mg, 60 % yield). ^{1}H-NMR (400 MHz, $CDCl_3$) δ/ppm: 9.59 (s, 2H), 9.29 (d, 4H, *J* = 3.9 Hz), 9.12 (d, 4H, *J* = 3.9 Hz), 7.75 (s, 2H), 7.25 (s, 2H), 7.05 (d, 2H, *J* = 16 Hz), 6.76 (d, 2H, *J* = 16 Hz), 3.21 (t, 3H, *J* = 7.14 Hz), 2.73 (s, 3H), 2.57 (d, 6H, *J* = 21.8 Hz), 2.40 (s, 3H), 2.04 (t, 3H, *J* = 6.9 Hz), 1.77 (s, 2H), 1.65-1.63 (m, 6H), 1.5-1.26 (m, 68H), 1.05-0.99 (m, 16H), 0.94-0.89 (m, 20H). MALDI-TOF MS (m/z): calculated for $C_{114}H_{148}N_4O_2S_6Zn$: 1860.92; found: 1865.29 (M+). FT-IR (ATR) υ/cm^{-1}: 2920, 2850, 2170, 1650, 1590, 1490, 1460, 1400, 1290, 1250, 1210, 972, 930, 791, 710, 663.

Synthesis of SA12

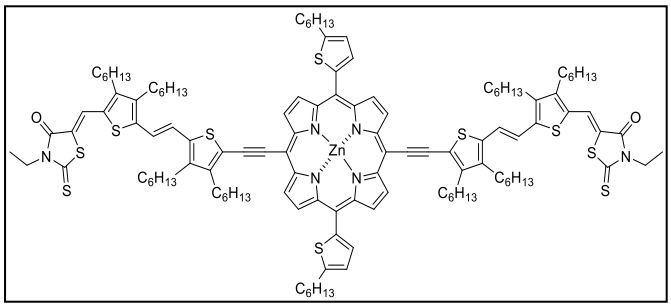

Using the general procedure for Knoevenaguel reaction with 3-ethylrhodanine with a modification of temperature of the reaction, 3-ethylrhodanine (43 mg, 0.26 mmol) and 4 drops of piperidine, were added to a solution of **A7** (50 mg, 0.26 mmol) in 10 mL of chloroform ($CHCl_3$, 370 mL/mmol). The solution was stirred at room temperature for 6 hours. Then the product was purified, as the general Knoevenagel with 3-ethylrhodanine procedure. The final product was a green-red solid (0.08 mmol, 20 mg, 34 % yield). ^{1}H-NMR (400 MHz, $CDCl_3$) δ/ppm: 9.58 (d, 4H, *J* = 4.6 Hz), 9.11 (d, 4H, *J* = 4.6 Hz), 7.79 (s, 2H), 7.72 (d, 2H, *J* = 3.2 Hz), 7.29 (d, 4H, *J* = 16 Hz), 7.15 (d, 2H, *J* = 16 Hz), 4.2-4.14 (m, 4H), 3.2-3.15 (m, 9H), 2.84 (d, 3H, *J* = 7.3 Hz), 2.67 (t, 6H, *J* = 6.9 Hz), 2.06-1.98 (m, 9H), 1.56-1.42 (m, 58H), 1.4-1.37 (m, 12H), 1.26 (t, 9H, *J* = 7.16 Hz), 1.04-0.96 (m, 18H), 0.95-0.89 (m, 12H). ^{13}C-NMR (100 MHz, THF-d8) δ/ppm: 193.49, 168.14, 153.22, 152.27, 151.43, 149.83, 149.76, 146.08, 143.89, 143.78, 142.19, 139.41, 134.76, 133.78, 132.16, 131.58, 124.87, 123.89, 123.44, 121.06, 120.41, 116.59, 103.27, 103.11, 92.20, 33.66, 33.50, 33.31, 33.21, 33.17, 33.11, 32.98, 32.73, 31.73, 31.39, 30.87, 30.80, 30.75, 30.58, 26.42, 26.29, 26.22, 26.09, 26.02, 25.99, 25.89, 25.80, 25.69, 25.60, 25.49, 25.38, 24.33, 24.21, 24.11, 15.22, 15.20, 15.16, 15.14, 15.04, 13.01. MP: >300°C. MALDI-TOF MS (m/z): calculated for

$C_{124}H_{158}N_6O_2S_{10}Zn$: 2146.89; found: 2148.16 (M+). FT-IR (ATR) υ/cm^{-1}: 2930, 2860, 1700, 1570, 1490, 1460, 1400, 1320, 1240, 1190, 1140, 1070, 957, 850, 789, 708.

1.13 References

[1] Brabec, C.; Dyakonov, V.; Scherf U. *Organic Photovoltaics: Materials, Device Physics, and Manufacturing Technologies*, 2nd. Ed.; Wiley-VCH: Weinheim, 2014.

[2] Somani, P. R.; Umeno, M. *New Concepts in Solar Cells*; Wiley-VCH: Weinheim, 2009.

[3] Mishra A.; Baüerle, P. *Angew. Chem. Int. Ed.* **2012**, *51*, 2020.

[4] Galagan, Y.; Andriessen, R. Organic Photovoltaics: Technologies and Manufacturing, Third Generation Photovoltaics, Dr. Vasilis Fthenakis (Ed.) [Online]. ISBN: 978-953-51-0304-2, DOI: 10.5772/25901. Published online: March 16, 2012. http://www.intechopen.com/books/third-generation-photovoltaics/organic-photovoltaics-technologies-and-manufacturing (accessed Jul 5, 2015).

[5] Kallmann, H.; Pope, M. *J. Chem. Phys*. **1959**, *30*, 585.

[6] Lin, Y.; Li, Y.; Zhan, X. *Chem. Soc. Rev*. **2012**, *41*, 4245.

[7] Shaheen, S. E.; Radspinner, R.; Peyghambarian, N.; Jabbour, G. E. *Appl. Phys. Lett*. **2001**, *79*, 2996.

[8] Gustafsson, G.; Cao, Y.; Treacy, G. M.; Klavetter, F.; Colaneri, N.; Heeger, A. *J. Nature.* **1992**, *357*, 477.

[9] Sun, Y.; Welch, G. C.; Leong, W. L.; Takacs, C. J.; Bazan,G.; Heeger, A.J. *Nature Materials* ***2012****, 11,* 44.

[10] Heeger, A. J. *Adv. Mater*. **2014**, *26*, 10.

[11] Walker, B.; Kim, C.; Nguyen T. Q. *Chem. Mater*. **2011**, *23*, 470.

[12] [a] Choi, J. H.; Son, K.-I.; Kim, T.; Kim, K.; Ohkubo, K.; Fukuzumi, S. *J. Mater. Chem.* **2010**, *20*, 475.[b] Zhang, Y.; Yip, H.-L.; Acton, O.; Hau, S. K.; Huan, F. *Jen, Chem. Mater*. **2009**, *21*, 2598.

[13] [a] Walker, B.; Tamayo, A. B.; X.-D. Dang; Zalar, P.; J. H. Seo; Garcia, A.; Tantiwiwat, M.; Nguyen, T.-Q. *Adv. Funct. Mater*. **2009**, *19*, 3063. [b] Lee, O. P.; Yiu, A. T.; Beaujuge, P. M.; C. H. Woo; Holcombe, T. W.; Millstone, J. E.; Douglas, J. D.; Chen, M. S.; Fréchet, J. M. J. *Adv. Mater.* **2011**, *23*, 5359. [c] Loser, S.; Bruns, C. J.; Miyauchi, H.; Ortiz, R. O. P.; Facchetti, A.; Stupp, S. I.; Marks, T. J. *J. Am. Chem. Soc.* **2011**, *133,* 8142. [d] Mei, J. G.; Graham, K. R.; Stalder, R.; Reynolds, J. R.. *Org. Lett.* **2010**, *12*, 660. [e] Graham, K. R.; Mei, J.; Stalder, R.; Shim, J. W.; Cheun, H.; Steffy, F.; So, F.; Kippelen, B.; Reynolds, J. R. *ACS Appl. Mater. Interfaces*. **2011**, *3*, 1210.

[14] [a] Sonar, P.; Fong Lim, J. P.; Chan, K. L. *Energy Environ. Sci.* **2011**, *4*, 1558. [b] Anthony, J. E. *Chem. Mater.* **2011**, *23*, 583.

[15] [a] Karsten, B. P.; Bijleveld, J. C.; Janssen, R. A. J. *Macromol. Rapid Commun.* **2010**, *31*, 1554. [b] Sonar, P.; Ng, G.-M.; Lin, T. T.; Dodabalapur, A.; Chen, Z.-K.. *J. Mater. Chem.* **2010**, *20*, 3626.

[16] [a] Shu, Y.; Lim, Y.-F.; Li, Z.; Purushothaman, B.; Hallani, R.; Kim, J. E.; Parkin, S. R.; Malliaras, G. G.; Anthony, J. E. *Chem. Sci.* **2011**, *2*, 363. [b] Brunetti, F. G.; Gong, X.; Tong, M.; Heeger, A. J.; Wudl, F. *Angew. Chem.* **2010**, *122*, 542; *Angew. Chem. Int. Ed.* **2010**, *49*, 532.

[17] [a] Kim, I.; Haverinen, H. M.; Wang, Z.; Madakuni, S.; Li, J.; Jabbour, G. E. *Appl. Phys. Lett.* **2009**, *95*, 023305. [b] Sharma, G. D.; Suresh, P.; Mikroyannidis, J. A.; Stylianakis, M. M. *J. Mater. Chem.* **2010**, *20*, 561. [c] Mikroyannidis, J. A.; Suresh, P.; Sharma, G. D. *Synth. Met.* **2010**, *160*, 932.

[18] [a] Zhan, X.; Facchetti, A.; Barlow, S.; Marks, T. J.; Ratner, M. A.; Wasielewski, M. R.; Marder, S. R.. *Adv. Mater.* **2011**, *23*, 268. [b] Würthner, F. *Chem. Commun.* **2004**, 1564. [c] Würthner, F.; Stolte, M. *Chem. Commun.* **2011**, *47*, 5109. [d] Bhosale, S. V.; Jani, C. H.; Langford; S. J. *Chem. Soc. Rev.* **2008**, *37*, 331.

[19] [a] Shin, R. Y. C.; Kietzke, T.; Sudhakar, S.; Dodabalapur, A.; Chen, Z.-K.; Sellinger, A. *Chem. Mater.* **2007**, *19*, 1892. [b] Shin, R. Y. C.; Sonar, P.; Siew, P. S.; Chen, Z.-K.; Sellinger, A. *J. Org. Chem.* **2009**, *74*, 3293. [c] Kietzke, T.; Shin, R. Y. C.; Egbe, D. A. M.; Chen, Z.-K.; Sellinger, A. *Macromolecules*. **2007**, *40*, 4424. [d] Woo, C. H.; Holcombe, T. W.; Unruh, D. A.; Sellinger, A.; Fréchet, J. M. J. *Chem. Mater.* **2010**, *22*, 1673. [e] Schubert, M.; Yin, C. H.; Castellani, M.; Bange, S.; Tam, T. L.; Sellinger, A.; Horhold, H. H.; Kietzke, T.; Neher, D. *J. Chem. Phys.* **2009**, *130*, 094703.[f] Ooi, Z. E.; Tam, T. L.; Shin, R. Y. C.; Chen, Z. K.; Kietzke, T.; Sellinger, A.; Baumgarten, M.; Mullen, K.; de Mello, J. C. *J. Mater. Chem.* **2008**, *18*, 4619.

[20] Sullivan, P.; Duraud, A.; Hancox, I.; Beaumont, N.; Mirri, G.; Tucker, J. H. R.; Hatton, R. A.; Shipman, M.; Jones, T. S. *Adv. Energy Mater.* **2011**, *1*, 352.

[21] Li, Z.; Lim, Y.-F.; Kim, J. B.; Parkin, S. R.; Loo, Y.-L.; Malliaras, G. G.; J. E. Anthony. *Chem. Commun.* **2011**, *47*, 7617.

[22] [a] Barbarella, G.; Pudova, O.; Arbizzani, C.; Mastragostino, M.; Bongini, A. *J. Org. Chem.* **1998**, *63*, 1742. [b] Barbarella, G.; Favaretto, L.; Sotgiu, G.; Zambianchi, M.; Antolini, L.; Pudova, O.; Bongini, A. *J. Org. Chem.* **1998**, *63*, 5497. [c] Ridolfi, G.; Fattori, V.; Favaretto, L.; Barbarella, G. *Appl. Phys. Lett.* **2004**, *84*, 1901. [d] Camaioni, N.; Ridolfi, G.; Fattori, V.; Favaretto, L.; Barbarella, G. *J. Mater. Chem.* **2005**, *15*, 2220. [e] Barbarella, G.; Favaretto, L.; Zanelli, A.; Gigli, G.; Mazzeo, M.; Anni, M.; Bongini, A. *Adv. Funct. Mater*. **2005**, *15*, 664.

[23] Camaioni, N.; Ridolfi, G.; Fattori, V.; Favaretto, L.; Barbarella, G. *Appl. Phys. Lett.* **2004**, *84*, 1901.

[24] Schwenn, P. E.; Gui, K.; Nardes, A. M.; Krueger, K. B.; Lee, K. H.; Mutkins, K.; Rubinstein-Dunlop, H.; Shaw, P. E.; Kopidakis, N.; Burn, P. L.; Meredith, P. *Adv. Energy Mater*. **2011**, *1*, 73.

[25] Uhrich, C.; Schueppel, R.; Petrich, A.; Pfeiffer, M.; Leo, K.; Brier, E.; Kilickiran, P.; Bauerle, P. *Adv. Funct. Mater.* **2007**, *17*, 2991.

[26] Zhou, T.; Jia, T.; Kang, B.; Li, F.; Fahlman, M.; Wang, Y. *Adv. Energy Mater.* **2011**, *1*, 431.

[27] Zhou, Y.; Pei, J.; Dong, Q.; Sun, X.; Liu, Y.; Tian, W. *J. Phys. Chem.* **2009**, *113*, 7882.

[28] Scharber, M. C.; Mchlbacher, D.; Koppe, M.; Denk, P.; Waldauf, C.; Heeger, A. J.; Brabec, C. *J. Adv. Mater.* **2006**, *18*, 789.

[29] Kiess, H.; Rehwald, W. *Sol. Energ. Mat. Sol. Cells* **1995**, *38*, 45.

[30] Kan, B.; Li, M.; Zhang, Q.; Liu,F.; Wan, X.; Wang, Y.; Ni, W.; Long, G.; Wang, Y.; Yang, X.; Feng, H.; Cao, Y.; Russell, T. P.; Chen, Y. *J. Am. Chem. Soc.* **2015**, *137*, 3886.

[31] Gao, K.; Li, L.; Lai, T.; Xiao, L.; Huang, Y.; Huang, F.; Peng, J.; Cao, Y.; Liu, F.; Russell, T. P.; Janssen, R. A. J.; Peng, X. *J. Am. Chem. Soc.* **2015**, *137*, 7282.

[32] Sun, Y.; Welch, G.; Leong, W. L.; Takacs, C. J.; Bazan, G. C.; Heeger, A. J. *Nature Materials* **2012**, *11*, 44.

[33] Sun, Q.; Dai, L.; Zhou, X.; Li, L.; Li, Q. *Appl. Phys. Lett.* **2007**, *91*, 253505.

[34] Wong, W.; W. H.; Khoury, T.; Vak, D.; Yan, C.; Jones, D. J.; Crossley, M. J.; Holmes, A. B. *J. Mater. Chem.* **2010**, *20*, 7005.

[35] Khan, S. M.; Sayyad, M. H. *J. Porphyrins Phthalocyanines* **2012**, *16*, 1.

[36] Cho, E. H.; Chae, S. H.; Kim, K.; Lee, S. J.; Joo, J. *Synth. Met.* **2012**, *162*, 813.

[37] Hatano, J.; Obata, N.; Yamaguchi, S.; Yasuda, T.; Matsuo, Y. *J. Mater. Chem.* **2012**, *22*, 19258.

[38] Luechai, A.; Gasiorowski, J.; Petsom, A.; Neugebauer, H.; Sariciftci, N. S.; Thamyongkit, P. *J. Mater. Chem.* **2012**, *22*, 23030.

[39] Huang, Y.; Li , L.; Peng, X.; Peng, J.; Cao, Y. *J. Mater. Chem.* **2012**, *22*, 21841.

[40] Li, L.; Huang, Y.; Peng, J.; Cao, Y.; Peng, X. *J. Mater. Chem. A* **2013**, *1*, 2144.

[41] Yamamoto, T.; Hatano, J.; Nakagawa, T.; Yamaguchi, S.; Matsuo, Y.; *Appl. Phys. Lett.* **2013**, *102*, 013305.

[42] Sharma, G.D.; Daphnomili, D. D.; Biswas, S.; Coutsolelos, A. G. *Org. Electron*. **2013**, *14*, 1811.

[43] Kengthanomma, T.; Thamyongkit, P.; Gasiorowski, J.; Ramil, A. M.; Sariciftci, N. S. *J. Mater. Chem. A* **2013**, *1*, 10524.

[44] Li, L.; Huang, y.; Peng, J.; Cao, Y.; Peng, X. *Org. Electron.* **2013**, *14*, 3430.

[45] Matsuo, Y.; Hatano, J.; Nakagawa, T.; *J. Phys. Org. Chem, **2014**, 27*, 87.

[46] Qin, H.; Li, L.; Guo, F.; Su, S.; Peng, J.; Cao, Y.; Peng, X.; *Energy Environ. Sci*. **2014**, *7*, 1397.

[47] Sharma, G. D.; Zervaki, G. E.; Angaridis, P. A.; Kitsopoulos, T. N.; Coutsolelos, A. G. *J. Phys. Chem.C* **2014**, *118*, 5968.

[48] Kumar, C.V.; Cabau, L.; Koukaras, E.N.; Sharma, G.D.; Palomares, E. *Nanoscale* **2015**, *7*, 179.

[49] Kumar, C. V.; Cabau, L.; Koukaras, E. N.; Sharma, A.; Sharma G. D.; Palomares, E. *J. Mater. Chem. A* **2015**, *3*, 16287.

[50] Gao, K.; Li, L.; Lai, T.; Xiao, L.; Huang, Y.; Huang, F.; Peng, J.; Cao, Y.; Liu, F.; Russell, T.; R. A. J.; Janssen, Peng, X. *J. Am. Chem. Soc.*, **2015**, *137*, 7282.

[51] Hoppe, H.; Sariciftci, N. S. *J. Mater. Chem.* **2006**, *16*, 45.

[52] Hoppe, H.; Glatzel, T.; Niggemann, M.; Schwinger, W.; Schaeffler, F.; Hinsch, A.; Lux-Steiner, M. C.; Sariciftici, N. S. *Thin Solid Films* **2006**, *511*, 587.

[53] Cugola, R.; Giovanella, U.; Di Gianvincenzo, P.; Bertini, F.; Catellani, M.; Luzzati, S. *Thin Solid Films* **2006**, *511*, 489.

[54] Ma, W. L.; Yang, C. Y.; Gong, X.; Lee K.; Heeger, A. J. *Adv. Funct. Mater.* **2005**, *15*, 1617.

[55] Peet, J.; Kim, J. Y.; Coates, N. E.; Ma, W. L.; Moses, D.; Heeger, A. J.; Bazan, G. C. *Nat. Mater.* **2007**, *6*, 497.

[56] Zhou, E. J.; Cong, J. Z.; Tajima, K.; Yang, C. H.; Hashimoto, K. *J. Phys. Chem. C* **2012**, *116*, 2608.

[57] Ren, G. Q.; Ahmed E.; Jenekhe, S. A. *Adv. Energy Mater.* **2011**, *1*, 946.

[58] Zhang F. L.; Jespersen, K. G.; Bjorstrom, C.; Svensson, M.; Andersson, M. R.; Sundstrom, V.; Magnusson, K.; Moons, E.; Yartsev, A.; Inganas, O. *Adv. Funct. Mater.* **2006**, *16*, 667.

[59]Alem, S.; Chu, T.Y.; Tse, S.C.; Wakim, S.; Lu, J.P.; Movileanu, R.; Tao, Y.; Belanger, F.; Desilets, D.; Zhang, Beaupre, S.; Leclerc, M.; Rodman, S.; Waller, D.; Gaudiana, R. *Org. Electron.* **2011**, *12*, 1788.

[60] Li, Y. F.; Zou, Y. P. *Adv. Mater.* **2008**, *20*, 2952.

[61] Hoffmann, M.; Wilson, C. J.; Odell, B.; Anderson, *H. L. Angew. Chem. Int. Ed.* **2007**, *46*, 3122.

[62] Milgrom LR. An Introduction to the Chemistry of Porphyrins and Related Compounds, Oxford University Press: Oxford, 1997; pp 249.

[63] Harima, Y.; Furusho, S.; Kunugi, Y.; Yamashita, K. *Chem. Phys. Lett.* **1996**, *258*, 213.

[64] Kroon JM, Veenstra SC, Slooff LH, Verhees WJH, Koetse MM, Sweelssen J, Schoo HFM, Beek WJE, Wienk MM, Janssen RAJ, Yang X, Loos J, Michailetchi VD, Blom PWM, Knol J and Hummelen JC. In *Polymer Based Photovoltaics: Novel Concepts, Materials and State-of-the Art Efficiencies 20th European Photovoltaic Solar Energy Conference and Exhibition*, Barcelona, Spain, 2005.

[65] Hauff EV, Dyakonov V and Parisi J. *Sol. Energy Mater. Sol. Cells* **2005**, *87*, 149.

[66] Kang, S.; Li, Q.; Chapman, B. D.; Pindak, R.; Cross, J. O.; Li, L.; Nakata, M.; Kumar, S. *Chem. Mater.* **2007**, *19*, 5657.

[67] Sun, Y.; Welch, G.; Leong, W. L.; Takacs, C. J.; Bazan, G. C.; Heeger, A. J. *Nature Materials* **2012**, *11*, 44.

[68]Roncali, J. *Acc. Chem. Res*. **2000**, *33*, 147.

[69]Jestin, I.; Frère, P.; Mercier, N.; Levillain, E.; Stievenard, D.; Roncali J. *J. Am. Chem. Soc*. **1998**, *120*, 8150.

[70]Benson, S. W.; Egger, K. W.; Golden, D. M. *J. Am. Chem. Soc*. **1965**, *87*, 468.

[71]Pellejà L., Dominguez R., Aljarilla A., Clifford J. N., de la Cruz P., Langa F., and Palomares E., *ChemElectroChem* **2014**, *1*, 1126.

[72] Joydev, K. L.; Dhanalekshmi, S.; Taniguchi, M.; Ambroise, A.; Lindsey J. S. *Org. Proc. Res. Dev.* **2003**, *7*, 799.

[73] Yu, L.; Muthukumaran, K.; Sazanovich, I.; Kirmaier, C.; Hindin, E.; Diers, J.; Boyle, D.; Bocian, D.; Holten D.; Lindsey J. *Inorg. Chem. Commun.* **2003**, *42*, 6629.

[74] Grozema, F.; Houarner-Rassin, C.; Prins, P.; Siebbeles, L.; Anderson, H. *J. Am. Chem. Soc.* **2007**, *129*, 13370.

[75] Sonogashira, K.; Tohda, Y.; Hagihara, N. *Tetrahedron Lett.* **1975**, *16*, 4467.

[76] Plater, J.; Aiken, S.; Bourhill, G. *Tetrahedron* **2002**, *58*, 2405.

[77] [a] Sonogashira, K. *J. Organomet. Chem.* **2002**, *653*, 46. [b] Ljungdahl, T.; Bennur, T.; Dallas, A.; Emtenäs, H.; Mårtensson, J. **2008**, *27*, 2490.

[78] Knoevenaguel, E. *Ber. Dtsch. Chem. Ges* **1898**, *31*, 2596.

[79] Cardona, C. M.; Li, W.; Kaifer, A. E.; Stockdale D.; Bazan, G. C. *Adv. Mater.* **2011**, *23*, 2367.

[80] [a] Cravino, A. *Appl. Phys. Lett.,* **2007**, *91*, 243502. [b] Dennler, G.; Scharber, M. C.; Brabec, C. J. *Adv. Mater.* **2009**, *21*, 1323. [c] Scharber, M. C.; Mühlbacher, D.; Koppe, M.; Denk, P.; Waldauf, C.; Heeger, A. J.; Brabec, C. J. *Adv. Mater.* **2006**, *18*, 789.

[81] Cravino, A. *Appl. Phys. Lett.,* **2007**, *91*, 243502.

[82] Huang, Y.; Kramer, E. J.; Heeger, A. J.; Bazan, G. C. *Chem. Rev*. **2014**, *114*, 7006.

[83] Guo, X.; Zhang, M.; Tan, J.; Zhang, S.; Huo, L.; Hu, W.; Li, Y.; Hou, J. *Adv. Matter*, **2012**, *24*, 6536.

[84] Sun, Y.; Welch, G.; Leong, W. L.; Takacs, C. J.; Bazan, G. C.; Heeger, A. J. *Nature Materials* **2012**, *11*, 44.

[85] Grozema, F.; Houarner-Rassin, C.; Prins, P.; Siebbeles, L.; Anderson, H. *J. Am. Chem. Soc.* **2007**, *129*, 13370.

[86] Maiti, N.; Lee, J.; Do, Y.; Hack, S. S.; Churchill, D. G. *J. Chem. Crystallogr.* **2005**, *35*, 949.

[87] [a]Joydev, K. L.; Dhanalekshmi, S.; Taniguchi, M.; Ambroise, A.; Lindsey J. S. *Org. Proc. Res. Dev.* **2003**, *7*, 799. [b] Yu, L.; Muthukumaran, K.; Sazanovich, I.; Kirmaier, C.; Hindin, E.; Diers, J.; Boyle, D.; Bocian, D.; Holten D.; Lindsey J. *Inorg. Chem. Commun.* **2003**, *42*, 6629.

[88] Grozema, F.; Houarner-Rassin, C.; Prins, P.; Siebbeles, L.; Anderson, H. *J. Am. Chem. Soc.* **2007**, *129*, 13370.

[89] Gaussian 03, Revision D.02, Frisch, M. J.; Trucks, G. W.; Schlegel, H. B.; Scuseria, G. E.; Robb, M. A.; Cheeseman, J. R.; Montgomery Jr., J. A.; Vreven, T.; Kudin, K. N.; Burant, J. C.; Millam, J. M.; Iyengar, S. S.; Tomasi, J.; Barone, V.; Mennucci, B.; Cossi, M.; Scalmani, G.; Rega, N.; Petersson, G. A.; Nakatsuji, H.; Hada, M.; Ehara, M.; Toyota, K.; Fukuda, R.; Hasegawa, J.; Ishida, M.; Nakajima, T.; Honda, Y.; Kitao, O.; Nakai, H.; Klene, M.; Li, X.; Knox, J. E.; Hratchian, H. P.; Cross, J. B.; Bakken, V.; Adamo, C.; Jaramillo, J.; Gomperts, R.; Stratmann, R. E.; Yazyev, O.; Austin, A. J.; Cammi, R.; Pomelli, C.; Ochterski, J. W.; Ayala, P. Y.; Morokuma, K.; Voth, G. A.; Salvador, P.; Dannenberg, J. J.; Zakrzewski, V. G.; Dapprich, S.; Daniels, A. D.; Strain, M. C.; Farkas, O.; Malick, D. K.; Rabuck, A. D.; Raghavachari, K.; Foresman, J. B.; Ortiz, J. V.; Cui, Q.; Baboul, A. G.; Clifford, S.; Cioslowski, J.; Stefanov, B. B.; Liu, G.; Liashenko, A.; Piskorz, P.; Komaromi, I.; Martin, R. L.; Fox, D. J.; Keith, T.; Al-Laham,

M. A.; Peng, C. Y.; Nanayakkara, A.; Challacombe, M.; Gill, P. M. W.; Johnson, B.; Chen, W.; Wong, M. W.; Gonzalez, C.; Pople, J. A. Gaussian, Inc., Wallingford CT, 2004.

[90] [a]Jestin, I.; Frère, P.; Mercier, N.; Levillain, E.; Stievenard, D.; Roncali J. *J. Am. Chem. Soc*. **1998**, *120*, 8150; [b] Roncali, J. *Acc. Chem*. *Res*. **2000**, *33*, 147.

[91] Joydev, K. L.; Dhanalekshmi, S.; Taniguchi, M.; Ambroise, A.; Lindsey J. S. *Org. Proc. Res. Dev.* **2003**, *7*, 799.

[92] Yu, L.; Muthukumaran, K.; Sazanovich, I.; Kirmaier, C.; Hindin, E.; Diers, J.; Boyle, D.; Bocian, D.; Holten D.; Lindsey J. *Inorg. Chem. Commun.* **2003**, *42*, 6629.

CHAPTER 2

Porphyrins for dye-sensitized solar cells (DSSCs)

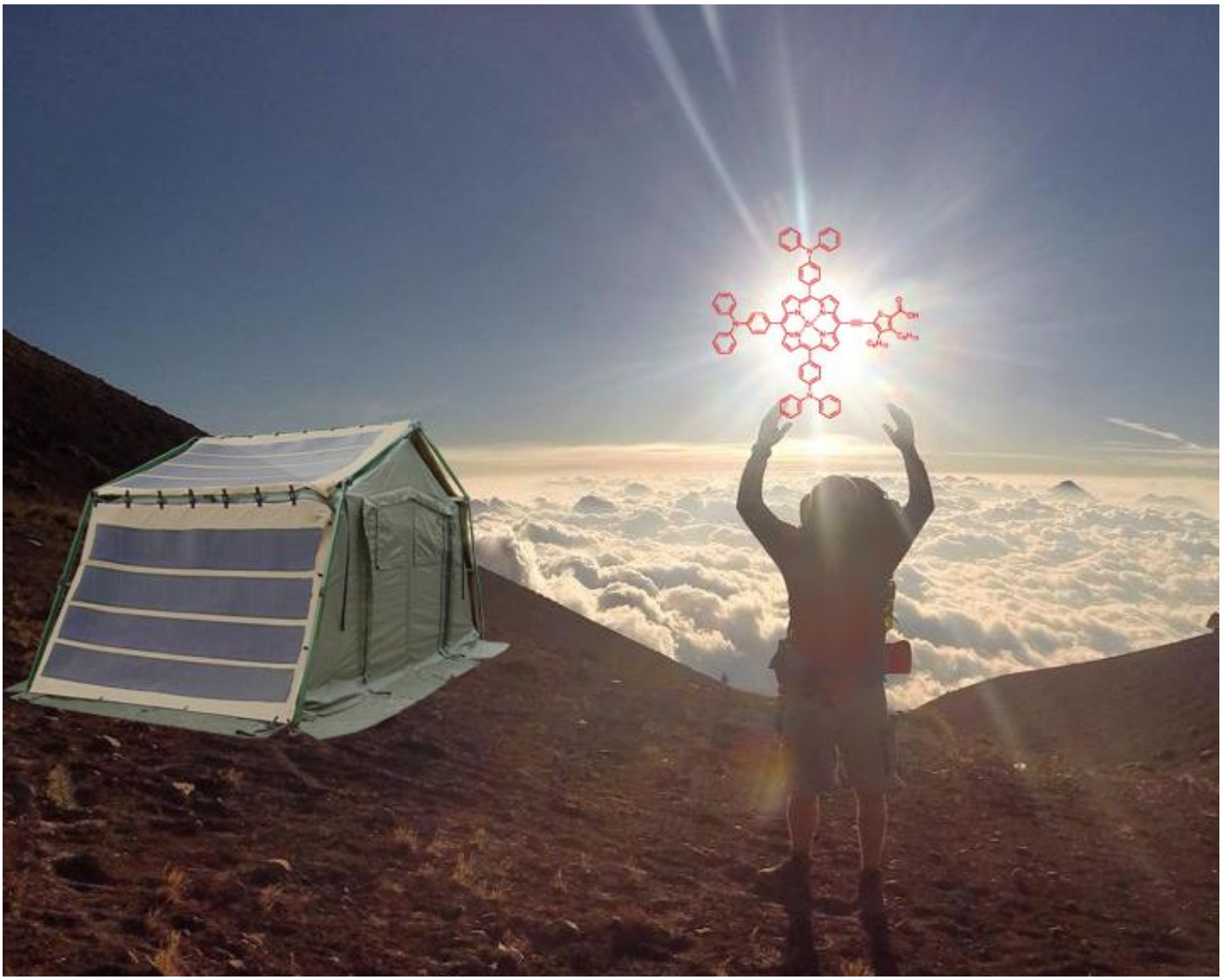

2. Porphyrins for dye-sensitized solar cells (DSSCs)

2.1 Dye Sensitized Solar Cells (DSSCs)

In 1991, O´Regan and Grätzel[1] developed a new photovoltaic cell (DSSC), working on the principles of photosynthesis. This alternative to conventional silicon-based solar cells, attracted great research interests because of low manufacturing costs and environmentally friendly character.[2] DSSCs represent a promising approach to solar energy: Industrial interest has emerged with the quickly developing technologies by companies such as Fujikura, Dyesol, G24 power, Sharp and Solaronix.[2] Figure 95 shows some products of G24 power.

Figure 95. Solar bag pack and solar powered keyboard folio for iPad Air 2, products of GCell by G24 power

The validated DSSC efficiency certified record is 12.4 $\pm$0.3%[3] reported by Grätzel and collaborators, and a new 13% record was described in 2014 by Nazzeruddin and collaborators,[4] both cells use a porphyrin derivate as sensitizer.

Typically, a DSSC comprise a transparent conducting oxide (TCO) electrode, a dye sensitized nanocrystalline titanium dioxide (TiO_2) film, a platinium (Pt) counter electrode, and between the electrodes an electrolyte redox couple (typically iodine I^- /triiodide I_3^-).This oxide layer is composed of nano sized particles that have been sintered together to allow electronic conduction to take place. It has a spongy structure that upon immersion in a dye solution picks up the dye molecules giving an intense coloration.[5] Figure 96 shows an exploded view of its components and assembly structure.

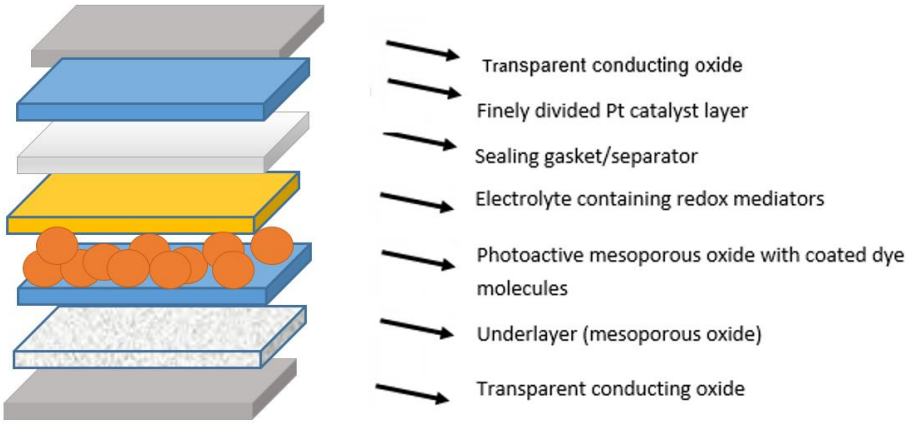

Figure 96. Schematic structure of DSSCs

Conventional dye sensitized solar cells have four principal processes (Figure 97):[18, 17]

- The photoexcitation of the sensitizer, (absorbs the light, leading to an excited state).[6]
- One electron is promoted from the excited state of the dye to the conduction band of the metal oxide (TiO_2, nanoparticles typically), (charge transfer process).
- Regeneration of the oxidized dye to the fundamental state by a reducing agent of the electrolyte.
- The photogenerated electrons at the anode flow through an external circuit to reach the Pt counter electrode (cathode), where the oxidized redox mediator is regenerated.

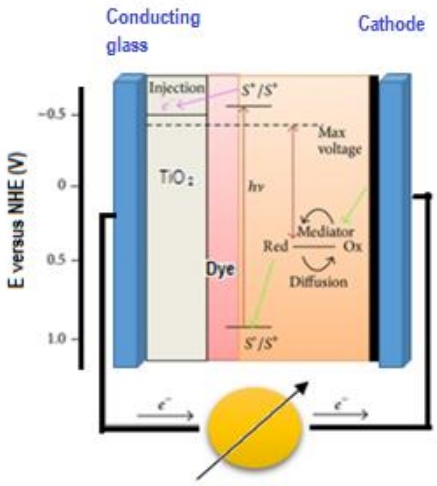

Figure 97. Scheme of physical process in DSSCs

For a better understanding of DSSCs, the next paragraphs describe widely each component of these devices, based on recent publications:[7,8]

- **Transparent conductive substrate**

The conductive highly transparent material provides a substrate for the deposition of the semiconductor and catalyst, acting also as current collector. The transparent (> 80%) substrates allows maximum sunlight into the cell. The electrical conductivity of the substrates should also be high for efficient charge transfer and to minimize energy loss.[8]

Typically are used as conductive substrates are: FTO (fluorine tin oxide) and ITO (indium tin oxide). FTO and ITO substrates consist of soda lime glass coated with fluorine tin oxide and indium tin oxide layers, respectively. The transmittance of ITO films and FTO are over 80% and 55% respectively and sheet resistance of 18 Ω/cm^2 and 8.5/cm^2 respectively. Polymers can also be used as an alternative to glass substrates because of their flexibility and low cost.

- **Mesoporous semiconductor**

Titanium oxide (TiO_2) is usually the mesoporous semiconductor, due to its better morphological and photovoltaics properties compared with other metal oxides such as zinc oxide,[9] and tin (IV) oxide.[10] The semiconductor provides a surface area for the adsorption of the dye, accepting electrons from the excited state of the dye and conducting them to the external circuit to produce an electric current.[11] The electron transport rate depends on the crystallinity, morphology, and the surface area of semiconductors. TiO_2 occurs in nature as minerals bookite, anatase and rutile. Anatase is preferred for its high conduction band edge energy (3.2 eV) and its best electron transport process due to the high packing density. High band gap energy makes anatase chemically more stable.[12] The short circuit photo current of an anatase-based DSSCs is 30% more than a rutile-based DSSCs. Rutile has a smaller surface area and absorbs less dye and therefore rutile-based DSSCs are less efficient.[13,14]

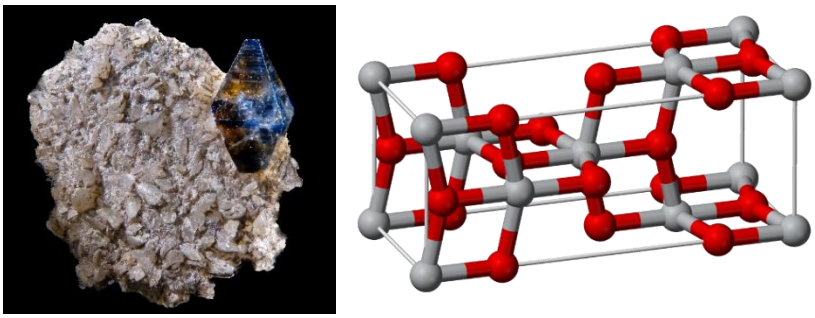

Figure 98. Photography and crystal structure of anatase[15,16]

- **Dye or photosensitizer**

The function of dye is to absorb light and transfer electrons to the conduction band of the semiconductor. Many types of compounds have been developed as sensitizer: as metal organic complexes, metal-free organic compounds and natural dyes. The electrochemical and photophysical properties of the sensitizer play an important role for charge transfer dynamics at the semiconductor interface.[17]

The molecular engineering is important for the preparation of high efficiency DSSCs, the HOMO-LUMO suitably spatially separated and the anchoring group must be bound (by coordination bounding) to the electron acceptor part of the molecular structure for stabilization of the photoexcited state, efficient injection of the generation of oxidized dyes and suppression of the back electron transfer.[2]

Some characteristics for efficient photosensitizers are:

- Must be HOMO level more positive than the redox potential of the electrolyte and the LUMO more negative than the CB of the semiconductor.
- Intense absorption in the visible region, from 400 to 900 nm.
- Adsorb strongly on the surface of the semiconductor.
- High extinction coefficient.
- Stable in its oxidized form allowing it to be re-reduced by an electrolyte.
- Stable enough to carry out ~10^8 turnovers (20 years of cell operation).

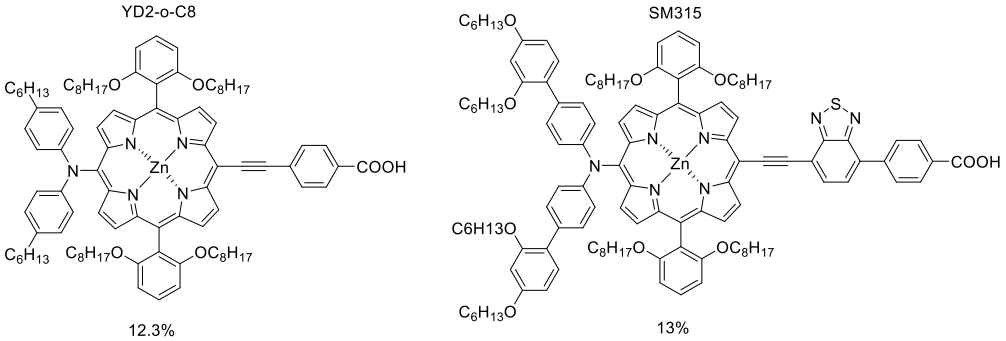

Figure 99. Dyes with the highest DSSCs efficiency (up to July 2015)

- **Electrolyte**

The electrolyte regenerates the dye after it injects electrons into the conduction band of the semiconductor, and acts as a charge transport medium to transfer positive charges towards the counter electrodes.

Some characteristics of the electrolytes are:[18]

- Not absorbing light in the visible region.
- A high electrical conductivity and low viscosity for faster diffusion of electrons.
- Good interfacial contact with the nanocrystalline semiconductor and the counter electrode.
- Not desorption of the dye from the oxidized surface and the degradation of the dye.

There are three types of electrolytes:

- Liquids (organics and room temperature ionic liquid (RTIL)).
- Solids.
- Quasisolids.

The redox couple is the major component of organic electrolytes and many types have been studied, but the good solubility, rapid dye generation, low absorbance of light in the visible region, suitable redox potential, very slow recombination kinetics has established the I_3^-/I^- as the most used couple.[19]

The RTIL are a group of organic salts containing cations such as pyridinium, imidazolium, and anions from the halide or pseudohalide family.[20,21] Nevertheless, their high viscosity limits their application as electrolytes in DSSCs produce low efficiency.

The solid state electrolytes have the advantage of long-term stability; they do not leak like the liquids electrolytes[22] and they use a *p*-type semiconductor or a hole transfer material (HTM). The band gap structure of the *p*-type semiconductor must be compatible with the HOMO level of the photosensitizer and the conduction band of the *n*-type semiconductor, TiO_2.[8,19]

The quasisolid state electrolyte is a composite of polymer and liquid electrolyte and they show better long-term stability, high electrical conductivity, and good interfacial contact when compared to liquid electrolytes,[23] as consequence of the polymers network structure.

- **Counter Electrode (CE)**

This electrode is used for the regeneration of the electrolyte. The oxidized electrolyte diffuses towards the counter electrode where it accepts electrons from the external circuit. A catalyst is required to accelerate the reduction reaction. Platinum (Pt) is considered the preferred catalyst because of its high exchange, current density, good catalytic activity, and transparency. The performance of the CE depends on the method of Pt deposition on TCO substrate. Among the deposition methods are: thermal decomposition of hexachloroplatinic salt in isopropanol, electrodeposition, sputtering,[24] vapor deposition, and screen printing.[25,26,27,28.]

2.2 Solar cells parameters in DSSCs

The power conversion efficiency, similarity to OPV, is given by the Equation 1. The next paragraphs will describe some improvements to the power conversion efficiency of DSSCs according to the key parameters described by Torres, Grätzel, Nazeeruddin, Urbi[17] and Han and collaborators:[2a]

The driving force for electron injection (ΔG_{ing}) is the difference between the LUMO level of the dye and the conduction band of the semiconductor (typically, TiO_2 CB lies at around −0.5 V versus NHE). To make the process of electron injection thermodynamically possible, the LUMO level of the dye must lie above the TiO_2 CB (in a conventional DSSC), and the resulting overpotential must satisfy a minimum value to make it efficient.[17]

The potential energy difference between the HOMO level of the oxidized dye and the potential of the redox mediators will govern the driving force for dye regeneration (ΔG_{reg}). The effect of ΔG_{reg} on the dye−regeneration kinetics (k_{reg}) has been largely unknown for a long time in DSSCs, and is subjected to controversies.[29] In high efficiency DSSCs, over 10%, the n_{inj} and n_{cc} are close to the unity.

The best strategy to increase the short circuit current is to improve the light harvesting efficiency (LHE). LHE quantify the capability of the device to absorb photons, as a function of the extinction coefficient of the dye and concentration/amount of dye adsorbed onto the TiO_2 surface.[17] The sensitizer has to match with the solar spectrum. It is important to prepare dyes with intense molar extinction in visible and NIR regions. The dissociation of the generated exciton needs to be efficient[30] (to inject an electro into the TiO_2 CB), and for this process, the charge separation energy proportional to the exciton binding energy, depends on the electronic structure and the geometry of the dye. The binding energy and intrinsic relaxation dynamics of the exciton, hence, constitute a first crucial factor that governs the electron-injection efficiency, and hence the J_{SC} of the cell.[31]

$$IPCE(\lambda) = LHE(\lambda) * n_{inj} * n_{cc}$$

Equation 3.

Where:

LHE = Light harvesting efficiency

n_{inj} = Electron injection yield from the photoexcited dye into TiO_2

n_{cc} = Charge collection efficiency at the electrodes

The distribution of the photon-flux irradiance is not constant over the solar spectrum; the 500−800 nm region is the richest part in photons. Based on AM 1.5G solar simulations, the expected current density between 400 and 900 nm is near to 7 mA·cm^{-2} for every 100 nm, with a maximum cumulated J_{SC} value around to 35 mA·cm^{-2} for an ideal dye that would harvest whole sunlight in this region. All organic dyes have a limited absorption bandwidth; an efficient dye should be able to absorb the maximum of sunlight in the widest range possible (especially between 400−920 nm) to produce the maximum photocurrent.[17]

Co-sensitizers can be used as strategy to improve LHE by using plural dyes with complementary absorption properties to co-sensitize the mesoporous film.[32] Another strategy is to increase the optical path length within TiO_2 films, adding large diffusive particles into the conventional nano-crystalline TiO_2 or adding scattering layer on the black side.[33]

Design, synthesis, and subtle changes in the molecular structure of the dye will help fine-tune the molecular orbital at adequate levels with respect to those of the semiconductor and electrolyte, as well as the orientation and geometry adopted by the dye onto the surface. A wide absorption of sunlight by the sensitizer and four optimal components are: (1) HOMO and (2) LUMO levels of the dye, (3) redox potential of the redox couple in the electrolyte, and (4) semiconductor conduction band. Accordingly, the redox shuttle must fulfill the compromise between high redox potential to attain high V_{OC} in the DSSCs and satisfy a minimum overpotential needed for an efficient dye-regeneration to avoid a drop in the J_{SC}.

To achieve high power conversion efficiency, is necessary to improve the morphology of semiconductors to reduce the dark current, find low volatile and less viscous electrolytes to improve the charge transfer rate, improve the mechanical contact between the two electrodes and use additives for dyes and electrolytes that enhance their properties.[2] The dyes must reach high electron injection (n_{inj}), dye regeneration (η_{reg}), light harvesting efficiencies (LHE), avoid recombination processes, absorb over the wider range of the solar spectrum, and be stable enough over a long period.[1,17]

2.3 Porphyrins for dye sensitized solar cells DSSCs

2.3.1 Porphyrins in DSSCs[17]: Background

Porphyrins have been used by scientists as efficient light harvesting molecules for dye sensitized solar cells and have drawn much attention as an alternative to silicon-based solar cells due to their low-cost production and high power conversion efficiency (η).[34,35] In addition, the porphyrins have appropriate redox properties for the sensitization of TiO_2 films. The LUMO level of the macrocycles lies above the TiO_2 conduction band, and the HOMO level is close to the redox potential of the electrolyte, which ensures efficient dye regeneration. The adjustment of the electronic levels of the macrocycle is possible by changing the porphyrin substitution at the meso and β positions, as well as changing the complexed metal.[36]

Recent developments on porphyrin-based solar cells exhibit a promising advance; Figure 100 shows a graphic of the PCE of some porphyrin-based DSSCs devices.

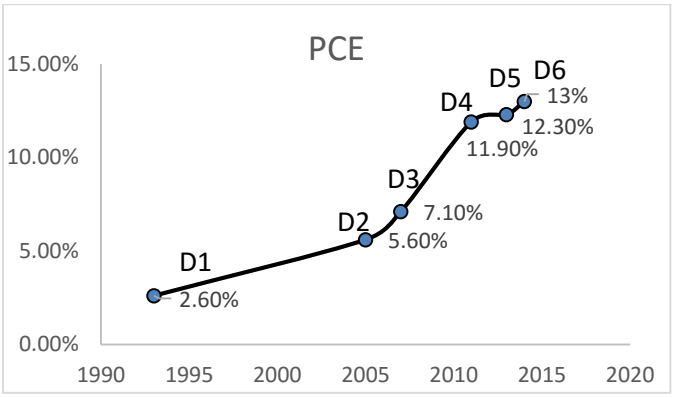

Figure 100. PCE of some porphyrin-based DSSCs

In 1993, was described the first DSSC based on porphyrin dye in TiO_2, with 2.6% of PCE, employing *β*-chlorophyll derivatives and natural porphyrins (**D1**).[37] After this result non significant progress was reported until 2005, when a porphyrin dye with the anchor group linked to the β position (**D2**) shown a PCE of 5.6%.[38,39] The extension of the conjugation in the bridge with another vynil group (**D3**) enhanced the efficiency to 7.1%.[40] In 2011, a *β*-porphyrin dye with a double anchor shown 7.5%, (**D4**).[41,42] Nevertheless, the same year a meso-linked zinc porphyrin dye sensitizer YD2-o-C8 achieving a PCE of 11.9% was prepared. The higher efficiency was due to the amine group linked directly to the porphyrin core and a superior light-harvesting ability through introduction of an extended chromophore at the meso-position of the macrocycle ring, (**D5**). This structural design, involving long alkoxyl chains to suppress the dye aggregation for a push–pull zinc porphyrin, and employing a redox electrolyte cobalt (III/II) tris(2,2′-bipyridine) allow a 12.3% PCE.[43] In 2014, a similar structural porphyrin with a stronger donor and a conjugated linker attached to the anchoring group shown a PCE of 13% (**D6**).[44]

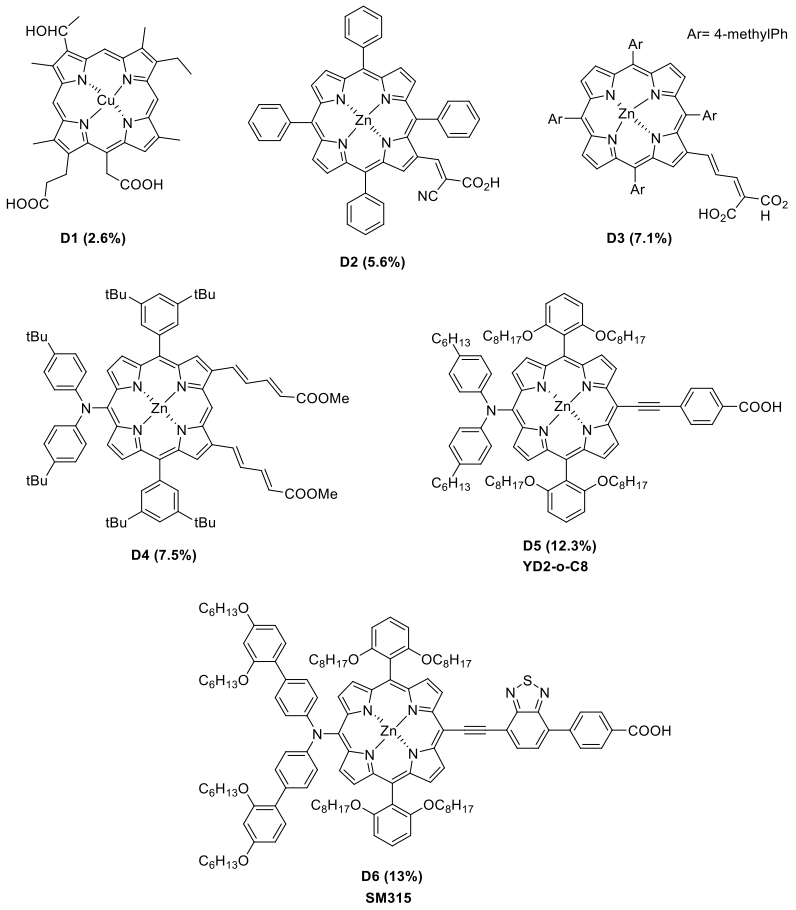

Figure 101. Structure of some porphyrins employed as sensitizers in DSSCs

Nevertheless, in order to improve the efficiency of porphyrin based DSSCs, the following challenges remain:

- Improvement of the light-harvesting ability in the visible and NIR regions.
- Suppression of porphyrin aggregation on TiO_2 to reduce undesirable quenching of the excited singlet state.
- Novel redox couples that can increase V_{OC}.
- Long-term stability under illumination.

The most viable method to enhance J_{SC} in DSSCs is to harvest a broader region of the solar spectrum. To extend the absorption of porphyrin dyes to the near infrared region, the energy gap between HOMO and LUMO levels must decrease. To this end, two approaches can be used: first is to introduce a highly conjugated π-extended chromophore coupled with the porphyrin ring (the best strategy is to functionalize the target porphyrin at the meso-positions).[35]

The second approach is to synthesize fused or dimeric porphyrins; fuse a chromophore to make an elongated macrocycle[45] or combine two porphyrins moieties through a chemical bond extending the conjugation and generating dimeric molecules.[46] However, in most cases, these molecules suffered from poor device performance due to their nearly co-planar structural feature favoring the formation of dye aggregates to deteriorate significantly the device performance. The solution to the aggregation problem is to implement the approach of co-sensitization.[35]

In the following sections, two strategies to diminish effectively dye aggregation for porphyrin-based DSSCs will be described:

The first strategy is to functionalize the porphyrins with long alkoxyl chains, protecting the core for retarded charge recombination and also to effectively decreasing the dye aggregation and so achieving efficient electron injection.

The second strategy is co-sensitation: this is an effective approach to enhance the device performance through a combination of two or more dyes with complementary spectral features sensitized on semiconductor films together, extending the light-harvesting ability to increase the photocurrents of the devices.[89]

The porphyrin sensitizer structure must have an anchoring group to allow the attachment of the dye to the TiO_2 metal oxide and act as an electron-withdrawing group.[47] Carboxylic acids such as benzoic acid and cyanoacrylic acid have been the most widely used functional groups for attaching sensitizers to metal oxides. However, carboxylic acids are prone to dissociate from the metal oxide surface under severe conditions, including exposure to aqueous and alkaline electrolytes. Such detachment of adsorbed dyes from TiO_2 is undesirable for practical applications, considering the necessary durability of DSSCs.

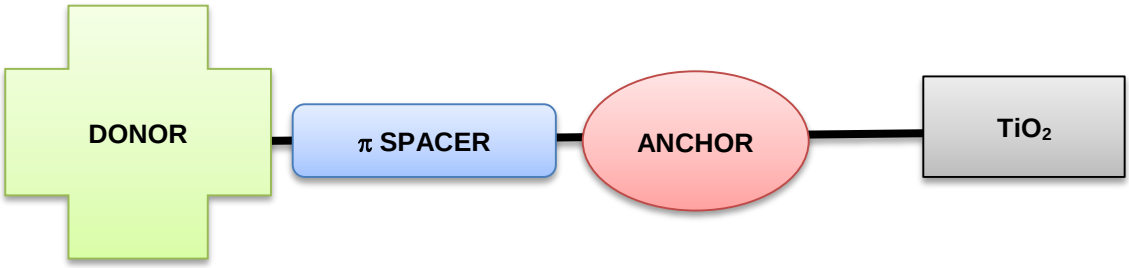

Figure 102. Schematic drawing of D–π–A type DSSCs

The use of π conjugated spacer between the porphyrin and the anchoring group enhance the electronic communication between the excited porphyrin and the semiconductor, promoting the electron-injection process between Dye and TiO_2.

Push–pull porphyrins with the configuration D–π–A type organic sensitizers, which consisting of an electron-donating group (D), π spacer and an electron-withdrawing anchoring group (A), have been widely investigated owing to their broad and intense absorption spectral features as well as efficient electron injection due to intramolecular charge transfer (CT) character.[34,48]

The use of five-member ring heteroaromatic moieties, as linkers between porphyrin and anchoring group have been scarcely reported in DSSCs. A five-member ring substituted at the meso position of a porphyrin allow less steric hindrance with the β-pyrrolic protons than a phenyl group, due to the smaller size and angle bonds, and show higher degree of conformational freedom and can adopt a planar structure, with an overlap of their π orbitals. The dihedral angle between the porphyrin and the heteroaromatic compound is lower than using phenyls (orthogonal to the macrocycle), and display red-shifted and broader absorption bands.

Thiophene, has been broadly utilized in ruthenium based[49] and metal-free organic solar cells[50] to enhance the coefficient absorption and red shift maximum absorption spectrum. Employing thiophene linked to a porphyrin core, through the meso position,[51] a PCE of 5.1% was obtained; this research showed that increasing the number of thiophene units does not extend the spectra. Nevertheless, more number of thiophene units have a negative effect on the performance.[52]

The introduction of a cyanoacrylic moiety as acceptor,[53,54] allows a red-shift of porphyrin absorption bands, in comparison to their carboxylic acid analogues. Nevertheless decreases absorption coefficients, amount of absorbed dye, IPCE, J_{SC}, and PCE. Consequently, the double bound of the cyanoacrylic spacer induces a more loosely and tilted orientation, increasing the electron recombination rate through space between oxidized dyes and TiO_2, leading to poor efficiencies, while the rigidly and linearly oriented carboxylic groups allow a densely packed and well organized arrangement of the dyes on the surface.

It can be foreseen that a PCE of 15% can be achieved if the structure and the fabrication of the device is optimized to reach: V_{OC} = 0.75 V, J_{SC} = 27 $mAcm^{-2}$ and FF= 0.75, with the I^-/I_3^- redox electrolyte,[55] or V_{OC} = 0.9 V, J_{SC} = 22 mA cm^{-2} and FF = 0.75[55,34] with cobalt redox electrolyte.

2.4 General objective

The main objective of this chapter is the design, synthesis and characterization of six news porphyrin-based dyes with the configuration D-π-A, and then analyze the influence of the structure of different porphyrin moieties in the performance of DSSCs.

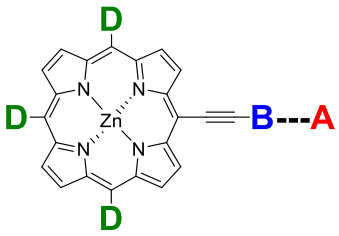

D) Study the effect of the **D** moiety linked to the porphyrin core:

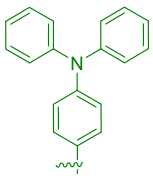

triphenylamine

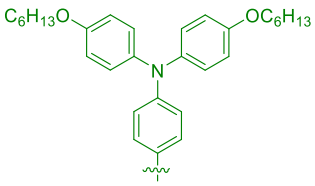

4-(hexyloxy)-N-(4-hexyloxy phenyl)-N-phenylaniline

E) Study the effect of different **B** bridges between porphyrin core and the acceptor:

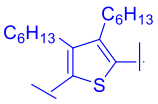

3,4-dihexylthiophene

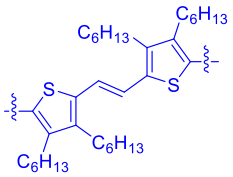

(E)-1,2-bis(3,4-dihexylthiophen-2-yl)ethylene)

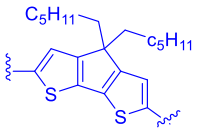

4,4-dihexyl-4H-cyclopenta[2,1-b:3,4-b']dithiophene

Benzene

F) Study the effect of change **A** acceptor as anchoring group:

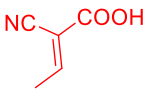

cyanoacetic acid

carboxylic acid

2.4.1 Specific objectives

VI. Design, synthesis and characterization of **SA13-14**, zinc porphyrins bearing different triphenylamine donor groups, and ethynylcarboxyphenyl anchor, to analyze the optical, electrochemical properties and evaluate the performance employing as electrolyte s I^-/I_3^- and tris(1,10-phenanthroline)cobalt in DSSCs.

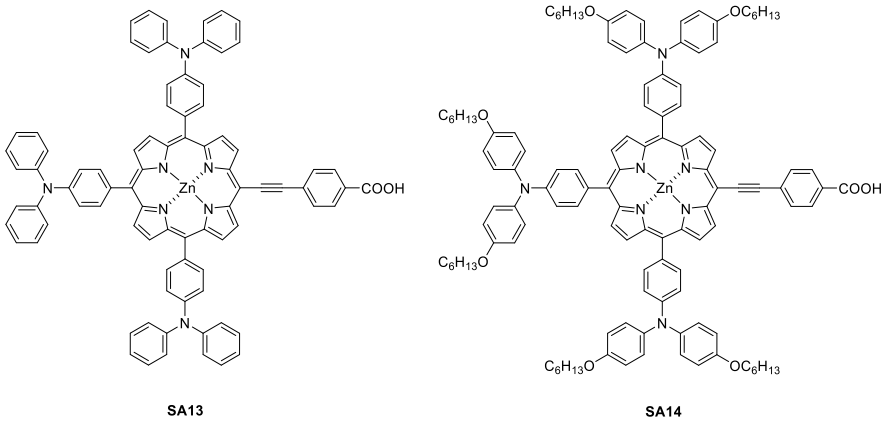

Figure 103. Dyes **SA13-14**

VII. Design, synthesis and characterization of zinc porphyrins **SA15**-**SA18**, bearing triphenylamine donor groups to analyze the difference between 3,4-di-hexyl thiophene and (*E*)-1,2-bis(3,4-dihexylthiophen-2-yl)ethylene as conjugated linkers using cyanoacrylic acid and arylcarboxylic acid, to analyze the optical, electrochemical properties and evaluate the performance in DSSCs.

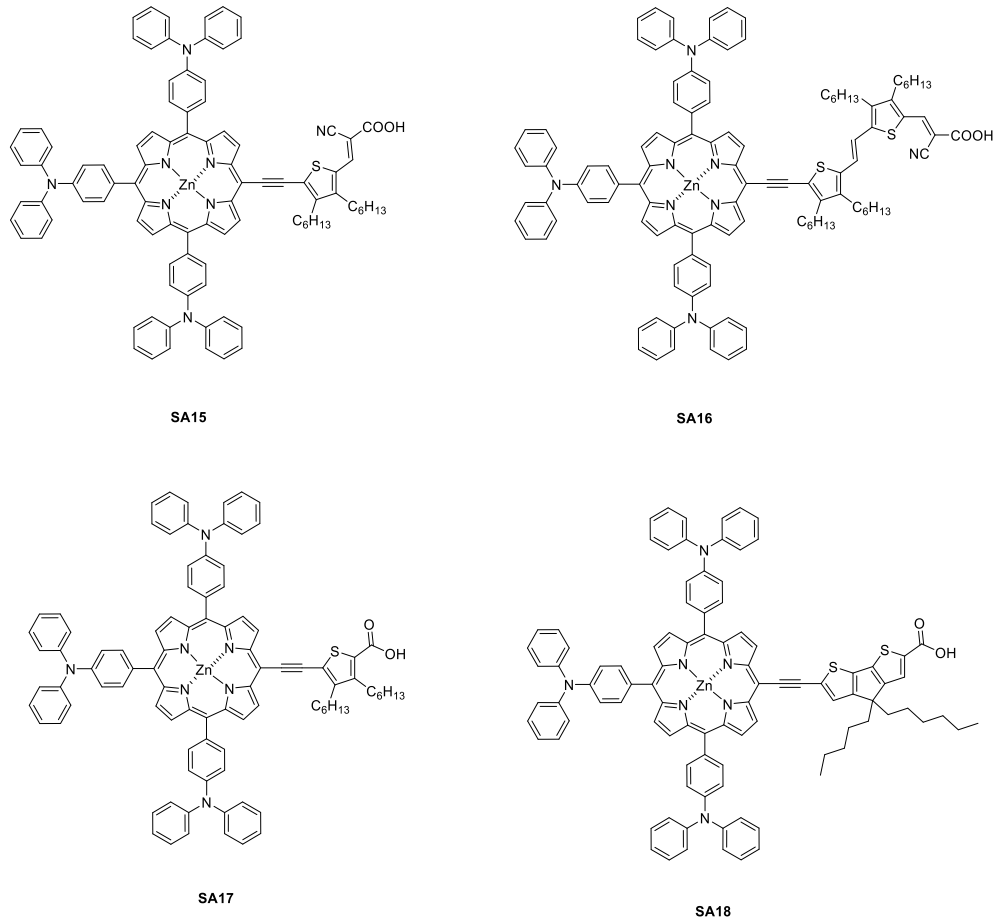

Figure 104. Dyes **SA15-18**

.

2.5 SA13 and SA14

2.5.1 Synthesis and characterization of SA13 and SA14

Scheme 13 shows the synthetic route to dyes **SA13** and **SA14**.[62] The synthesis began with the preparation of [10,15,20-*tri*(*N*,*N*-diphenylaniline)-5-ethynyltrimethylsilane]porphyrin (**P4**) and [10,15,20-*tri*(*N*,*N*-(*bis*(4-hexyloxy)phenyl)aniline)-5-ethynyltrimethylsilane]porphyrin (**P5**) in 14% and 11% yield respectively, according to the Lindsey method.[56] This procedure improves significantly the yield with respect to previous procedures described for similar porphyrins (4-6%).[57] Free porphyrins **P4** and **P5** were reacted with zinc acetate in chloroform giving the metallized porphyrins **P4S** and **P5S** in 91% and 95% yield after purification by column chromatography (silica gel, Hex/$CHCl_3$, 1:1).

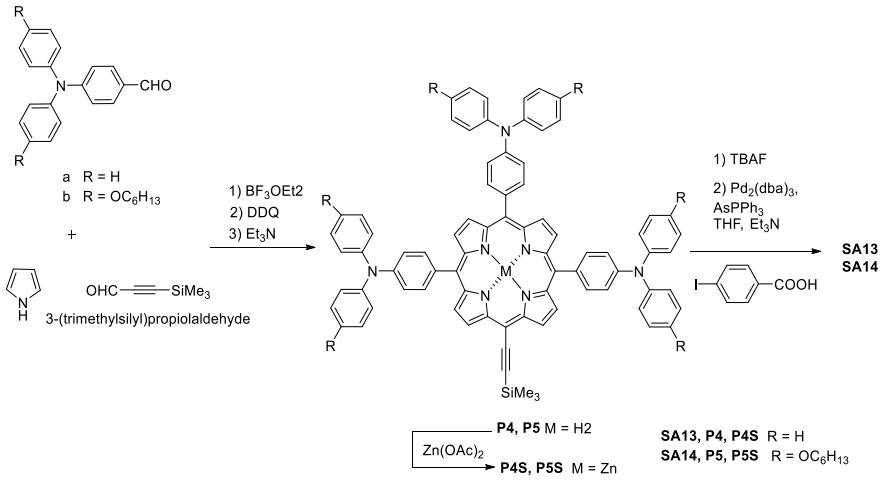

Scheme 13. Synthesis of **SA13-14**

^{1}H-NMR spectrum of **P4S** shows signals at 9.79, 9.14, 9.07 and 9.05 ppm corresponding to the protons of the porphyrin macrocycle and does not show the signals at -2.32 ppm indicating the successful metalation of the porphyrin core. ^{1}H-NMR spectra of **P5S** show a similar pattern that **P4S** with signals at 9.75, 9.13, 9.05 and 9.03 ppm assigned to the protons of the porphyrin ring and does not show at -2.27 ppm, corresponding to the successful metalation, (see experimental part Figure 234 and Figure 215). The ^{13}C-NMR spectra of **P4S** and **P5S** show signals at 0.35 ppm and 0.41 ppm, respectively corresponding to the carbon of the trimethylsylil groups, (see experimental section from Figure 216 to Figure 219). Structures of all compounds were confirmed by MALDI-TOF mass spectrometry (see experimental section from Figure 220 to Figure 223).

Finally, the trimethylsylil group was quantitatively removed by TBAF and *in situ* reacted to *p*-iodobenzoic acid under Pd-catalyzed Sonogashira coupling conditions, affording the target dyes **SA13** and **SA14** after purification by column chromatography (silica gel, CHCl3: MeOH 10:1) in

70 and 63% yield respectively, (for more details see experimental section at the end of this chapter).

The structures of the final compounds were also confirmed by MALDI-TOF mass spectrometry; **SA13** and **SA14** showed 1245.40 (M^+), 1846.40 (M^+) respectively, (see the experimental section, Figure 228 and Figure 229).

The TGA of compounds **SA13** and **SA14** were evaluated and decomposition temperatures (T_d) were estimated from the TGA plot as the temperature of the intercept of the leading edge of the weight loss curve. Under these conditions, compounds **SA13** and **SA14** display excellent thermal stability up to 220 ^oC (Figure 105).

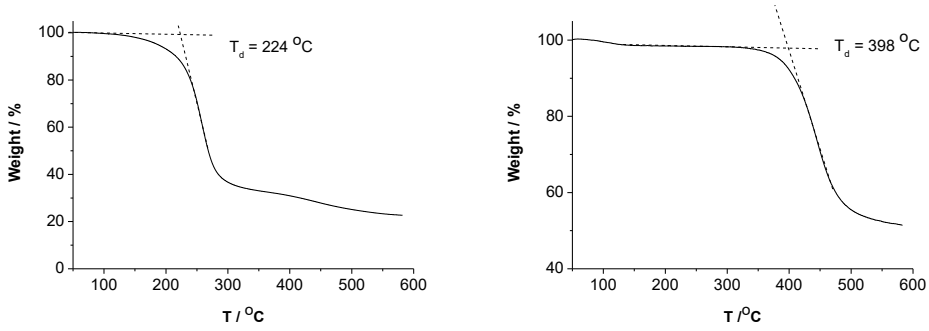

Figure 105. Thermogravimetric analysis of **SA13** (left) and **SA14** (right)

2.5.2 Optical Properties

Figure 106 shows the absorption spectra of dyes **SA13** and **SA14** in dichloromethane (CH_2Cl_2) solution. Both dyes exhibit the typical features of zinc porphyrins, with an intense Soret band between 400-500 nm and less intense Q bands in the range 550 to 700 nm (see Table 19 and Figure 239 in experimental section at the end of this chapter).

The addition of carboxyphenyl moiety to **SA13** and **SA14** provokes a bathochromic effect in the Soret band and the maxima are shifted by 6 nm and 8 nm in comparison to the precursors **P4S** and **P5S** respectively (see the experimental section Figure 236 and Figure 237).

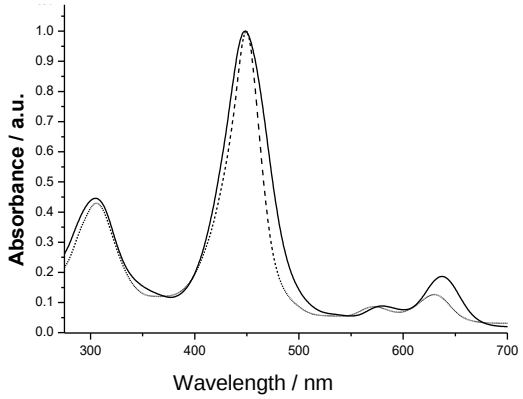

Figure 106. Normalized absorption spectra of dyes **SA13** (dash line) and **SA14** (solid line) in CH_2Cl_2 solution (10^{-5} M)

Table 19. UV-Vis Absorption, Fluorescense emission and OSWV data of dyes **SA13** and **SA14**

Dye	λ_{max}/nm (log ε)[a]	λ_{em}/nm[a]	E^1_{red} (V)[b]	E^1_{ox} (V)[b]	E_{HOMO} (eV)[c]	E_{LUMO} (eV)[d]
SA13	630 (4.18)	652	-0.52	0.33	-5.43	-3.50
	572 (4.02)					
	450 (5.08)					
	306 (4.71)					
SA14	637 (4.39)	669	-0.58	0.28	-5.38	-3.49
	579 (4.07)					
	449 (5.12)					
	305 (4.77)					

[a] 10^{-5} M, CH_2Cl_2; [b] [10^{-3} M] in THF versus Fc/Fc^+, glassy carbon, Pt counter electrode, 20 ºC, 0.1 M Bu_4NClO_4, scan rate = 100 mV s^{-1}; [c] Calculated using equation E_{LUMO} (vs. vacuum) = -5.1 - E^1_{ox} (vs. Fc/Fc+) in eV;[58] [d] E_{LUMO} was calculated using the first reduction potential.

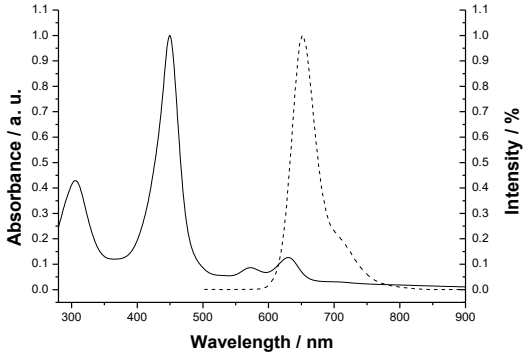

Figure 107. Normalized UV-Vis absorption and fluorescence emission spectra of **SA13** (λ_{exc}= 450 nm) in CH_2Cl_2

In order to have an indication of dye loading in these devices, the absorption spectra of thin films of transparent TiO_2 films (6 μm) were measured after 1.5 hours and 6 hour sensitization in 0.2 mM solutions of **SA13** and **SA14** in chlorobenzene (Figure 108). These data indicate that there are roughly twice as much dye loading on the films for 6 hours compared to 1.5 hours sensitization.

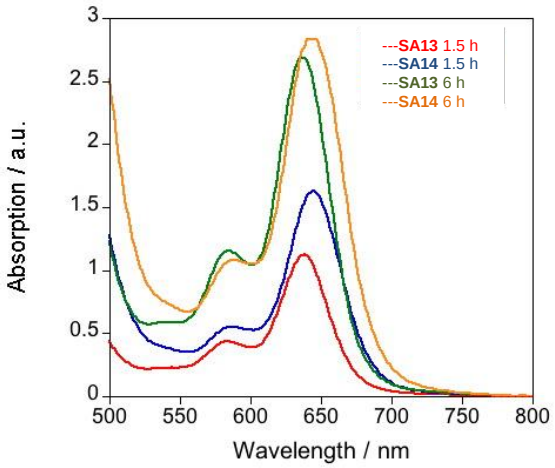

Figure 108. Absorption spectra of thin films of transparent TiO_2 films (6 μm) following 1.5 and 6 hour sensitization in 0.2 mM solutions of **SA13** and **SA14** in chlorobenzene

Fluorescence spectra were recorded in CH_2Cl_2, exciting at the absorption maxima (λ_{exc}= 450 nm for **SA13**, and λ_{exc}= 449 nm for **SA14**), showing intense emission of 652 nm and 669 nm respectively (see Figure 107). Interestingly, emissions of porphyrin were totally quenched after adsorption onto TiO_2, suggesting efficient photoinduced electron transfer from the dyes to the TiO_2 nanoparticles (see Figure 109).

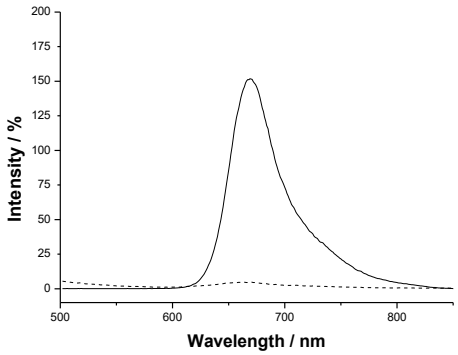

Figure 109. Fluorescence emission spectra in absence (solid line) and presence of TiO_2 (dash line) of compound **SA13** (λ_{exc} = 450 nm) (left) and **SA14** (λ_{exc} = 449 nm) in CH_2Cl_2

2.5.3 Electrochemical Properties

The redox properties of **SA13** and **SA14** were investigated by cyclic voltammetry and square wave voltammetry in tetrahydrofurane (THF) (Table 19, Figure 110 and Figure 111). On the cathodic side, compounds **SA13** and **SA14** show the first reversible oxidation peaks at 0.33 and 0.28 V respectively; the presence of the electron-donating alkoxy groups significantly reduces the oxidation potential of **SA14** compared to **SA13** by 0.05 V.

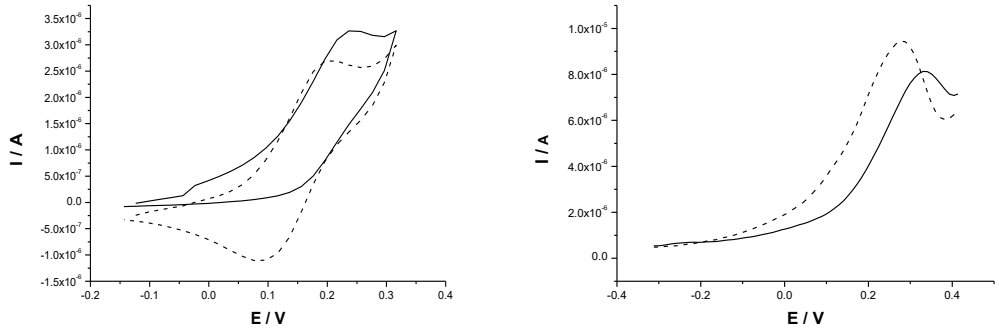

Figure 110. CV (left) and OSWV (right), of compounds **SA13** (solid line) and **SA14** (dash line) (anodic window)

On the reduction side, both compounds show a first reduction potential at -0.52 V and -0.57 V as irreversible waves, showing that the electron-donating alkoxy groups in **SA14** increase its reduction potential with respect to **SA13**, as we would expect. The LUMO of **SA13** to **SA14** vary only by 0.05 eV and were determined as -5.43 eV (**SA13**) and -5.38 eV (**SA14**), indicating that regeneration by I/I_3^- (E_{redox} = -4.75 eV) and $Co(II)(pheno)_3/Co(III)(pheno)_3$ (E_{redox} = -5.06 eV) is energetically feasible. The E_{LUMO} values indicate that efficient electron injection into the TiO_2 conduction band (E_{TiO2} = -4.00 eV) is also energetically possible.

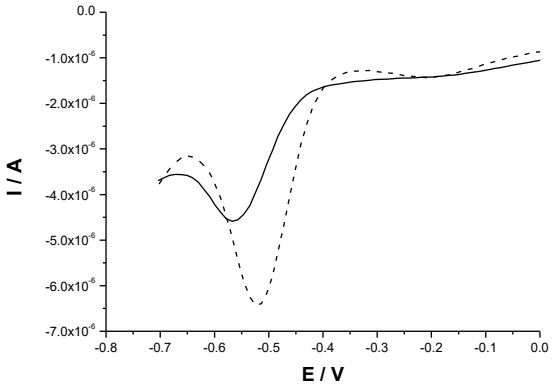

Figure 111. OSWV of compounds **SA13** (solid line) and **SA14** (dash line) (anodic window)

2.5.4 Theoretical Calculations

The optimized structures of **SA13** and **SA14** were calculated, in order to gain insight into the geometries and electronic properties. The computational studies were performed employing density functional theory (DFT) at the B3LYP/6-31G level.

The geometry of both dyes shows similar dihedral angles between the phenyl ring and the porphyrin macrocycle ($\varphi \sim -65^{o}$) and are in agreement with those calculated for similar systems (Figure 112).[59] The angle between the porphyrin and the carboxyphenyl ($\varphi \sim 1.65$ and 1.82 for **SA13** and **SA14** respectively), shows the planarity of the system, allowing the extension of the conjugation.

The calculated HOMO levels of **SA13** and **SA14** are found to be delocalized through the porphyrin macrocycle and TPA, however the LUMO levels are extended along the porphyrin system, the linker and the acid group, indicating that electronic coupling with the TiO_2 nanocrystals is possible. The HOMO-LUMO gap is similar for both dyes (2.29 and 2.20 eV for **SA13** and **SA14** respectively), the LUMO level of **SA14** is higher (-2.45 eV) than **SA13** (-2.61 eV) due to the electronic coupling of the alkoxy groups of the TPA moieties (Figure 113).

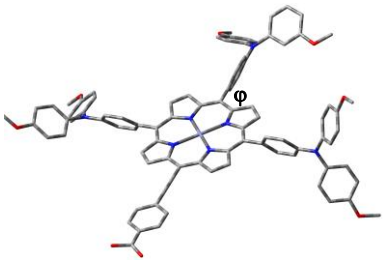

Figure 112. Optimized structure for dye **SA14** (hexyl groups have been replaced by methyl for calculations)

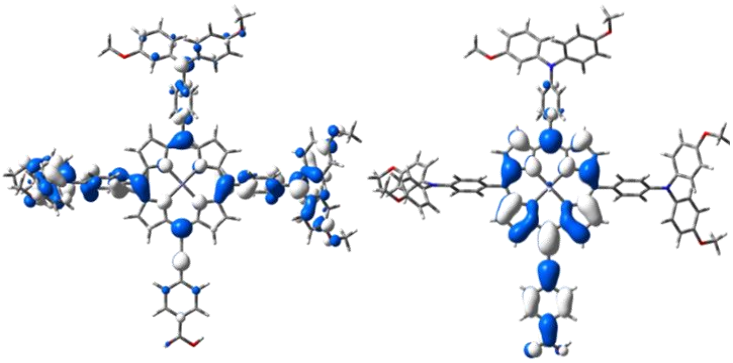

Figure 113. Electronic density contours calculated at the B3LYP/6-31G** level for dye **SA14**

2.5.5 Photovoltaic properties

DSSCs devices were fabricated in collaboration with Prof. Emilio Palomares at the Institute of Chemical Research of Catalonia (ICIQ). The efficiency of the devices was optimized by modifying the electrolyte and the sensitization time.

The best efficiency (5.14%) achieved for **SA13** is consequence of the combination of the parameters V_{OC} (0.63 V), FF (67%) and J_{SC} (10.09 mA/cm^{-2}); in the case of **SA14,** similar V_{OC} (0.62 V) and FF (70%) are found, nevertheless J_{SC} (7.83 mA/cm^{-2}) decreased and the best efficiency (4.15%) is lower than **SA13**. In both cases, the best efficiencies were employing I^-/I_3^- electrolyte, after 1.5 hours of sensitization time (without mask, see Figure 114a). These results match with the study of Liu et al, involving similar dyes. [57] Upon longer sensitization time of 6 hours the device efficiency drops to 3.93 and 3.60% for **SA13** and **SA14** respectively (without mask), as consequence of the decrease in J_{SC}.

The devices fabricated with cobalt electrolyte, afforded the best results after a longer sensitization time (6 hours) with 3.11 and 2.45% for **SA13** and **SA14** respectively. The increased V_{OC} (approx. 140 mV) afforded by employing Co(II)(pheno)$_3$/Co(III)(pheno)$_3$ with respect to I^-/I_3^- is in line with other studies,[60] nevertheless the decrease in J_{SC} in comparison to the other electrolyte produce a lower efficiency, (Figure 114c). Finally, under similar conditions the device prepared with **YD2-o-C8** (used as reference) gave an efficiency of 12.57% (without mask), indicating that tested conditions are comparable with other studies.[61]

Figure 114 (b and d) show the IPCE spectra for all of the studied devices. These spectra show the contributions to device current from the Soret and Q bands, centered at around 450 and 650 nm, respectively. The integration of these spectra exhibit an agreement with the J_{SC} values for the same devices in Figure 114 (a and c).

Table 20 show the device performance, J_{SC} and V_{OC}, fill factor (*FF*) and overall efficiency (η), for sensitizers **SA13** and **SA14** in DSSCs devices based on I^-/I_3^- and Co(II)(pheno)$_3$/Co(III)(pheno)$_3$ electrolytes.

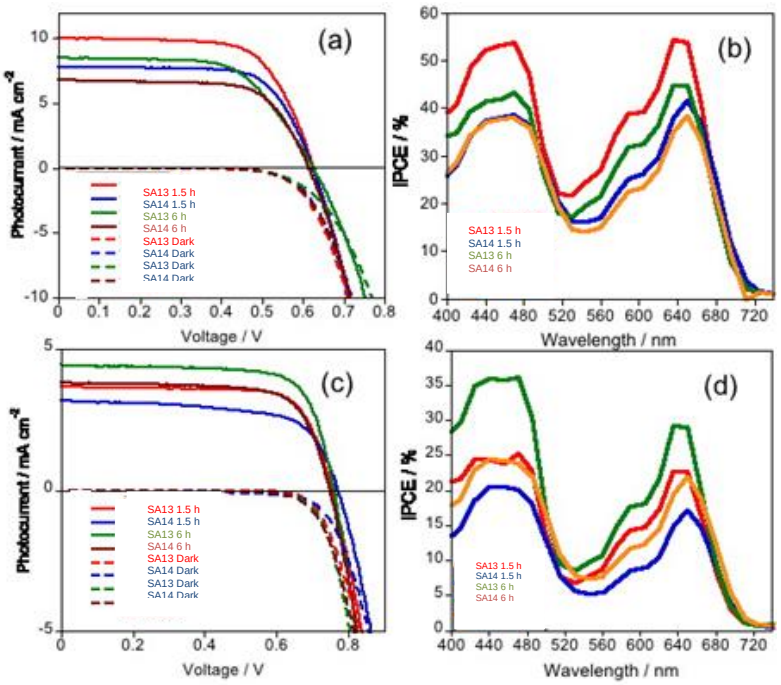

Figure 114. *J-V* curves and IPCE spectra of DSSCs devices composed of sensitizers **SA13** and **SA14** based on I^-/I_3^- ((a) and (b)) and $Co(II)(pheno)_3/Co(III)(pheno)_3$ electrolytes ((c) and (d))

Table 20. Photovoltaic performance of cells recorded under AM 1.5G 1 sun illumination

Dye	Electrolyte	Time (h)	J_{SC} (mA/cm^2)	V_{OC} (V)	FF (%)	PCE (%)*
SA13	a	1.5	10.09	0.624	67	4.19 (5.14)
SA13	a	6	8.51	0.624	62	3.27 (3.93)
SA14	a	1.5	7.83	0.624	70	3.40 (4.15)
SA14	a	6	6.18	0.614	69	2.54 (3.60)
SA13	b	1.5	3.67	0.754	75	2.06 (2.53)
SA13	b	6	4.44	0.759	74	2.48 (3.11)
SA14	b	1.5	3.17	0.769	66	1.61 (2.01)
SA14	b	6	3.82	0.749	72	2.05 (2.45)
YD2-o-C8	c		20.13	0.754	66	10.04(12.57)

[a] Electrolyte: 0.6 M 1-butyl-3-methylimidazolium iodide (BMII), 0.1 M lithium iodide, 0.05 M iodine and 0.5 M 4-*tert*-butylpyridine in a 1:1 mixture of acetonitrile/valeronitrile; [b] Electrolyte: 0.2 M tris(1,10-phenanthroline)cobalt(II)$(TFSI)_2$, 0.02 M tris(1,10-phenanthroline) cobalt(III)$(TFSI)_3$, 0.1 M lithium perchlorate and 0.5 M 4-*tert*-butylpyridine in a 85:15 mixture of acetonitrile/valeronitrile; [c] Electrolyte: 1 M 1-butyl-3-methylimidazolium iodide (BMII), 0.05 M lithium iodide, 0.03 M iodine, 0.1 M GuNCS and 0.5 M 4-*tert*-butylpyridine in a 85:15 mixture of acetonitrile/valeronitrile. *Data in parenthesis recorded

2.6 Dyes SA15 and SA16

2.6.1 Synthesis and characterization of SA15 and SA16

To complete the results obtained in the last section; two new porphyrins were synthesized, employing the porphyrin core of **SA13** (see chapter 2 section 2.5.1) and thiophene substituent as conjugated spacers between the porphyrin core and the anchoring, dicyanovinylene moiety. The synthesis of dyes **SA15-16** was performed according to Scheme 14, starting from trimethylsilyl porphyrin **P4S**, previously prepared (see Scheme 13).[62]

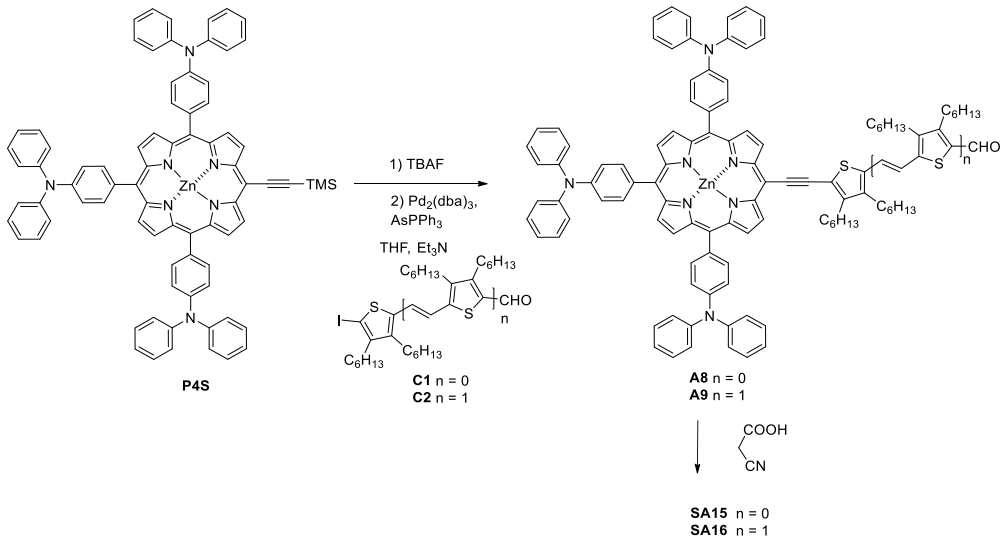

Scheme 14. Synthetic route to dyes **SA15** and **SA16**

Firstly, the trimethylsilyl group was quantitatively removed by reaction with TBAF, followed by cooper-free Sonogashira coupling reaction[63] with 2-iodothiophene derivatives **C1** and **C2**,[64] affording aldehydes **A8** and **A9** in 83% and 80% yield respectively.

Subsequently, dyes **SA15-16** were synthesized by Knoevenagel condensation of **A8** and **A9** with cyanoacetic acid, using piperidine as base, affording after purification by column chromatography (silica gel, $CHCl_3$: MeOH 10:1), dyes **SA15** and **SA16** in 89% and 82% yields, respectively. Satisfactory solubility of **SA15** and **SA16** in several common organic solvents, such as CH_2Cl_2, $CHCl_3$, and THF allowed the preparation of DSSCs. ^{1}H-NMR spectra of **SA11** and **SA16**, (Figure 116) showed the signals corresponding to the attached anchoring cyanovinylene at 8.54 and 8.45 ppm, respectively and did not showed the signals at 9.90 and 9.76 ppm, respectively, corresponding to the H atoms of the precursors aldehydes **A8** and **A9** (Figure 115). The *trans* character of the double bond in **A9** and **SA16** was confirmed by the coupling constant of around 15.4 Hz between the two vinyl protons (see the ^{1}H-NMR spectrum in the experimental section).

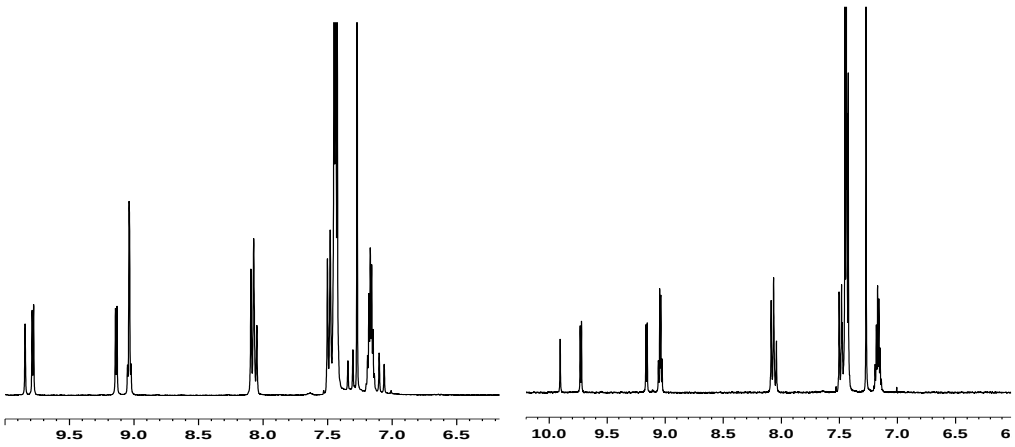

Figure 115. 6 to 10 ppm ^{1}H-NMR spectra (400 MHz, THF-d_8) of compounds **A8** (right) and **A9** (left)

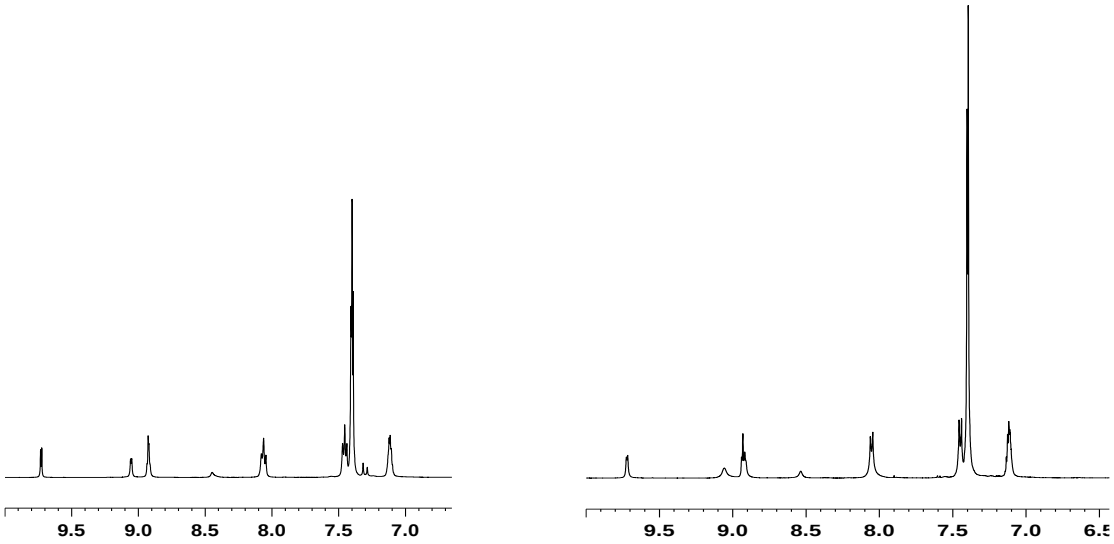

Figure 116. 6 to 10 ppm ^{1}H-NMR spectra (400 MHz, THF-d_8) of compounds **SA15** (right) and **SA16** (left)

All new compounds were fully characterized by means of FT-IR, ^{1}H and ^{13}C-NMR spectroscopies and MALDI-TOF mass spectrometry (see the experimental section at the end of the chapter).

The MALDI-TOF mass spectrometry show a molecular ion pick (m/z) of 1470.53 to **SA15** and 1747.17 to **SA16** (Figure 117), according with the expected molecular mass, (see the complete spectra in experimental section Figure 246 and Figure 247, and the previous aldehydes **A8** and **A9** Figure 240 and Figure 241).

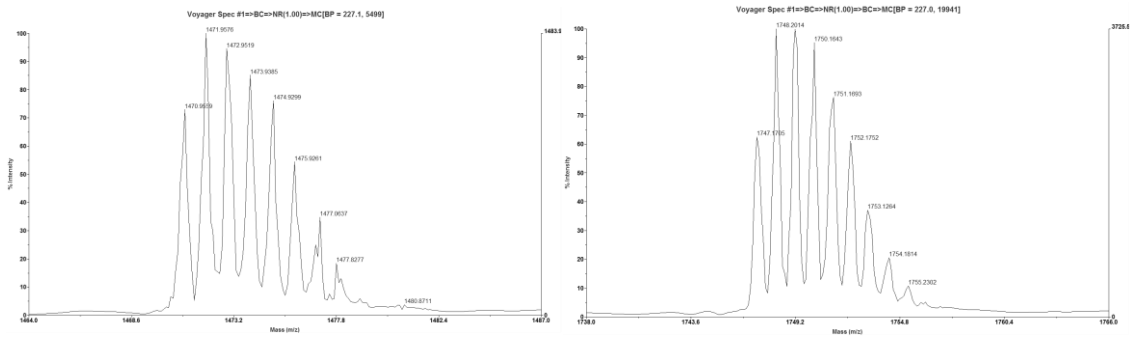

Figure 117. MALDI-MS spectra of compound **SA15** (left) and **SA16** (right) (Matrix: Dithranol).

The TGA profile of **SA15** and **SA16** shows a similar pattern that porphyrin **SA13**, therefore decomposition temperatures (T_d) display good thermal stability up to 200ºC for both compounds (Figure 118).

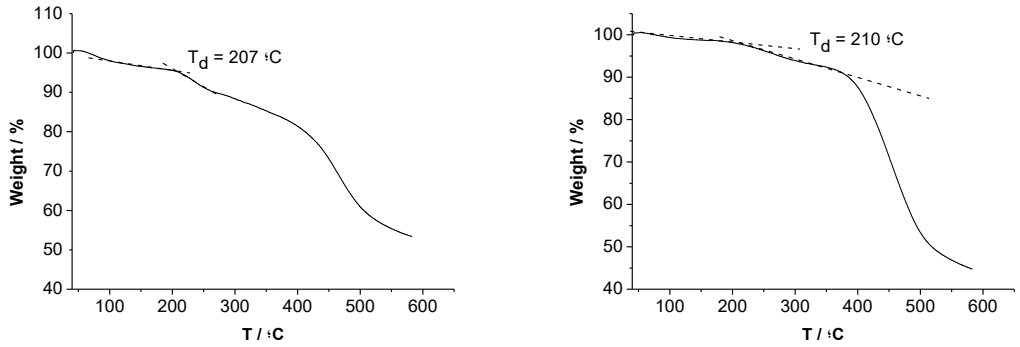

Figure 118. Thermogravimetric analysis of **SA15** (left) and **SA16** (right)

2.6.2 Optical properties

The optical properties of **SA15** and **SA16** were studied by UV-Visible spectroscopy in THF solution and both compounds exhibited absorption in the visible region. The solution of **SA15** in THF displays an intense Soret band at 471 nm (log ε = 4.99) and an intense intermolecular charge transfer (ICT) band at 662 nm (log ε = 4.53); between these bands, one of the Q bands was observed at 583 nm (log ε = 3.93). Extension of the conjugation on the bridge by the introduction of a new thienylenevinylene unit had a significant effect on the absorption spectra of **SA16**, leading to a panchromatic absorption as the Soret band was red-shifted to 460 nm (log ε = 5.21) and a new absorption band appeared at 523 nm (log ε = 4.87), which is attributed to the conjugated oligomer bridge. Furthermore, the ICT band was observed at 668 nm (log ε = 4.91) with an increased absorption coefficient (see Figure 119 and Table 21).

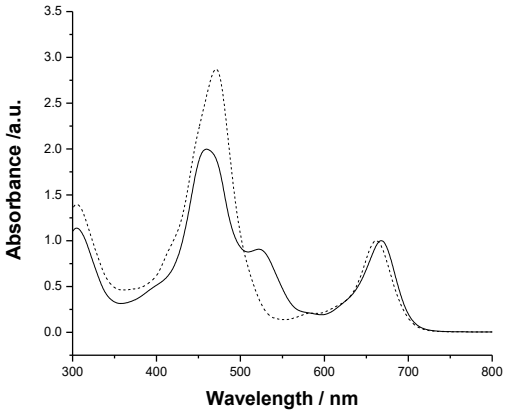

Figure 119. Absorption spectra of dyes **SA15** (dash line) and **SA16** (solid line) in THF solution (10^{-6} M)

A) B)

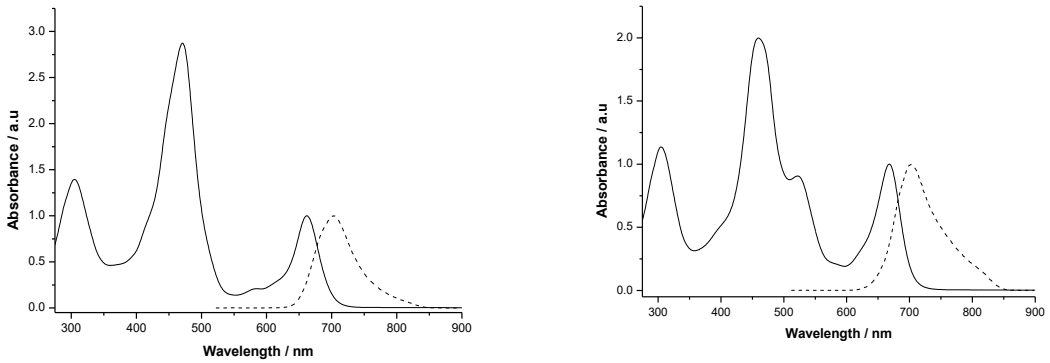

Figure 120. +UV-Vis absorption (solid line) and fluorescence emission spectra (dash line) of **SA15** (A, λ_{exc} = 471 nm) and **SA16** (B, λ_{exc} = 460 nm) in THF

The steady state fluorescence spectra of dyes **SA15** and **SA16** measured in THF show an emission band at 703 nm in both cases (**SA15** λ_{exc} = 471 nm and **SA16** λ_{exc} = 460 nm, Figure 120). It is also noteworthy that significant differences were not observed in the emission band as a result of the increased conjugation due to the inclusion of an additional thienylenevinylene unit. The emission bands were totally quenched after adsorption onto TiO_2 and this suggesting an efficient photoinduced electron transfer from the excited state of the dye to the TiO_2 nanoparticles (Figure 121).

A) B)

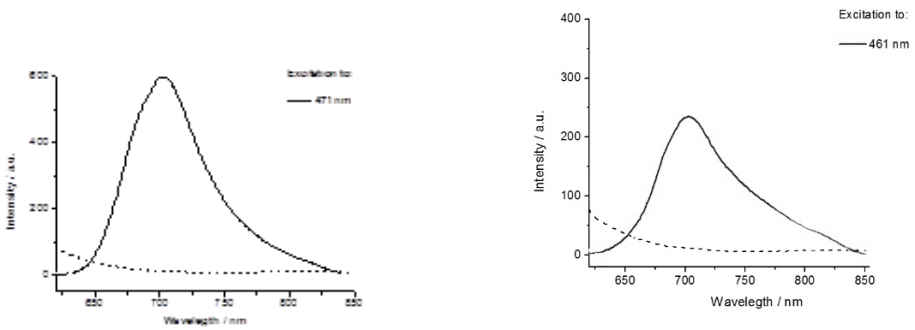

Figure 121. Fluorescence emission spectra in absence (solid line) and presence of TiO_2 (dash line) of **SA15** (A) and **SA16** (B) in THF

Table 21. UV-Vis Absorption, Fluorescence Emission[a] and OSWV[b] data for compounds **SA15-16**

Dye	λ_{max} / nm	log ε	λ_{em} /nm	E^1_{ox} /V	E^2_{ox}/V	E^1_{red} /V	E_{HOMO} /eV[c]	E_{LUMO} /eV[d]	E_g /eV[e]
SA15	662	4.53	703	0.29	0.44	-1.62	-5.39	-3.48	1.91
	583	3.93							
	471	4.99							
	305	4.68							
SA16	668	4.91	703	0.26	0.49	-1.71	-5.36	-3.39	1.97
	523	4.87							
	460	5.21							
	305	4.97							

[a] **SA15**: 8.70 x 10^{-6} M, THF; **SA16**: 5.15 x 10^{-6} M, THF. [b] [10^{-3} M] in THF versus Fc/Fc+, glassy carbon, Pt counter electrode, 20 ºC, 0.1 M Bu_4NClO_4, scan rate = 100 mV s^{-1}. [c] Calculated using equation E_{HOMO} (*vs*. vacuum) = -5.1 - E^1_{ox} (vs. Fc/Fc^+) in eV.[25] [d] E_{LUMO} was calculated with E^1_{Red}.[e] $E_g = E_{HOMO} - E_{LUMO}$.

2.6.3 Electrochemical properties

Electrochemical properties of **SA15** and **SA16** were measured by cyclic voltammetry and square wave voltammetry in THF (Table 1, Figure 123 and Figure 124). Compounds **SA15** and **SA16** show the first oxidation peaks at 0.29 and 0.26 V respectively (vs Fc/Fc^+). This first oxidation potential is assigned to the porphyrin core by comparison with the porphyrin precursor **P4S** (0.35 eV, Figure 122), and the extended conjugation gives rise to a decrease of the E_{ox} value by 30 mV of **SA16** respecting to **SA15**. The second oxidation processes are attributed to the thienylenevinylene moieties. On the reduction side, both compounds show first reduction potentials at -1.62 V and -1.71 V, respectively, as irreversible waves, and they are attributed to the reduction of the thienylenevinylene moieties. It was also observed a second reduction potential at -1.76 V for **SA15**, which is attributed to the reduction of the porphyrin core. This

second reduction potential is sensed also in the case of **SA16** as a shoulder of the first wave of reduction. The E_{HOMO} values deduced from the oxidation potentials are -5.39 eV and -5.36 eV for **SA15** and **SA16** respectively., indicating that the regeneration is energetically feasible by I/I_3^- (E_{redox} = -4.75 eV). The E_{LUMO} values, -3.48 for **SA15** and -3.39 for **SA16**, also indicate that efficient electron injection into the TiO_2 conduction band (E_{TiO2} = -4.00 eV) is energetically possible as well.

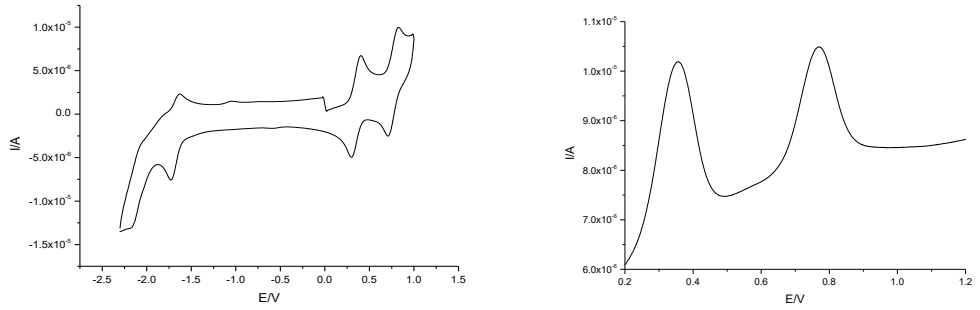

Figure 122. Cyclic Voltammetry (cathodic window) and Squave Wave Voltammetry plot of **P4S** (referred to Fc/Fc^+)

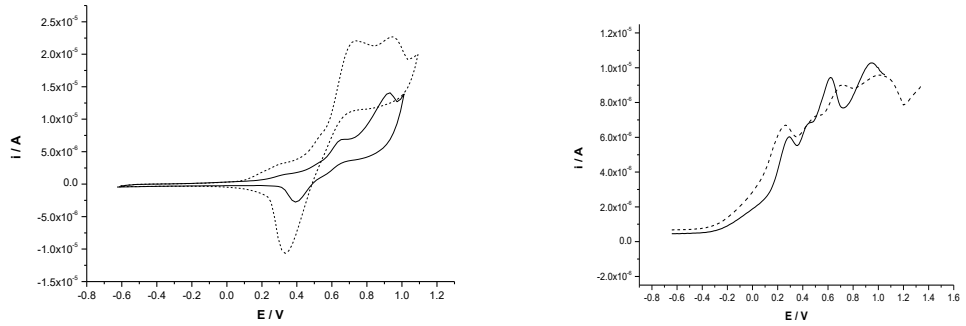

Figure 123. Cyclic Voltammetry and Square Wave Voltammetry plot (cathodic window) of **SA15** (solid line) and **SA16** (dash line) (referred to Fc/Fc^+)

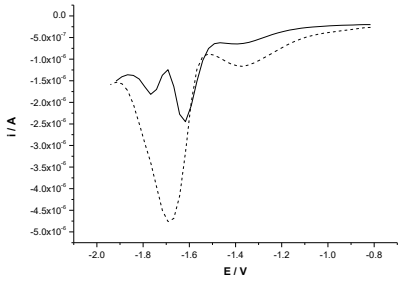

Figure 124. Square Wave Voltammetry plot (anodic window) of **SA15** (solid line) and **SA16** (dash line) (referred to Fc/Fc^+)

2.6.4 Theoretical Calculations

To gain insight into the geometrical and electronic properties of dyes **SA15** and **SA16**, DFT calculations were performed. The calculated ground state geometries (Figure 125) for both dyes (**SA15** and **SA16**) show that the aryl rings in position meso of the porphyrin, are twisted, respect to the macrocyclic Zn-porphyrin core with a dihedral angle around 61-63º. The phenyl groups bounded to the nitrogen atoms of the TPAs have a dihedral angle about 42º, thus triphenylamine units act as bulky groups difficulting the π-π stacked aggregation of the dyes. These characteristics improves the photoelectron injection efficiency from the dye to the TiO_2 electrode and, as a consequence, increases the conversion efficiency. Moreover, the thiophene fragments of dyes **SA15** and **SA16**, including the anchor group, lie in the same plane of the porphyrin core. In dye **SA16** the planarity between the macrocycle and the thiophene ring, bounded to the triple bond, is slightly greater ($\varphi \approx 5º$) than that in dye **SA15** ($\varphi \approx 8º$). This planarity between the porphyrin and the anchor group ensures effective electron coupling between both electroactive fragments. The bond distances in the conjugated systems based on thiophene are around 1.40 Å (both double and single), and this provides evidence of the push-pull character and the effective conjugation between the porphyrin and the anchor group.

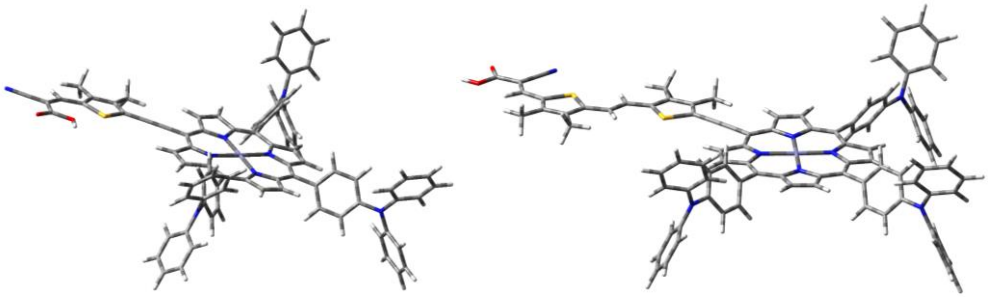

Figure 125. Structures of dyes **SA15** (left) and **SA16** (right) optimized by B3LYP/6-31G(d)

The molecular orbital analysis of the frontier orbitals of dyes **SA15**-**16** together with their energy levels are showed in Figure 126. The HOMO-LUMO energy levels and consequently HOMO-LUMO energy gap of dye **SA15** (1.99 eV) and **SA16** (1.88 eV) are similar. Nevertheless, these types of sensitizers have sufficient driving force for electron injection to TiO_2.

The electron distribution of both dyes (Figure 126), **SA15** and **SA16**, show that HOMO levels are mainly localized over the porphyrin macrocycle with some delocalization onto the *n*TVs fragments and the anchor group, whereas the HOMO -1 and HOMO -2 are confined on the triphenylamine addends.

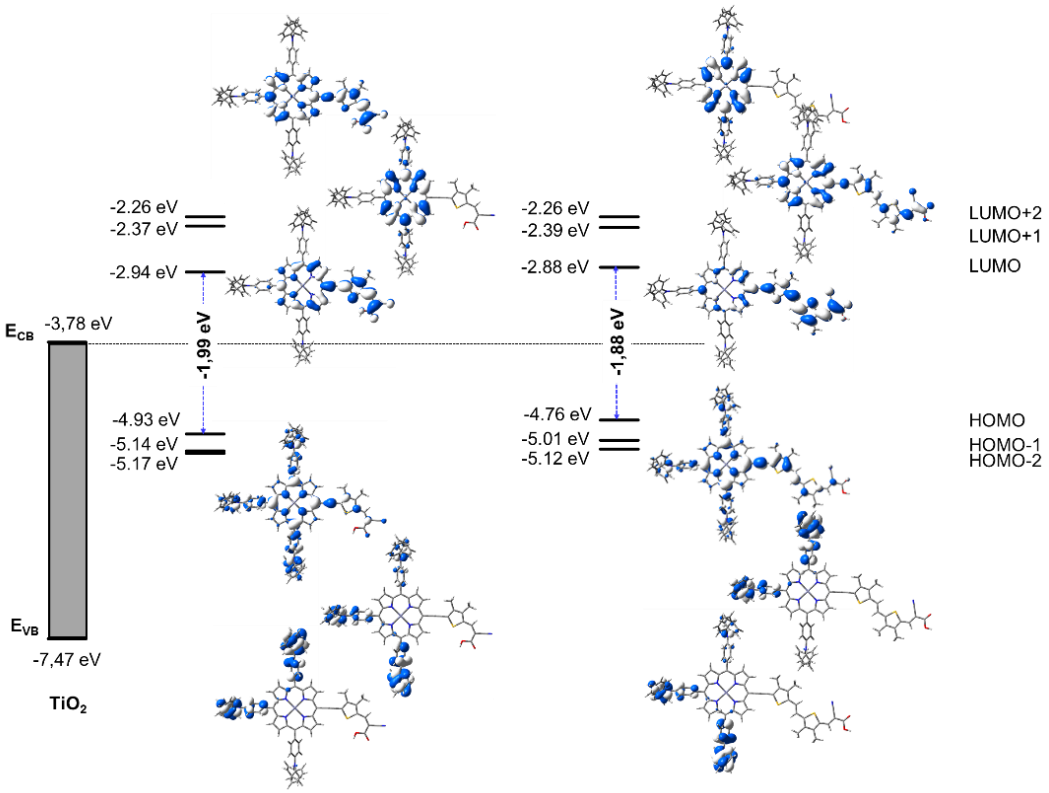

Figure 126. Energy levels of occupied and unoccupied MO and the electron density distribution of the corresponding frontier orbitals calculated using B3LYP/6-31G(d) for **SA15** (left) and **SA16** (right)

The first two LUMO orbitals are scattered along the porphyrin ring, the thiophene units and the anchor group. For dye **SA15**, the LUMO +1 is exclusively distributed on porphyrin ring while for the LUMO +1 of dye **SA16** there is an allocation of the electron density along all conjugated system, even on the anchor group. These facts confirm the data obtained on the electrochemical studies. The first oxidation potential (**SA15**: E^1_{ox} = 0.29 V; **SA16**: 0.26 V) corresponds to the formation of the porphyrin radical cation.[62]

2.6.5 Photovoltaic properties

Like **SA13-14**, DSSCs devices of **SA15-16** were fabricated in collaboration with Prof. Emilio Palomares at the Institute of Chemical Research of Catalonia (ICIQ). Two different sets of porphyrin sensitized solar cells were prepared depending on the electrolyte used. The electrolytes were denoted as LP1 and LP2 (see experimental section at the end of this chapter), and they differed only in the presence of 0.5 M *tert*-butyl pyridine (4-TBP) in LP1. The current vs. voltage (J-V curves) under 100 mW/cm^2 sun (1.5 AMG) simulated light are shown in Figure 127. **SA15** with the electrolyte LP1 shows the high PCE value (6%) as consequence of the high J_{SC} (12.3 mA cm^{-2}) and the good V_{OC} (0.684 V). As can be seen, there is a marked difference in the device open circuit voltage (V_{OC}) between the two porphyrin sensitized TiO_2 solar cells using the different elctrolytes (Table 22).

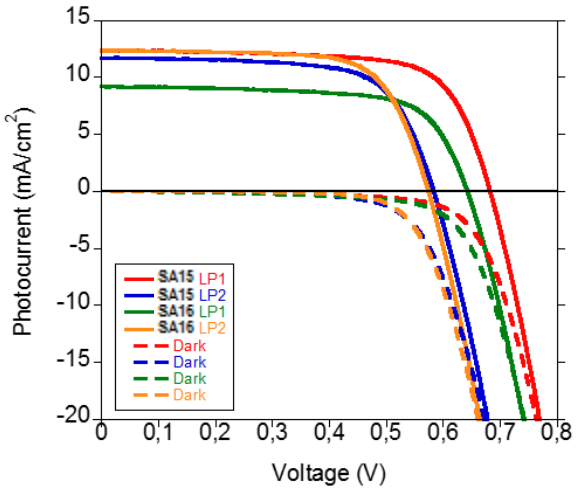

Figure 127. J-V measurements for the two different DSSCs (cell area 0.16 cm^2). Dashed lines correspond to measurements made in the dark

Table 22. Measured parameters for the optimized DSSCs LP1 and LP2

Dye	*Electrolyte*	*Sensitization (time/hours)*	*J_{SC} (mA cm^{-2})*	*V_{OC} (V)*	*FF (%)*	*PCE (%)*
SA15	LP1	3	12.3	0.684	71	6.0
SA15	LP2	3	11.7	0.584	68	4.7
SA16	LP1	1*	9.20	0.644	70	4.1
SA16	LP2	3	12.35	0.574	70	5.0

*Longer sensitization times led to lower photocurrent and worse device performance.

Subsequent measurements aimed at characterizing the solar cells were carried out to analyze the differences in photocurrent. The IPCE (Incident Photon to Current Efficiency) measurements (Figure 128) are in good agreement with the registered J_{SC} values under 1 sun (Table 22). As can be observed, in all measurements two bands can be clearly differentiated and these correspond to the Soret band of the porphyrins and the ICT band. Integration of the IPCE spectrum with respect to the 1.5 AM G solar spectrum gave the expected photocurrent of 13 mA/cm^2 for **SA15** on using electrolyte LP1 and 12.8 mA/cm^2 for **SA16** on using electrolyte LP2.

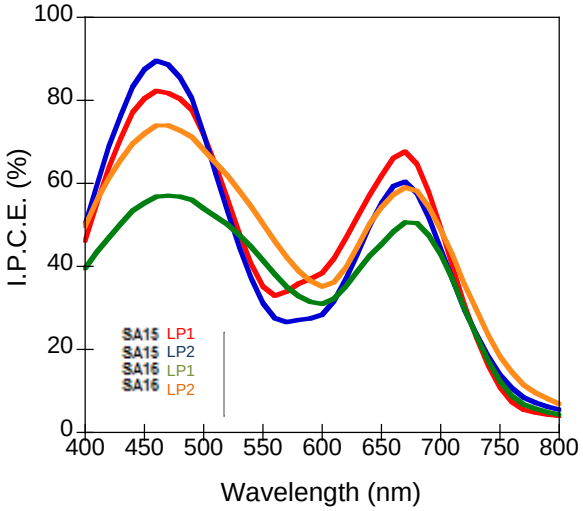

Figure 128. IPCE measurements for the optimized DSSCs

Photo-induced charge recombination studies were carried out to analyze the differences in V_{OC}. Firstly, the charge density (total charge upon different light irradiation) was measured using the photo-induced charge extraction method. The different exponential curves obtained with different light bias values (cell voltage upon different light illumination intensities) are shown in Figure 129. As one would expect, the use of 4-TBP with the LP1 electrolyte leads to a shift in the measured curves towards higher V_{OC}. The use of 4-TBP induces an up-shift in the conduction band (CB) edge of the TiO_2 and this leads to an increase in cell voltage. Interestingly, for porphyrin **SA15** the shift in the CB edge of the TiO_2 did not lead to a concomitant decrease in the cell J_{SC} value as a consequence of the more unfavourable electron transfer from the dye excited state to the TiO_2 CB, which is the case for porphyrin **SA16**. This result led to consider that the presence of 4-TBP, in combination with porphyrin **SA15**, results in a better charge transfer from the dye excited state due to a lower concentration of **SA16** molecular aggregates.

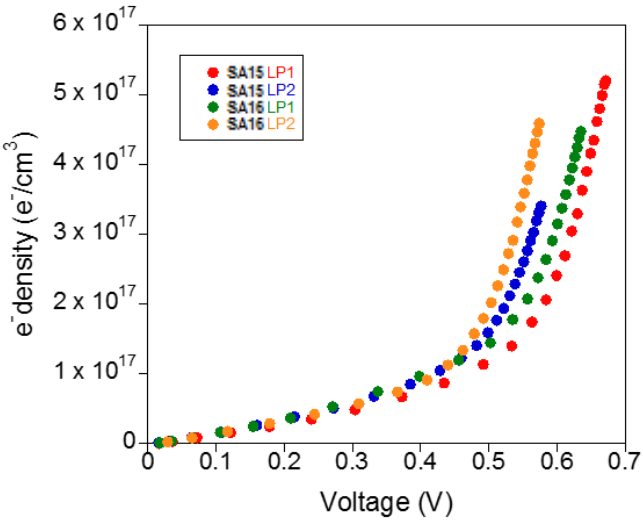

Figure 129. Photo-induced charge extraction measurements for all DSSCs (cell area 0.16 cm^2)

Measurement of the electron lifetimes for the different set of solar cells (Figure 130) shows that for solar cells sensitized with **SA15** the factor that has the most marked effect on solar cell performance is the use of 4-TBP in the electrolyte. It is noticeable that the presence of 4-TBP in the LP1 electrolyte leads to slower charge recombination kinetics between the electrons at the TiO_2 and the oxidized electrolyte when compared to the solar cells based on **SA15** with the electrolyte LP2. In contrast, for porphyrin **SA16** the presence of 4-TBP does not have an influence on the electron lifetime and in both cases a similar value was obtained. Thus, the higher V_{OC} obtained for DSSCs sensitized with **SA15** and the electrolyte LP1 is due to the up-shift of the TiO_2 CB edge and not to slower charge combination kinetics between the photo-injected electrons on the TiO_2 and the oxidized electrolyte.

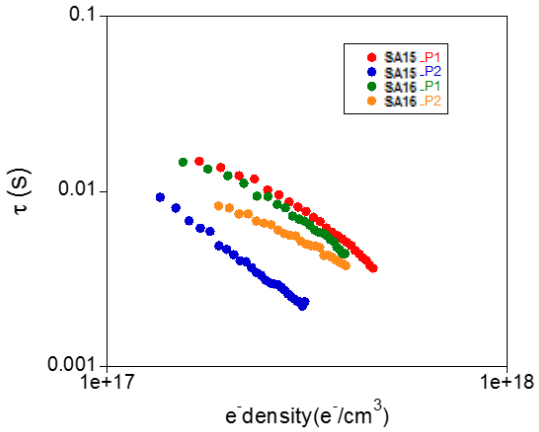

Figure 130. Electron lifetimes measured using TPV *vs* device charge density at different light bias for all different DSSCs

2.7 Dyes SA17 and SA18

2.7.1 Synthesis and characterization of SA17 and SA18

The synthesis of dyes **SA17** and **SA18** was prepared according to Scheme 15, starting from precursor aldehydes **A8** and **A9** in dryed acetone was added slowly $NaClO_2$ (3.0 eq), then was added drop to drop a solution of NH_2SO_3H in water and the mixture was stirred during 4 hours at room temperature. The reaction was quenched with a saturated solution of hydrochloride acid, stirring for 1 hour and extracted with CH_2Cl_2. The combined organic phases were dried over anhydrous $MgSO_4$ and filtered, then the solvent was removed by rotary evaporation. The product was purified by column chromatography (silica gel, $CHCl_3$:MeOH 95:5), dyes **SA17** and **SA18** in 53% and 50% yields, respectively.

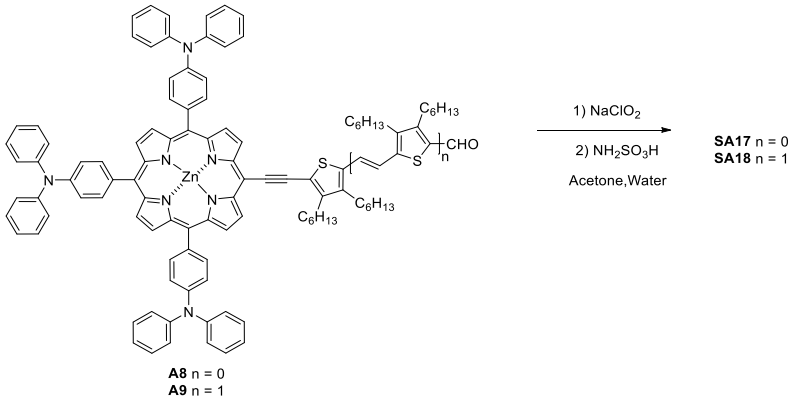

Scheme 15. Synthetic route to dyes **SA17** and **SA18**

The ^{1}H-NMR spectra of **SA17** and **SA18** showed the signals at 9.74, 9.01, 8.95 ppm and 9.76, 9.06, 8.95 ppm respectively, corresponding to the protons of the porphyrin core, (see Figure 131).

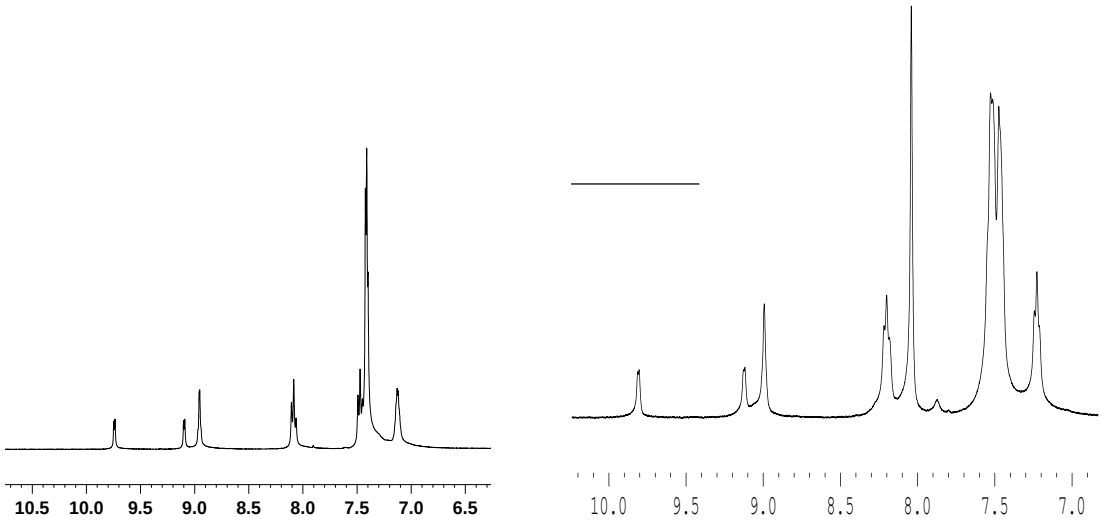

Figure 131. 7 to 10 ppm ^{1}H-NMR spectra (400 MHz, THF-D_8) of compound **SA17** and **SA18**

Finally, **SA17-18** mass spectra showed a molecular ion peak (m/z) at 1419.51 (M^+) and 1515.40 (M^+) respectively, according to the calculated molecular mass (see the experimental section, Figure 249 and Figure 250).

Thermal analysis plays an important role in the study of dyes, therefore the resistance to heat at elevated temperature is one of the main properties required. Thermal stabilities of **SA17-18** were evaluated by TGA employing the same conditions that in **SA13-14**. The weight losses show the decomposition temperatures (Td) at 362°C for **SA17** and at 359°C for **SA18**, therefore both dyes can be used for solar cells applications (Figure 132).

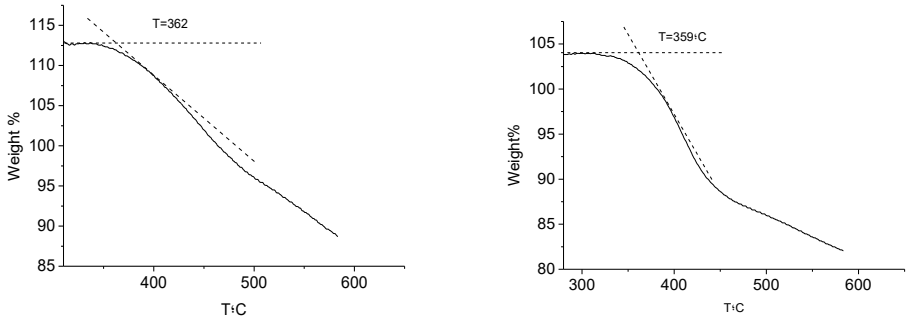

Figure 132. Thermogravimetric analysis of **SA17** (left) and **SA18** (right)

2.7.2 Optical properties

The UV-Vis absorption spectra of **SA17-18** in THF exhibit the typical pattern of zinc porphyrin spectrum with an intense Soret band and two Q bands (see Figure 133 and Table 4).

UV-Vis spectrum of **SA17** in THF showed the Soret band at 456 nm (log ε = 5.59) and Q bands at 584 nm (log ε = 4.59) and at 640 nm (log ε =4.80). Under similar concentration conditions that **SA17**, the UV-Vis spectrum of **SA18** shows a Soret band at 472nm (log ε = 5.32), this band has a bathochromic shift of 17 nm in comparison to **SA17**, as consequence of the extension in the conjugation on the bridge. Additionally Q bands are also observed 582 (log ε = 4.87) and 652 (log ε = 4.64). Fluorescence emission at 655 nm for **SA17** (λ_{exc}= 456 nm) and at 668 nm for **SA18** (λ_{exc}= 474 nm) were observed.

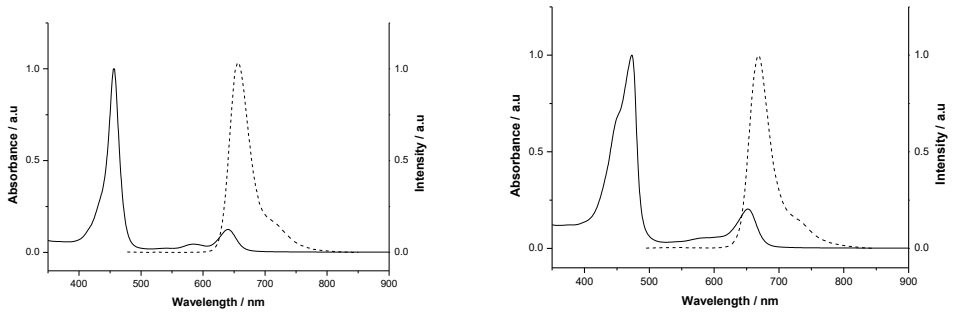

Figure 133. Normalized absorption spectra (solid line) and fluorescence emission (dash line) of **SA17** (right, λ_{exc}= 456 nm) and **SA18** (left,(dash line, λ_{exc}= 474 nm) in THF solution (10^{-6} M)

Table 23. UV-Vis Absorption, Fluorescence Emission[a] and OSWV[b] data for compounds **SA17** and **SA18**

Dye	λ_{max} / nm	log ε	λ_{em} /nm	E^1_{ox} /V	E^2_{ox}/V	E^1_{red} /V	E_{HOMO} /eV[c]	E_{LUMO} /eV[d]	E_g /eV[e]
SA17	640	4.80	655	0.26	0.49	-1.72	-5.36	-3.38	1.98
	584	4.59							
	456	5.59							
SA18	652	4.64	668	0.21	0.53	-1.43	-5.31	-3.67	1.64
	582	4.19							
	473	5.32							

[a] **SA17**: 8.43 x 10^{-6} M, THF; **SA18**: 7.98 x 10^{-6} M, THF; [b] [10^{-3} M] in THF versus Fc/Fc+, glassy carbon, Pt counter electrode, 20 ºC, 0.1 M Bu_4NClO_4, scan rate = 100 mV s^{-1}; [c] Calculated using equation E_{HOMO} (*vs*. vacuum) = -5.1 - E^1_{ox} (vs. Fc/Fc^+) in eV;[58] [d] E_{LUMO} was calculated using E^1_{red}. [e] E_{HOMO}-E_{LUMO}

2.7.3 Electrochemical properties

Electrochemical techniques were employed to measure the oxidation and reduction of the dyes **SA17-18** and before their HOMO and LUMO orbitals were calculated (Table 23, Figure 251, Figure 134 and Figure 135).

The square wave voltammetry in THF of **SA17** and **SA18** show the first oxidation peak at 0.23 and 0.26 V respectively (vs Fc/Fc^+), assigned to the porphyrin core. The second oxidation processes are attributed to the thiophene linker units and the third oxidation corresponded to the triphenylamine moieties. Therefore from the oxidation potentials were deduced E_{HOMO} values of -5.36 eV and -5.31 eV for **SA17** and **SA18** respectively, indicating that the regeneration is energetically feasible by I/I_3^- (E_{redox} = -4.75 eV).

The square wave voltammetry of **SA17-18** show the first reduction potentials at -1.72 V and -1.43 V respectively. Moreover E_{LUMO} values of -3.38 for **SA17** and -3.67 for **SA18** indicate that efficient electron injection into the TiO_2 conduction band (E_{TiO2} = -4.00 eV) is energetically possible as well.

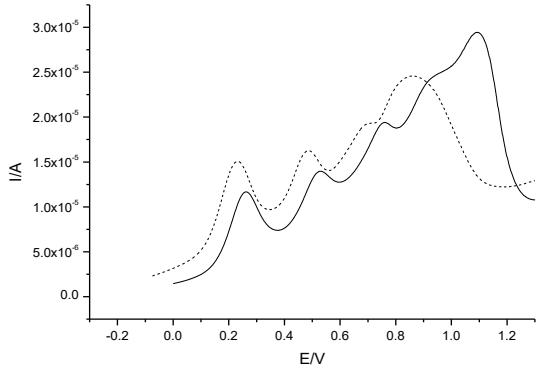

Figure 134. Square Ware Voltammetry plot (cathodic window) of compounds **SA17** (solid line) and **SA18** (dash line) (referred to Fc/Fc^+)

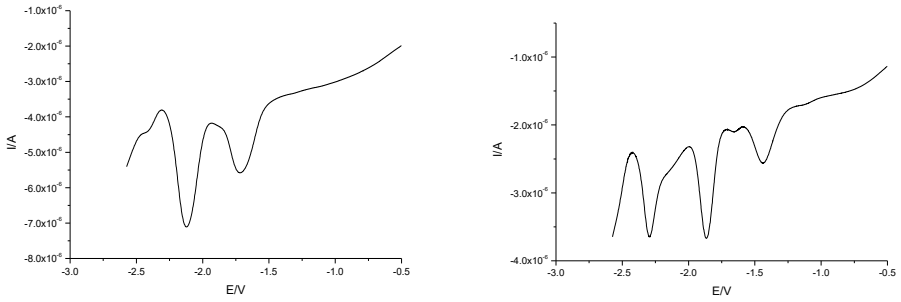

Figure 135. Square Ware Voltammetry plot (anodic window) of compounds **SA17** (left) and **SA18** (right) (referred to Fc/Fc^+)

2.7.4 Photovoltaic properties

DSSCs devices were fabricated in collaboration with Prof. Emilio Palomares at the Institute of Chemical Research of Catalonia (ICIQ). Two different sets of porphyrin sensitized solar cells were prepared changing the sensitized time: overnight (ON) and 4 hours (4h).

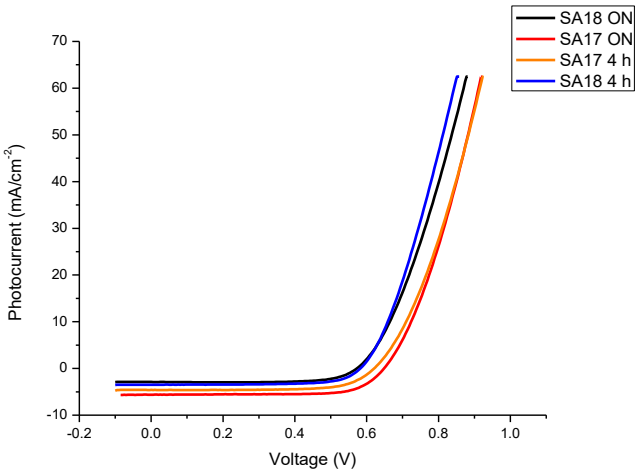

Figure 136. J-V of DSSCs **SA17-18**

The sensitized overnight in both dyes allow higher J_{SC}. **SA17** ON shows similar FF (~70%) and V_{OC} (~0.6V) that **SA13**, moreover J_{SC} of **SA17** ON is lower (5.6 mA cm^{-2}) that J_{SC} of **SA13** (12.3 mA cm^{-2}) and this parameter influence in the PCE affording 6% for **SA13** and a lower 2.6% for **SA17** (Table 24). The devices values are not favorable, probably as consequence of the alkyl groups near to the anchor group, these long chains do not allow the anchorage of the molecules, also it has lower surface with TiO_2, and therefore less voltage and photocurrent, due to the tri-iodide electrolyte reaching the TiO_2 surface more easily.

Table 24. Measured parameters for optimized DSSCs

*Dye**	*V_{OC} (V)*	*J_{SC}(mA cm^{-2})*	*FF (%)*	*PCE (%)*
SA17 (ON)	0.648	5.61	74	2.67
SA17 (4 h)	0.623	4.59	70	2.01
SA18 (ON)	0.572	2.88	72	1.19
SA18 (4 h)	0.583	3.47	70	1.43

* All devices were fabricated with **LP1** electrolyte, (the same that was used in **SA13-14**)

2.8 Chapter 2. Summary

Six new dyes porphyrins with structure A_3B were synthesized and characterized by ^{1}H and ^{13}C-NMR, FT-IR spectroscopies, MALDI-MS spectrometry and TGA. Furthermore, absorption spectra of all the dyes showed the typical porphyrin pattern, with an intense Soret band and Q bands. In order to gain insight the oxidation and reduction properties, electrochemical values were measured and HOMOs and LUMOs were determined. Additionally the performance of these dyes in DSSCs was measured.

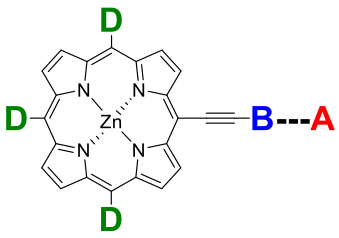

D

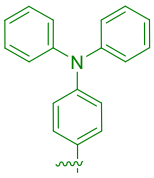

triphenylamine

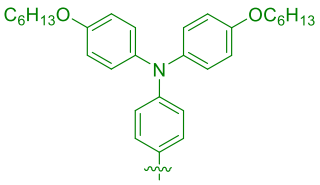

4-(hexyloxy)-N-(4-hexyloxy phenyl)-N-phenylaniline

B

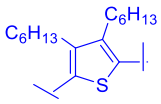

3,4-dihexylthiophene

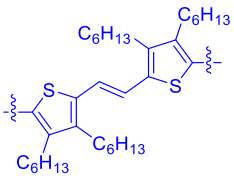

(E)-1,2-bis(3,4-dihexylthiophen-2-yl)ethylene)

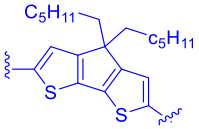

4,4-dihexyl-4H-cyclopenta[2,1-b:3,4-b']dithiophene

Benzene

A

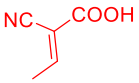

cyanoacetic acid

carboxylic acid

Table 25. Donor, bridge and acceptor moieties of **SA13-18** porphyrins

D	B	A	Molecules
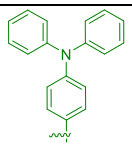		—COOH	**SA13**
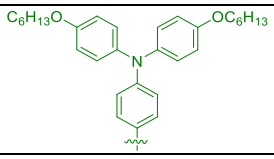		—COOH	**SA14**
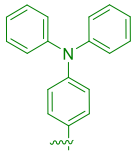	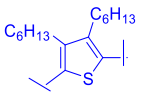	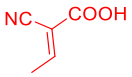	**SA15**
	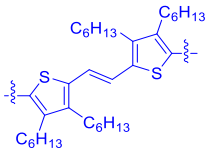	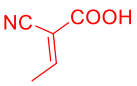	**SA16**
	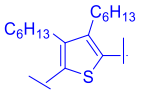	—COOH	**SA17**
	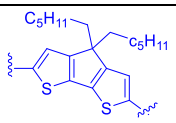	—COOH	**SA18**

In order to analyze the behavior of porphyrins with different **D** donor moieties and carboxylic acid as anchoring group; the absorption spectra, electrochemical properties and photovoltaic performance of porphyrin with triphenylamine moieties (**SA13**) and porphyrin with 4-(hexyloxy)-N-(4-hexyloxy phenyl)-N-phenylaniline moieties (**SA14**) were described in section 2.5. Dyes **SA13-14** were measured in DSSCs devices employing I^-/I_3^- and $Co(II)(pheno)_3/Co(III)(pheno)_3$ electrolytes. Optimized sensitization times were found to depend on the electrolyte used with devices based on I^-/I_3^- showing better efficiencies with shorter sensitization times (1.5 hours) while those based on $Co(II)(pheno)_3/Co(III)(pheno)_3$ showed better efficiencies with longer sensitization times (6 hours). . The absorption spectra indicate that there is roughly twice as much dye loaded onto the TiO_2 film sensitized for 6 hours. The experimental V_{OC} for both devices was similar (0.62 V), and FF was similar as well (67% for **SA13** and 70% for **SA14)**. Nevertheless, J_{SC} was higher for those porphyrins with triphenylamine moieties, achieving a higher PCE.

The general trending of different **B** bridges in porphyrins carrying triphenylamine groups was studied, employing the same **D** moiety and **A** acceptor (see Table *26*). The absorption spectra

of **SA17-18** and **SA15-16** were analyzed (See Figure 137). The spectra of triphenylamine substituted porphyrin with arylcarboxylic acid and 4,4-dihexyl-4H-cyclopenta[2,1-b:3,4-b']dithiophene as bridge (**SA18**) exhibited a broader absorption than that of triphenylamine porphyrin with arylcarboxylic acid and 3,4-dihexylthiophene as bridge (**SA17**). The Soret band of **SA18** showed a red-shifted of 15 nm respecting to that of **SA18**. In addition, the spectra of **SA15-16** showed a broader due to the higher conjugation.

Table 26. Synthesized Porphyrins with different **B** bridges and same **D** donor and **A** acceptor.

D	B	A	Molecules
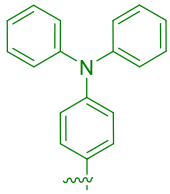	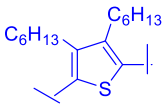		**SA17**
	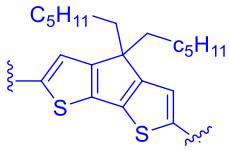		**SA18**
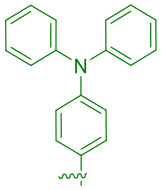	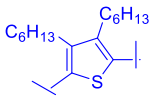	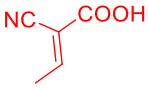	**SA15**
	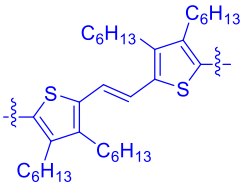	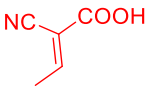	**SA16**

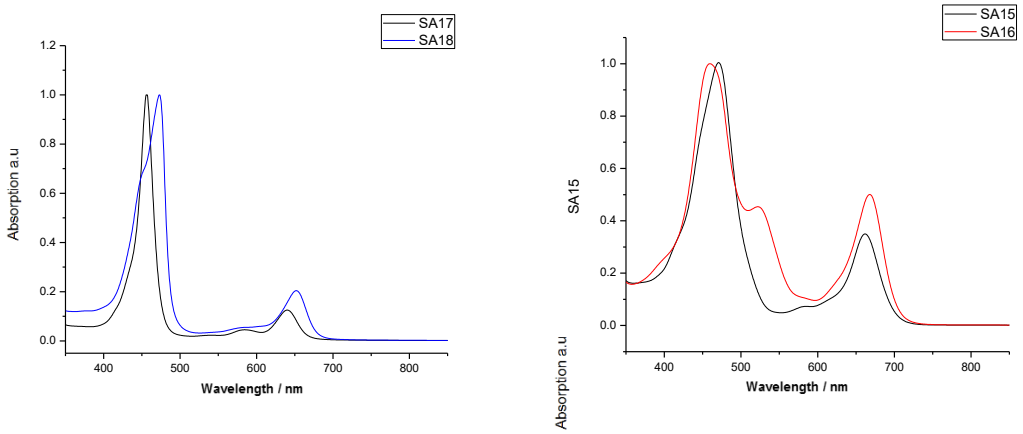

Figure *137.* Normalized spectra of triphenylamine porphyrins with carboxylic acid and different bridges (left) and triphenylamine porphyrins with cyanoacrylic acid and different bridges (right). Bridges: 3,4-dihexylthiophene (black), 4,4-dihexyl-4H-cyclopenta[2,1-b:3,4-b′]dithiophene (blue) and (E)-1,2-bis(3,4-dihexylthiophen-2-yl)ethylene (red)

HOMO levels were calculated from the data afforded by the electrochemical results; those porphyrin having triphenylamine, 3,4-dihexylthiophene as bridge and cyanoacrylic acid as acceptor, **SA15,** showed a lower HOMO than that with cyanoacrylic acid as acceptor and E)-1,2-bis(3,4-dihexylthiophen-2-yl)ethylene as bridge, **SA16**, as was expected. Additionally triphenylamine substituted porphyrin with benzoic acid as terminal group, **SA13,** showed a lower HOMO than triphenylamine porphyrin with carboxylic acid and 3,4-dihexylthiophene as bridge **SA17**, followed by triphenylamine porphyrin with 4,4-dihexyl-4H-cyclopenta[2,1-b:3,4-b′]dithiophene **SA18** (see Table 16). Consequently, the higher voltage should be expected for **SA15** and the lower for **SA18** as experimental data confirms (*vide infra*,Table 3).

Table 27. HOMO levels and photovoltaic parameters of triphenylamine functionalized porphyrins with different bridges and acceptor groups (**SA 15-18**).

Molecule	*HOMO**	*V_{OC} (V)*	*J_{SC} (mA cm^{-2})*	*FF (%)*	*PCE [Highest](%)*
SA15[a]	-5.50	0.684	12.30	71	6.0
SA16[b]	-5.36	0.574	12.35	70	5.0
SA13[c]	-5.43	0.624	10.09	67	4.19
SA17[a]	-5.36	0.648	5.61	74	2.67
SA18[d]	-5.31	0.572	2.88	72	1.19

*calculated by $E_{HOMO=}$ –5.1 eV- $E^{1}_{ox.}$ Bridges: [a] 3,4-dihexylthiophene [b] *E)*-1,2-bis(3,4-dihexylthiophen-2-yl)ethylene [c] benzene, [d] 4,4-dihexyl-4H-cyclopenta[2,1-b:3,4-b′]dithiophene

The photovoltaic parameters were measured. However, the devices were tested in different conditions, and this comparison is only a general reference to study the behavior of triphenylamine based porphyrins with different **B** bridges. Experimental V_{OC} of triphenylamine-

porphyrin with 3,4-dihexylthiophene as bridge **SA15** showed a higher value than triphenylamine porphyrin with *E)*-1,2-bis(3,4-dihexylthiophen-2-yl)ethane **SA16**, as was expected. In the case of triphenylamine porphyrins with carboxylic acid and different bridges, **SA18** with 4,4-dihexyl-4H-cyclopenta[2,1-b:3,4-b′]dithiophene as bridge showed the lowest V_{OC} of these kind of porphyrins, as was expected. Nevertheless, **SA13** and **SA17** showed a different behavior, and V_{OC} for porphyrin **SA13** with benzene as bridge (0.62 V) was lower than for porphyrin **SA17** with 3,4-dihexylthiophene as bridge (0.65 V).

J_{SC} showed similar values (~12.3 $mAcm^{-1}$) for those porphyrins with cyanoacrylic acid and 3,4-dihexylthiophene as bridge **SA15** and *E)*-1,2-bis(3,4-dihexylthiophen-2-yl)ethylene as bridge **SA16**, specific details were described in the section 2.6.5. For porphyrins with arylcarboxylic acid, triphenylamine porphyrin with benzoic acid. **SA13.** showed a higher J_{SC} than porphyrin with 3,4-dihexylthiophene4,4-dihexyl-4H-cyclopenta[2,1-b:3,4-b′]dithiophene as bridge **SA18**. Probably, porphyrin with arylbenzoic acid showed a better anchoring with the TiO_2 and therefore the alkyl groups near to the carboxylic acid interrupt the anchoring achieving a worse current. Then, FF showed similar values for all the porphyrins (between 67% and 72 %) indicating a good morphology of the devices. Finally, a remarkable PCE of 6.0 % was achieved with **SA15**.

.

2.9 Conclusions

I. Six new dyes based on porphyrin with structure D-π-A were designed, synthesized and properly characterized by spectroscopic techniques.

II. The performance of all new porphyrin based systems in DSSCs devices was evaluated.

III. Devices with triphenylamineporphyrin, 3,4-dihexylthiophene as bridge and cyanoacrylic acid as anchoring group, **SA15**, exhibited 0.68 V_{OC} and 12.30 mA cm^{-2} J_{SC} achieving the higher PCE (6%), in comparison to the other devices.

IV. Triphenylamineporphyrin devices with carboxylic acid as anchoring group achieved better J_{SC} (10.09 mA cm^{-2}) with benzene as bridge, **SA13,** than devices with 3,4-dihexylthiophene as bridge, **SA15,** (5.61 mA cm^{-2}) and porphyrins with 4,4-dihexyl-4H-cyclopenta[2,1-b:3,4-b′]dithiophene as bridge **SA18** (2.88 mA cm^{-2}).

V. Triphenylamineporphyrin devices with cianoacrylic acid or carboxylic acid as anchoring group and 3,4-dihexylthiophene as bridge, showed a higher V_{OC} (0.68 V and 0.64 V, respectively) in comparison to the other devices with values between 0.57 and 0.57 V.

VI. FF of all prepared devices showed excellent values, between 67 and 72%.

2.10 Experimental details of chapter 2

2.10.1 General Experimental Details of chapter 2

Materials

Synthetic procedures were carried out under inert argon atmosphere, in dry solvent unless otherwise noted. All reagents and solvents were reagent grade and were used without further purification. Chromatographic purifications were performed using silica gel 60 SDS (particle size 0.040-0.063 mm).

Instruments

Analytical thin-layer chromatography was performed using Merck TLC silica gel 60 F254. ^{1}H-NMR spectra were obtained on Bruker AV-400 (400 MHz) spectrometer. Chemical shifts are reported in parts per million (ppm) relative to the solvent residual peak ($CDCl_3$, 7.27 ppm; $THF_{d8,}$ 1.73 ppm, 3.58 ppm). ^{13}C-NMR chemical shifts are reported relative to the solvent residual peak ($CDCl_3$, 77.00 ppm, THF-$d_{8,}$ 67.57 ppm, 25.37 ppm). UV-Vis measurements were carried out on a Shimadzu UV 3600 spectrophotometer. For extinction coefficient determination, solutions of different concentration were prepared in CH_2Cl_2, HPLC grade or THF HPLC grade, with absorption between 0.1-1 of absorbance using a 1 cm UV cuvette. The emission measurements were carried out on Cary Eclipse fluorescence spectrophotometer. Mass spectra (MALDI-TOF) were recorded on a VOYAGER DE^{TM} STR mass spectrometer using dithranol as matrix. The thermal stability was evaluated by TGA on Mettler Toledo TGA/DSC Start^{e} System under nitrogen, with a heating rate of 10 ºC/min. Heating of crystalline samples leads to melting of the solids, but no recrystallization was observed.

2.10.2 Experimental details of the devices of DSSCs

SA13 and SA14

Highly transparent thin films of 4-8 µm were used for L-TAS measurements and UV-Vis absorption studies. Efficient DSSCs devices were prepared using 4 µm or 8 µm thick films consisting of 20 nm TiO_2 nanoparticles (Dyesol paste) for $Co(II)(pheno)_3/Co(III)(pheno)_3$ and I^-/I_3^- electrolytes respectively.

Scatter layer of 4 µm of 400 nm TiO_2 particles (Dyesol paste) was then deposited on these films. Prior to the deposition of the TiO_2 paste the conducting glass substrates were immersed in a solution of $TiCl_4$ (40 mM) for 30 min and then dried. The TiO_2 nanoparticle paste was deposited onto a conducting glass substrate (NSG glass with 8 Ω cm^{-2} resistance) using the screen printing technique. The TiO_2 electrodes were gradually heated under airflow at 325ºC for 5 min, 375ºC for 5 min, 450ºC for 15 min and 500ºC for 15 min. The heated TiO_2 electrodes were immersed again in a solution of $TiCl_4$ (40 mM) at 70ºC for 30 min and then washed with

ethanol. The electrodes were heated again at 500ºC for 30 min and cooled before sensitization. In order to reduce scattered light from the edge of the glass electrodes of the dyed TiO_2 layer, a light shading mask was used on the DSSCs, so the active area of DSSCs was fixed to 0.16 cm^2. The counter electrode was made by spreading a 5 mM solution of H_2PtCl_6 in isopropyl alcohol onto a conducting glass substrate (TEC15, Pilkington) with a small hole to allow the introduction of the liquid electrolyte using vacuum, followed by heating at 390ºC for 15 min. Dye solutions of **SA13** and **SA14** at concentrations of 0.2 mM in chlorobenzene were prepared and films immersed for different periods of time at r.t. The sensitized electrodes were washed with chlorobenzene and dried under air. Finally, the working and counter electrodes were sandwiched together using a thin thermoplastic (Surlyn) frame that melts at 100ºC. The iodide/tri-iodide electrolyte used consisted of 0.6 M 1-butyl-3-methylimidazolium iodide (BMII), 0.1 M lithium iodide, 0.05 M iodine and 0.5 M 4-*tert*-butylpyridine in a 1:1 mixture of acetonitrile/valeronitrile. The cobalt electrolyte consisted of 0.2 M tris(1,10-phenanthroline)cobalt(II)$(TFSI)_2$ 0.02 M tris(1,10-phenanthroline)cobalt(III)$(TFSI)_3$, 0.1 M lithium perchlorate and 0.5 M 4-*tert*-butylpyridine in a 85:15 mixture of acetonitrile/valeronitrile. The cobalt complexes were synthesized as reported elsewhere.

Reference devices containing **YD2-o-C8** dye were made by sensitizing overnight films consisting of 8 µm transparent and 4 µm scatter TiO_2 in 0.3 mM ethanol solutions containing 0.3 mM chenoxydecholic acid. The electrolyte consisted of 1 M 1-butyl-3-methylimidazolium iodide (BMII), 0.05 M lithium iodide, 0.03 M iodine, 0.1 M GuNCS and 0.5 M 4-*tert*-butylpyridine in 85:15 mixture of acetonitrile/valeronitrile.

The IV characteristics of cells were measured using a Sun 2000 Solar Simulator (150 W, ABET Technologies). The illumination intensity was measured to be 100 mW/m^2 with a calibrated silicon photodiode. The appropriate filters were utilized to faithfully simulate the AM 1.5G spectrum. The applied potential and cell current were measured with a Keithley 2400 digital source meter. The IPCE (Incident Photon to Current conversion Efficiency) was measured using a homemade set up consisting of a 150 W Oriel Xenon lamp, a motorized monochromator and a Keithley 2400 digital source meter.[65]

SA15 and SA18

The working electrodes for the best devices were made using 8 µm thick transparent mesoporous TiO_2 and 4 µm thick TiO_2 layer, so-called 8+4, deposited onto fluorine-doped tin-oxide glass (FTO, Pilkington Glass Inc., with 15 Ohms/square sheet resistance). The counter electrode was fabricated using the same FTO with a thermalized Pt layer from H_2PtCl_6 (8% in water). The subsequent steps to prepare the complete devices, as well as the photocurrent vs voltage (IV curves).

Photo-induced charge extraction was carried out as described in **SA13**. In brief, white light from a series of LEDs was used as the light source. When the LEDs were turned off, the cell

was immediately short-circuited and the charge was extracted, thus allowing the electron density in the cells to be calculated. By changing the intensity of the LEDs, the electron density can be estimated as a function of cell voltage. In photo-induced transient photovoltage (TPV) measurements, in addition to the white light applied by the LEDs, a diode pulse (660 nm, 10 mW) was applied to the sample to induce a change of 2–3 mV within the cell. The resulting photovoltage decay transients were collected and the τ values were determined by fitting the data to the equation $\exp(-t/\tau)$.

2.10.3 Synthetic procedure and experimental details

2.10.3.1 Experimental details in the synthesis of SA13 and SA14

General procedure for P4 and P5

To a solution of corresponding (diphenylamino)benzaldehyde (3 eq), pyrrol (4 eq) and 3-(trimethylsilyl)propynal (1 eq) in $CHCl_3$ (100 mL/mmol), under argon and degassed, was added $BF_3(OEt)_2$ (0.9 eq). The mixture was allowed to stir under argon for 3 hours. Then, DDQ (2.8 eq) was added and stirring for one hour; after addition of Et_3N (2 mL) for 30 min, the solvent was removed by rotary evaporation and the product was purified by column chromatography (silica gel, Hex:$CHCl_3$, 1:1).

Synthesis of [10,15,20-*tri*(*N*,*N*-diphenylaniline)-5-ethynyltrimethylsilane] porphyrin (P4)

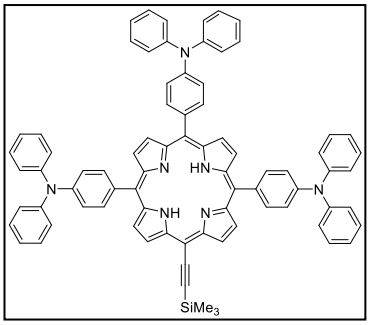

A solution of (diphenylamino)benzaldehyde (11.0 mmol, 3.00 g), pyrrol (14.7 mmol, 1.02 mg) and 3-(trimethylsilyl)propiolaldehyde (3.7 mmol, 0.547 mL), reacted according to the general procedure, affording the product was obtained as a green solid (0.51 mmol, 600 mg, 14% yield). ^{1}H-NMR (400 MHz, $CDCl_3$) δ/ppm: 9.69 (d, *J* = 4.7 Hz, 2H,), 9.05 (d, *J* = 4.7 Hz, 2H), 8.96 (d, *J* = 4.7 Hz, 2H), 8.93 (d, *J* = 4.7 Hz, 2H), 8.07 (dd, *J* = 8.5, 6.4 Hz, 6H), 7.49 (d, *J* = 8.5 Hz, 6H), 7.45-7.42 (t, *J* = 7.0 Hz, 24H), 7.20-7.15 (m, 6H), 0.64 (s, 9H), -2.31 (s, 2H). ^{13}C-NMR (100 MHz, $CDCl_3$) δ/ppm: 147.77, 147.74, 147.59, 135.68, 135.59, 135.52, 135.34, 129.51, 129.22, 124.90, 123.33, 122.12, 121.32, 121.17, 120.92, 107.16, 101.63, 98.57, 0.35. MS (*m/z*) (MALDI-TOF): calculated for $C_{79}H_{61}N_7Si$: 1135.48; found: 1135.50 (M+). FT-IR ν/cm^{-1}: 3315, 3058, 3030, 2954, 2137, 1595, 1492, 1328, 1313, 1270, 848, 798, 749, 695.

Synthesis of [10,15,20-*tri*(*N*,*N*-(*bis*(4-hexyloxy)phenyl)aniline)-5-ethynyltrimethylsilane]porphyrin (P5)

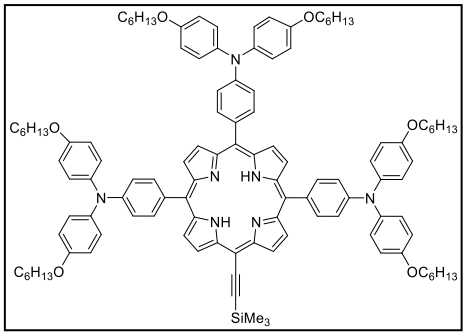

From 4-(*N*,*N*-di-4-(hexyloxy)phenylamino) benzaldehyde (6.3 mmol, 3.00 g, 3 eq),[66] pyrrol (8.5 mmol, 0.6 mL, 4 eq) and (trimethylsilyl)propiolaldehyde (2.1 mmol, 0.31 mL, 1 eq) reacted according to the general procedure affording the product **P5S** as yellow solid (0.23 mmol, 397 mg, 11% yield). ^{1}H-NMR (400 MHz, $CDCl_3$) δ/ppm: 9.65 (d, *J* = 4.7 Hz, 2H), 9.04 (d, *J* = 4.7 Hz, 2H), 8.94 (d, *J* = 4.7 Hz, 2H), 8.92 (d, *J* = 4.7 Hz, 2H), 7.98 (dd, *J* = 8.6, 6.1 Hz, 6H), 7.39-7.34 (m, 12H), 7.30 (t, *J* = 8.6 Hz, 6H), 7.00-6.95 (m, 12H), 4.00 (dd, *J* = 12.6, 6.6 Hz, 12H), 1.87-

1.78 (m, 12H), 1.54-1.46 (m, 12H), 1.41-1.35 (m, 24H), 0.96-0.92 (s, 18H), 0.63 (s, 9H), -2.27 (s, 2H). ^{13}C-NMR (100 MHz, $CDCl_3$) δ/ppm: 155.73, 148.47, 140.65, 140.61, 135.52, 133.55, 133.18, 127.12, 122.60, 117.95, 117.76, 115.40, 107.36, 101.28, 98.12, 68.25, 31.62, 29.33, 25.78, 22.63, 14.07, 0.40. MS (*m/z*) (MALDI-TOF): calculated for $C_{115}H_{133}N_7O_6Si$: 1736.01; found: 1736.00 (M+). FT-IR ν/cm^{-1}: 3314, 2951, 2927, 2857, 2137, 1599, 1504, 1469, 1239.

General procedure for porphyrin metalation

To a solution of corresponding porphyrin **P4** or **P5** (eq) in $CHCl_3$ (84 mL/mmol), under argon, $Zn(OAc)_2$ x 2 H_2O (5 eq) in MeOH (2.5 mL/mmol) was added. The mixture was stirred at room temperature overnight. The reaction was quenched with water and the mixture extracted with $CHCl_3$ (3 x 50 mL). The combined organic extracts were washed with H_2O and dried over anhydrous $MgSO_4$. The solvent was removed under reduced pressure and the product was purified by column chromatography (silica gel, Hex:$CHCl_3$, 1:1).

Synthesis of [10,15,20-*tri*-(*N*,*N*-diphenylaniline)-5-ethynyltrimethylsilane] porphinato zinc (II) (P4S)

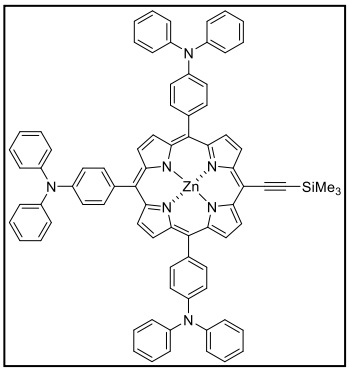

From **P4** (0.22 mmol, 250 mg), reacted according to the general procedure, affording the product **P4S** as a green solid (0.21 mmol, 251mg, 95% yield). ^{1}H-NMR (400 MHz, $CDCl_3$) δ/ppm: 9.79 (d, *J* = 4.7 Hz, 2H), 9.14 (d, *J* = 4.7 Hz, 2H), 9.07 (d, *J* = 4.7 Hz, 2H), 9.05 (d, *J* = 4.7 Hz, 2H), 8.10-8.05 (m, 6H), 7.49 (t, *J* = 8.4 Hz, 6H), 7.46-7.43 (t, 24H), 7.19-7.14 (m, 6H), 0.66 (s, 9H). ^{13}C-NMR (100 MHz, $CDCl_3$) δ/ppm: 150.04, 149.94, 147.85, 147.82, 147.36, 136.32, 135.40, 135.32, 132.23, 131.79, 130.93, 129.48, 124.81, 123.21, 122.93, 121.82, 121.36, 121.26, 107.66, 101.12, 99.37, 0.41. MS (*m/z*) (MALDI-TOF): calculated for $C_{79}H_{59}N_7SiZn$: 1197.39; found: 1197.60 (M+). FT-IR ν/cm^{-1}: 3060, 3030, 2955, 1924, 2853, 2138, 1589, 1490, 1329, 1315, 1280, 996, 842, 699.

Synthesis of [10,15,20-*tri*-(*N*,*N*-(*bis*(4-hexyloxy)phenyl)aniline)-5-ethynyltrimethylsilane]porphinato zinc (II) (P5S)

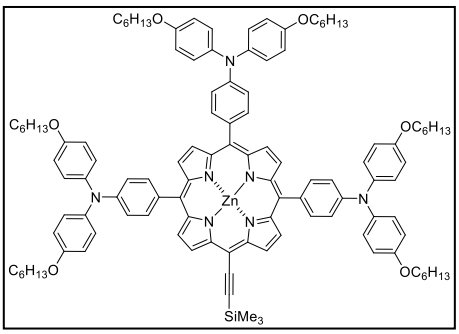

From porphyrin **P5** (0.13 mmol, 230 mg), reacted according to the general procedure, was obtained the product as green solid (0.12 mmol, 217 mg. 91% yield). ^{1}H-NMR (400 MHz, $CDCl_3$) δ/ppm: 9.75 (d, *J* = 4.7 Hz, 2H), 9.13 (d, *J* = 4.7 Hz, 2H), 9.05 (d, *J* = 4.7 Hz, 2H), 9.03 (d, *J* = 4.7 Hz, 2H), 7.98 (dd, *J* = 8.6, 7.0 Hz, 6H), 7.36 (dd, *J* = 9.0, 5.8 Hz, 12H), 7.30 (t, *J* = 8.6 Hz, 6H), 6.95 (dd, *J* = 9.0, 6.7 Hz, 12H), 3.97 (dd, *J* = 13.0, 6.5 Hz, 12H), 1.85-1.75 (m, 12H),

1.54-1.45 (m, 12H), 1.41-1.35 (m, 24H), 0.95-0.91 (m, 18H), 0.63 (s, 9H). ^{13}C-NMR (100 MHz, $CDCl_3$) δ/ppm: 152.45, 150.88, 150.17, 150.07, 148.27, 140.81, 140.77, 135.29, 135.23, 134.06, 132.99, 132.22, 131.73, 130.68, 127.00, 123.37, 122.15, 118.03, 117.91, 115.42, 107.95, 100.87, 98.47, 68.28, 31.62, 29.32, 25.77, 22.63, 14.07, 0.43. MS (*m/z*) (MALDI-TOF): calculated for $C_{115}H_{131}N_7O_6SiZn$: 1797.92; found: 1798.50 (M+). FT-IR ν/cm^{-1}: 2954, 2951, 2854, 2138, 1604, 1503, 1235.

General procedure for Sonogashira coupling

To a solution of the corresponding porphyrin **P4S** or **P5S** (1 eq) in CH_2Cl_2 (200 mL/mmol), TBAF (1.25 mmol, 1M in THF) was added under argon. The solution was stirred at room temperature for 1 hour. The mixture was quenched with H_2O and extracted with CH_2Cl_2 (3 x 50 mL). The combined organic layer was dried over anhydrous $MgSO_4$ and the solvent was removed under reducer pressure. The residue and 4-iodobenzoic acid (5 eq) were dissolved in dry THF (200 mL/mmol) and Et_3N (120 mL/mmol). The solution was degassed with argon for 15 min, $Pd_2(dba)_3$ (0.3 eq) and $AsPh_3$ (2 eq) were added to the mixture and the solution was refluxed over night. The solvent was removed under reduced pressure. The product was purified by column chromatography (silica gel, $CHCl_3$: MeOH, 95:5).

Synthesis of [10,15,20-*tri*(*N*,*N*-diphenylaniline)-5-carboxyphenylethynyl-porphyrinato] zinc (II) (SA13)

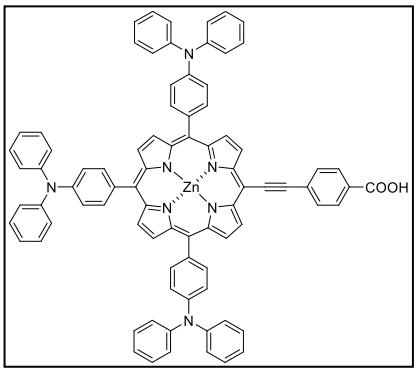

Using the general procedure to **SA13** previously described, **P4S** (0.22 mmol, 247 mg) and TBAF (0.27 mmol, 0.27 mL) reacted in 44 mL of CH_2Cl_2, in the next step the product reacted with 4-iodobenzoic acid (1.1 mmol, 272 mg) in 44 mL of THF and 26 mL of Et_3N. The product **SA13** was obtained as a green solid (0.15 mmol, 173 mg, 70% yield). ^{1}H-NMR (400 MHz, $CDCl_3$/d_5-pyridine) δ/ppm: 9.80 (d, *J* = 4.6 Hz, 2H), 9.09 (d, *J* = 4.6 Hz, 2H), 8.97 (d, *J* = 4.6 Hz, 2H), 8.94 (d, *J* = 4.6 Hz, 2H), 8.34 (d, *J* = 8.3 Hz, 2H), 8.11 (d, *J* = 8.3 Hz, 2H), 8.05 (t, *J* = 8.3 Hz, 6H), 7.70-7.64 (m, 4H), 7.57-7.52 (m, 2H), 7.49-7.38 (m, 24H), 7.16-7.11 (m, 6H). ^{13}C-NMR (100 MHz, $CDCl_3$/d_5-pyridine) δ/ppm: 207.05, 152.81, 152.28, 150.68, 149.80, 147.91, 147.09, 137.04, 132.94, 132.74, 132.10, 132.00, 131.92, 131.89, 131.41, 131.06, 130.25, 130.08, 128.52, 128.40, 124.64, 121.67, 121.41, 121.33. MS (*m/z*) (MALDI-TOF): calculated for $C_{83}H_{55}N_7O_2Zn$: 1245.37; found: 1245.40 (M+). FT-IR ν/cm^{-1}: 3436, 3061, 3031, 2956, 2924, 2186, 1738, 1589, 1405, 1330, 1316, 1278, 1173, 698.

Synthesis of [10,15,20-*tri*(*N*,*N*-(*bis*(4-hexyloxy)phenyl)aniline)-5-5-carboxy-phenylethynyl-porphyrinato] zinc (II) (SA14)

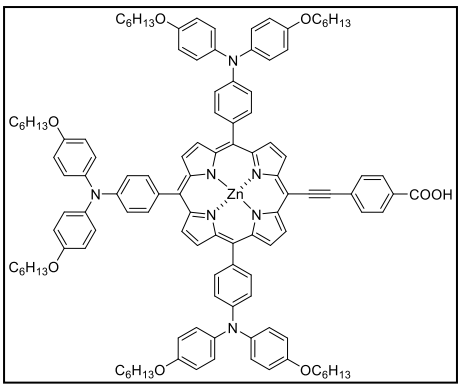

Using the general procedure to **P5S** (0.13 mmol, 224 mg) and TBAF (0.16 mmol, 0.16 mL) reacted in 26 mL of CH_2Cl_2. Then the intermediate product and 4-iodobenzoic acid (0.65 mmol, 161 mg) in 26 mL of THF and 16 mL of Et_3N was added to $Pd_2(dba)_3$ (0.03 mmol, 36 mg) and $AsPh_3$ (0.26 mmol, 80 mg). The product **SA14** was obtained as a green solid (0.08 mmol, 141 mg, 63% yield). ^{1}H-NMR (400 MHz, $CDCl_3$/d_5-pyridine) δ/ppm: 9.71 (d, *J* = 4.5 Hz, 2H), 9.03 (d, *J* = 4.5 Hz, 2H), 8.90 (d, *J* = 4.5 Hz, 2H), 8.87 (d, *J* = 4.5 Hz, 2H), 8.27 (d, *J* = 6.8 Hz, 2H), 8.03 (d, *J* = 6.8 Hz, 2H), 7.90 (dd, *J* = 8.5, 6.7 Hz, 6H), 7.30-7.19 (m, 24H), 6.91-6.86 (m, 6H), 3.93-3.88 (m, 12H), 1.72 (q, *J* = 6.7 Hz, 12H), 1.45-1.37 (m, 12H), 1.31-1.24 (m, 24H), 0.83 (t, *J* = 7.0 Hz, 18H). ^{13}C-NMR (100 MHz, $CDCl_3$/d_5-pyridine) δ/ppm: 207.01, 155.58, 152.19, 150.87, 149.94, 149.90, 148.03, 140.87, 140.83, 135.70, 135.21, 134.76, 131.94, 131.02, 130.08, 126.91, 123.40, 123.16, 122.91, 118.04, 117.92, 115.37, 97.37, 95.06, 68.21, 31.58, 30.86, 29.32, 25.75, 22.62, 14.04. MS (*m/z*) (MALDI-TOF): calculated for $C_{119}H_{127}N_7O_8Zn$: 1845.90; found: 1846.40 (M+). FT-IR ν/cm^{-1}: 3424, 3120, 3039, 2852, 2927, 2859, 2185, 1799, 1688, 1603, 1503, 1467, 1314, 1278, 1240, 1167, 998, 828, 794.

2.10.3.2 Experimental details in the synthesis of SA15 and SA16

Synthesis of A6

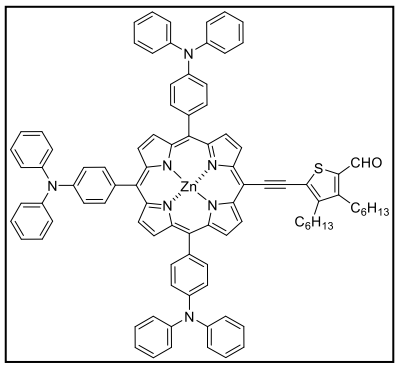

Using the general procedure to Sonogashira coupling previously described, **P4S** (0.13 mmol, 100 mg), **C1** (0.27 mmol, 109 mg), 4 mL of Et_3N in 21 mL of THF was added over a mixture of $Pd_2(dba)_3$ (0.02 mmol, 20 mg) and $AsPh_3$ (0.22 mmol, 54 mg). The product **A8** was obtained as a green solid (107 mg, 0.076 mmol, 83% yield). ^{1}H-NMR (400 MHz, $CDCl_3$) δ/ppm: 9.90 (s, 1H), 9.73 (d, *J* = 4.7 Hz, 2H), 9.16 (d, *J* = 4.7 Hz, 2H), 9.05 (d, *J* = 4.7 Hz, 2H), 9.03 (d, *J* = 4.7 Hz, 2H), 8.07 (t, *J* = 8.7 Hz, 6H), 7.50-7.42 (m, 6H), 7.49-7.38 (m, 24H), 7.16-7.11 (m, 6H), 2.97 (m, 2H), 2.78 (m, 2H), 1.94 (m, 2H), 1.72-1.62 (m, 4H), 1.50-1.46 (m, 4H), 1.41-1.36 (m,6), 0.95 (t, *J* = 7.1 Hz, 3H), 0.88 (t, *J* = 7.1 Hz, 3H). ^{13}C-NMR (100 MHz, $CDCl_3$) δ/ppm: 181.67, 152.00, 151.26, 151.16, 151.00, 147.87, 147.84, 147.69, 147.52, 137.18, 136.17, 136.00, 135.38, 135.34, 133.27, 132.44, 132.00, 130.35, 129.53, 124.91, 123.32, 122.45, 121.33, 121.26, 32.27, 31.86, 31.54, 30.95, 29.86, 29.39, 28.60, 22.81, 22.61, 14.15, 14.12. MS

(*m/z*) (MALDI-TOF): calculated for $C_{93}H_{77}N_7OSZn$: 1403.52; found: 1403.90. FT-IR ν/cm^{-1}: 2957, 2922, 2855, 1652, 1590, 1489, 1318, 1282, 996, 696.

Synthesis of A7

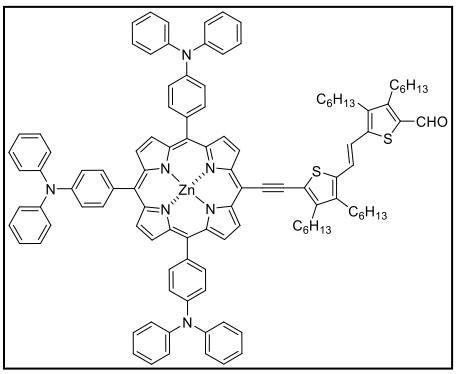

Using the general procedure to Sonogashira coupling previously described, **P4S** (0.11 mmol, 130 mg), **C2** (0.33 mmol, 225 mg), 5 mL of Et_3N in 25 mL of THF was added over a mixture of $Pd_2(dba)_3$ (0.03 mmol, 30 mg) and $AsPh_3$ (0.22 mmol, 67 mg). The product **A9** was obtained as a green solid (135 mg, 0.080 mmol, 80% yield). ^{1}H-NMR (400 MHz, $CDCl_3$/d_5-pyridine) δ/ppm: 9.84 (s, 1H), 9.78 (d, *J* = 4.6 Hz, 2H), 9.14 (d, *J* = 4.6 Hz, 2H), 9.03 (dd, *J* = 4.6, 6.7 Hz, 4H), 8.07 (dd, *J* = 7.6, 9.7 Hz, 6H), 7.49 (d, *J* = 8.6 Hz, 6H), 7.45-7.41 (m, 24H), 7.32 (d, *J* = 15.5 Hz, 1H), 7.19-7.13 (m, 6H), 7.08 (d, *J* = 15.5 Hz, 1H), 3.13 (dd, *J* = 6.0, 10.0 Hz, 2H), 2.77 (t, *J* = 7.0 Hz, 2H), 2.74 (t, *J* = 7.0 Hz, 2H), 2.61 (dd, *J* = 6.0, 10.0 Hz, 2H), 2.00 (q, *J* = 7.0 Hz, 2H), 1.78-1.52 (m, 12H), 1.46-1.33 (m, 18H), 1.02-0.86 (m, 12H). ^{13}C-NMR (100 MHz, $CDCl_3$) δ/ppm: 181.82, 152.97, 151.85, 150.78, 150.28, 149.90, 148.34, 147.89, 147.86, 147.46, 146.82, 142.77, 141.93, 137.17, 136.30, 136.18, 135.38, 134.78, 132.94, 138.28, 131.96, 130.47, 129.52, 124.86, 123.28, 122.91, 122.18, 121.40, 121.31, 119.24, 118.90, 32.30, 31.95, 31.71, 31.66, 31.57, 31.25, 29.93, 29.50, 29.42, 27.58, 27.12, 22.84, 22.72, 22.70, 22.60, 14.24, 14.18, 14.10. MS (*m/z*) (MALDI-TOF): calculated for $C_{111}H_{105}N_7OS_2Zn$: 1679.71; found: 1680.10. FT-IR ν/cm^{-1}: 3030, 2952, 2921, 2850, 1650, 1589, 1487, 1311, 1276, 995, 696.

General procedure for Knoevenagel condensations with cyanoacetic acid

To a solution of **A8**-**A9** (1 eq) in $CHCl_3$ (40 mL/mmol), were added cyanoacetic acid (1.5 eq) and piperidine (0.1 eq). The reaction mixture was refluxed, under argon, during 18 h. After removing the solvent, the residue was purified by column chromatography using silica gel in CHCl3:MeOH 10:1 mixture as the eluent.

Synthesis of SA15

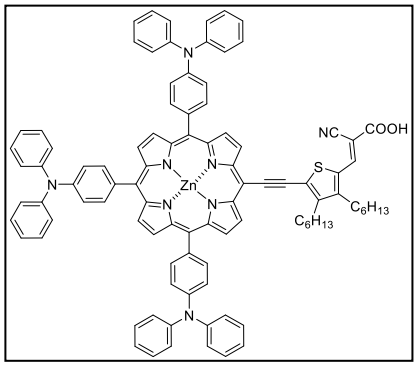

Using the general procedure to Knoevenaguel condensation previously described, to a solution of **A8** (0.04 mmol, 60 mg) in 1.6 mL of CH_2Cl_2, was added cyanoacetic acid (0.13 mmol, 11 mg). **SA15** was obtained as a green solid (0.038 mmol, 56 mg, 89% yield). ^{1}H-NMR (400 MHz, THF-d_8) δ/ppm: 9.72 (d, *J* = 4.2 Hz, 2H), 9.06 (s broad, 2H), 8.94-8.90 (m, 4H), 8.54 (s, 1H), 8.05 (d, *J* = 8.1 Hz, 6H), 7.45 (d, *J* = 8.1 Hz, 6H), 7.40-7.39 (m, 24H), 7.13-7.96 (m, 6H), 3.29 (m, 2H), 3.00 (m,

2H), 2.08 (m, 2H), 1.77 (m, 2H), 1.61-1.50 (m, 6H), 1.47-1.41 (m, 6H), 0.98 (s broad, 3H), 0.87 (s broad, 3H). ^{13}C-NMR (125 MHz, THF-d_8) δ/ppm: 151.59, 150.75, 150.55, 148.82, 148.79, 148.24, 147.13, 137.78, 137.62, 136.24, 133.38, 132.47, 131.99, 130.47, 130.11, 125.48, 125.45, 124.01, 123.90, 123.85, 122.80, 121.99, 121.82, 32.84, 32.69, 32.57, 31.80, 31.55, 30.58, 30.44, 30.28, 23.51, 23.45, 14.34. MS (*m/z*) (MALDI-TOF): calculated for $C_{96}H_{78}N_8O_2SZn$: 1470.53; found: 1470.96. FT-IR ν/cm^{-1}: 3419, 3068, 3033, 2955, 2925, 2155, 1600, 1495, 1386, 1317, 1282, 698.

Synthesis of SA16

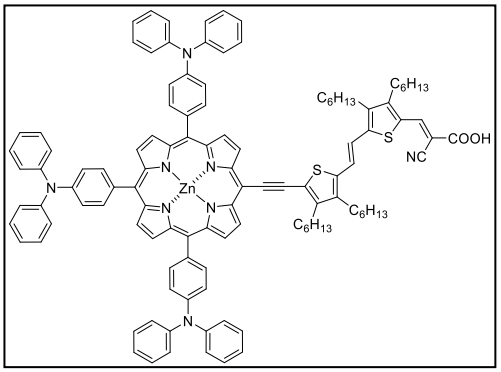

Using the general procedure to Knoevenaguel condensation previously described, in a solution of **A9** (0.078 mmol, 130 mg) in 3 mL of CH_2Cl_2, was added cyanoacetic acid (0.23 mmol, 20 mg). **SA16** was obtained as a green solid (110 mg, 0.063 mmol, 82% yield). ^{1}H-NMR (400 MHz, THF-d_8) δ/ppm: 9.73 (d, *J* = 4.4 Hz, 2H), 9.05 (d, *J* = 4.4 Hz, 2H), 8.94-8.91 (m, 4H), 8.45 (s, 1H), 8.06 (t, *J* = 8.6 Hz, 6H), 7.45 (t, *J* = 8.6 Hz, 6H), 7.41-7.38 (m, 25H), 7.30 (d, *J* = 15.4 Hz, 2H), 7.13-7.09 (m, 6H), 3.24 (m, 2H), 2.91 (m, 2H), 2.82 (m, 6H), 2.07 (m, 2H), 1.78 (m, 4H), 1.65 (m, 4H), 1.56 (m, 8H), 1.50-1.36 (m, 18H), 1.03-0.93 (m, 9H), 0.89 (t, *J* = 7.2 Hz, 3H). ^{13}C-NMR (125 MHz, THF-d_8) δ/ppm: 151.45, 150.85, 150.47, 148.83, 148.80, 148.44, 148.21, 137.86, 137.74, 136.25, 136.22, 133.09, 132.36, 132.02, 130.48, 130.11, 125.46, 125.45, 123.87, 123.86, 122.55, 121.99, 121.85, 32.75, 32.50, 32.43, 32.30, 32.01, 31.90, 30.60, 30.45, 30.13, 30.07, 29.95, 23.55, 23.46, 23.40, 14.41, 14.37. MS (*m/z*) (MALDI-TOF): calculated for $C_{114}H_{106}N_8O_2S_2Zn$: 1746.72; found: 1747.17. FT-IR ν/cm^{-1}: 3389, 3059, 3032, 2950, 2932, 2924, 2855, 1595, 1564, 1491, 1386, 1277, 978, 796, 752, 691.

2.10.3.3 Experimental details in the synthesis of SA17 and SA18

General procedure for oxidation reaction

At 0°C to a solution of the aladehyde (1eq) in dryed acetone (217 mL/mmol) was added slowly $NaClO_2$ (3.0 eq), then was added drop to drop a mix of NH_2SO_3H (3.0 eq) in 21 mL/mmol of water, the mixture was stirred during 4 hours at room temperature. The reaction was quenched with a saturated solution of chloride acid (0.1M), stirring for 1 hour and extracted with CH_2Cl_2. The combined organic phases were dried over anhydrous $MgSO_4$ and filtered. The solvent was removed by rotary evaporation.

Synthesis of SA17

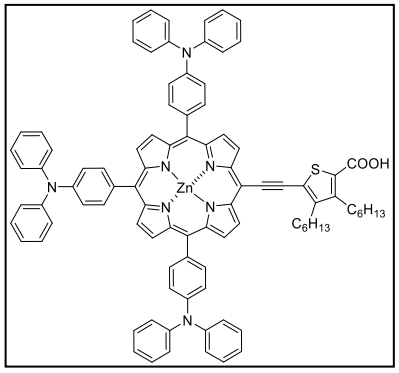

Using the general procedure for oxidation, previously described, $NaClO_2$ (0.65 mmol, 60 mg) was added in a solution of **A8** (0.22 mmol, 124 mg) in 48 mL of dryed acetone, then was added NH_2SO_3H (0.65 mmol, 63 mg) in 5 mL of water. The product was purified by column chromatography (silica gel, $CHCl_3$: MeOH 95:5). **SA17** was obtained as green solid (174 mg, 0.12 mmol, 53%). ^{1}H-NMR (400 MHz, $CDCl^3$) δ/ppm: 9.74, (d, *J* = 4.46 Hz, 2H), 9.01, (d, *J*= 4.46 Hz, 2H), 8.95(d, 4.46 Hz, 4H), 8.10-8.06 (m, 6H), 7.47 (t, 8.4 Hz, 6H), 7.42-7.39 (m, 24H), 7.12-7.19 (m,6H), 3.23 (t, *J* = 7.37 Hz, 2H), 3.12(t, *J* = 7.37 Hz, 2H), 2.08 (m,4H), 1.54 (t, 4H), 1.43 (m, 6H), 1.30 (m, 2H), 0.97 (m, 2H), 0.89 (t, *J* = 7.19 Hz, 4H). ^{13}C-NMR (100 MHz, $CDCl_3$) δ/ppm: 152.69, 151.64, 150.33, 148.84, 148.89, 148.14, 147.43, 137.88, 137.82, 136.44, 133.58, 131.57, 131.20, 130.37, 130.21, 125.44, 125.26, 124.10, 123.95, 123.55, 122.99, 120.99, 34.64, 32.70, 32.55, 31.95, 31.35, 31.08, 30.94, 30.19, 16.14. MALDI-TOF MS (*m/z*): calculated for $C_{93}H_{77}N_7O_2SZn$:1419.52, found: 1419.51 (M+). FT-IR ν/cm^{-1}: 3695, 3536, 3463, 3054, 3035, 2950, 2923, 2850, 2310, 2167, 1589, 1488, 1322, 1280, 1180, 1065, 998, 802, 755.

Synthesis of SA18

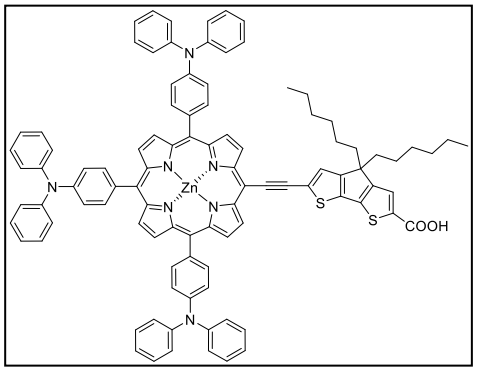

Using the general procedure for oxidation, previously described, $NaClO_2$ (0.55 mmol, 50 mg) was added in a solution of **A9** (0.18 mmol, 269 mg) in 39 mL of dryed acetone, then was added NH_2SO_3H (0.5 mmol, 53 mg) in 4 mL of water. The product was purified by column chromatography (silica gel, $CHCl_3$: MeOH 95:5). **SA18** was obtained as green solid (131 mg, 0.09 mmol, 48%). ^{1}H-NMR (400 MHz, $CDCl_3$) δ/ppm: 9.76, (d, *J* = 4.46 Hz, 2H), 9.09, (d, *J* = 4.46 Hz, 2H), 8.95 (d, 4.46 Hz, 4H), 8.08 (m, 6H), 7.79 (s, 2H), 7.41 (m, 30H), 7.12 (m,6H), 2.11 (m, 6H), 1.31 (m, 14H), 0.91 (m, 6H). ^{13}C-NMR (100 MHz, $CDCl_3$) δ/ppm: 158.74, 151.73, 150.69, 150.04, 149.71, 148.01, 147.42, 137.09, 136.92, 135.52, 134.85, 132.35, 131.61, 131.27, 129.84, 129.36, 126.02, 124.99, 124.71, 123.12, 122.69, 121.74, 121.13, 99.36, 98.42, 90.19, 78.66, 78.34, 78.00, 54.26, 37.95, 32.10, 31.75, 29.87, 29.70, 26.40, 22.87, 22.70, 13.57. MALDI-TOF MS (*m/z*): calculated for $C_{98}H_{79}N_7O_2S_2Zn$: 1513.50, found: 1513.40 (M+). FT-IR ν/cm^{-1}: 3517, 3472, 3070, 3035, 2950, 2917, 2850, 2351, 1589, 1488, 1392, 1326, 1276, 1065, 998, 790.

2.11 References

[1] O'Regan, B.; Grätzel, M. *Nature* **1991**, *353*, 737.

[2] Zhang, S.; yang, X.; Numata, Y.; Han, L. *Energy Environ. Sci.* **2013**, *6*, 1443.

[3] Yella, A.; Lee, H.-W.; Tsao, H. N.; Yi, C.; Chandiran, A. K.; Nazeeruddin, M. K.; Diau, E. W.-G.; Yeh, C.-Y.; Zakeeruddin, S. M.; Grätzel, M. *Science* **2011**, *334*, 629.

[4] Mathew, S.; Yella, A.; Gao, P.; Humphry-Baker, R.; Curchod, B. F. E.; Ashari-Astani, N.; Tavernelli, I.; Rothlisberger, U.; Nazeeruddin, M. K.; Gratzel, M. *Nat Chem.* **2014**, *6*, 242.

[5] Kalyanasundaram, K.; Grätzel, M. *Material Matters* **2009**, *4*, 88.

[6] Ribó, J. M.; Bofill, J. M.; Crusats, J.; Rubires, R. *Chem. Eur. J*. **2001**, *7*, 2733.

[7] Mehmood, U.; Rahman, S-U.; Harrabi, K.; Ibnelwaleed A. Hussein I., Reddy, B. V. S.; *Advances in Materials Science and Engineering* **2014**, Article ID 974782, doi:10.1155/2014/974782,1.

[8] Gong, J.; Jing, L.; Sumathy, K. *Renewable and Sustainable Energy Reviews*, **2012**, *16*, 5848.

[9] Lupan, O.; Guérin, V. M.; Tiginyanu I. M. *J. Photochem. Photobiol. C* **2010**, *211*, 65.

[10] Han D.-W.; Heo, J.-H.; Kwak, D.-J.; Han, C.-H.; Sung, Y.-M. *JEET* **2009**, *4*, *1*, 93.

[11] Hoffmann, M. R.; Martin, S. T.; Choi, W.; Bahnemann, D. W. *Chem. Rev.* **1995**, *95*, *1*, 69.

[12] Rodríguez, J. A.; Fernández-García, M. *Metal Oxide Nanoparticles*, **2007** http://www0.bnl.gov/isd/documents/41042.pdf (accessed Jul 3, 2015).

[13] Park, N.-G.; Van de Lagemaat, J.; Frank, A. J. *J. Phys. Chem. B* **2000**, *104*, 8989.

[14] Longo, C.; de Paoli, M. A. *J. Braz. Chem. Soc.* **2003**, *14*, 889.

[15] Descouens, D. via *Wikimedia Commons*, http://creativecommons.org/licenses/by/3.0, (accessed Sep 10, 2015).

[16] Benjah-bmm27 B. via Wikimedia Commons, http://creativecommons.org/licenses/by/3.0, (accessed Sep 10, 2015).

[17] Urbani, M.; Gratzel, M.; Nazeeruddin, M.; Torres, T. *Chem. Rev*. **2014**, *14*, 12330.

[18] Kusama H.; Arakawa, H. *Sol. Energ. Mat. Sol. Cells* **2005**, *85*, 333.

[19] Wu, J.; Lan, Z.; Haoetal, S. *Pure Appl. Chem.* **2008**, *80*, 2241.

[20] Zakeeruddin, S. M.; Grätzel, M. *Adv. Funct. Mater.* **2009**, *19*, 2187.

[21] Wang, P.; Zakeeruddin, S. M.; Moser, J.-E.; Grätzel, M. J. Phys. Chem. B **2003**, *107*, 13280.

[22] Li, B.; Wang, L.; Kang, B.; Wang, P.; Qiu, Y. *Sol. Energy Mater. Sol. Cells* **2006**, *90*, 549.

[23] Mohmeyer, N.; Wang, P.; Schmidt, H.-W.; Zakeeruddin, S. M.; Grätzel, M. *J. Mater. Chem.* **2004**, *14*, 1905.

[24] Fang, X.; Ma, T.; Guan, G.; Akiyama, M.; Abe, E. *J. Photochem. Photobiol. A* **2004**, *164*, 179.

[25] Khelashvili, G.; Behrens, S.; Weidenthaler C. *Thin Solid Films* **2006**, *511*, 342.

[26] Syrrokostas, G.; *Sol. Energy Mater. Sol. Cells* **2012**, *103*, 119.

[27] Papageorgiou, N.; Maier, W. F.; Grätzel, M. *J. Electrochem. Soc* **1997**, *144*, 876.

[28] Andrade, L.; Ribeiro, H.A.; Mendes, A. "Dye-sensitized solar cells: an overview," In Encyclopedia of Inorganic and Bioinorganic Chemistry, **2011**, 1.

[29] Zhang, B.; Xu, X.; Zhang, X.; Huang, D.; Li, S.; Zhang, Y.; Zhan, F.; Deng, M.; He, Y.; Chen, W.; Shen, Y.; Wang, M. *ChemPhysChem* **2014**, *15*, 1182.

[30] Huijser, A.; Savenije, T. J.; Kroeze, J. E.; Siebbeles, L. D. A. *J. Phys. Chem. B* **2005**, *109*, 20166.

[31] Verma, S.; Ghosh, H. N. *J. Phys. Chem. Lett.* **2013**, *3*, 1877.

[32] Yum, J.-H.; Baranoff, E.; Wenger, S.; Nazeeruddin, M. K.; Grätzel, *Energy Environ. Sci.* **2011**, *4*, 842.

[33] Rothenberger, G.; Comte, P.; Grätzel, M. *Sol. Energy Mater. Sol. Cells* **1999**, *58*, 321.

[34] Imahori, H.; Higashino, T. *Dalton Trans.* **2015**, *44*, 448.

[35] Li, L.; Diau, E. W-G. *Chem. Soc. Rev.* **2013**, 42, 291

[36] Dos-Santos, T.; Morandeira, A.; Koops, S.; Mozer, A. J.; Tsekouras, G.; Dong, Y.; Wagner, P.; Wallace, G.; Earles, J. C.; Gordon, K. C.; Officer, D.; Durrant, J. R. *J. Phys. Chem. C* **2010**, *114*, 3276.

[37] Kay, A.; Grätzel, M. *J. Phys. Chem.* **1993**, *97*, 6272.

[38] Nazeeruddin, M. K.; Humphry-Baker, R.; Officer, D. L.; Campbell, W. M.; Burrell, A. K.; Grätzel, M. *Langmuir* **2004**, *20*, 6514.

[39] Wang, Q.; Campbell, W. M.; Bonfantani, E. E.; Jolley, K. W.; Officer, D. L.; Walsh, P. J.; Gordon, K.; Humphry-Baker, R.; Nazeeruddin, M. K.; Grätzel, M. *J. Phys. Chem. B* **2005**, *109*, 15397.

[40] Campbell, W. M.; Jolley, K. W.; Wagner, P.; Wagner, K.; Walsh, P. J.; Gordon, K. C.; Schmidt-Mende, L.; Nazeeruddin, M. K.; Wang, Q.; Grätzel, M.; Officer, D. L. *J. Phys. Chem. C* **2007**, *111*, 11760.

[41] Ishida, M.; Park, S. W.; Hwang, D.; Koo, Y. B.; Sessler, J. L.; Kim, D. Y.; Kim, D. *J. Phys. Chem. C* **2011**, *115*, 19343.

[42] Park, J. K.; Lee, H. R.; Chen, J.; Shinokubo, H.; Osuka, A.; Kim, D. *J. Phys. Chem. C* **2008**, *112*, 16691.

[43] Yella, A; Lee, H.-W.; Tsao, H. N.; Yi, C.; Chandiran, A.K.; Nazzeurddin, M. K.; Diau, E. W.-G.; Yeh, C.-Y.; Zakeeruddin, S. M.; Grätzel, M. *Science* **2011**, *334*, 629.

[44] Mathew, S.; Yella, A.; Gao, P.; Humphry-Baker, R.; Curchod, B. F. E.; Ashari-Astani, N.; Tavernelli, I.; Rothlisberger, U.; Nazeeruddin, M. K.; Grätzel, M. *Nat. Chem.* **2014**, *6*, 242.

[45] [a] Tanaka, M.; Hayashi, S.; Eu, S.; Umeyama, T.; Matano, Y.; Imahori, H. *Chem. Commun*. **2007**, 2069. [b] Hayashi, S.; Tanaka, M.; Hayashi, H.; Eu, S.; Umeyama, T.; Matano, Y.; Araki, Y.; Imahori, H. *J. Phys. Chem. C* **2008**, *112*, 15576. [c] Hayashi, S.; Matsubara, Y.; Eu, S.; Hayashi, H.; Umeyama, T.; Matano, Y.; Imahori, H. *Chem. Lett.* **2008**, *37*, 846.

[46] Mozer, A. J.; Griffith, M. J.; Tsekouras, G.; Wagner, P.; Wallace, G. G.; Mori, S.; Sunahara, K.; Miyashita, M.; Earles, J. C.; Gordon, K. C.; Du, L. C.; Katoh, R.; Furube, A.; Officer, D. L. *J. Am. Chem. Soc.* **2009**, *131*, 15621.

[47] Ladomenou, K.; Kitsopoulos, T. N.; Sharma, G. D.; Coutsolelos, A. G. *RSC Adv.* **2014**, *4*, 21379.

[48] [a] Mishra, A.; Fischer, M. K. R.; Bäuerle, P. *Angew. Chem., Int. Ed.* **2009**, 48, 2474. [b] Ooyama, Y.; Harima, Y. *Eur. J. Org. Chem.* **2009**, 2903. [c] Zeng, W.; Cao, Y.; Bai, Y.; Wang, Y.; Shi, Y.; Zhang, M.; Wang, F.; Pan, C.; Wang, P. *Chem. Mater.* **2010**, *22*, 1915. [d] Tan, L.-L.; Huang, J.-F.; Shen, Y.; Xiao, L.-M.; Liu, J.-M.; Kuang D.-B.; Su, C.-Y. *J. Mater. Chem. A* **2014**, *2*, 8988.

[49] [a] Chen, C. Y.; Wang, M. K.; Li, J. Y.; Pootrakulchote, N.; Alibabaei, L.; Ngoc-le, C. H.; Decoppet, J. D.; Tsai, J. H.; Grätzel, C.; Wu, C. G.; Zakeeruddin, S. M.; Grätzel, M. *ACS Nano*, **2009**, *3*, 3103. [b] Cao, Y. M.; Bai, Y.; Yu, Q. J.; Cheng, Y. M.; Liu, S.; Shi, D.; Gao, F. F.; Wang, P. *J. Phys. Chem. C*, **2009**, *113*, 6290. [c] Yu, Q. J.; Wang, Y. H.; Yi, Z. H.; Zu, N. N. Zhang, J.; Zhang, M.; Wang, P. *ACS Nano*, **2010**, *4*, 6032.

[50] [a] Robertson, N. *Angew. Chem. Int. Ed.* **2006**, *45*, 2338. [b] Mishra, A.; Fischer, M. K. R.; Bäuerle, P. *Angew. Chem. Int. Ed.* **2009**, *48*, 2474. [c] Ning, Z. J.; Fu, Y.; Tian, H. *Energy Environ. Sci.* **2010**, *3*, 1170.

[51] Liu, Y.; Xiang, N.; Feng, X.; Shen, P.; Zhou, W.; Weng, C.; Zhao B.; Tan, S. *Chem. Commun.*, **2009**, 2499.

[52] Ambre, R.; Chen, K.-B.; Yao, C.-F.; Luo, L.; Diau E. W.-G.; Hung, C.-H. *J. Phys. Chem. C*, **2012**, *116*, 11907.

[53] Ripolles-Sanchis, T.; Guo, B.-C.; Wu, H.-P.; Pan, T.-Y.; Lee, H.-W.; Raga, S. R.; Fabregat-Santiago, F.; Bisquert, J.; Yeh, C.-Y.; Diau, E. W.-G. *Chem. Commun*. **2012**, *48*, 4368.

[54] Chang, Y.-C.; Wu, H.-P.; Reddy, N. M.; Lee, H.-W.; Lu, H.-P.; Yeh, C.-Y.; Diau, E. W.-G. *Phys. Chem. Chem. Phys.* **2013**, *15*, 4651.

[55] Smestad, G. P.; Krebs, F. C.; Lampert, C. M.; Granqvist, C. G.; Chopra, K. L.; Mathew, X.; Takakura, H. *Sol. Energy Mater. Sol. Cells*, **2008**, *92*, 37.

[56] Lindsey, J. S.; Prathapan, S.; Johnson T. E.; Wagner, R. W. *Tetrahedron* **1994**, *50*, 8941.

[57] Liu, B.; Zhu, W.; Wang, Y.; Wu, W.; Li, X.; Chen, B.; Y.-T. Long and Y. Xie, *J. Mater. Chem.*, **2012**, *22*, 7434.

[58]Cardona, C. M.; Li, W.; Kaifer, A. E.; Stockdale D.; Bazan, G. C. *Adv. Mater.* **2011**, *23*, 2367.

[59] R. D. Gaussian 03, Frisch, M. J.; Trucks, G. W.; Schlegel, H. B.; Scuseria, G. E.; Robb, M. A.; Cheeseman, J. R.; Montgomery, Jr. J. A.; Vreven, T.; Kudin, K. N.; Burant, J. C.; Millam, J. M.; Iyengar, S. S.; Tomasi, J.; Barone, V.; Mennucci, B.; Cossi, M.; Scalmani, G.; Rega, N.; Petersson, G. A.; Nakatsuji, H.; Hada, M.; Ehara, M.; Toyota, K.; Fukuda, R.; Hasegawa, J.; Ishida, M.; Nakajima, T.; Honda, Y.; Kitao, O.; Nakai, H.; Klene, M.; Li, X.; Knox, J. E.; Hratchian, H. P.; Cross, J. B.; Bakken, V.; Adamo, C.; Jaramillo, J.; Gomperts, R.; Stratmann, R. E.; Yazyev, O.; Austin, A. J.; Cammi, R.; Pomelli, C.; Ochterski, J. W.; Ayala, P. Y.; Morokuma, K.; Voth, G. A.; Salvador, P.; Dannenberg, J. J.; Zakrzewski, V. G.; Dapprich, S.; Daniels, A. D.; Strain, M. C.; Farkas, O.; Malick, D. K.; Rabuck, A. D.; Raghavachari, K.; Foresman, J. B.; Ortiz, J. V.; Cui, Q.; Baboul, A. G.; Clifford, S.; Cioslowski, J.; Stefanov, B. B.; Liu, G.; Liashenko, A.; Piskorz, P.; Komaromi, I.; Martin, R. L.; Fox, D. J.; Keith, T.; Al-Laham, M. A.; Peng, C. Y.; Nanayakkara, A.; Challacombe, M.; Gill, P. M. W.; Johnson, B.; Chen, W. ; Wong, M. W.; Gonzalez, C.; Pople, J. A. Gaussian Inc. Wallingford CT, **2004**.

[60] Bai, Y.; Zhang, J.; Zhou, D.; Wang, Y.; Zhang, M.; Wang, P. *J. Am. Chem. Soc.* **2011**, *133*, 11442.

[61] Cao, Y.; Bai, Y.; Yu, Q.; Cheng, Y.; Liu, S.; Shi, D.; Gao, F.; Wang, P. *J. Phys. Chem. C* **2009**, *113*, 6290.

[62] Ragoussi, M.-E.; de la Torre, G.; Torres, T. *Eur. J. Org. Chem*. **2013**, *51*, 2832.

[63] Wagner, R. W.; Johnson, T. E.; Li, F.; Lindsey, J. S. *J.Org. Chem*. **1995**, *60*, 5266.

[64] Pellejà, L.; Dominguez, R.; Aljarilla, A.; Clifford, J. N.; de la Cruz, P.; Langa, F.; Palomares, E. *ChemElectroChem*. **2014**, *1*, 1126.

[65] Zewdu, T.; Clifford, J. N.; Hernandez, J. P.; Palomares, E. *Energy Environ. Sci.* **2011**, *4*, 4633.

[66] Nguyen, H.-M.; Mane, R. S.; Ganesh, T.; Han, S.-H.; Kim, N. *J. Phys. Chem. C*, **2009**, *113*, 9206.

Additional information, spectroscopy chapter 1

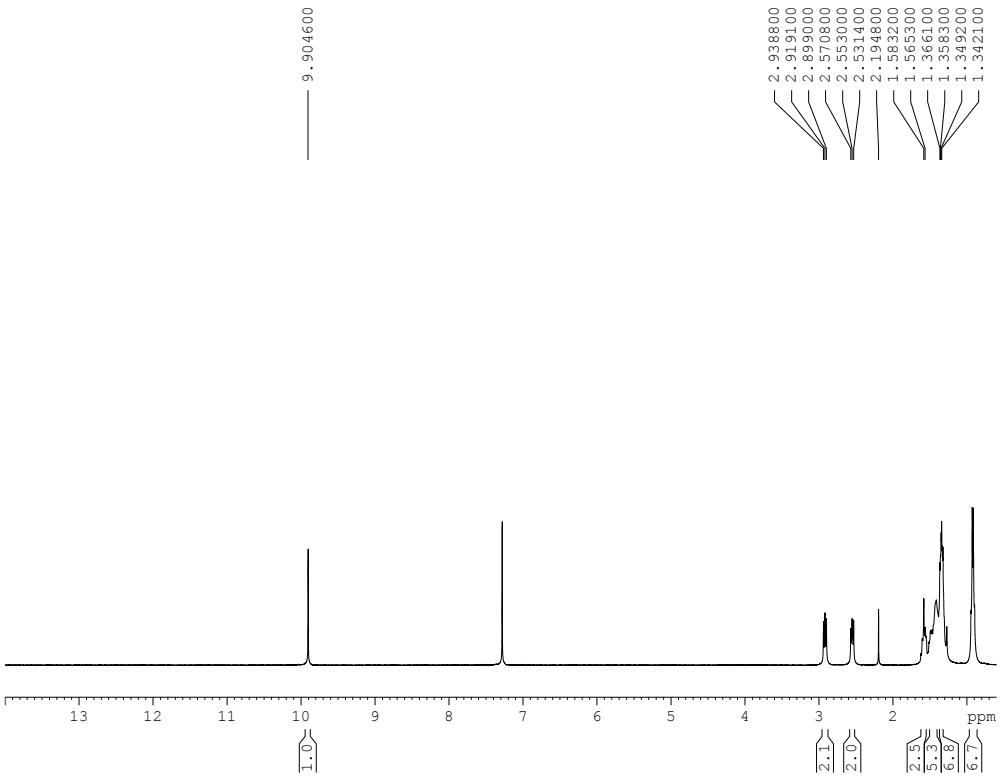

Figure 138. ^{1}H-NMR spectrum (400 MHz, $CDCl_3$) of **C1**

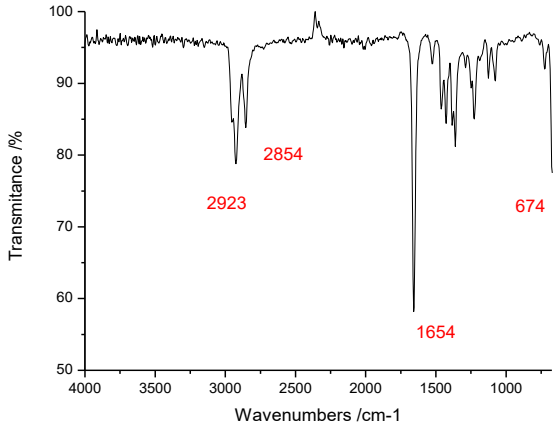

Figure 139. FT-IR spectrum of **C1**

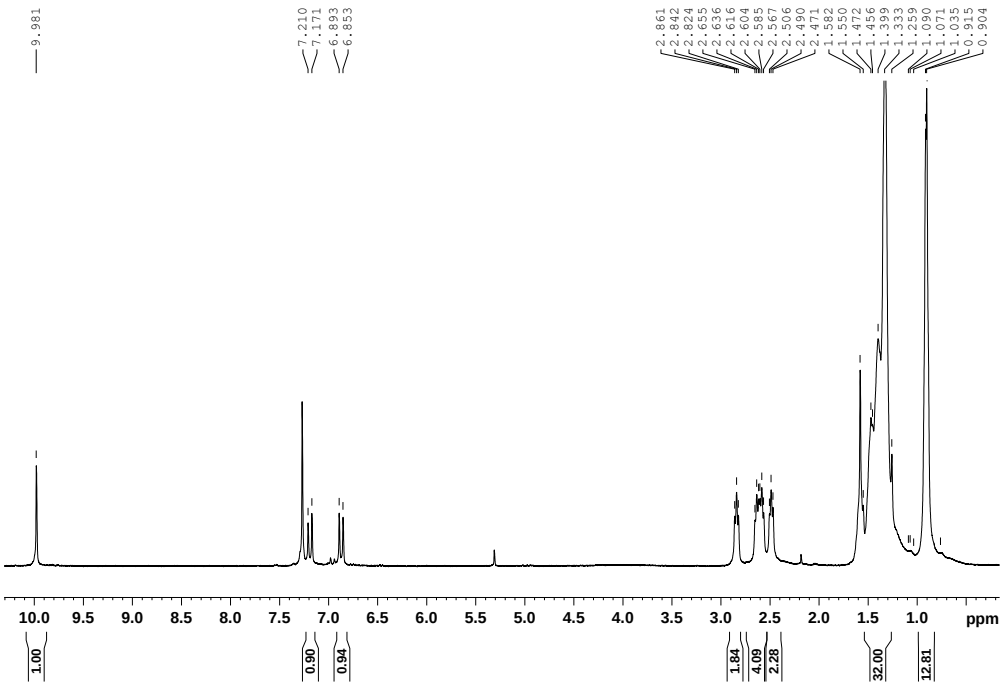

Figure 140. ^{1}H-NMR spectrum (400 MHz, $CDCl_3$) of **C2**

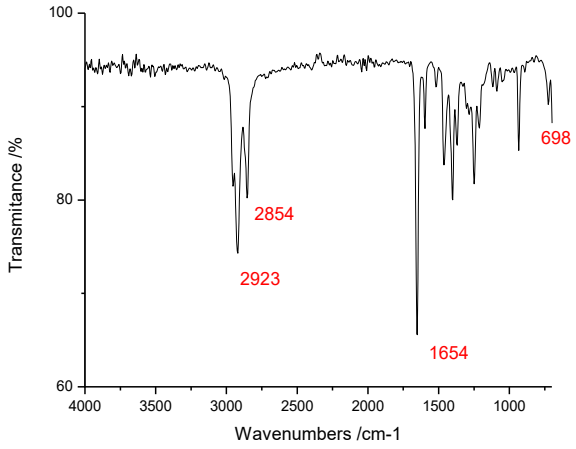

Figure 141. FT-IR spectrum of **C2**

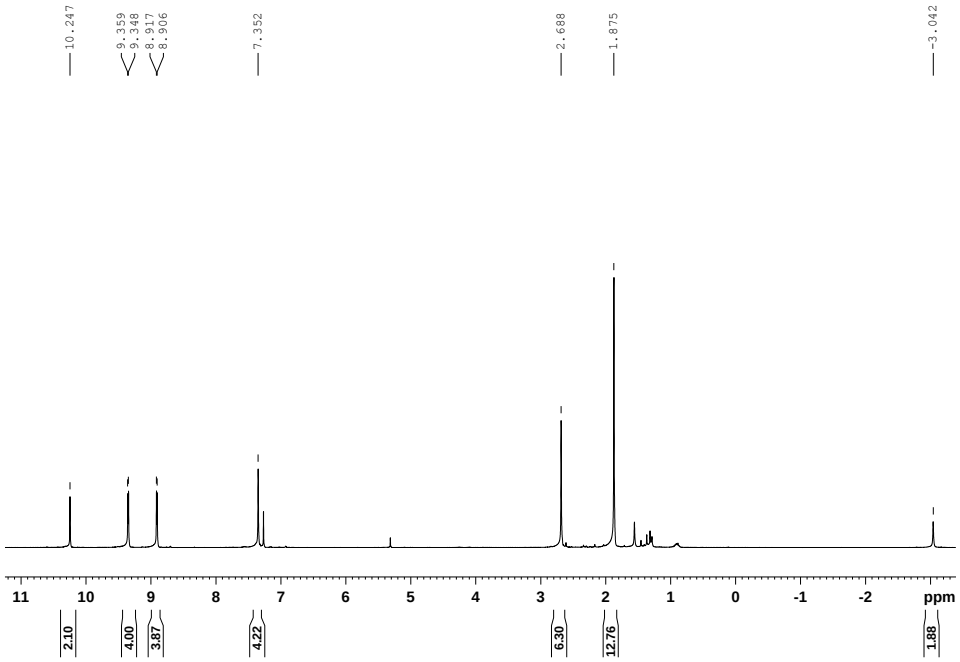

Figure 142. ^{1}H-NMR spectrum (400 MHz, $CDCl_3$) of of 5,15-bis-(2,4,6-trimethylphenyl)porphyrin

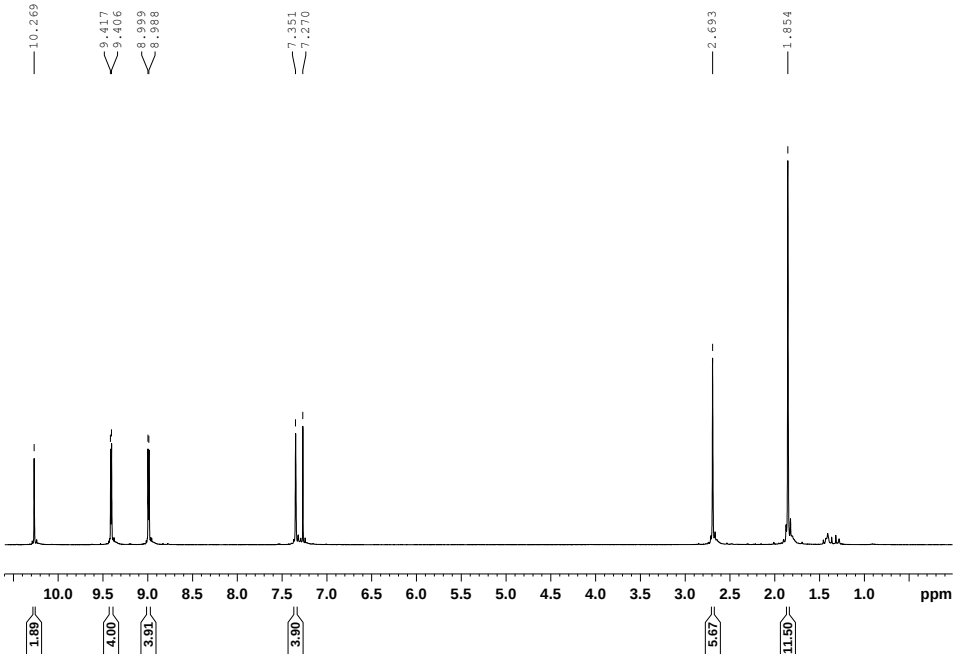

Figure 143. ^{1}H-NMR spectrum (400 MHz, $CDCl_3$) of [5,15-dimesitylporphyrinato] zinc

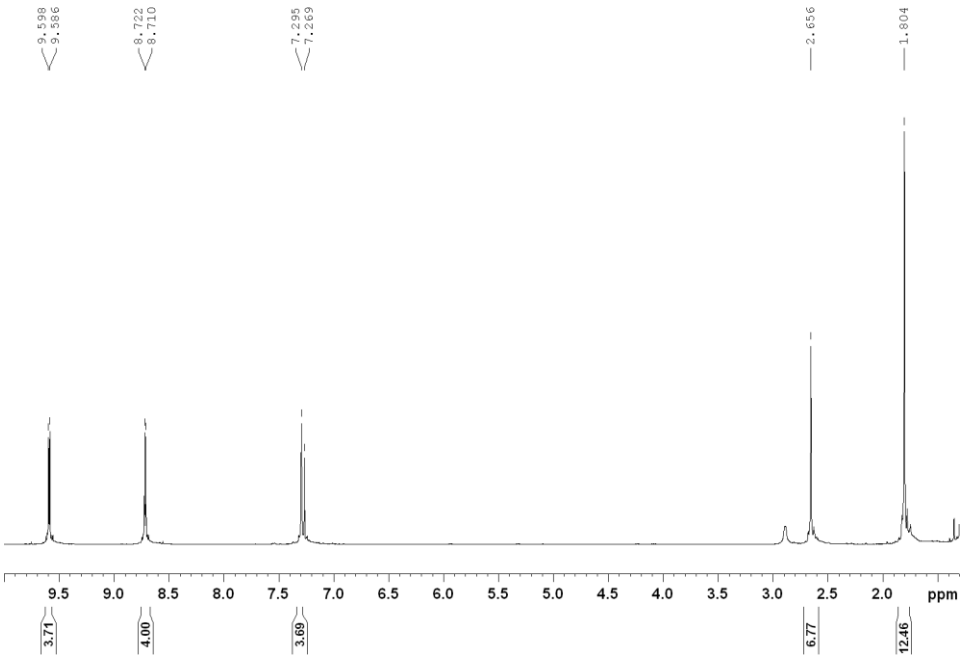

Figure 144. ^{1}H-NMR spectrum (400 MHz, $CDCl_3$) of [5,15-dibromo-10,20-dimesitylporphyrinato] zinc (II)

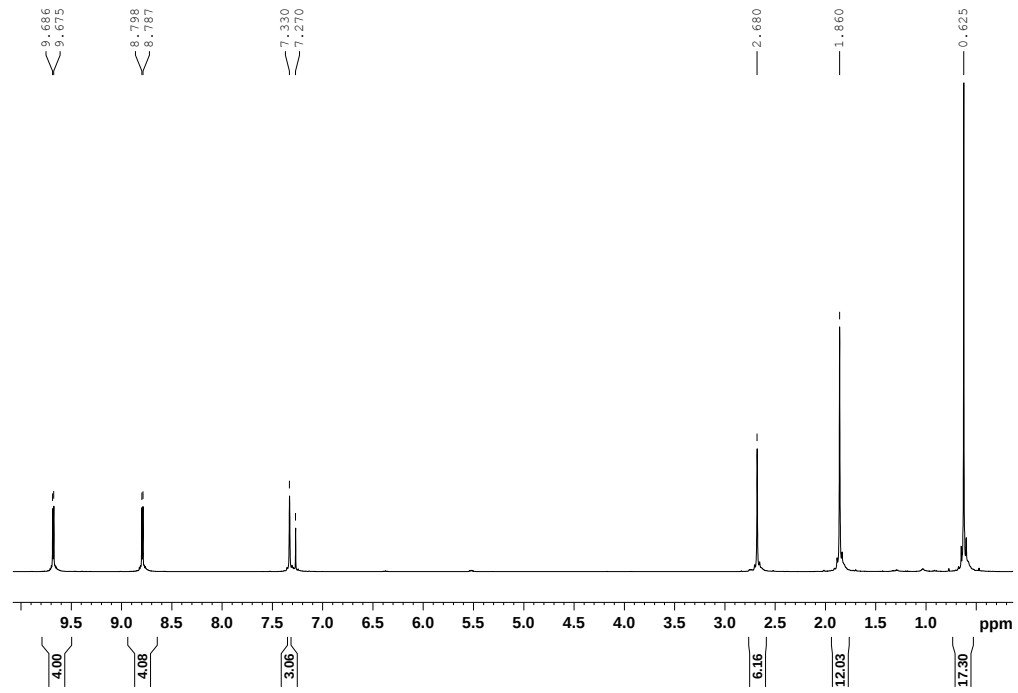

Figure 145. ^{1}H-NMR spectrum (400 MHz, $CDCl_3$) of [5,15-bis-(trimethylsilyl)ethynyl)-10,20-dimesitylporphyrinato] zinc (II), **P1**

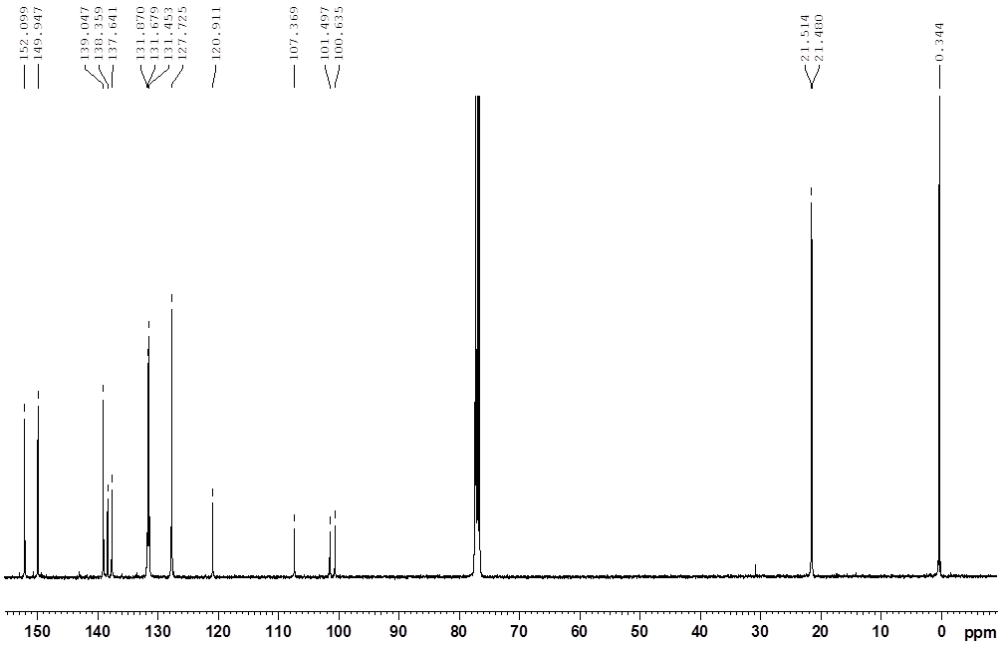

Figure 146. ^{13}C-NMR spectrum (100 MHz, $CDCl_3$) of [5,15-bis-(trimethylsilyl)ethynyl)-10,20-dimesitylporphyrinato] zinc (II) (**P1**)

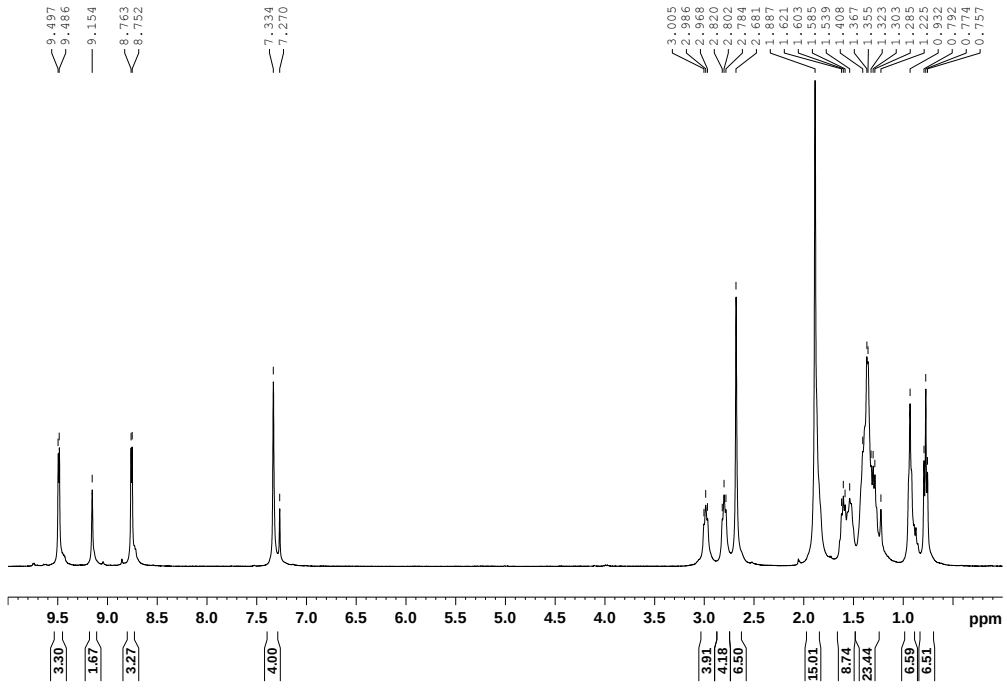

Figure 147. ^{1}H-NMR spectrum (400 MHz, $CDCl_3$) of **A1**

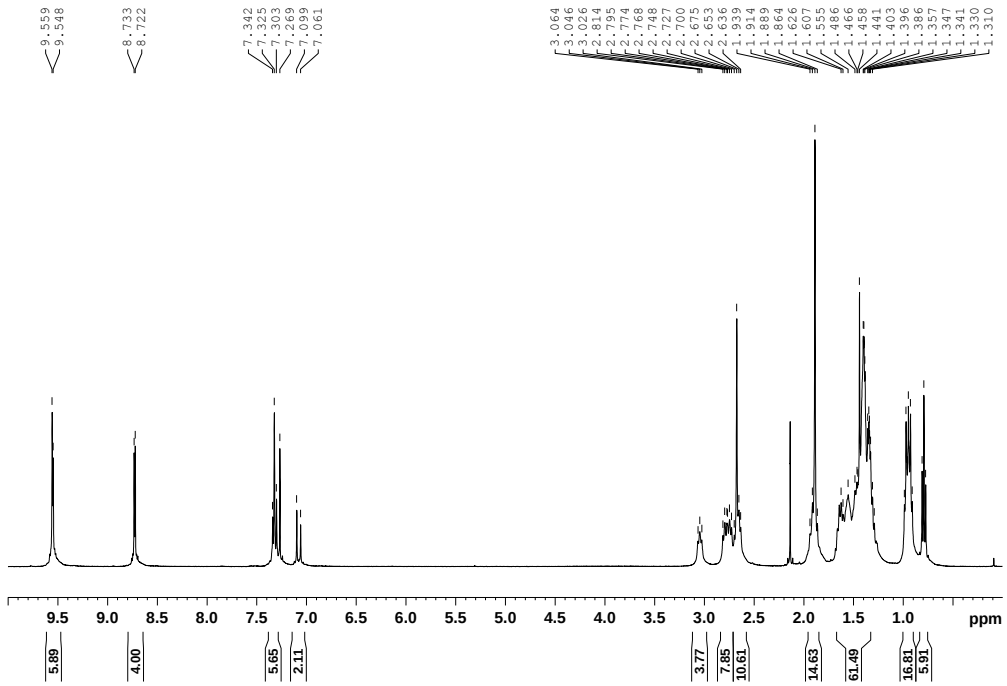

Figure 148. ^{1}H-NMR spectrum (400 MHz, $CDCl_3$) of **A2**

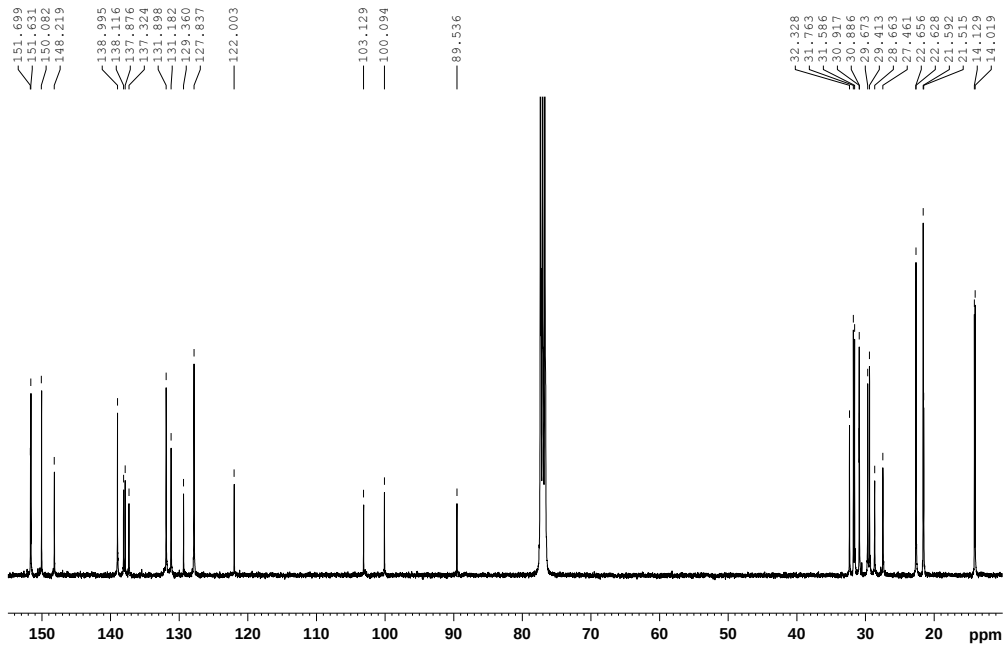

Figure 149. ^{13}C-NMR spectrum (100 MHz, $CDCl_3$) of **A1**

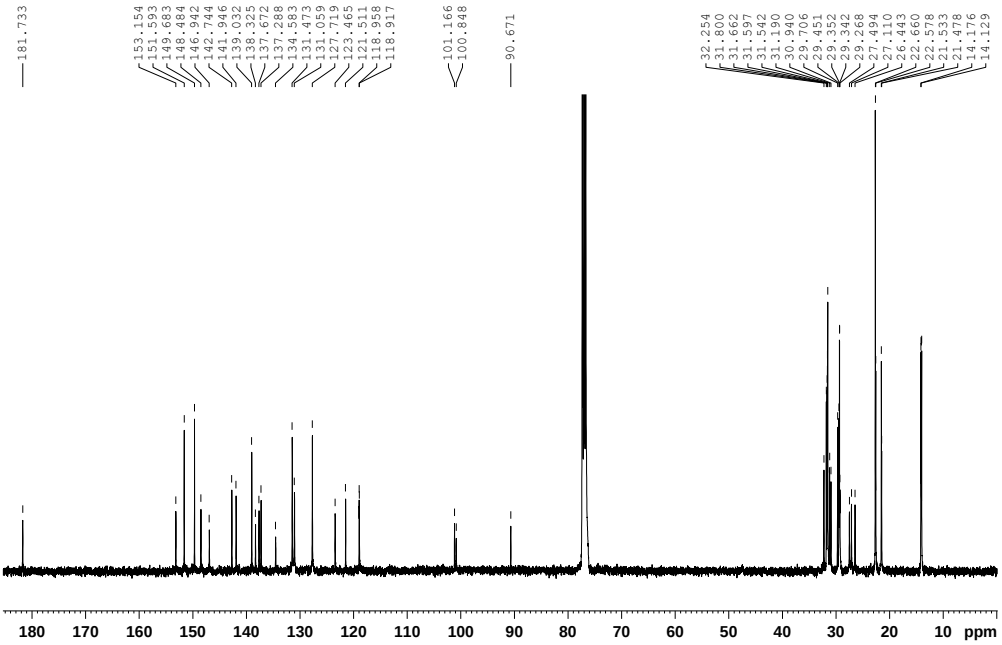

Figure 150. ^{13}C-NMR spectrum (100 MHz, CDCl3) of **A2**

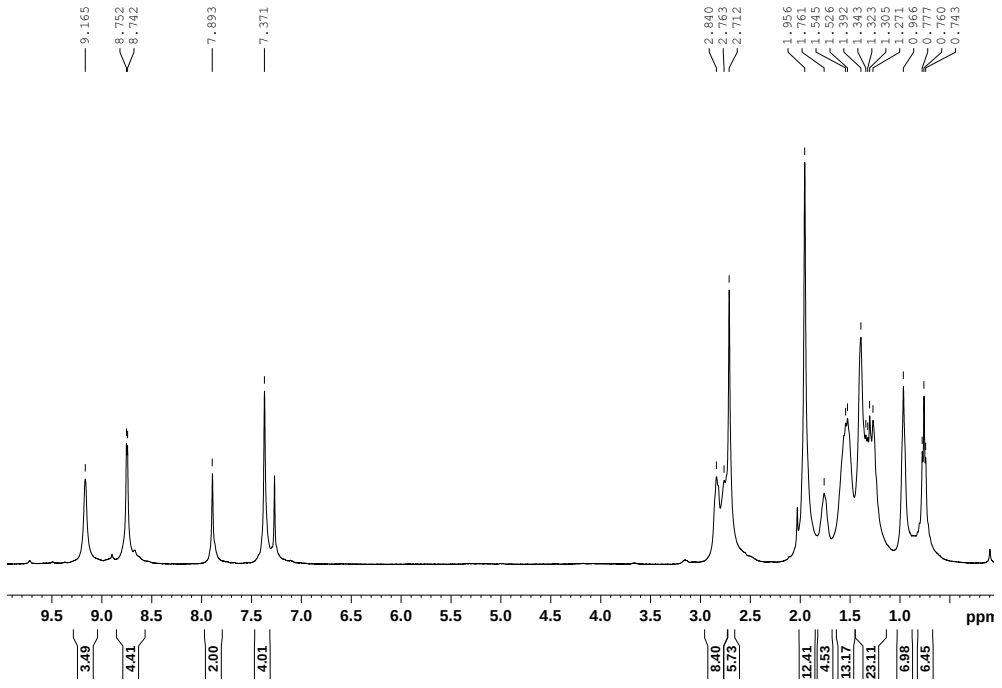

Figure 151. ^{1}H-NMR spectrum (400 MHz, $CDCl_3$) of **SA1**

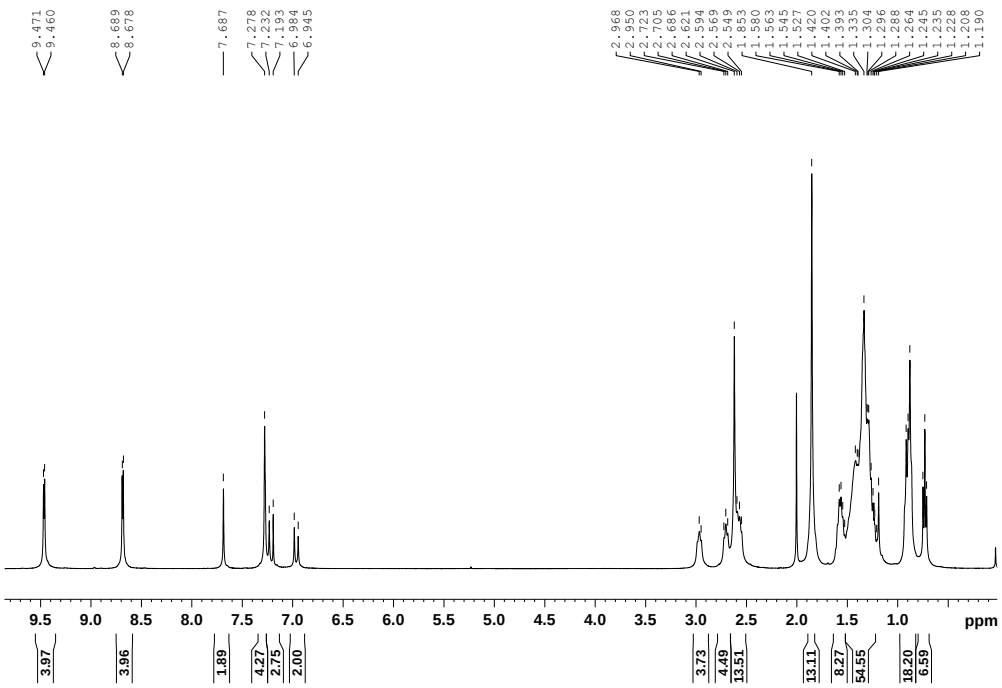

Figure 152. ^{1}H-NMR spectrum (400 MHz, $CDCl_3$) of **SA2**

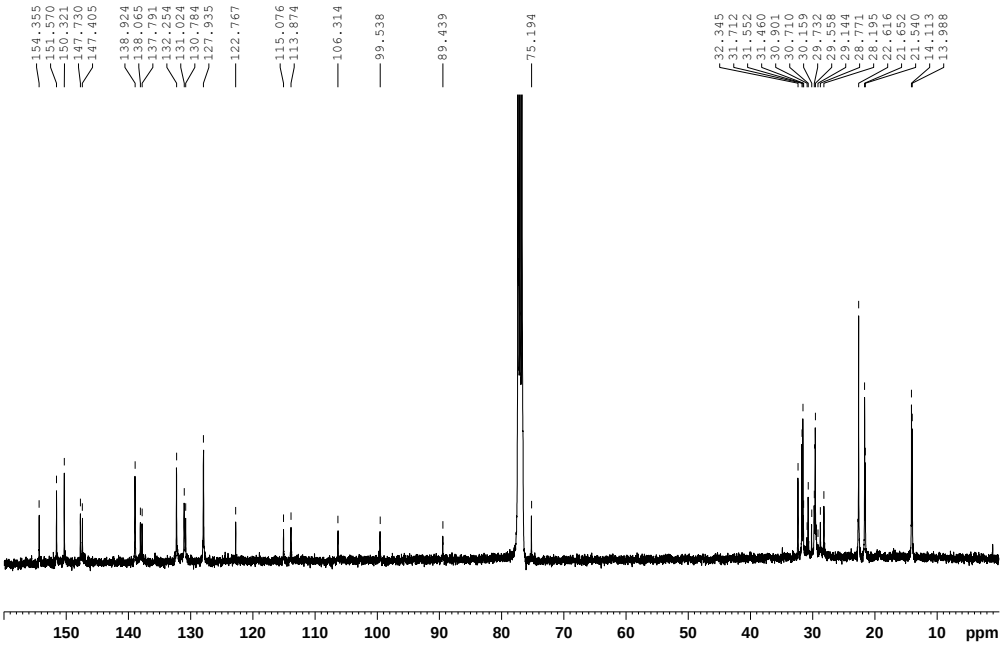

Figure 153. ^{13}C-NMR spectrum (100 MHz, $CDCl_3$) of **SA1**

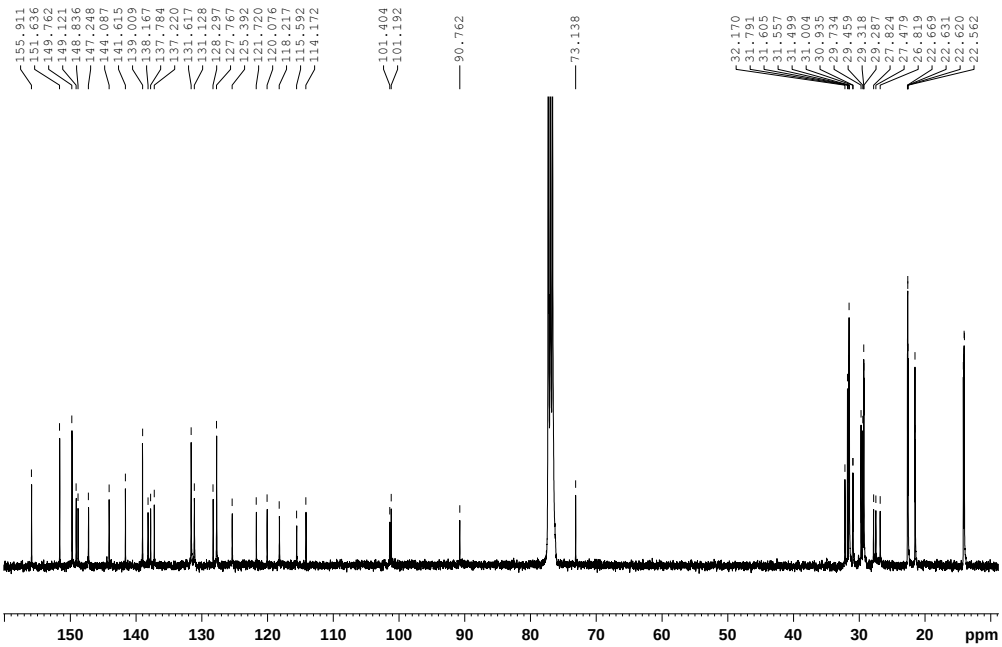

Figure 154. ^{13}C-NMR spectrum (100 MHz, $CDCl_3$) of **SA2**.

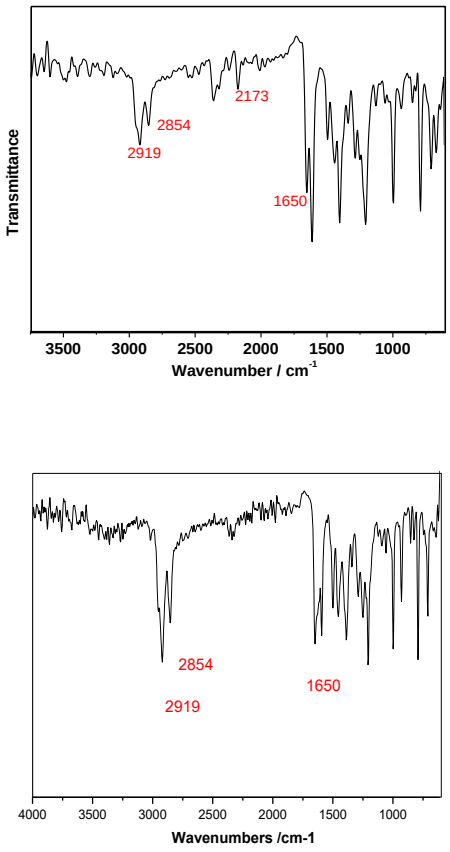

Figure 155. FT-IR spectra of compounds **A1** (left) and **A2** (right) (KBr)

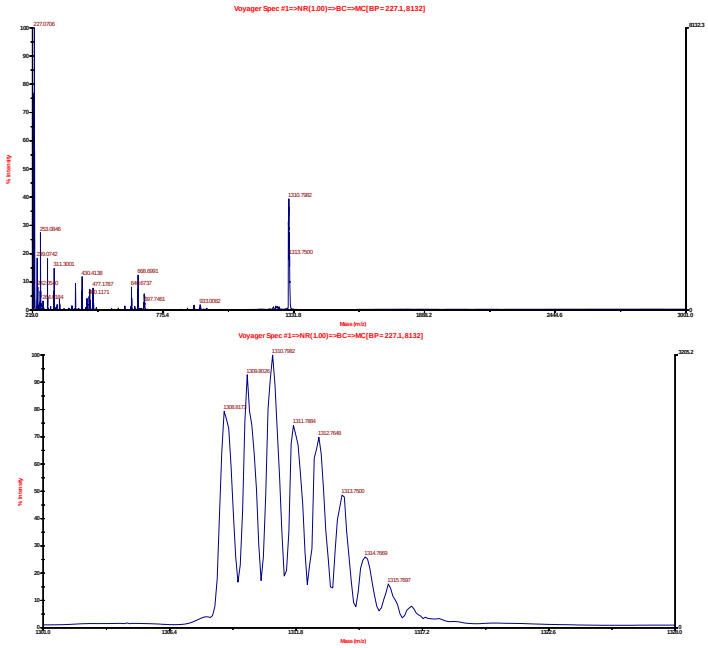

Figure 156. MALDI-MS spectrum of compound **SA1** (Matrix: Dithranol)

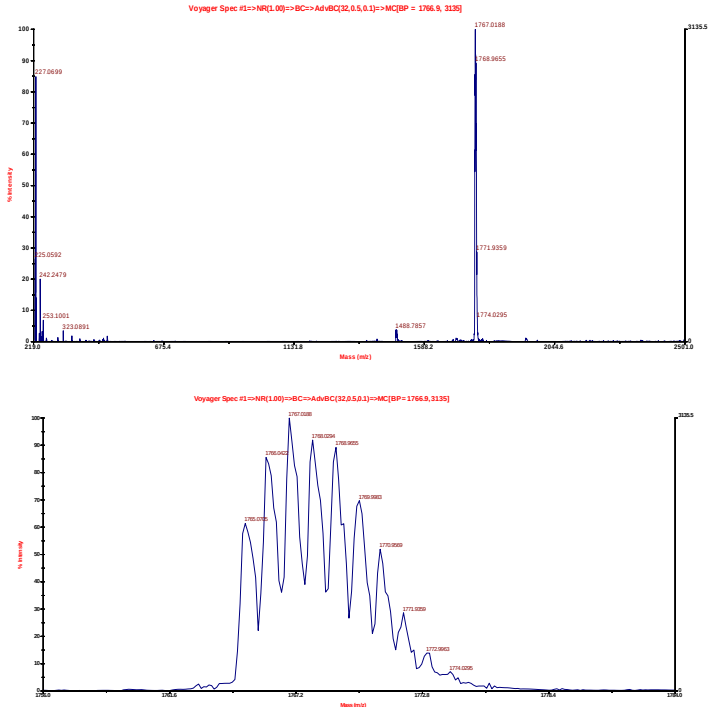

Figure 157. MALDI-MS spectrum of compound **SA2** (Matrix: Dithranol)

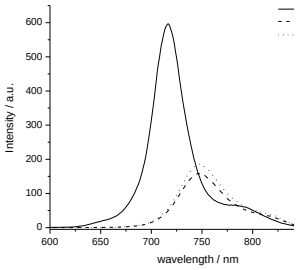

Figure 158. Emission spectrum of compounds **A2** and **SA2** (solid line λ_{exc} = 486nm, dash line λ_{exc} = 540 nm) in dichloromethane (10^{-5} M)

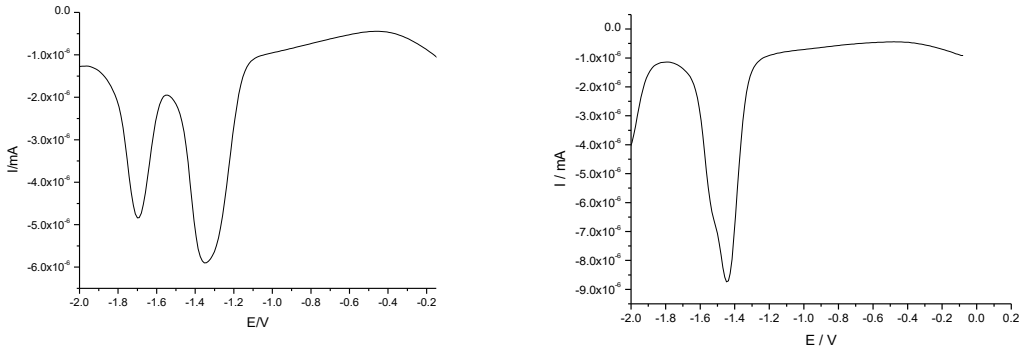

Figure 159. OSWV of compounds **SA1** (left) and **SA2** (right) (cathodic window)

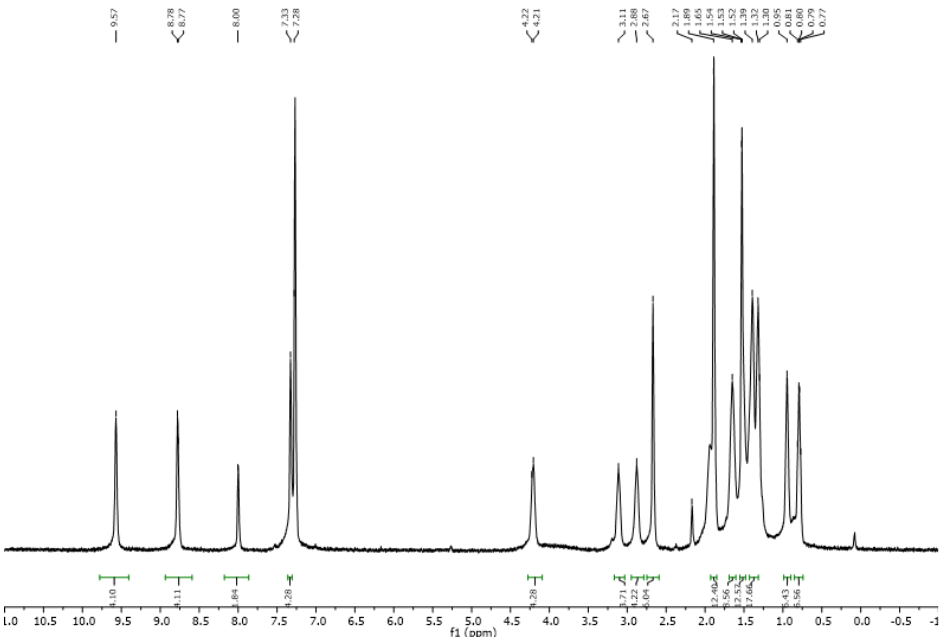

Figure 160. ^{1}H-NMR spectrum (400 MHz, $CDCl_3$) of **SA3**

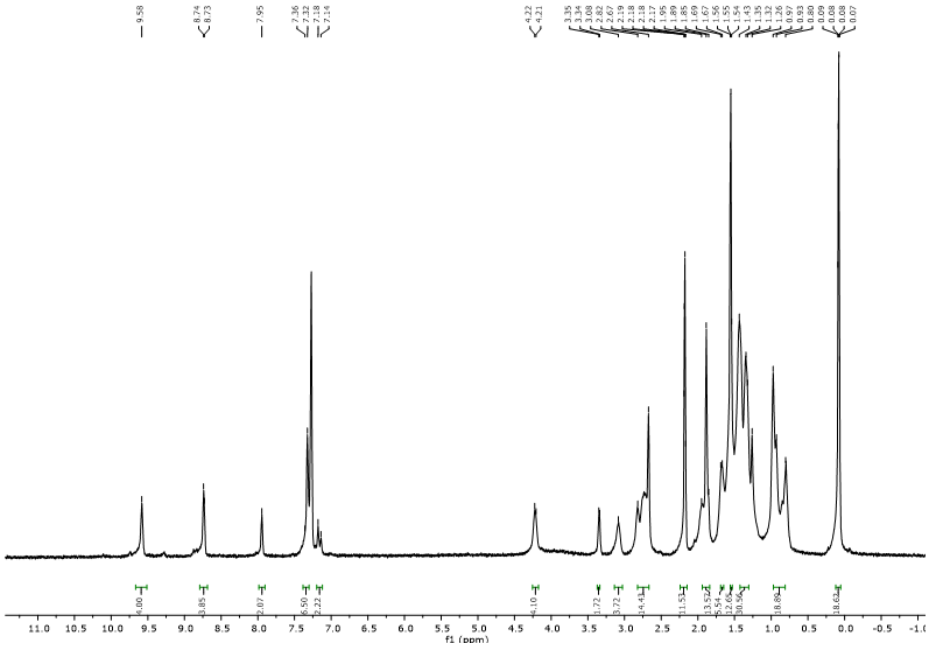

Figure 161. ^{1}H-NMR spectrum (400 MHz, $CDCl_3$) of **SA4**

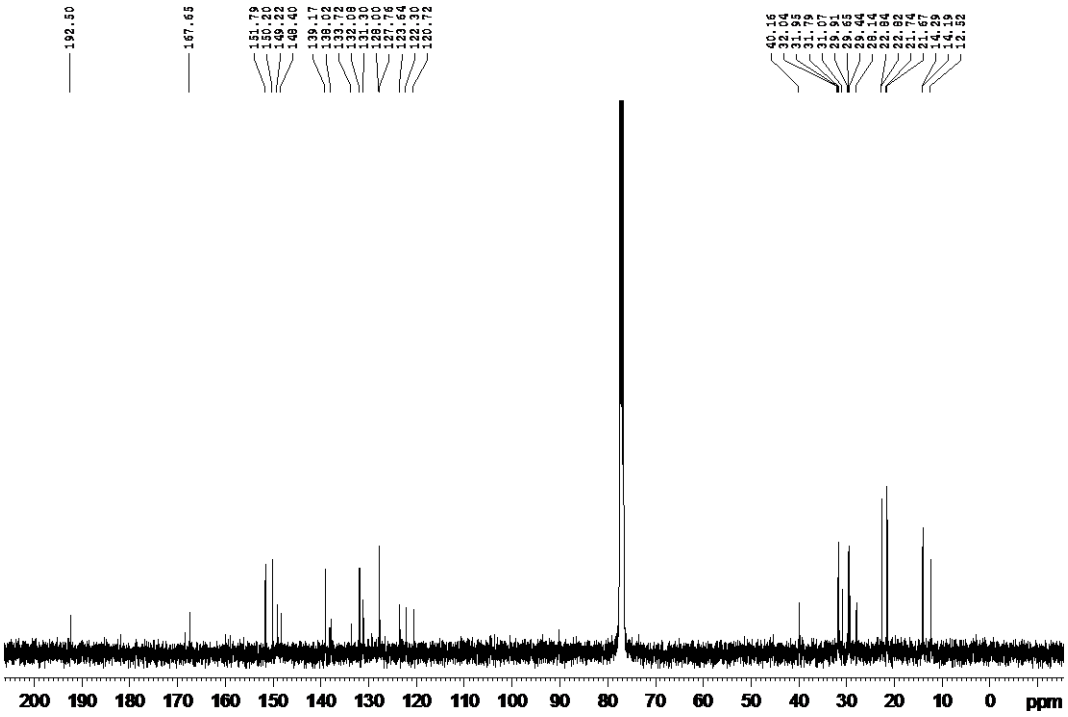

Figure 162. ^{13}C-NMR spectrum (100 MHz, $CDCl_3$) of **SA3**

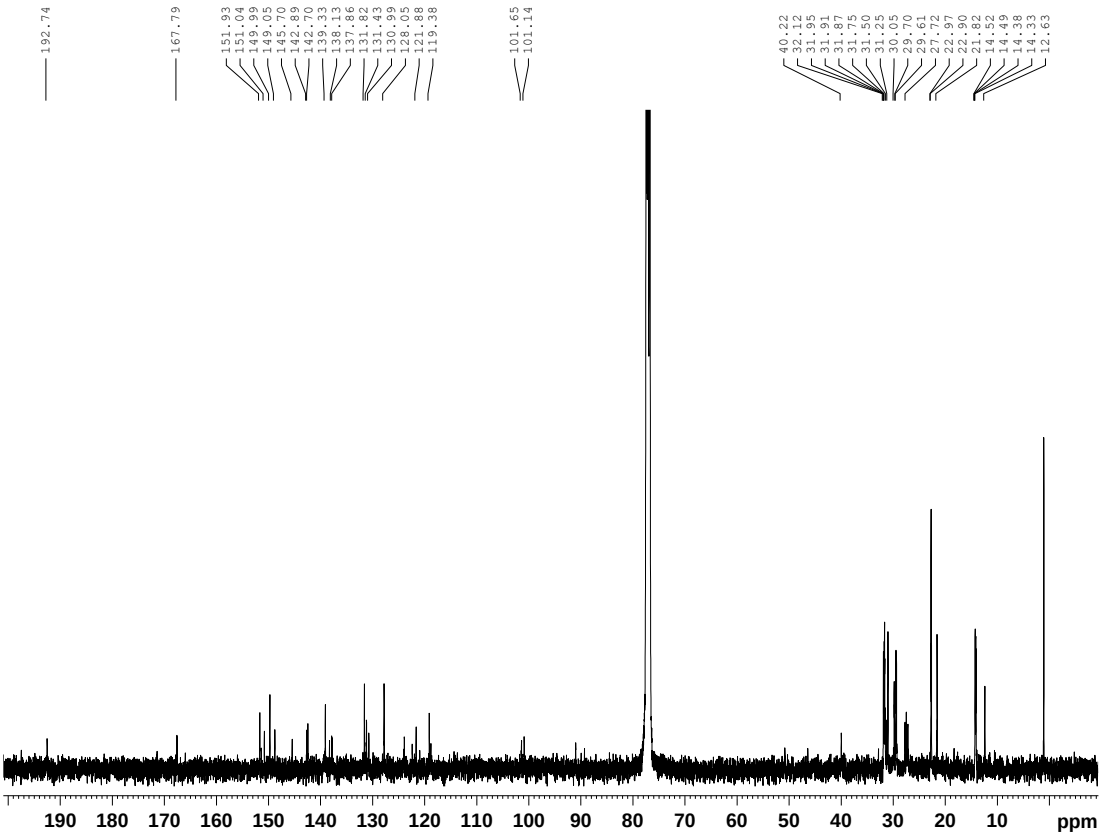

Figure 163. ^{13}C-NMR spectrum (100 MHz, $CDCl_3$) of **SA4**

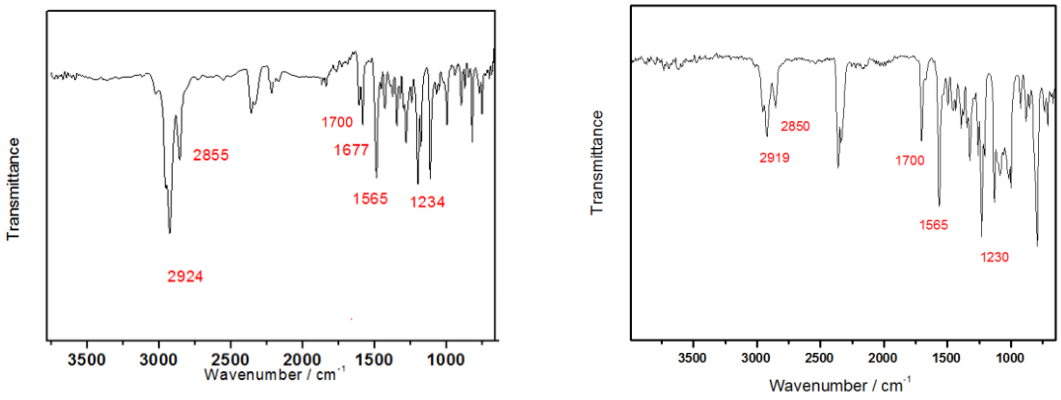

Figure 164. FT-IR spectra of **SA3** (left) and **SA4** (right) (NaCl window)

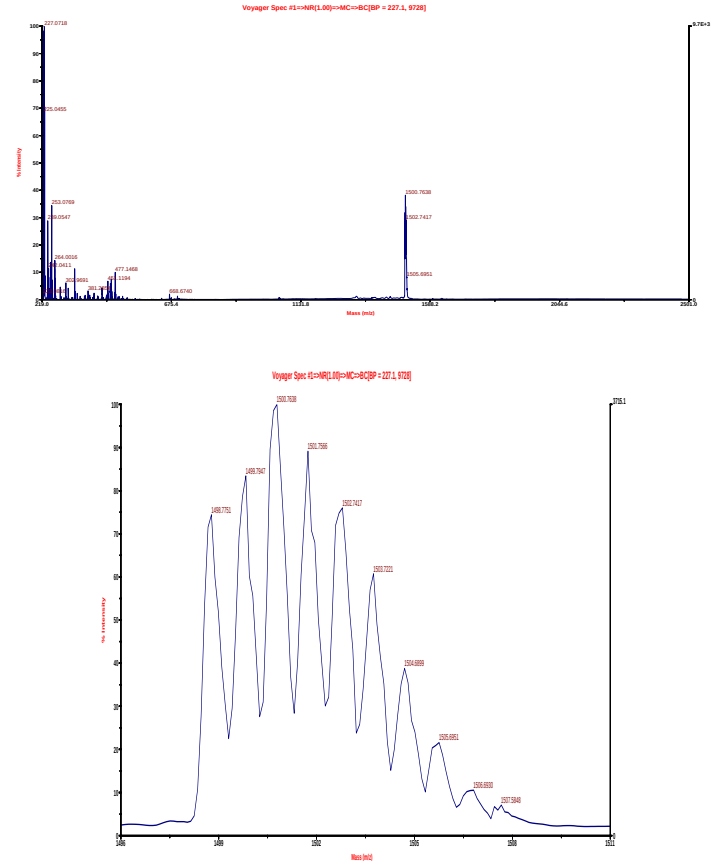

Figure 165. MALDI-MS spectrum of compound **SA3** (Matrix: Dithranol)

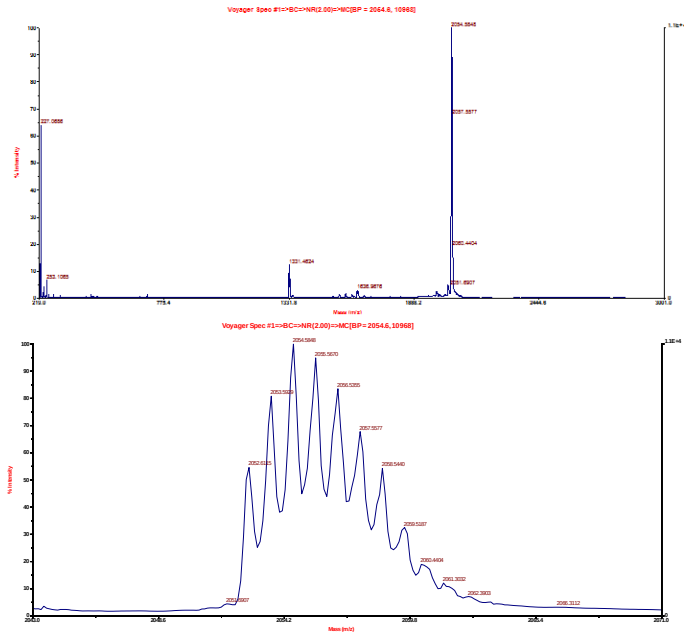

Figure 166. MALDI-MS spectrum of compound **SA4** (Matrix: Dithranol)

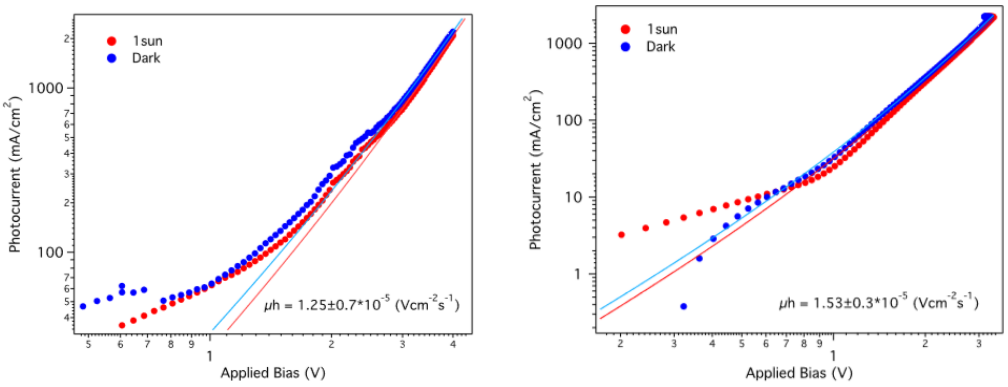

Figure 167. J-V curves for the hole only device of a) **SA3** and b) **SA4** at 1 sun (Red) and dark (Blue); the solid lines represents the fitting to the SCLC equation

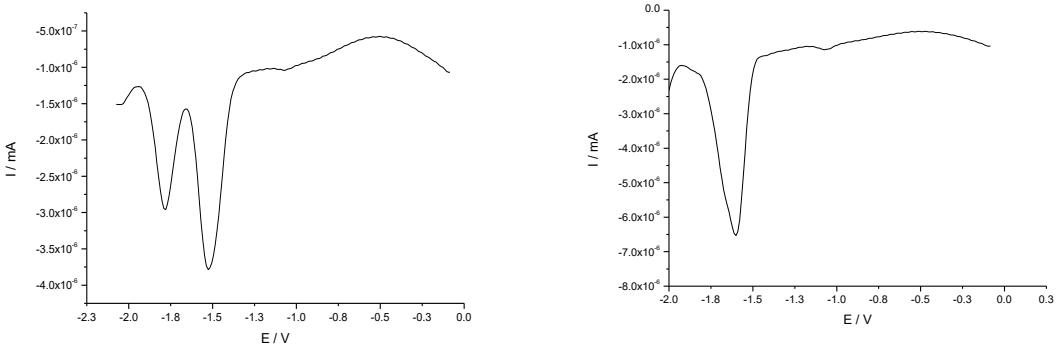

Figure 168. OSWV of compounds **SA3** and **SA4** (cathodic window)

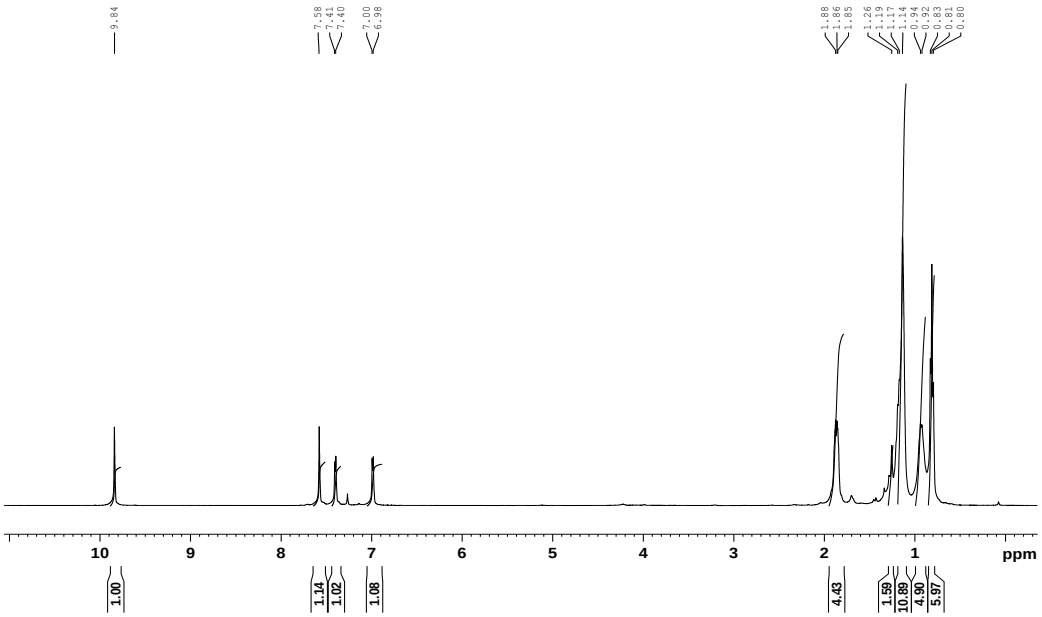

Figure 169. ^{1}H-NMR spectrum (400 MHz, $CDCl_3$) of **BTCCHO**

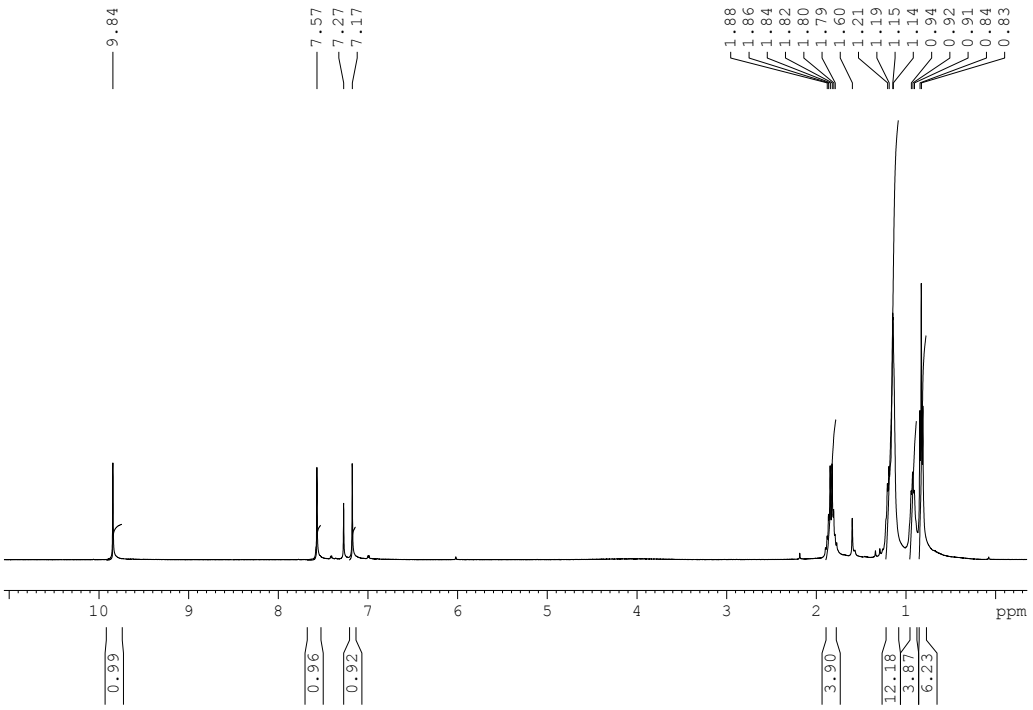

Figure 170. ^{1}H-NMR spectrum (400 MHz, $CDCl_3$) of **C3**

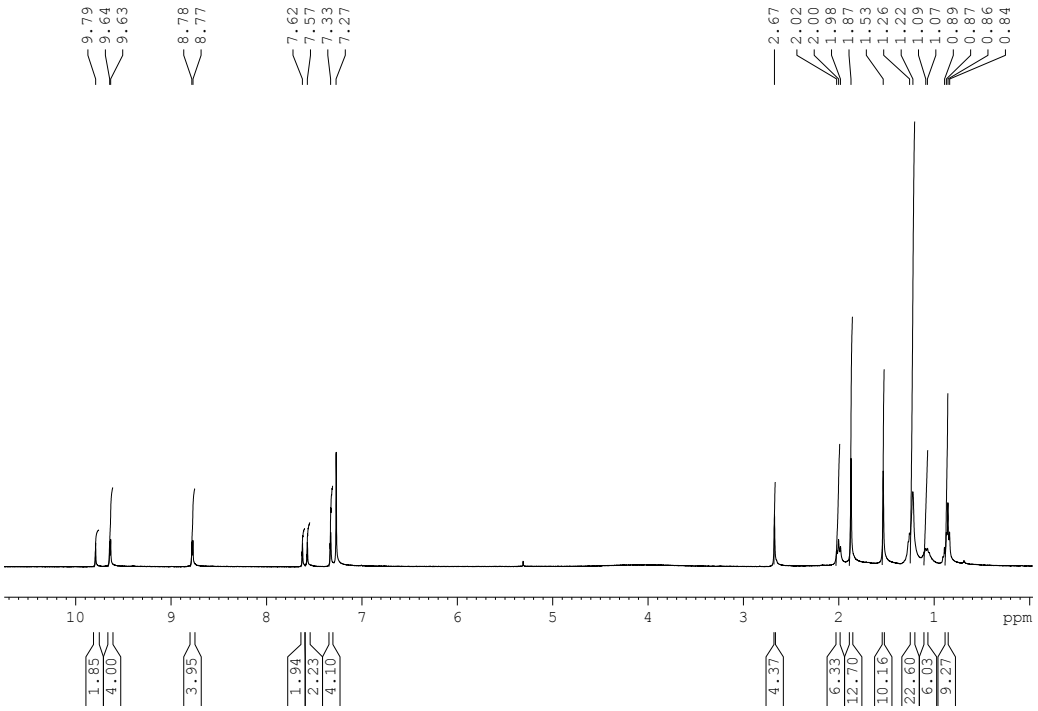

Figure 171. ^{1}H-NMR spectrum (400 MHz, $CDCl_3$) of **A3**

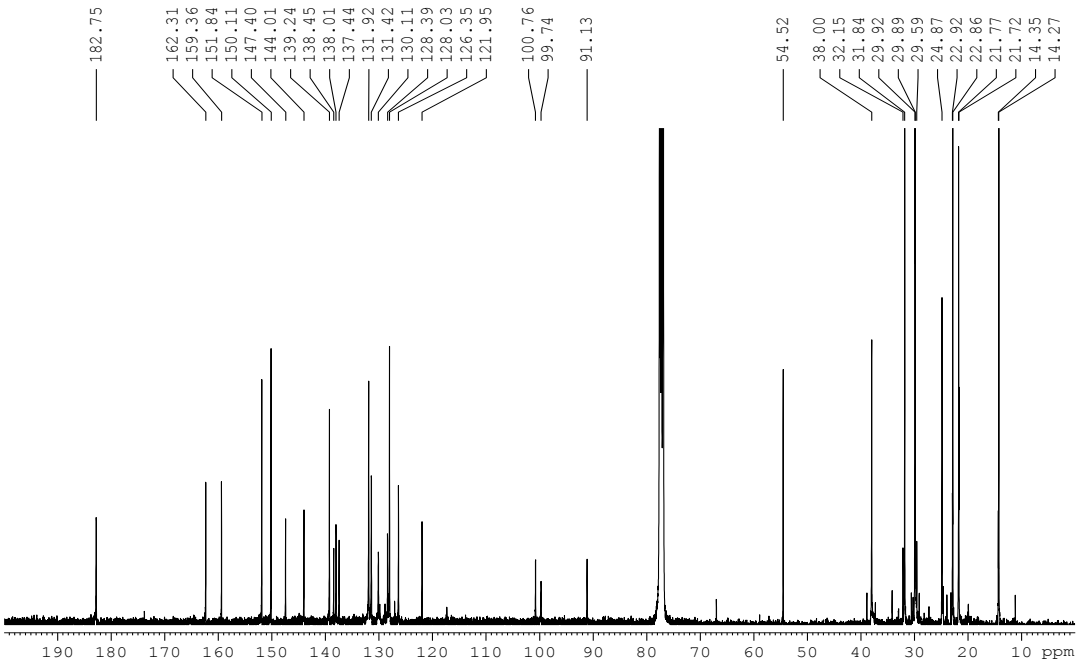

Figure 172. ^{13}C-NMR spectrum (100 MHz, $CDCl_3$) of **A3**

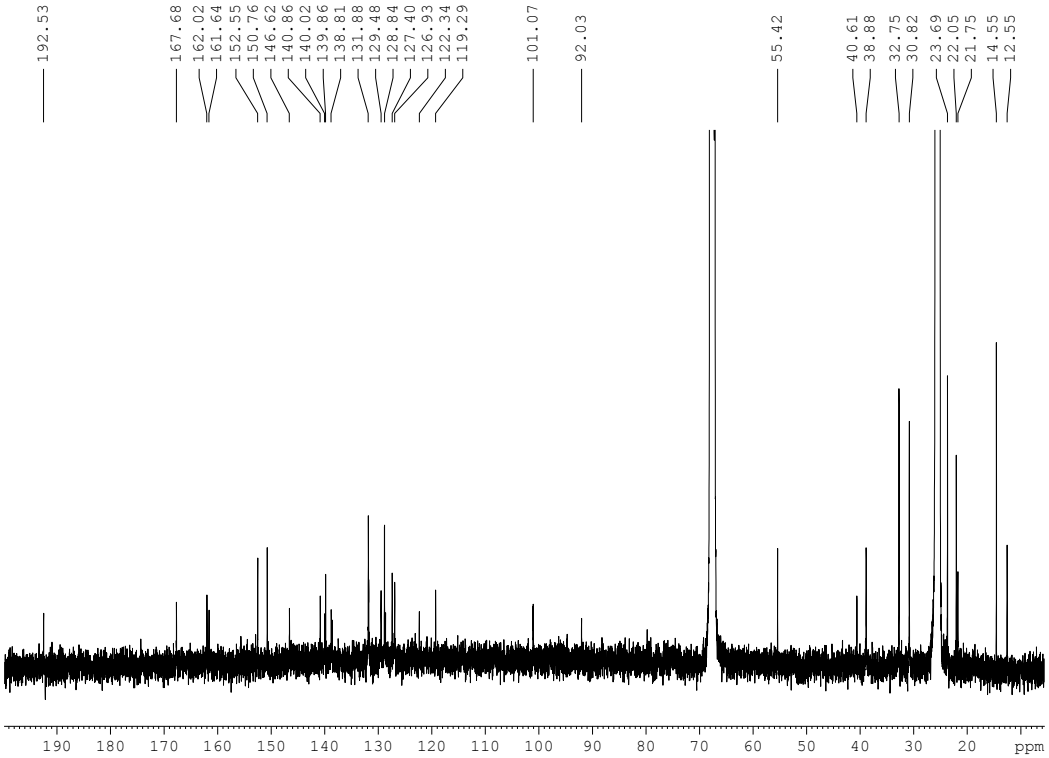

Figure 173. ^{13}C-NMR spectrum (100 MHz, $CDCl_3$) of **SA5**

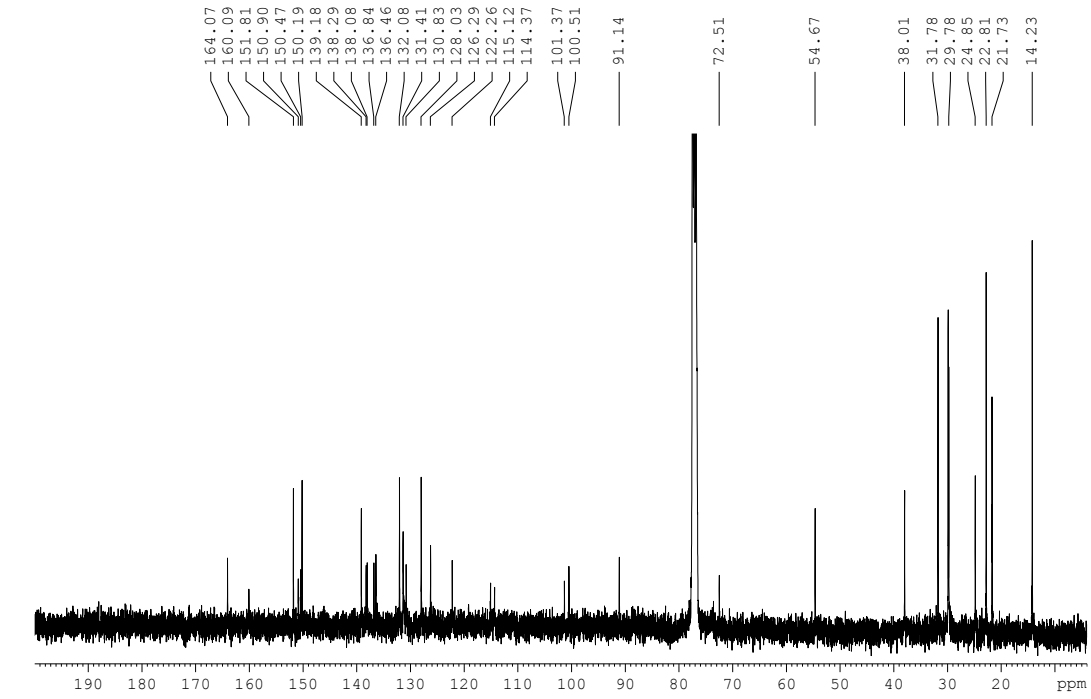

Figure 174. ^{13}C-NMR spectrum (100 MHz, $CDCl_3$) of **SA6**.

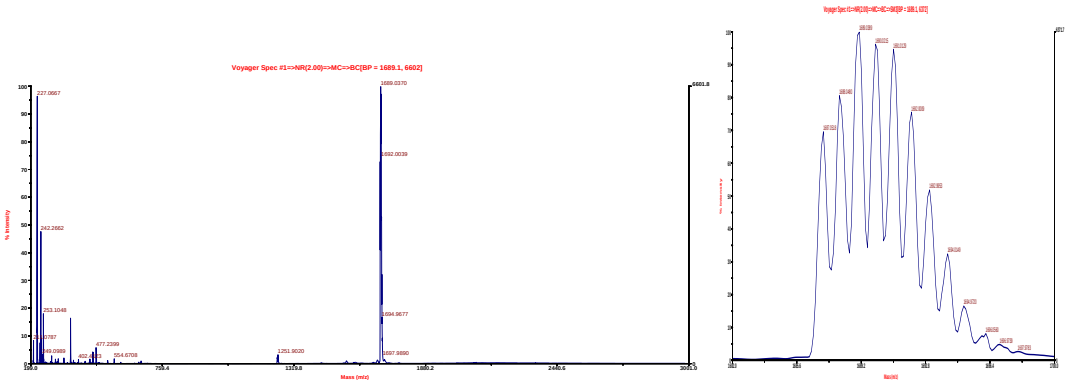

Figure 175. MALDI-MS spectrum of compound **SA5** (Matrix: Dithranol)

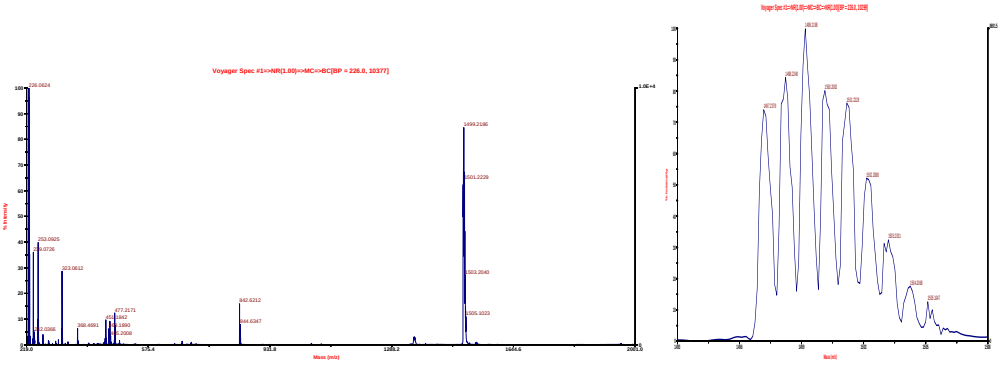

Figure 176. MALDI-MS spectrum of compound **SA6** (Matrix: Dithranol)

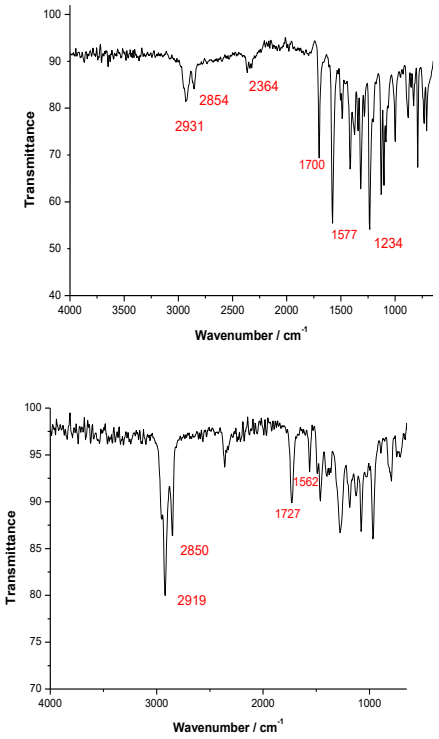

Figure 177. FT-IR spectra of compounds **SA5** and **SA6**

A) B)

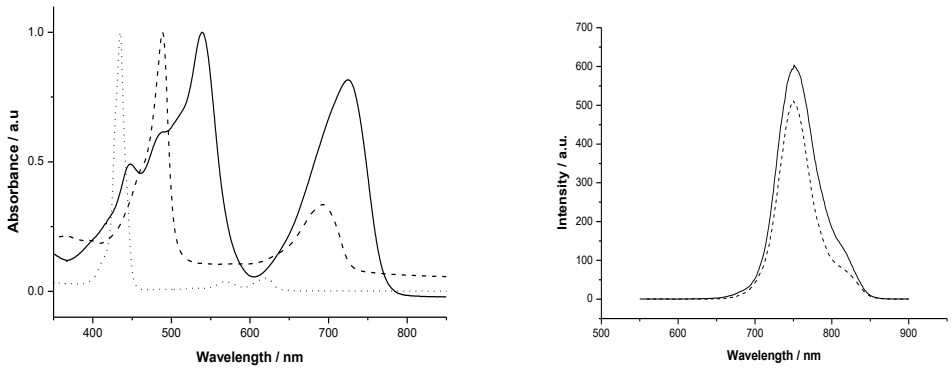

Figure 178. A) Normalized UV-Vis absorption spectra of compounds **SA6** (solid line) and precursors **A3** (dash line) and **P1** (dot line). B) Fluorescence spectra were recorded in CH_2Cl_2, exciting at the maxima of absorption (λ_{exc}= 539 nm for **SA5** (solid line), and λ_{exc}= 530 nm for **SA6** (dash line))

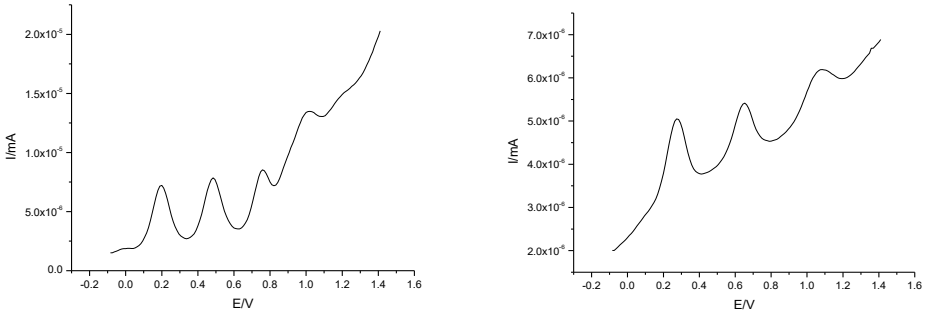

Figure 179. OSWV of compounds **SA5** (left) and **SA6** (right) referred to Fc/Fc^{+})

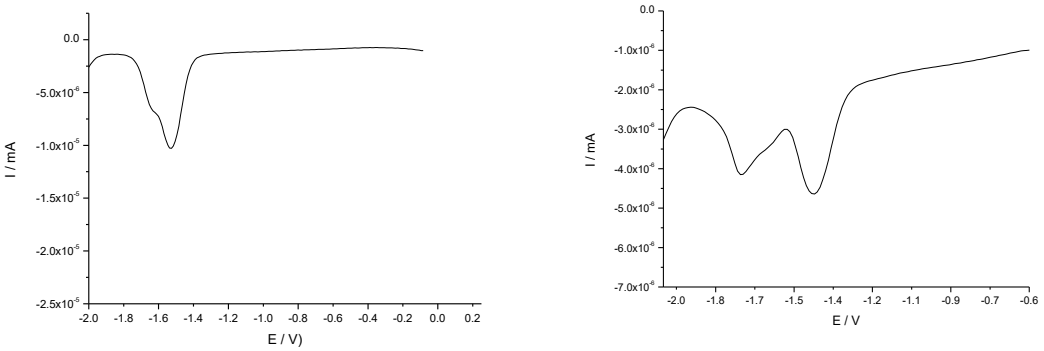

Figure 180. OSWV of compounds **SA5** (left) and **SA6** (right) (cathodic window)

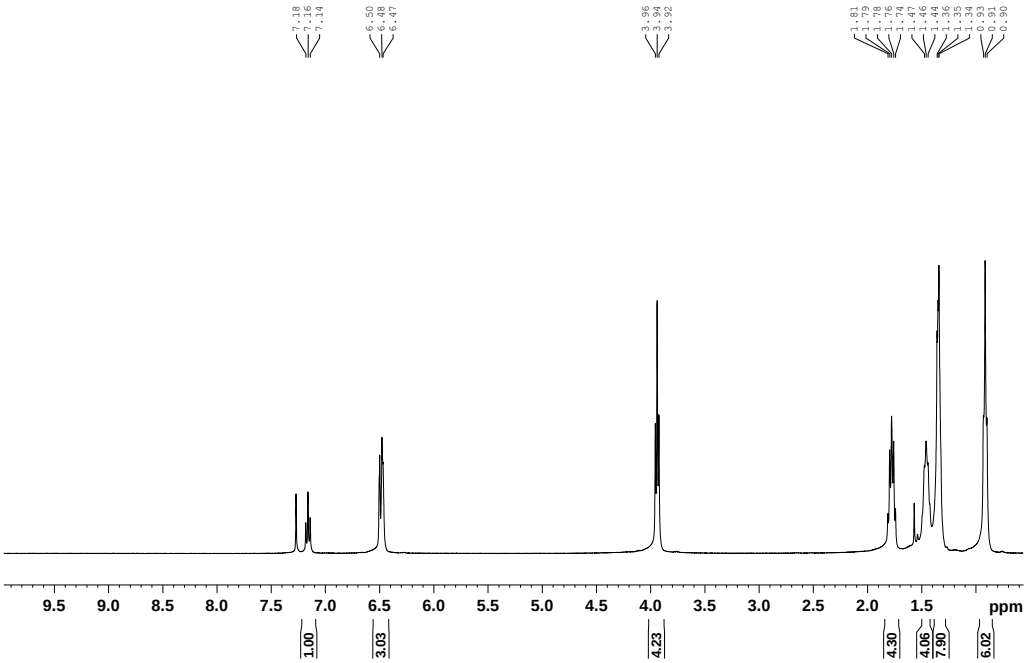

Figure 181. ^{1}H-NMR spectrum (400 MHz, $CDCl_3$) of 1,3-dihexyloxybenzene

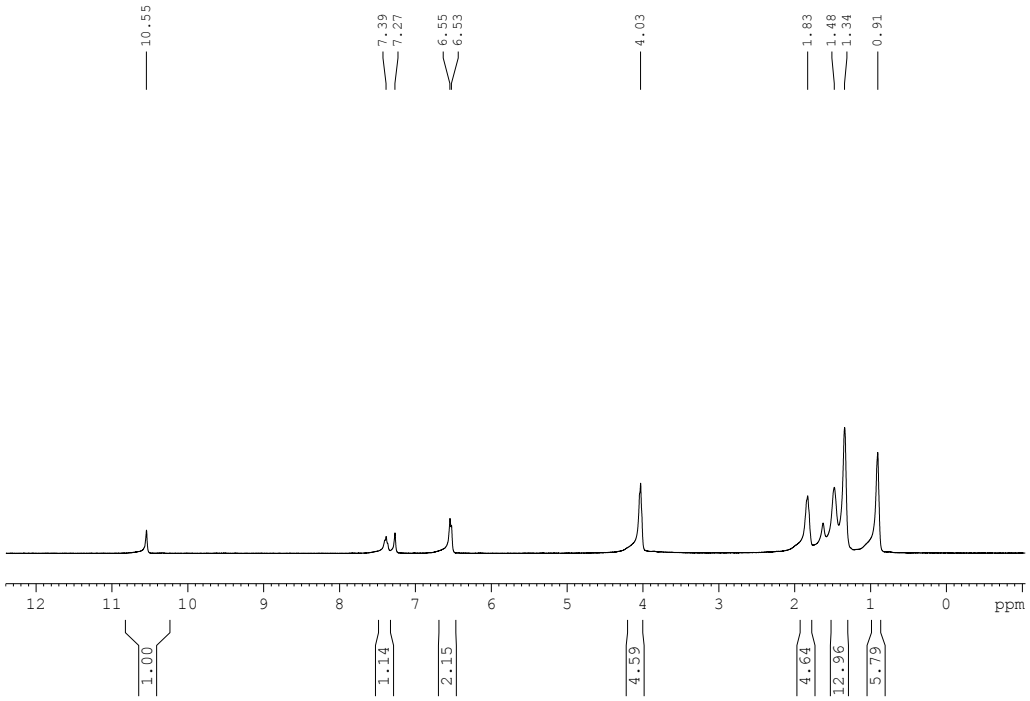

Figure 182. ^{1}H-NMR spectrum (400 MHz, $CDCl_3$) of 2,6-dihexyloxybenzaldehyde

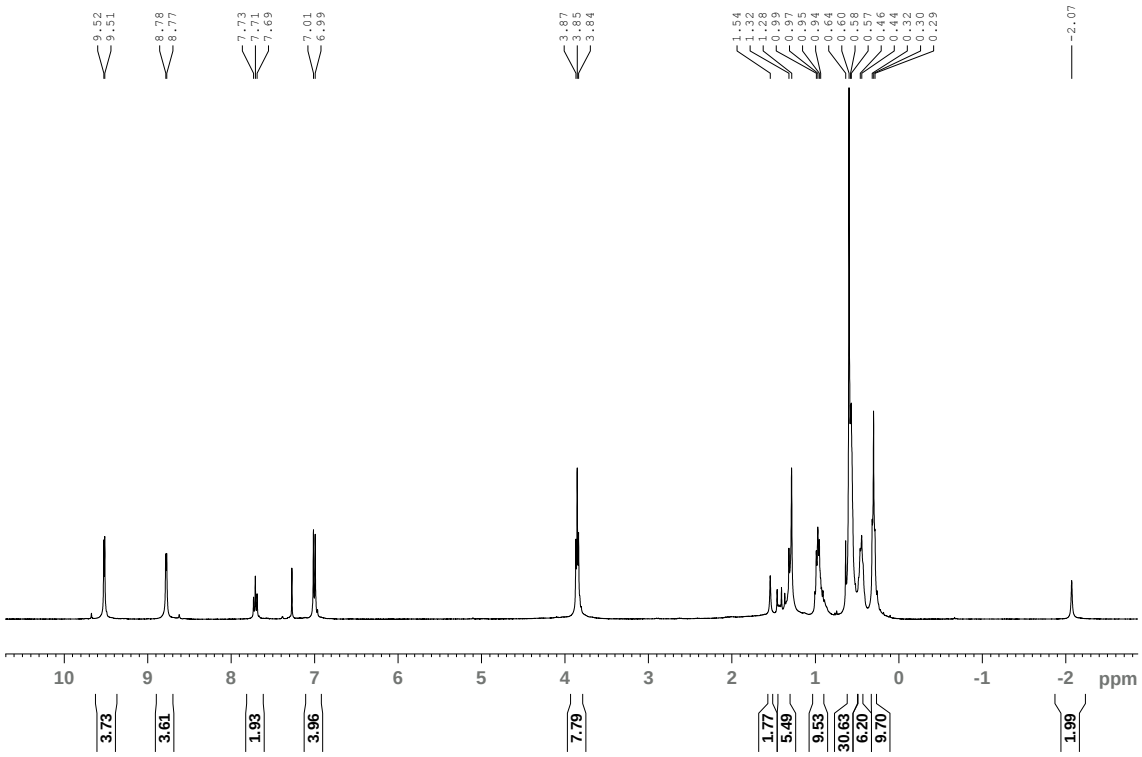

Figure 183. ^{1}H-NMR spectrum (400 MHz, CDCl3) of **P4**

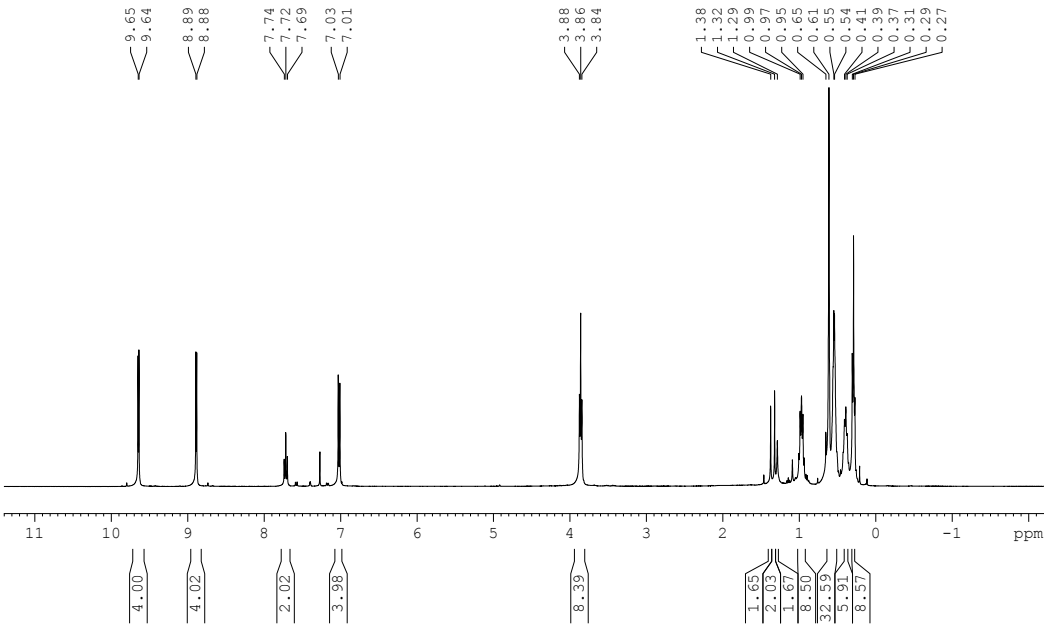

Figure 184. ^{1}H-NMR spectrum (400 MHz, $CDCl_3$) of **P4S**

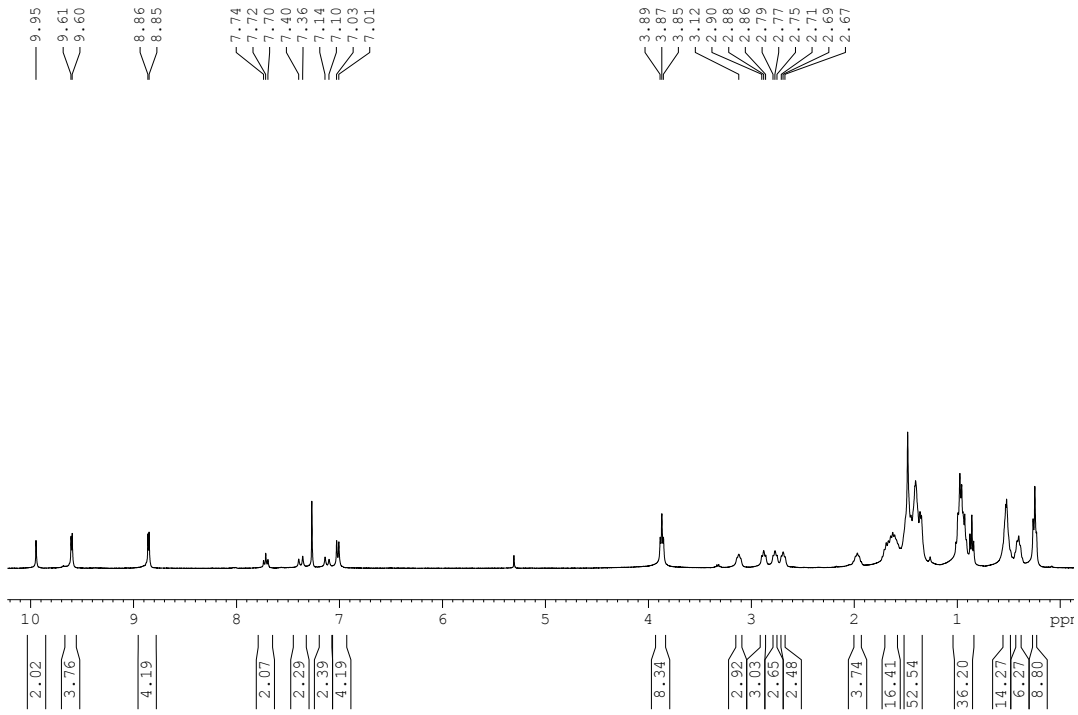

Figure 185. ^{1}H-NMR spectrum (400 MHz, $CDCl_3$) of **A4**

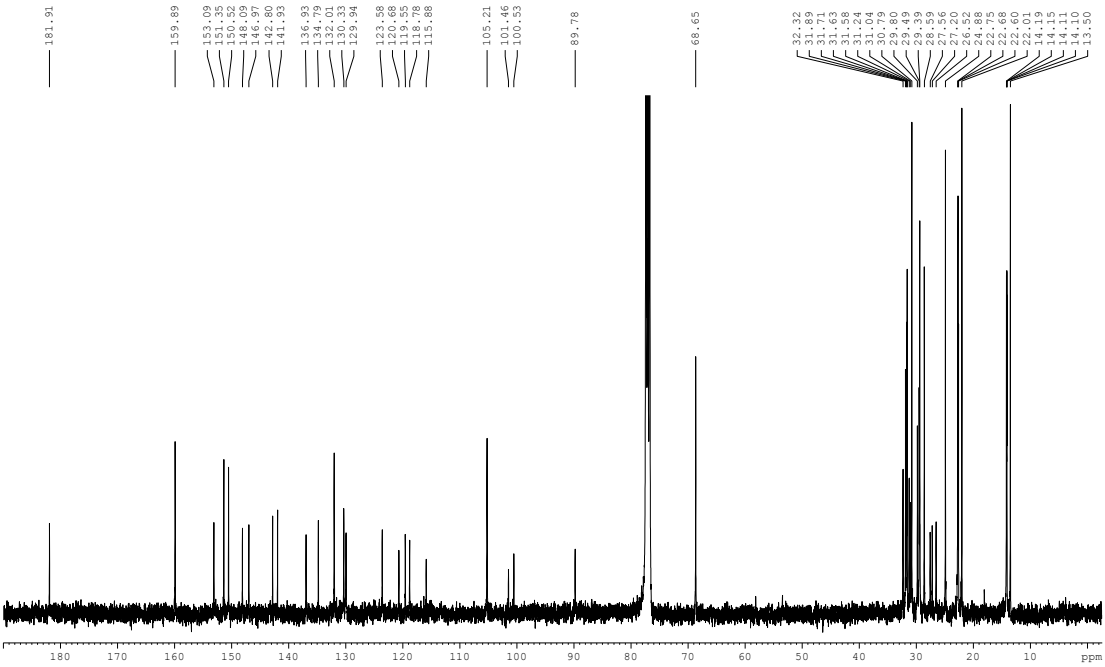

Figure 186. ^{13}C-NMR spectrum (100 MHz, $CDCl_3$) of **A4**

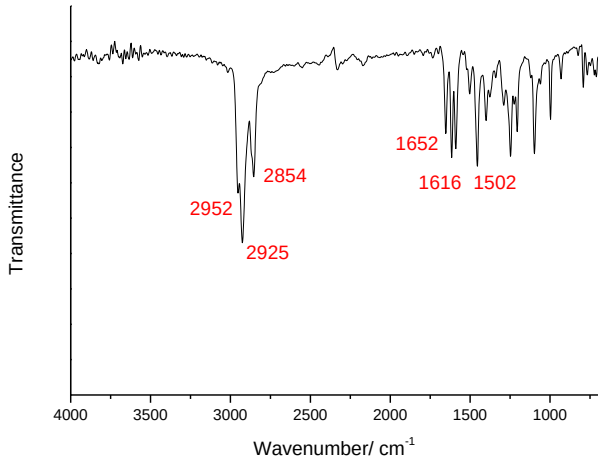

Figure 187. FT-IR spectrum of **A4**

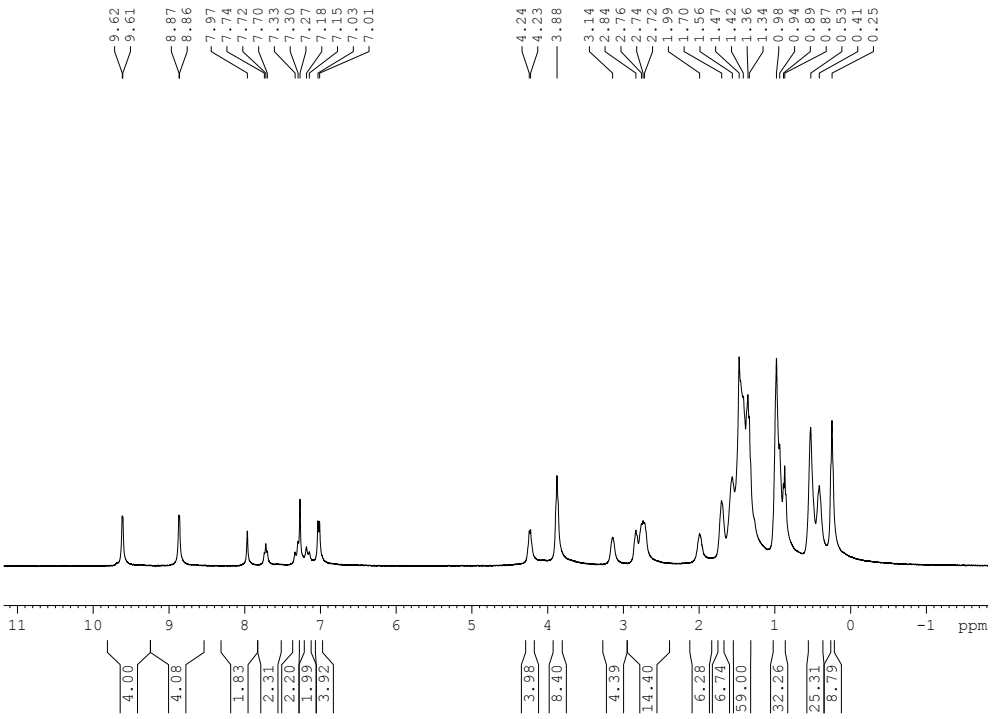

Figure 188. ^{1}H-NMR spectrum (400 MHz, $CDCl_3$) of **SA7**

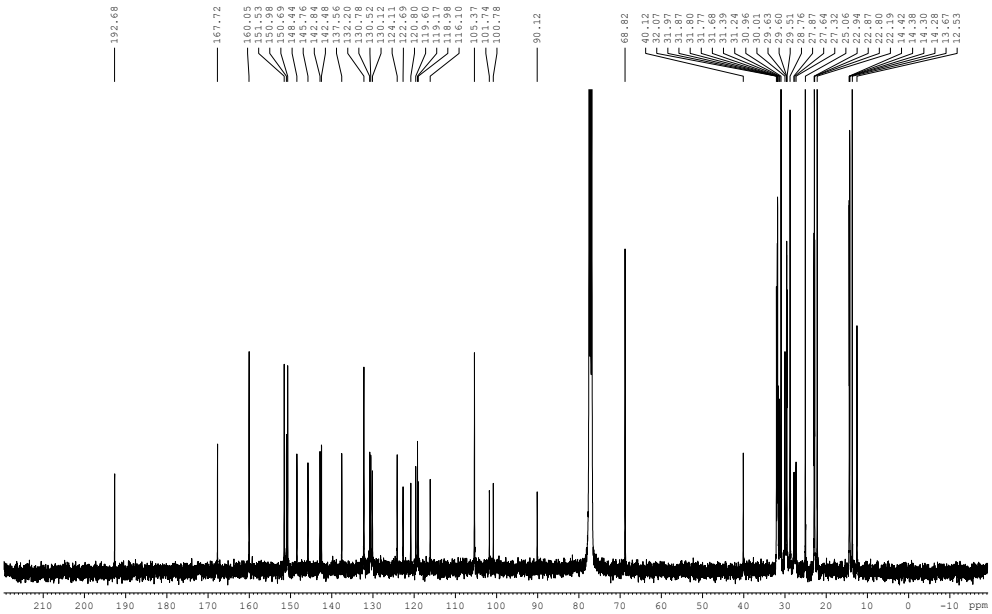

Figure 189. ^{13}C-NMR spectrum (100 MHz, $CDCl_3$) of **SA7**

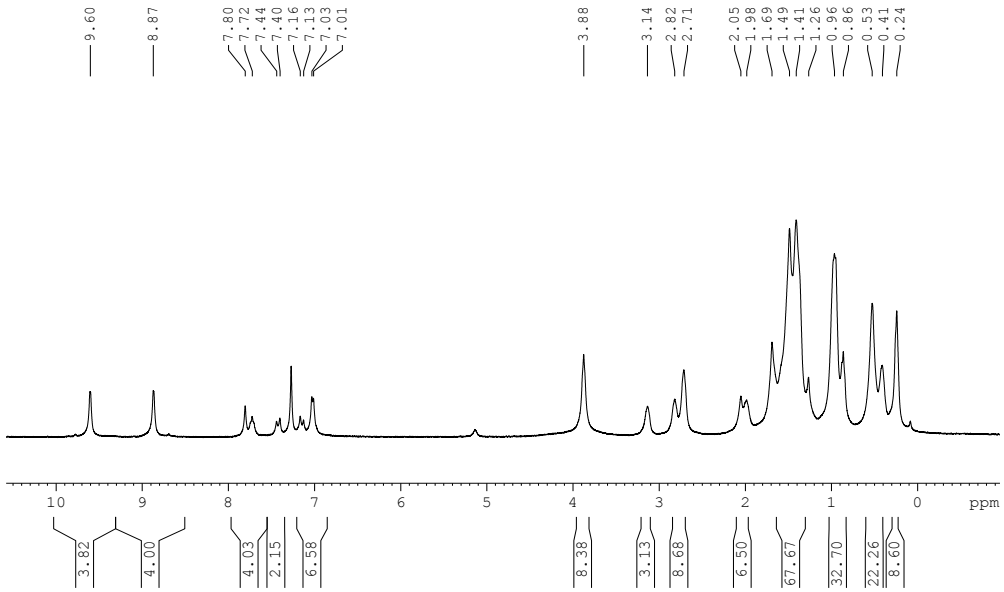

Figure 190. ^{1}H-NMR spectrum (400 MHz, $CDCl_3$) of **SA8**

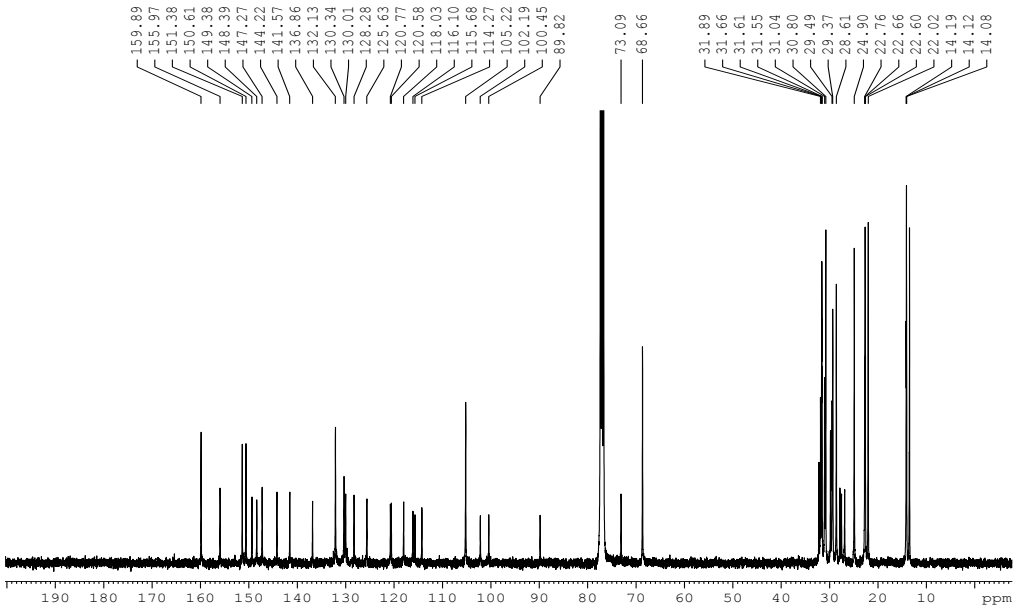

Figure 191. ^{13}C-NMR spectrum (100 MHz, $CDCl_3$) of **SA8**

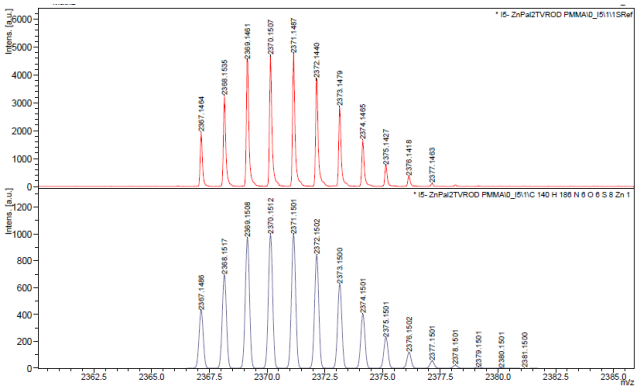

Figure 192. Mass spectrum of **SA7**

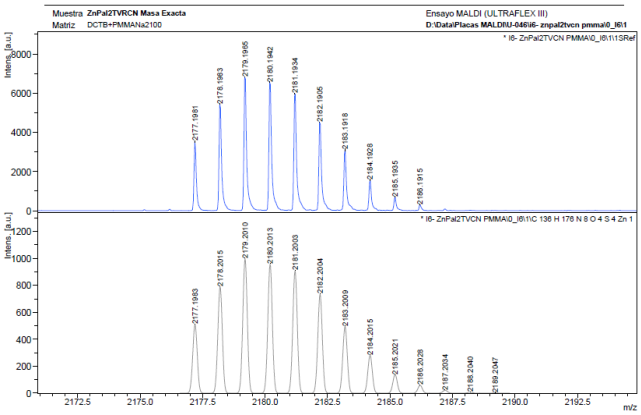

Figure 193. Mass spectrum of **SA8**

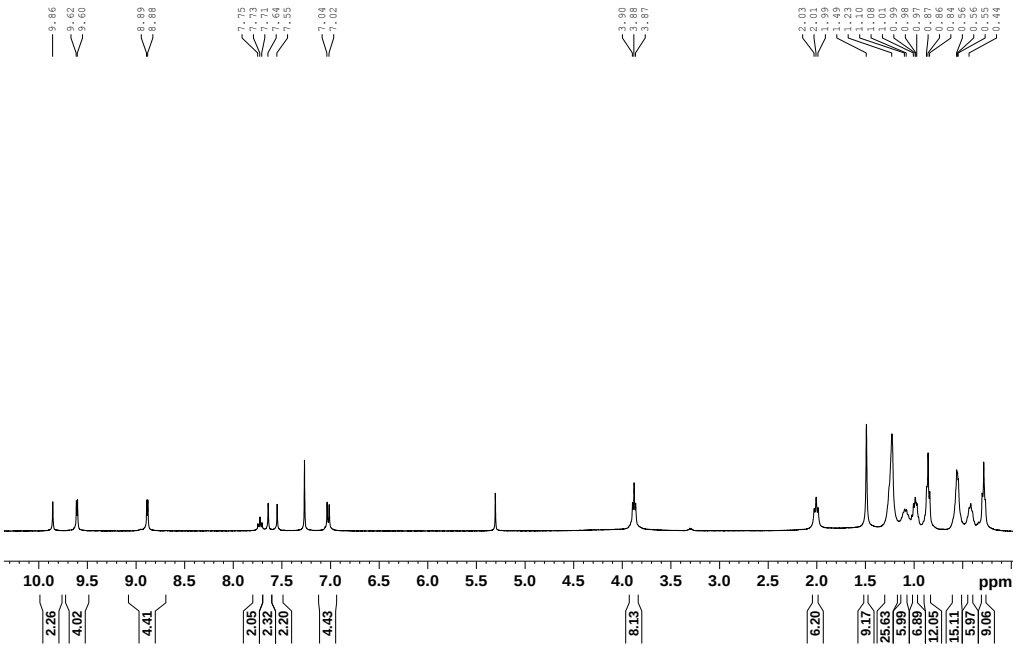

Figure 194. ^{1}H-NMR spectrum (400 MHz, $CDCl_3$) of **A5**

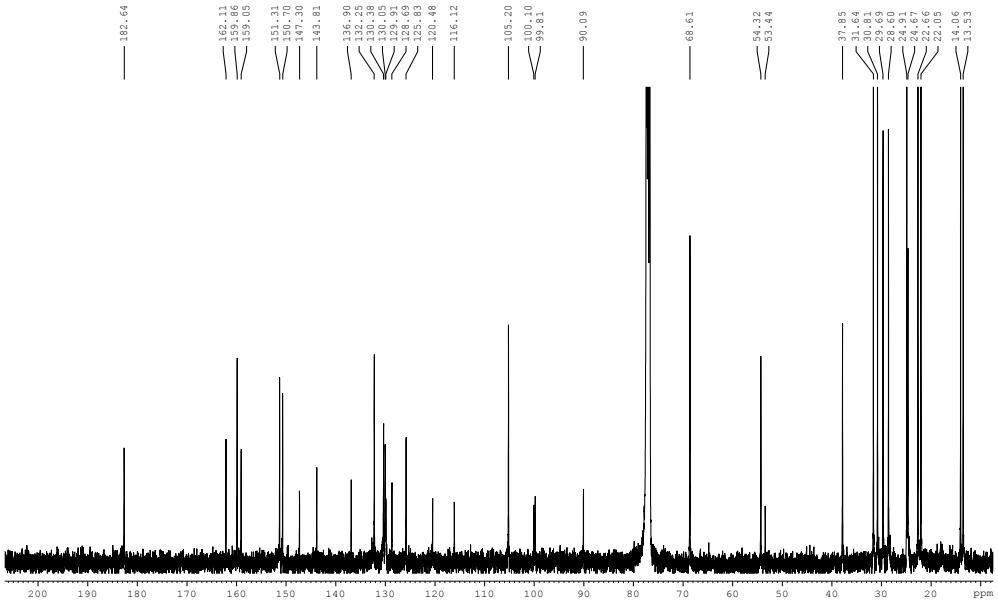

Figure 195. ^{13}C-NMR spectrum (100 MHz, $CDCl_3$) of **A5**

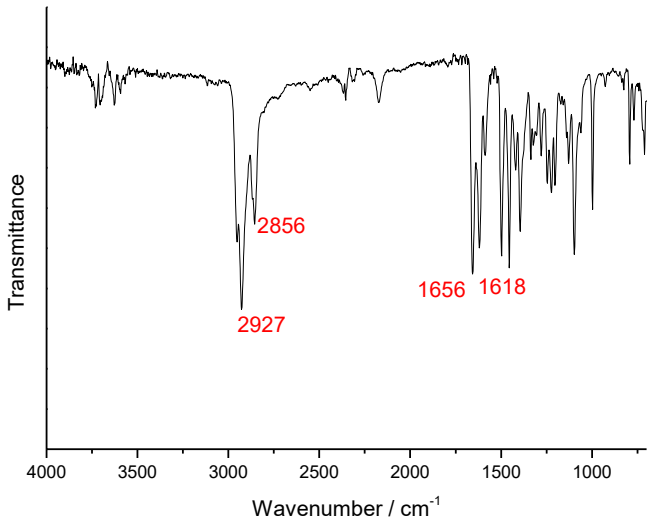

Figure 196. FT-IR spectrum of **A5**

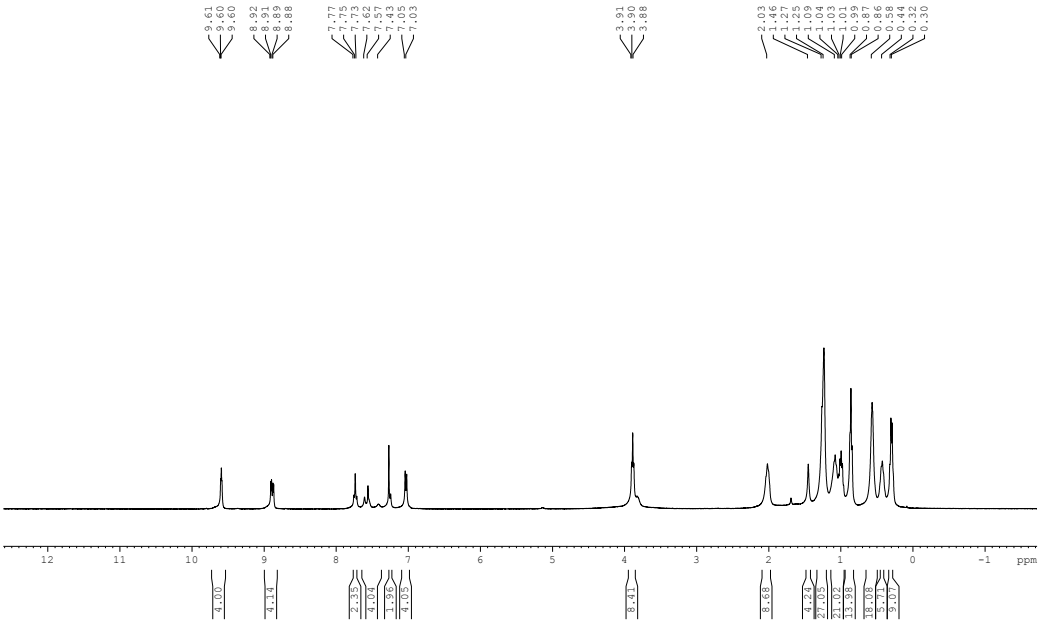

Figure 197. ^{1}H-NMR spectrum (400 MHz, $CDCl_3$) of **SA9**

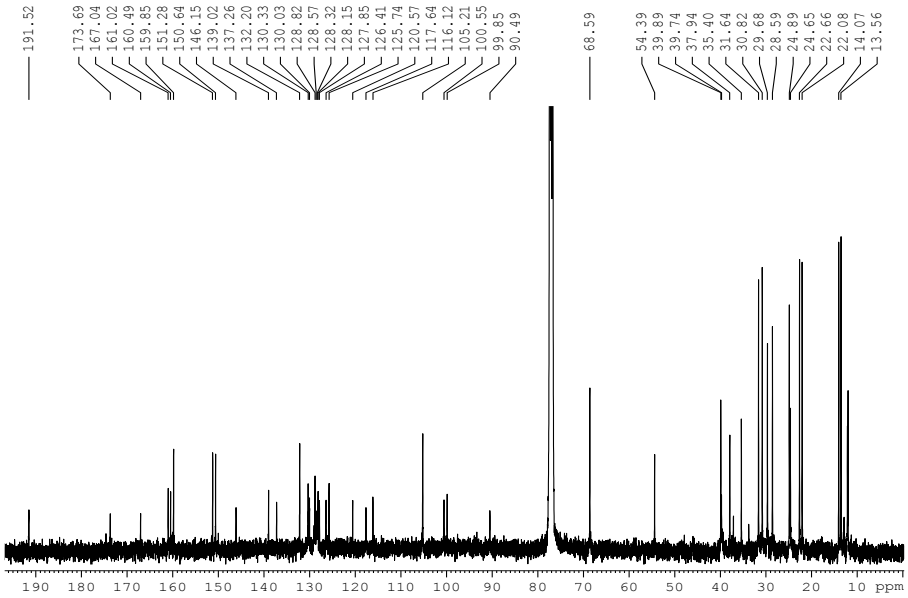

Figure 198. ^{13}C-NMR spectrum (100 MHz, $CDCl_3$) of **SA9**

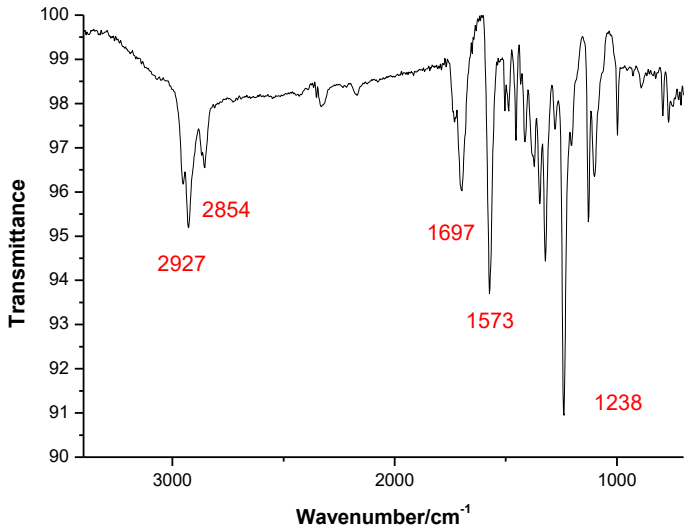

Figure 199. FT-IR spectrum of **SA9**

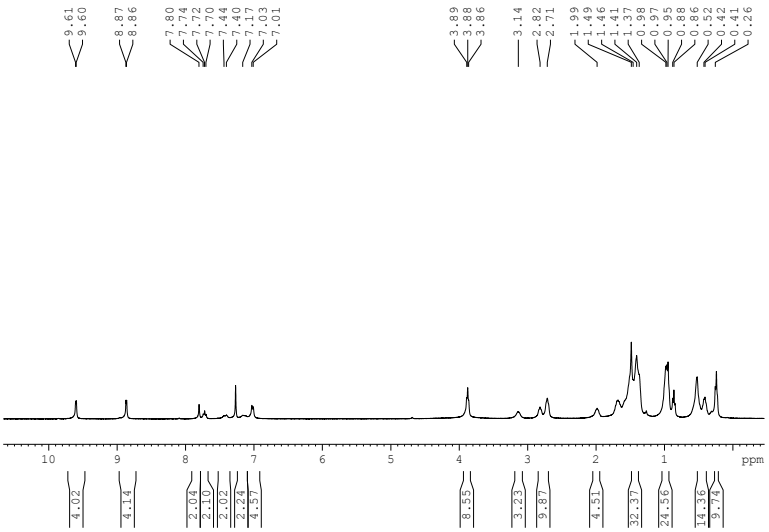

Figure 200. ^{1}H-NMR spectrum (400 MHz, $CDCl_3$) of **SA10**

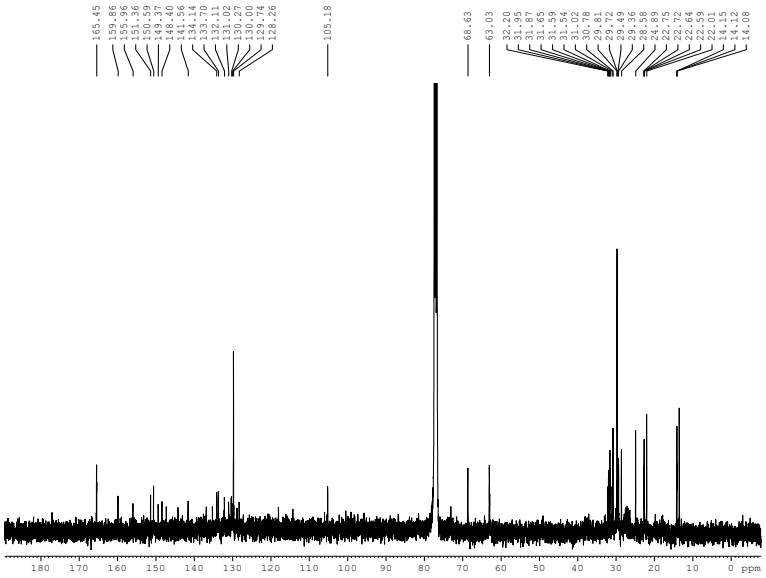

Figure 201. ^{13}C-NMR spectrum (100 MHz, $CDCl_3$) of **SA10**

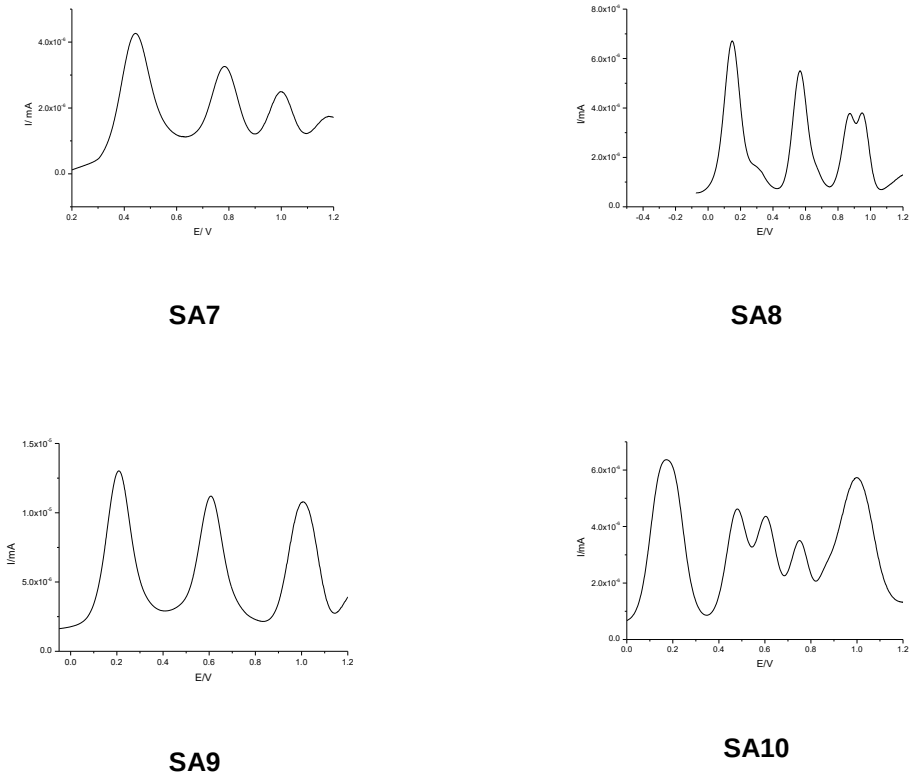

SA7 **SA8**

SA9 **SA10**

Figure 202. OSWV plot of compounds **SA7-SA10**

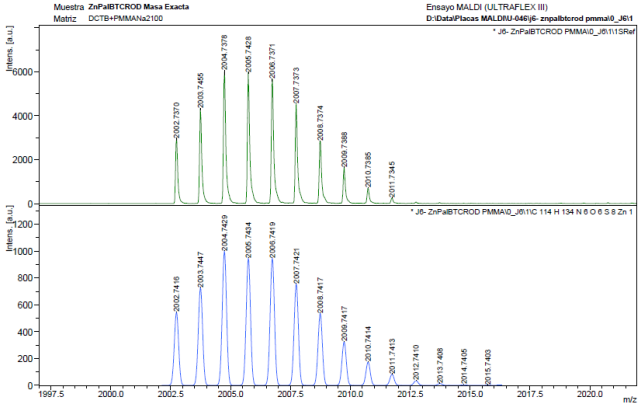

Figure 203. Mass spectrum of **SA9**

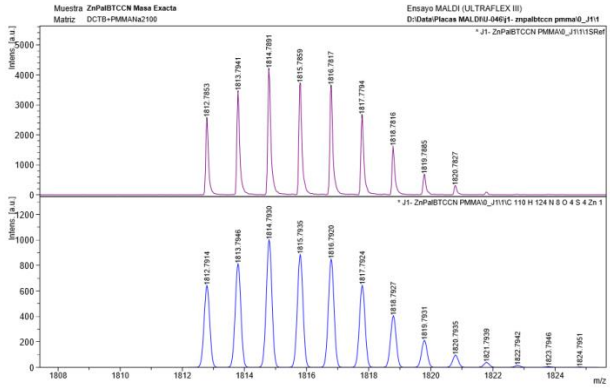

Figure 204. Mass spectrum of **SA10**

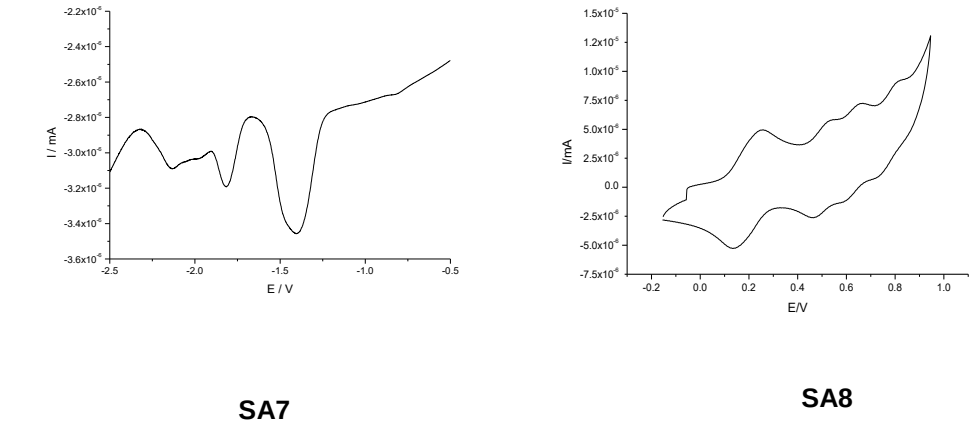

SA7 **SA8**

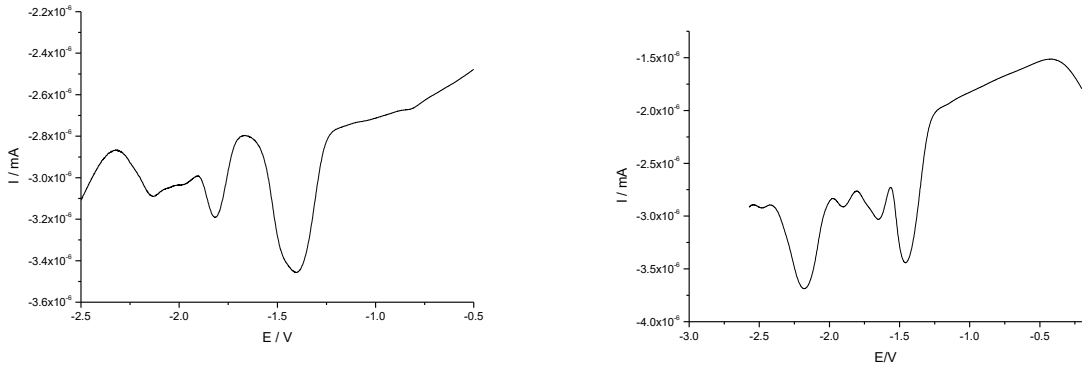

SA9 **SA10**

Figure 205. OSWV of **SA7-SA10**, referred to Fc/Fc^+ (cathodic window)

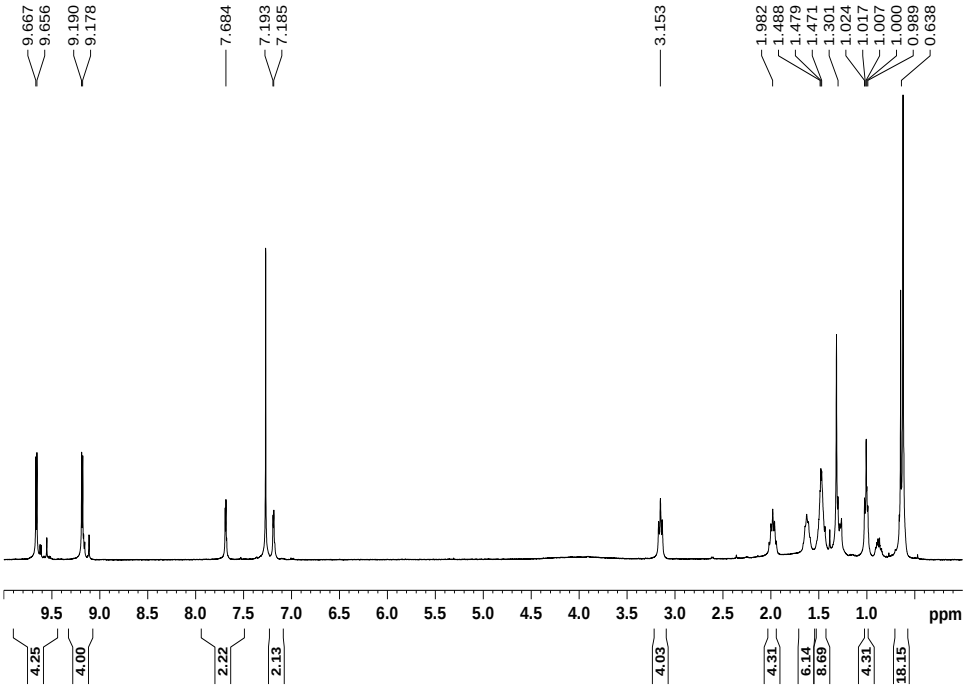

Figure 206. ^{1}H-NMR spectrum of **P3**

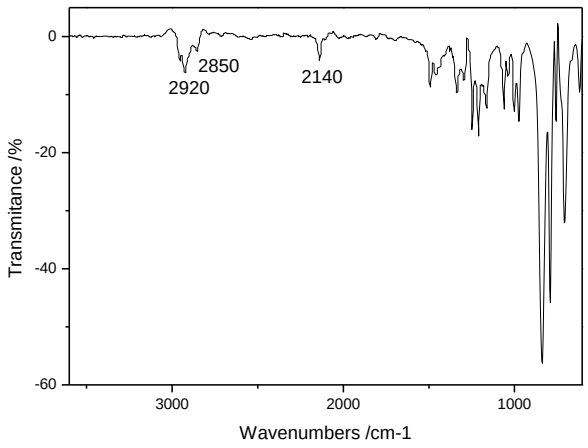

Figure 207. FT-IR spectrum of **P3**

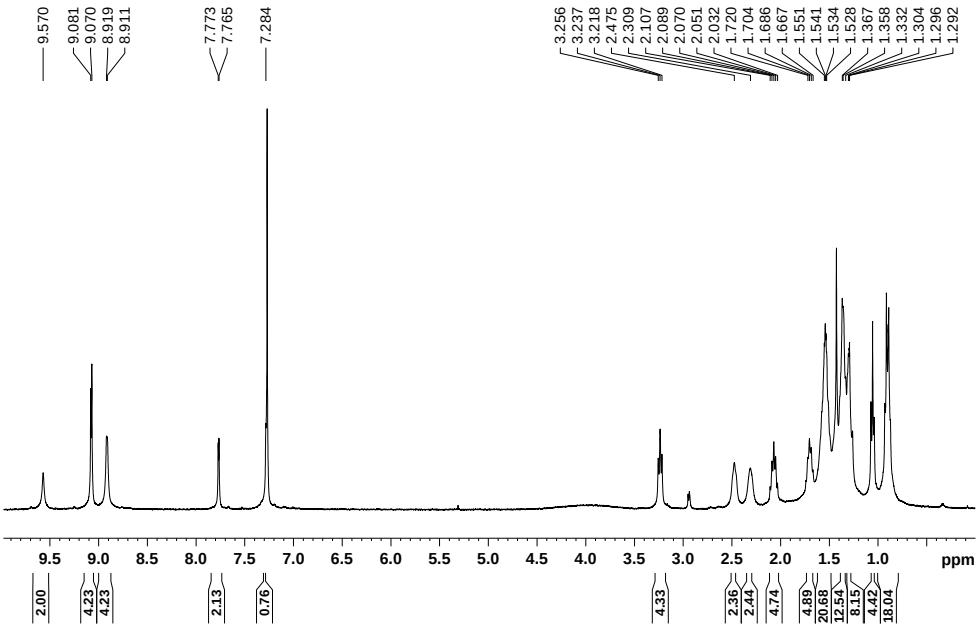

Figure 208. [1]H-NMR spectrum of **SA11**

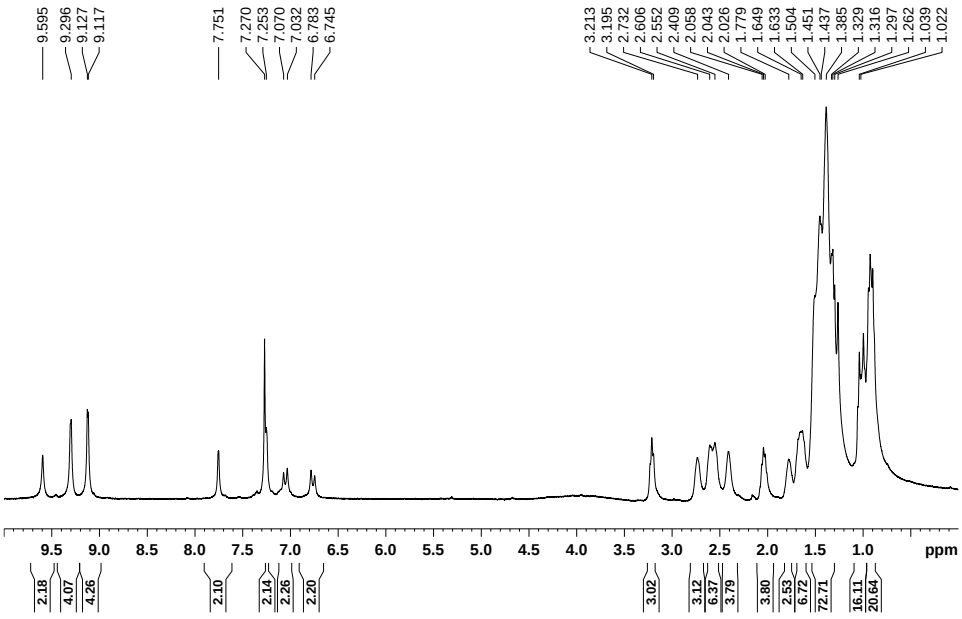

Figure 209. [1]H-NMR spectrum of **SA12**

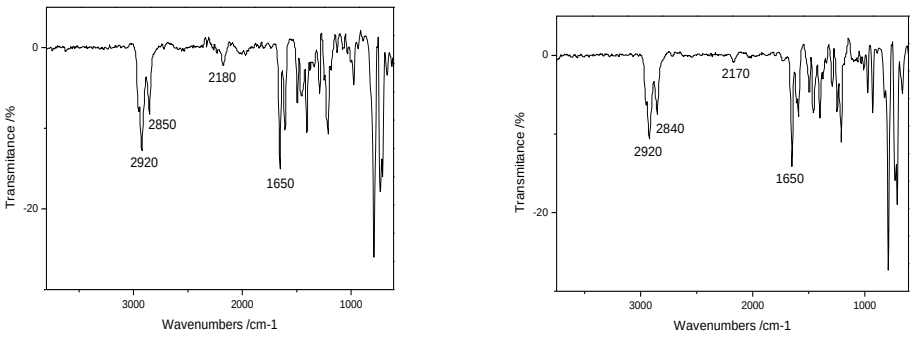

Figure 210. FT-IR spectra of **SA11** (left) and **SA12** (right)

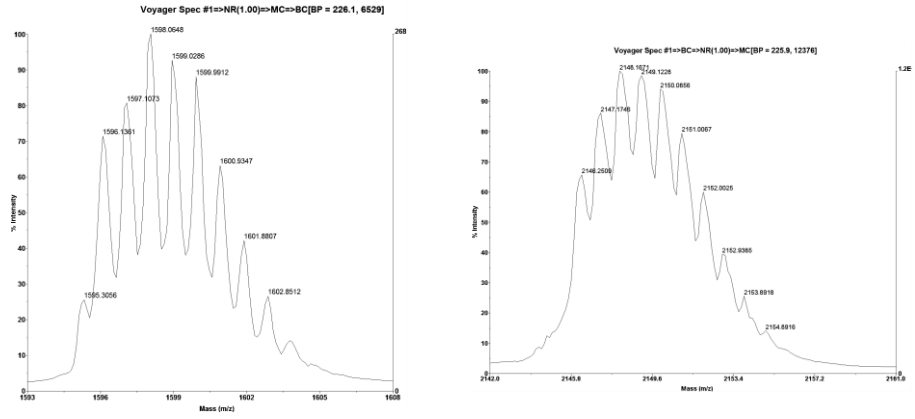

Figure 211. MALDI-TOF mass spectrum and isotopic distribution of **SA11** (left) and **SA12** (right)

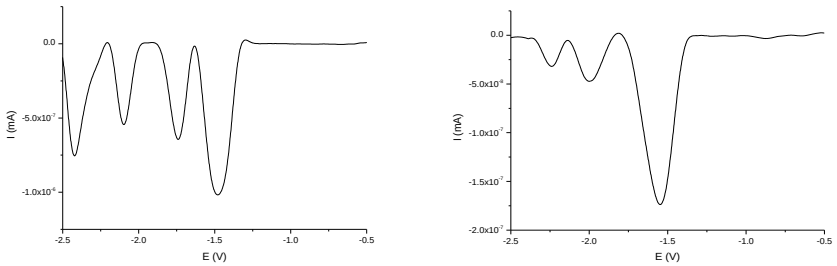

Figure 212. OSWV for reduction potentials of **SA11** (left) **SA12** (right)

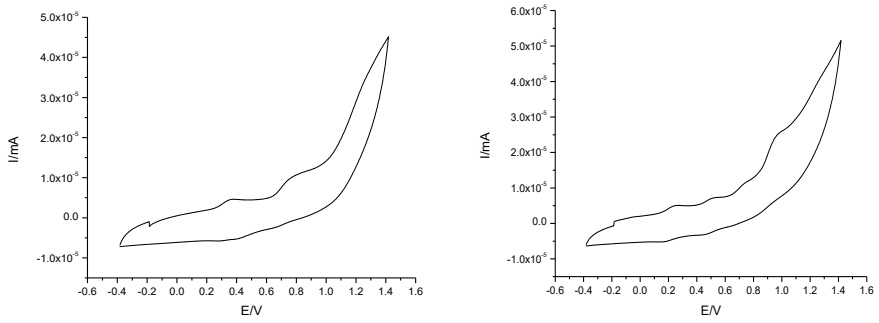

Figure 213. Cyclic voltammetry **SA11** (left) and **SA12** (right), (anodic window)

Additional information, Spectroscopy chapter 2

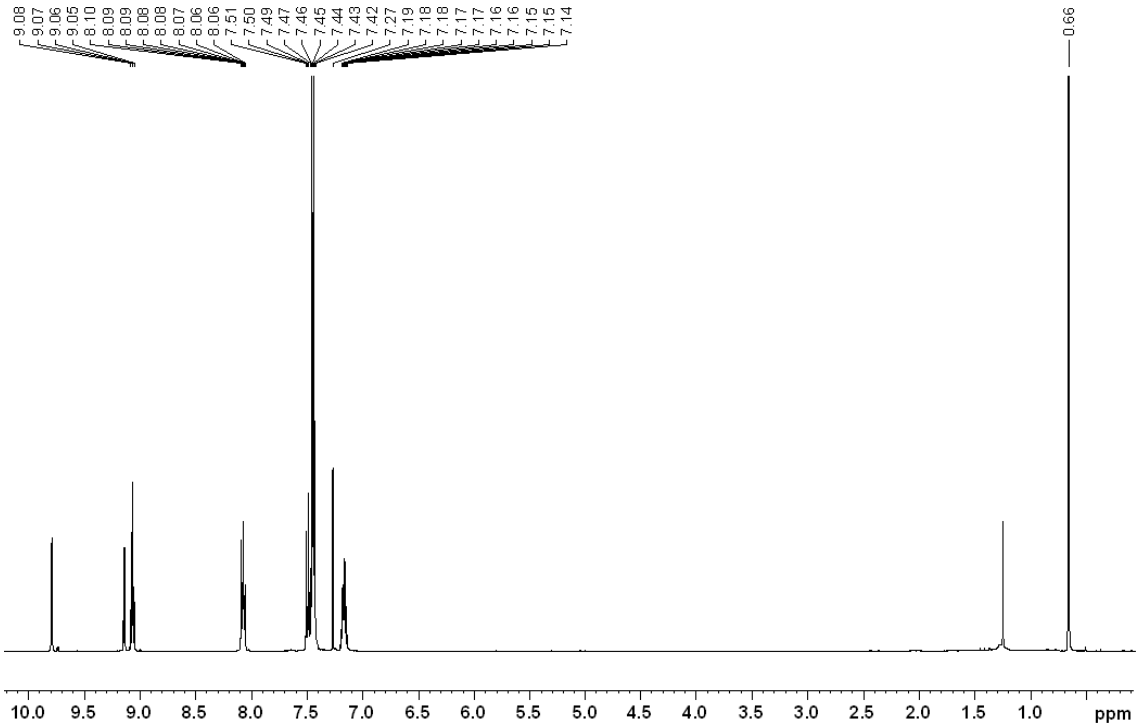

Figure 214. ^{1}H-NMR spectrum (400 MHz, $CDCl_3$) of compound **P4S**

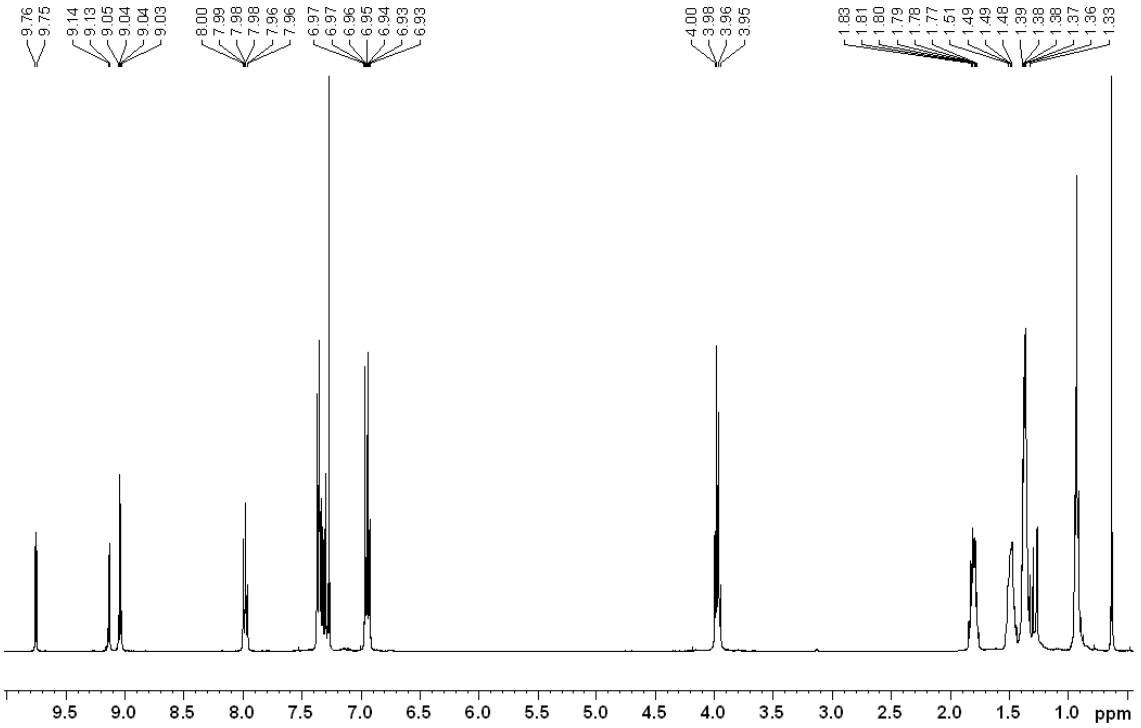

Figure 215. ^{1}H-NMR spectrum (400 MHz, $CDCl_3$) of compound **P5S**

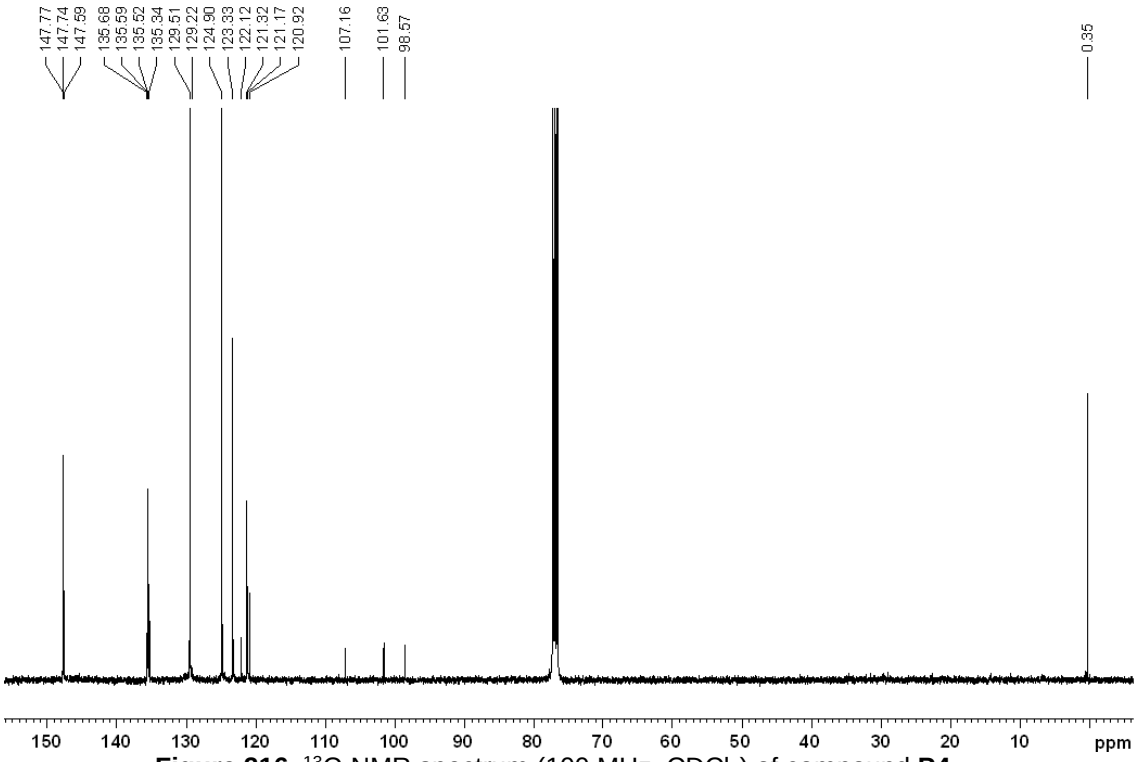

Figure 216. ^{13}C-NMR spectrum (100 MHz, $CDCl_3$) of compound **P4**

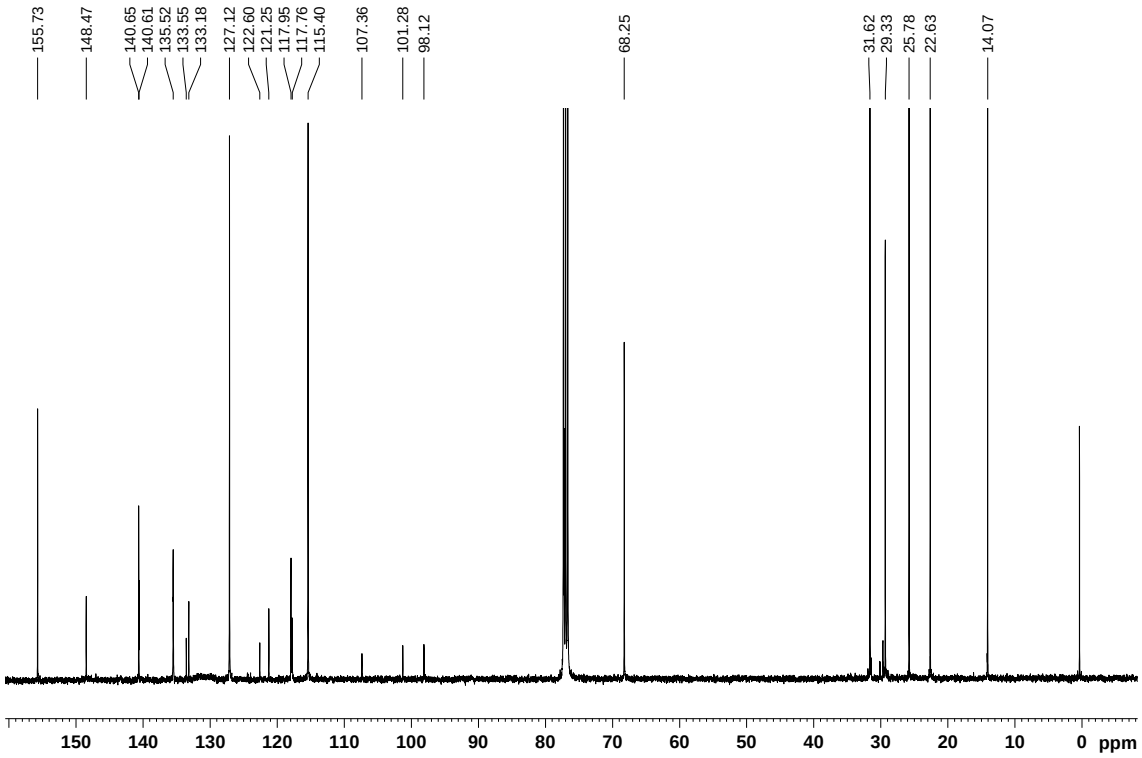

Figure 217. ^{13}C-NMR spectrum (100 MHz, $CDCl_3$) of compound **P5**

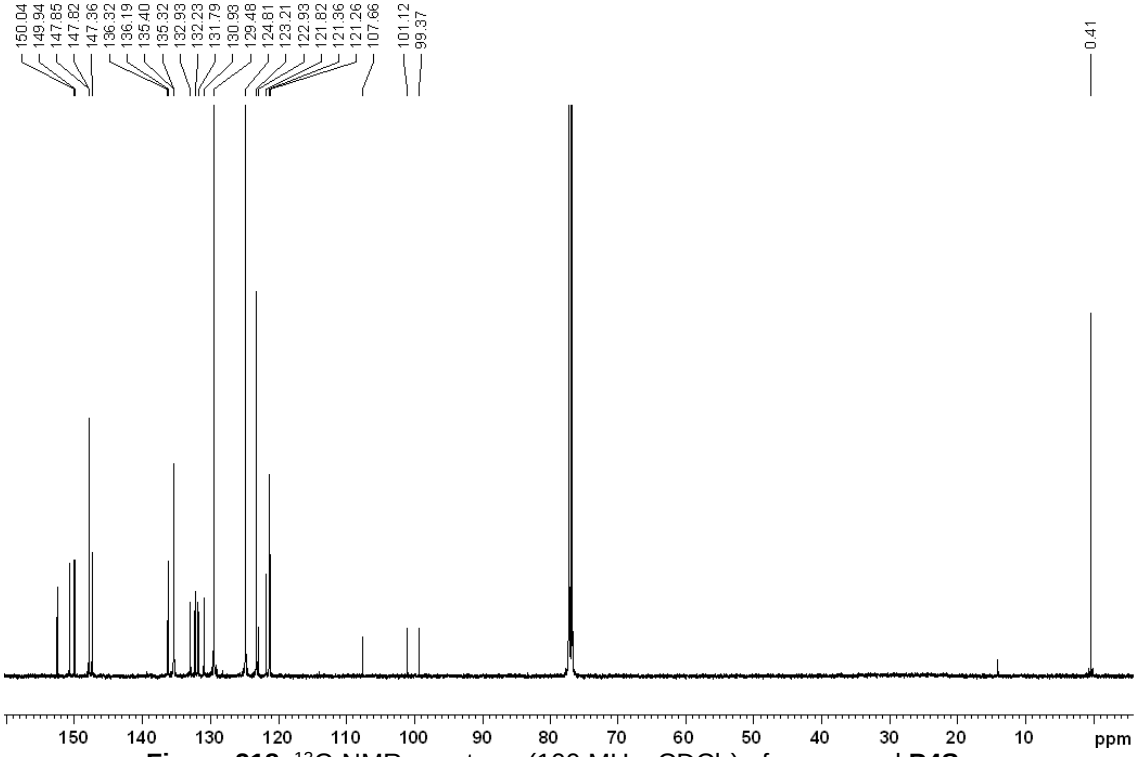

Figure 218. ^{13}C-NMR spectrum (100 MHz, $CDCl_3$) of compound **P4S**

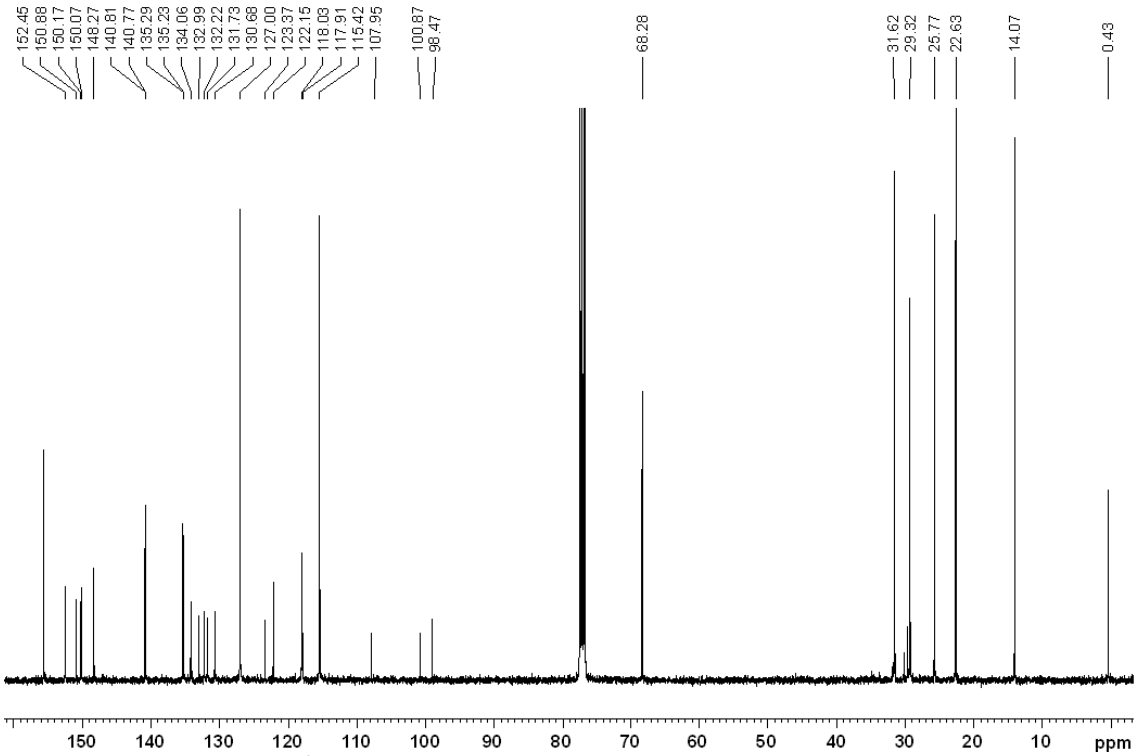

Figure 219. ^{13}C-NMR spectrum (100 MHz, $CDCl_3$) of compound **P5S**

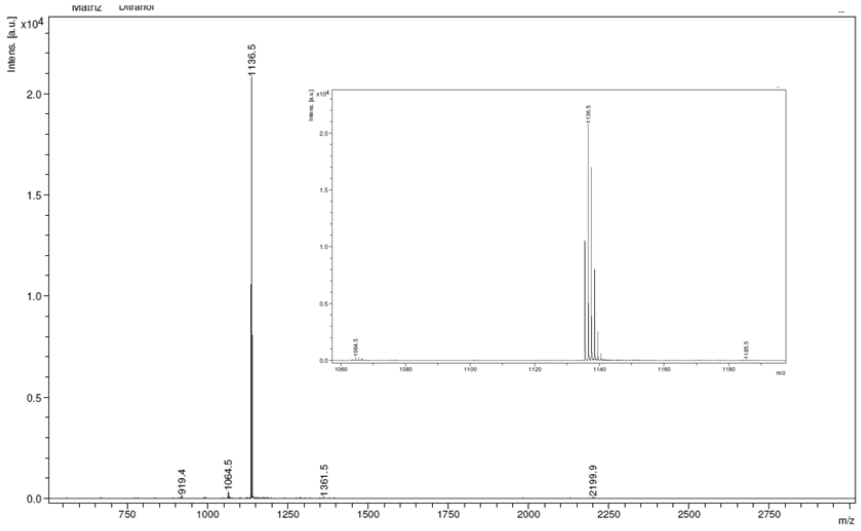

Figure 220. MALDI-MS spectrum of compound **P4** (Matrix: Dithranol)

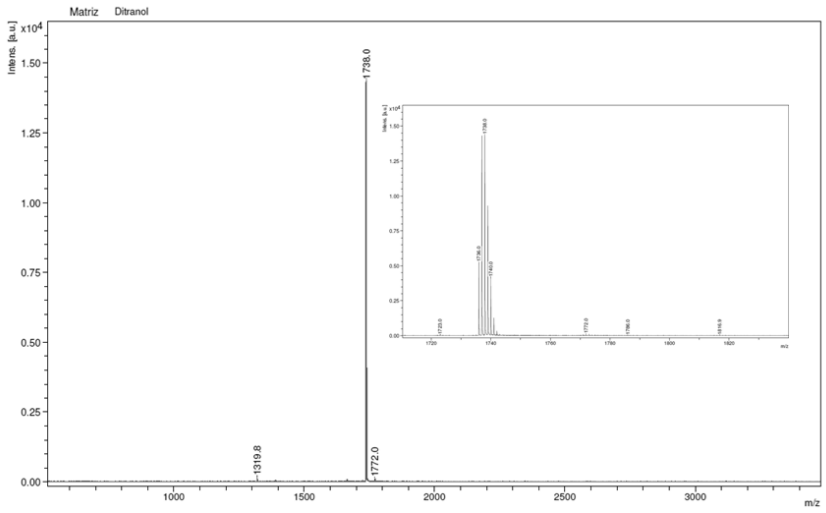

Figure 221. MALDI-MS spectrum of compound **P5** (Matrix: Dithranol).

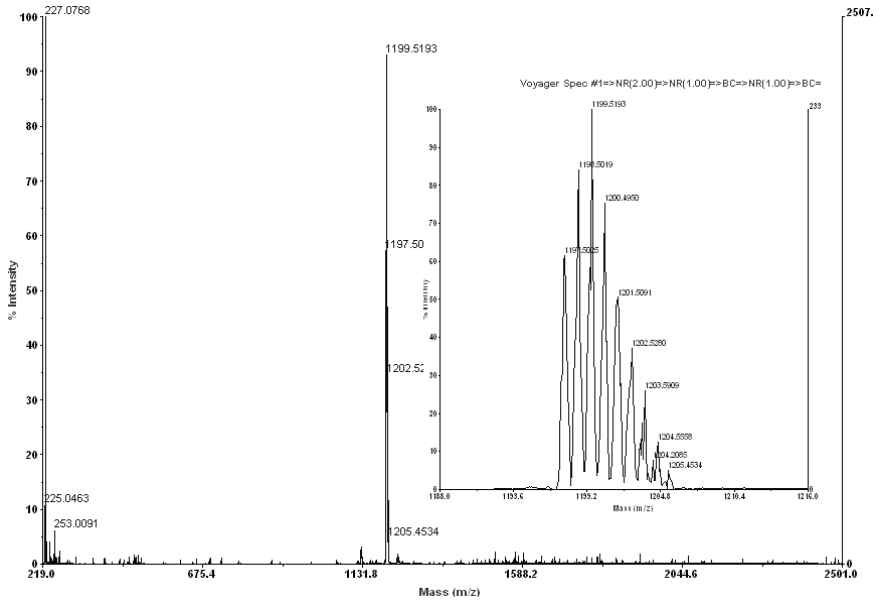

Figure 222. MALDI-MS spectrum of compound **P4S** (Matrix: Dithranol)

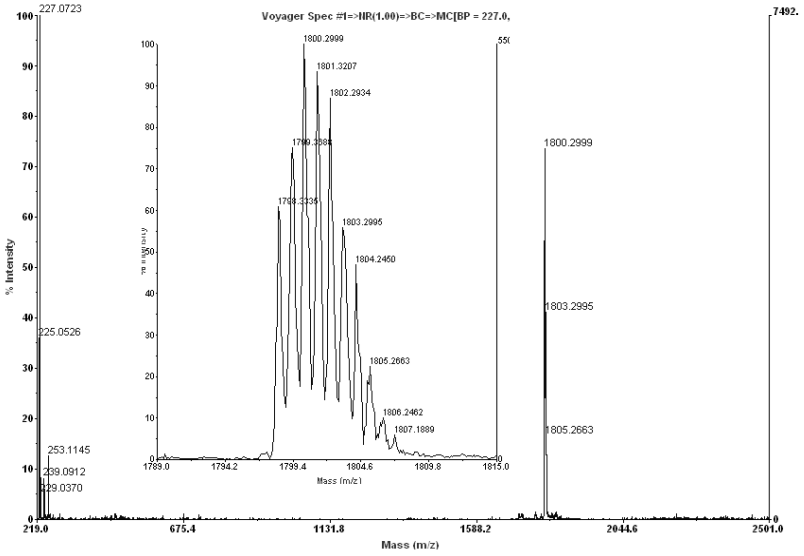

Figure 223. MALDI-MS spectrum of compound **P5S** (Matrix: Dithranol)

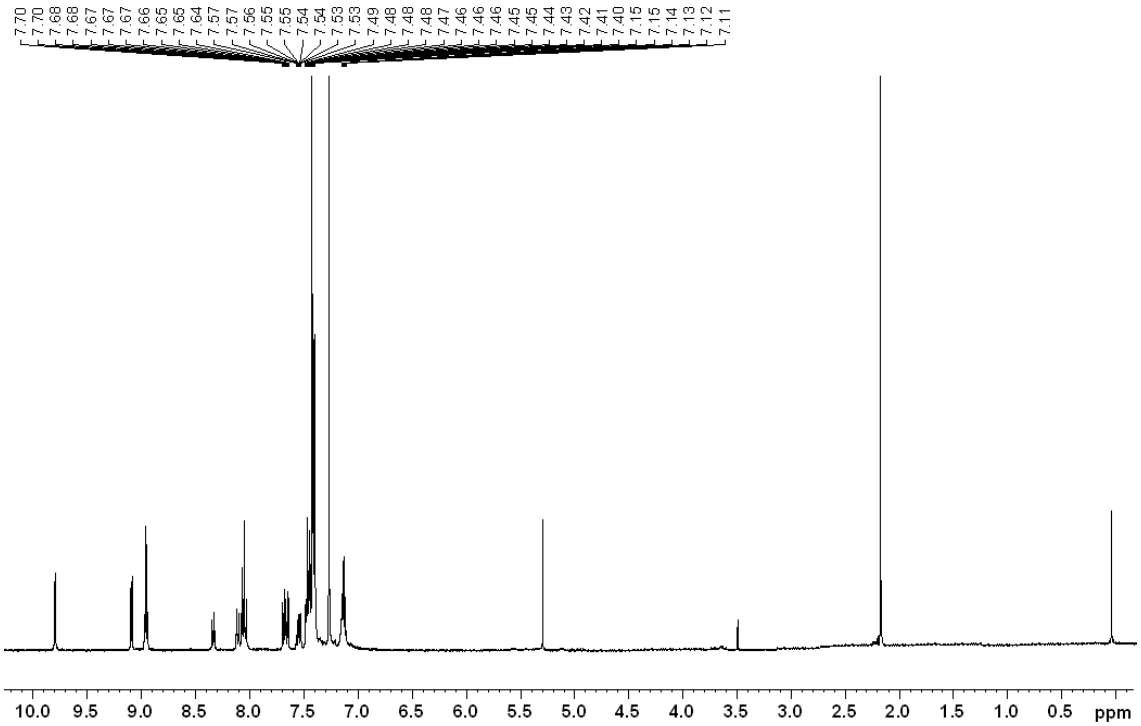

Figure 224. ^{1}H-NMR spectrum (400 MHz, $CDCl_3$) of compound **SA13**

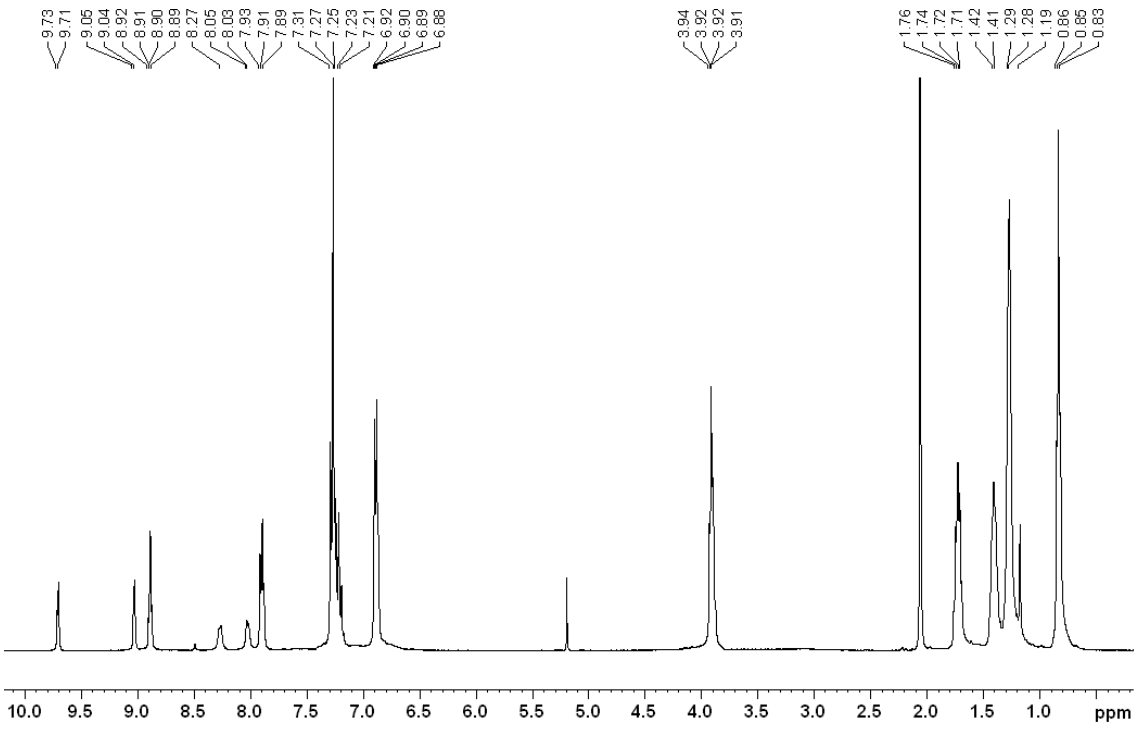

Figure 225. ^{1}H-NMR spectrum (400 MHz, $CDCl_3$) of compound **SA14**

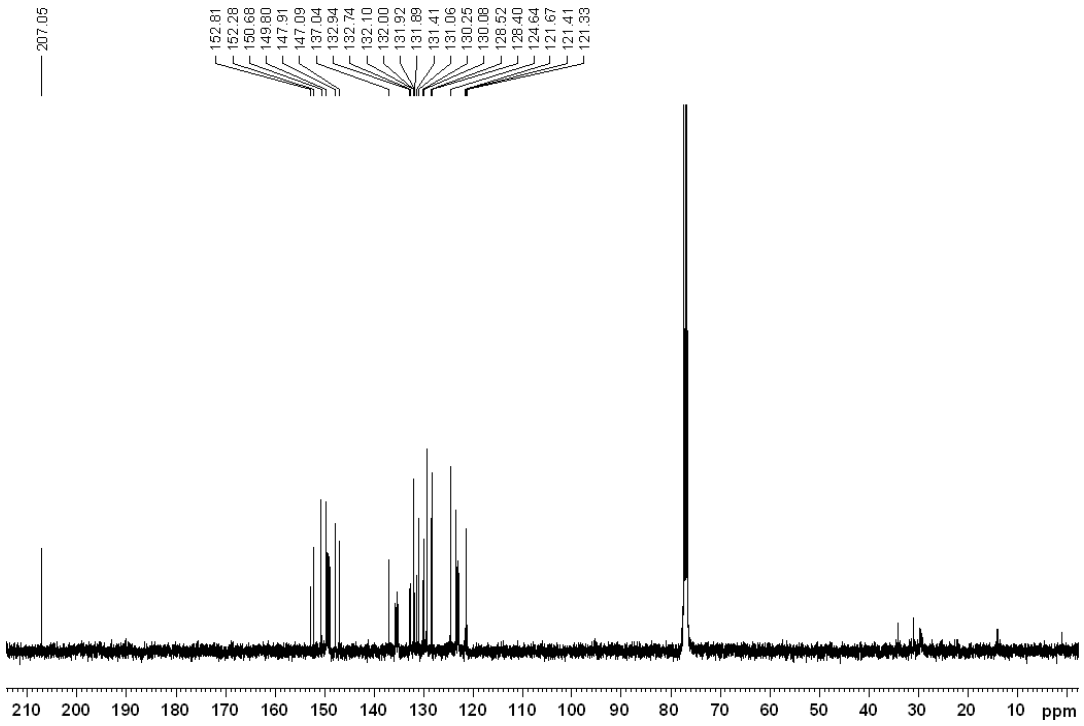

Figure 226. ^{1}H-NMR spectrum (400 MHz, CDCl3) of compound **SA13**

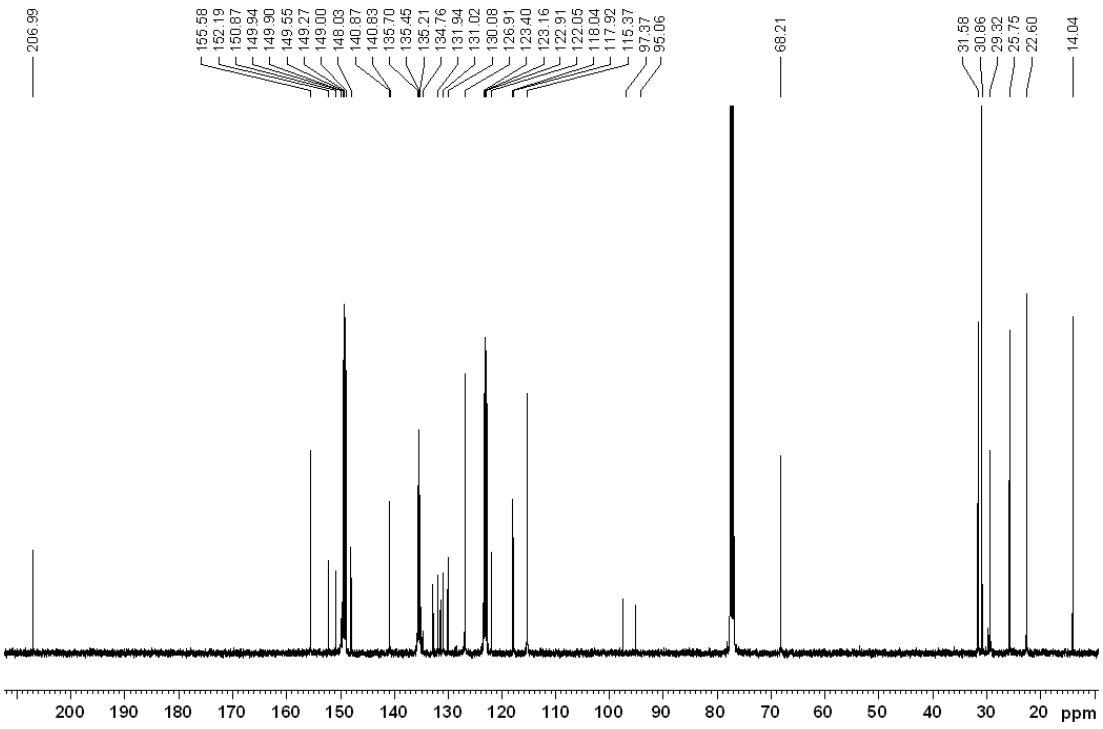

Figure 227. ^{13}C-NMR spectrum (100 MHz, $CDCl_3$) of compound **SA14**

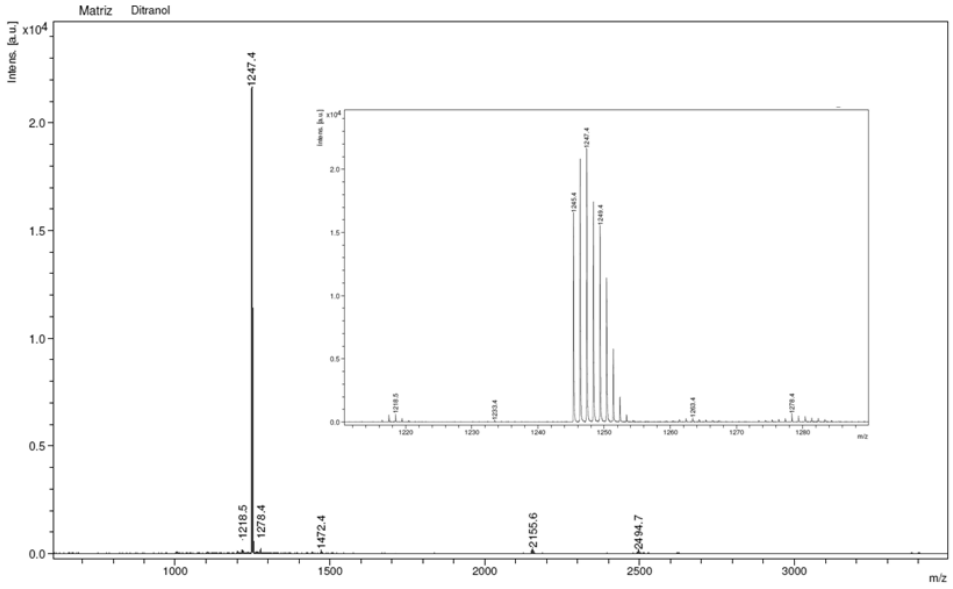

Figure 228. MALDI-MS spectrum of compound **SA13** (Matrix: Dithranol)

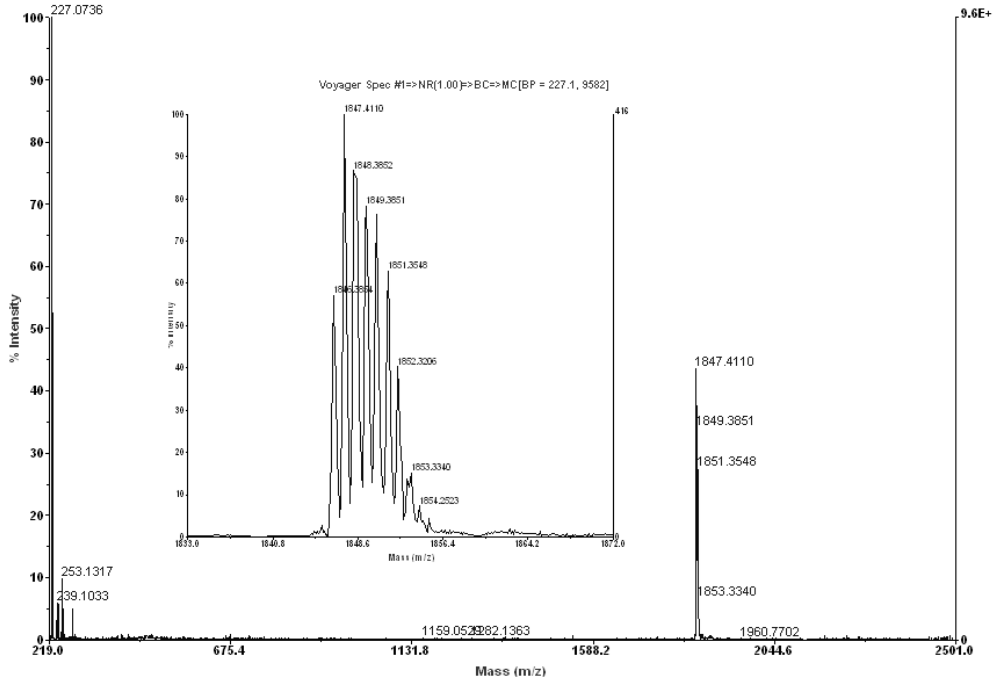

Figure 229. MALDI-MS spectrum of compound **SA14** (Matrix: Dithranol)

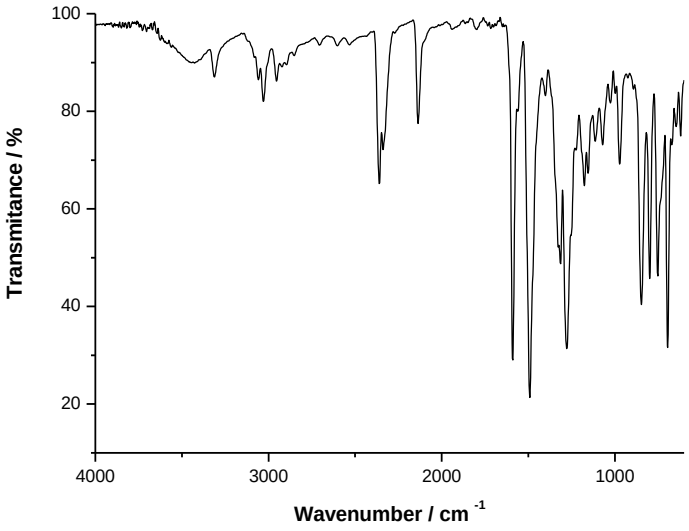

Figure 230. FT-IR spectrum of compound **P4**, KBr

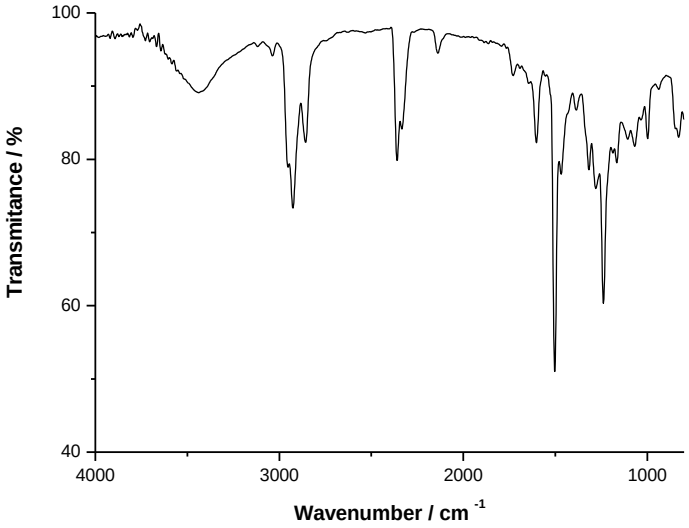

Figure 231. FT-IR spectrum of compound **P5**, KBr

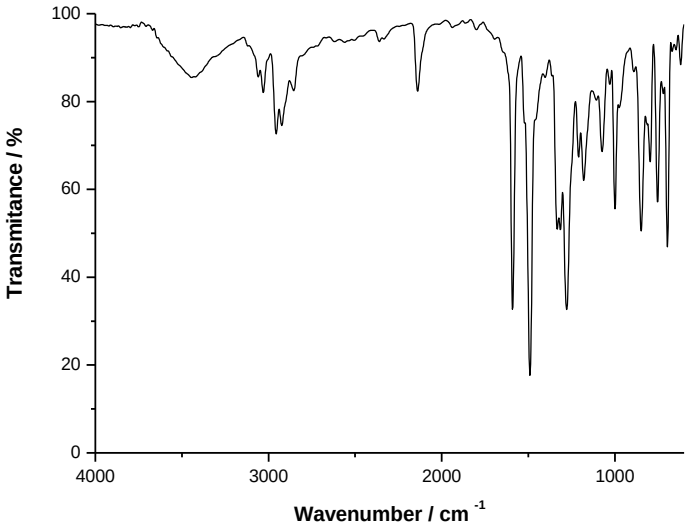

Figure 232. FT-IR spectrum of compound **P4S**, KBr

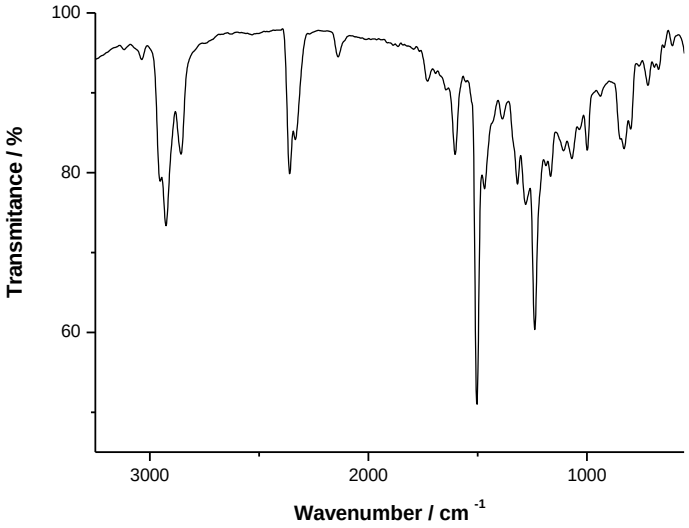

Figure 233. FT-IR spectrum of compound **P5S**, KBr

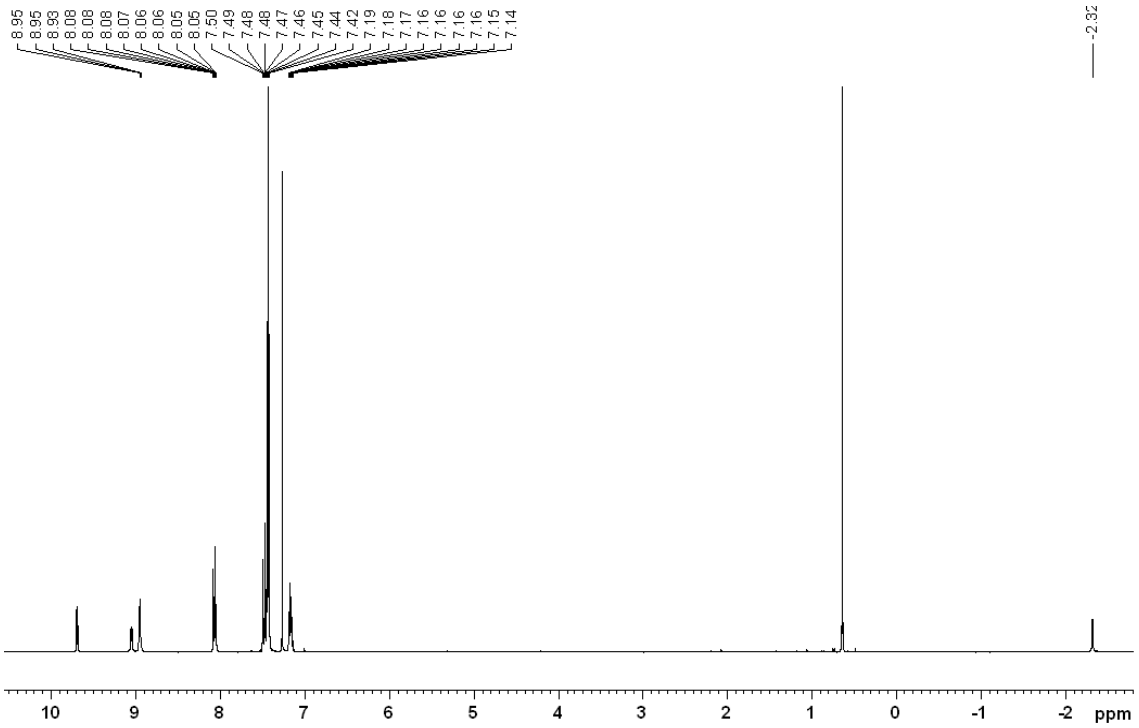

Figure 234. ^{1}H-NMR spectrum (400 MHz, $CDCl_3$) of compound **P4**

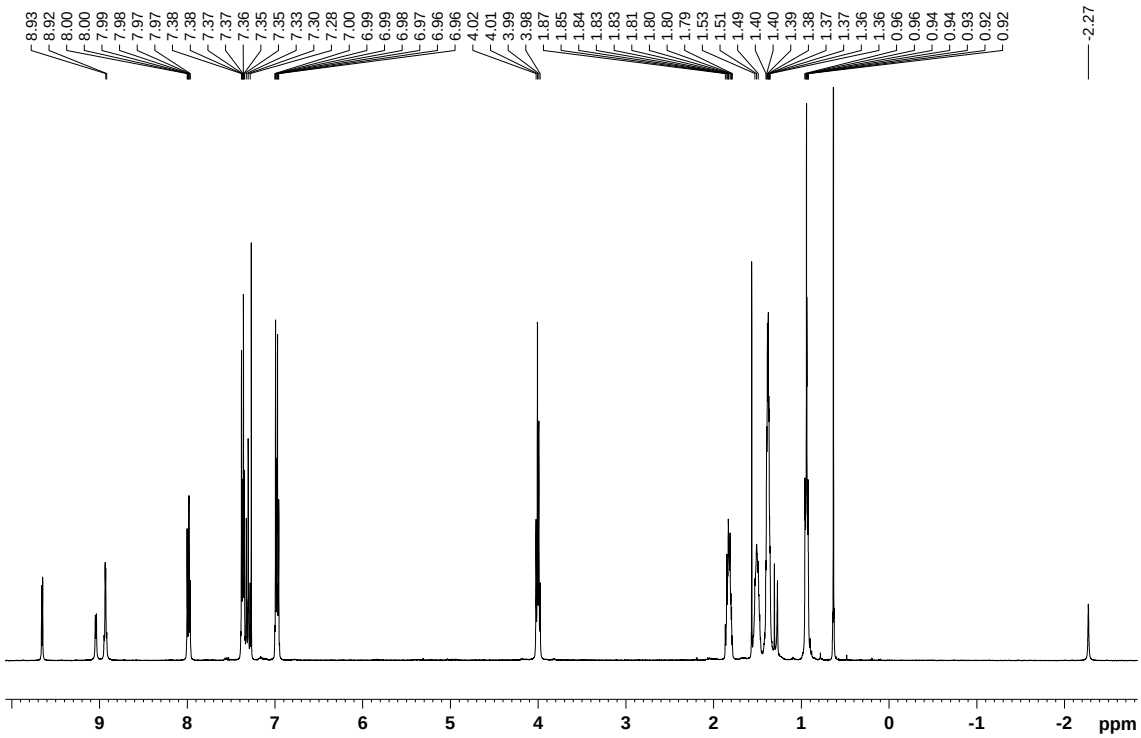

Figure 235. ^{1}H-NMR spectrum (400 MHz, $CDCl_3$) of compound **P5**

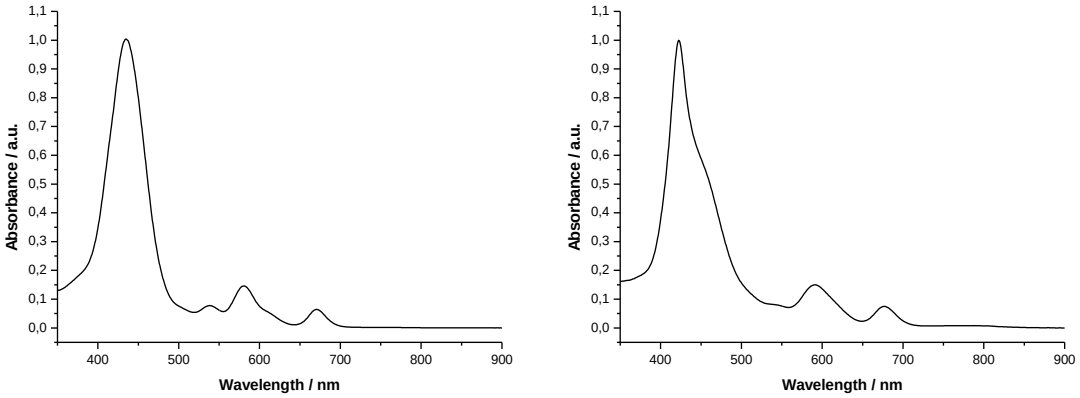

Figure 236. Normalized UV-Vis absorption spectra of compounds **P4** (left) and **P5** (right) in CH_2Cl_2

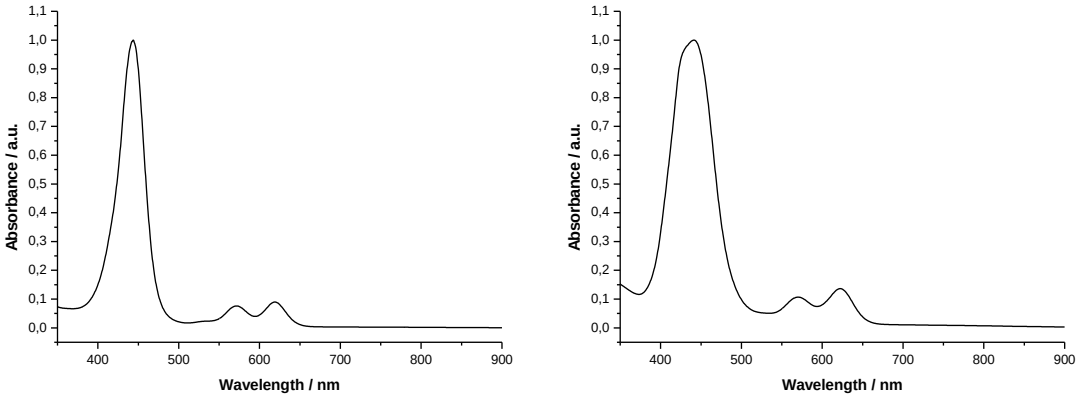

Figure 237. Normalized UV-Vis absorption spectra of compounds **P4S** (left) and **P5S** (right) in CH_2Cl_2

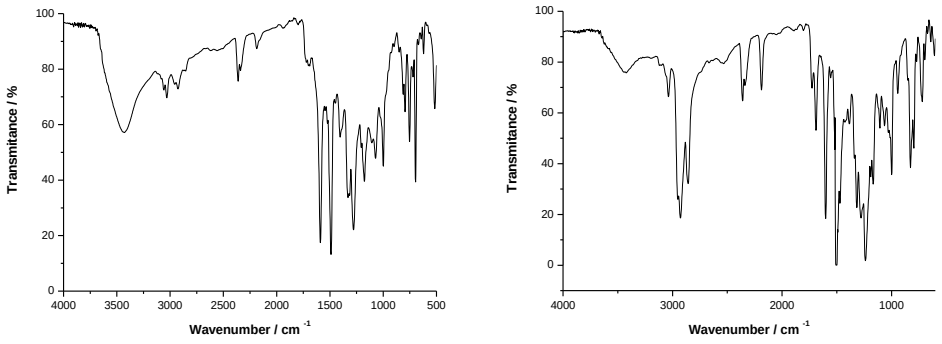

Figure 238. FT-IR spectrum of compound **SA13** (left) and **SA14** (right), (KBr)

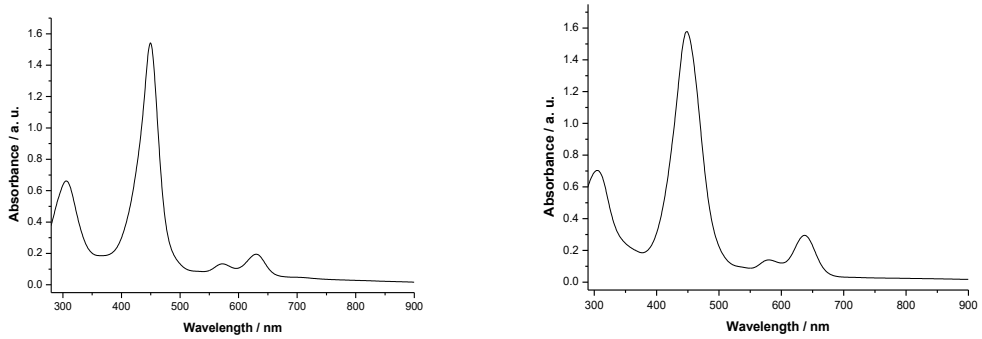

Figure 239. UV-Vis absorption spectrum of compound **SA13** (left) and **SA14** (right) in CH_2Cl_2, 1.28 x 10^{-5} M and 1.19x10^{-5} M respectively

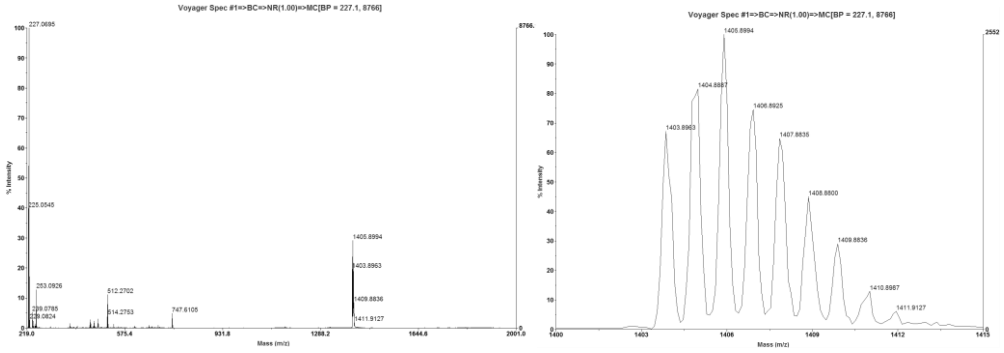

Figure 240. MALDI-MS spectrum of compound **A8** (Matrix: Dithranol)

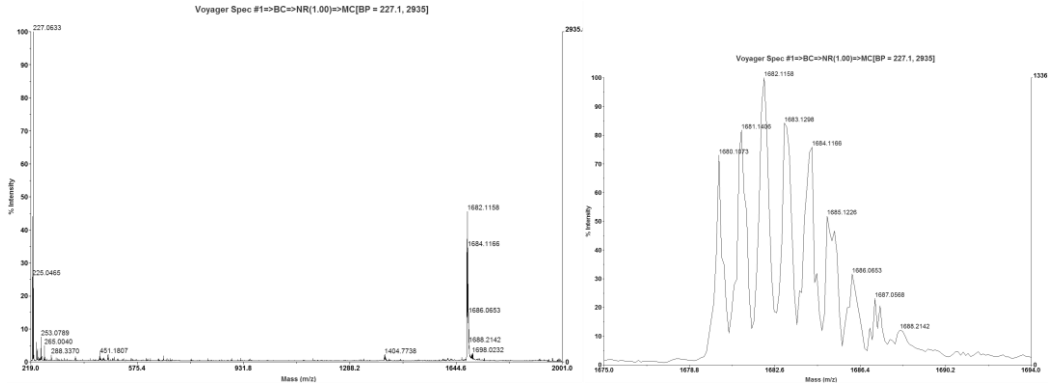

Figure 241. MALDI-MS spectrum of compound **A9** (Matrix: Dithranol)

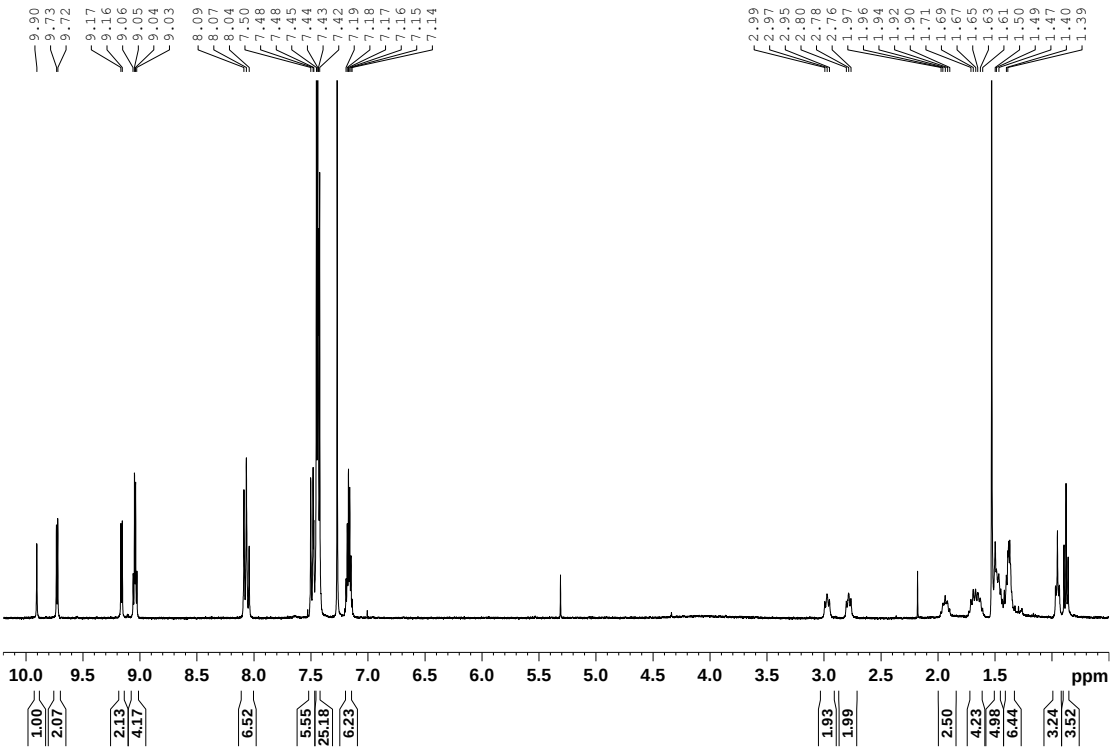

Figure 242. ^{1}H-NMR spectrum (400 MHz, $CDCl_3$) of compound **A8**

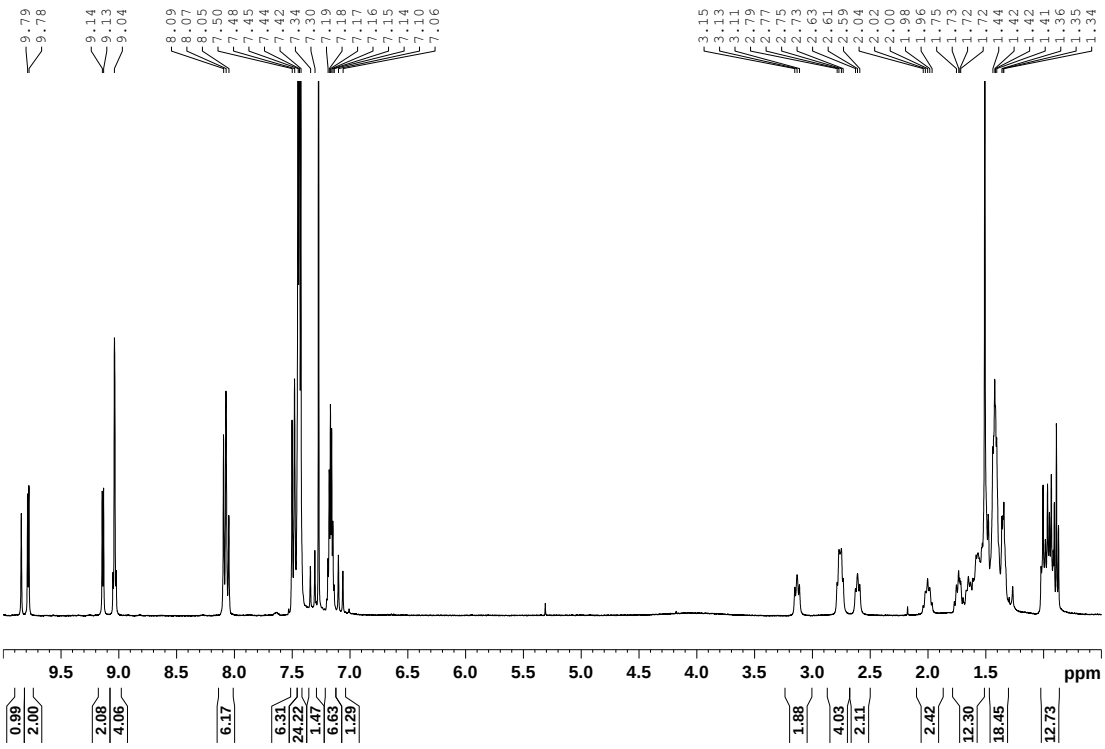

Figure 243. ^{1}H-NMR spectrum (400 MHz, $CDCl_3$) of compound **A9**

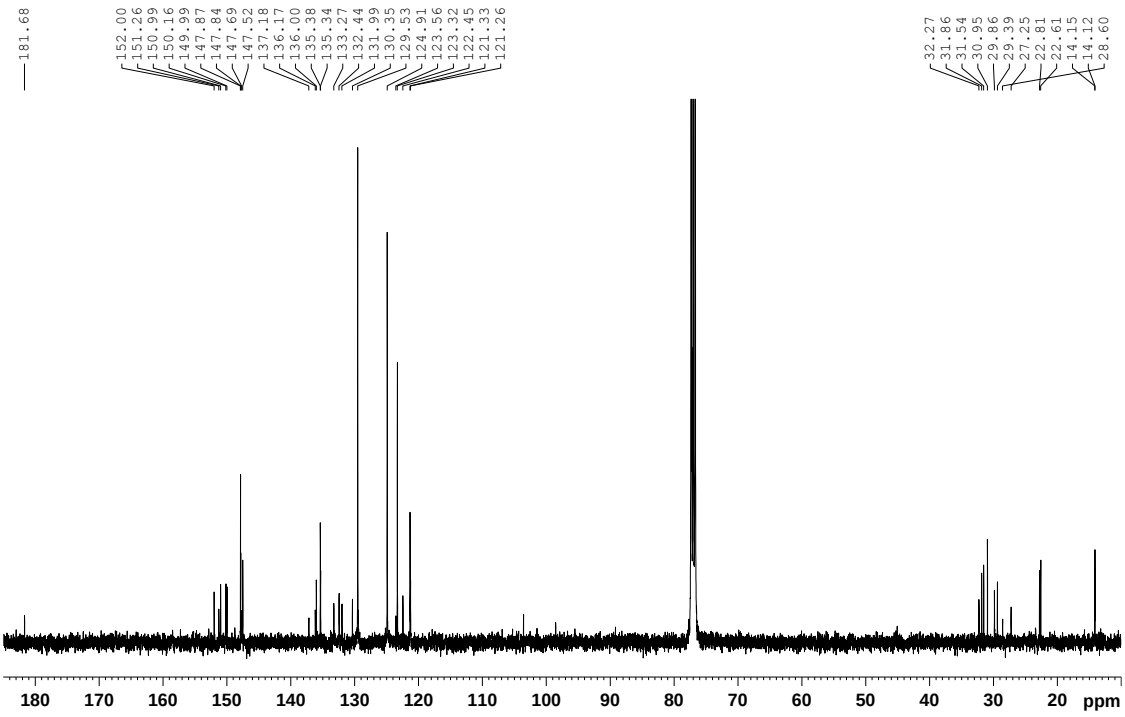

Figure 244. ^{13}C-NMR spectrum (100 MHz, $CDCl_3$) of compound **A8**

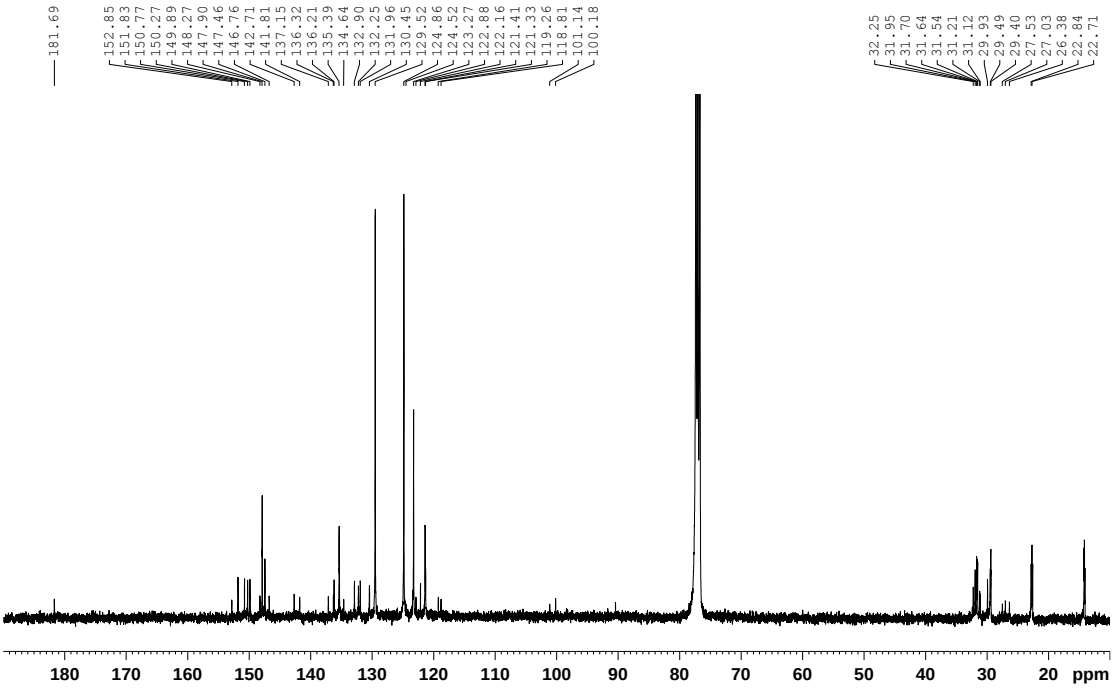

Figure 245. ^{13}C-NMR spectrum (100 MHz, $CDCl_3$) of compound **A9**

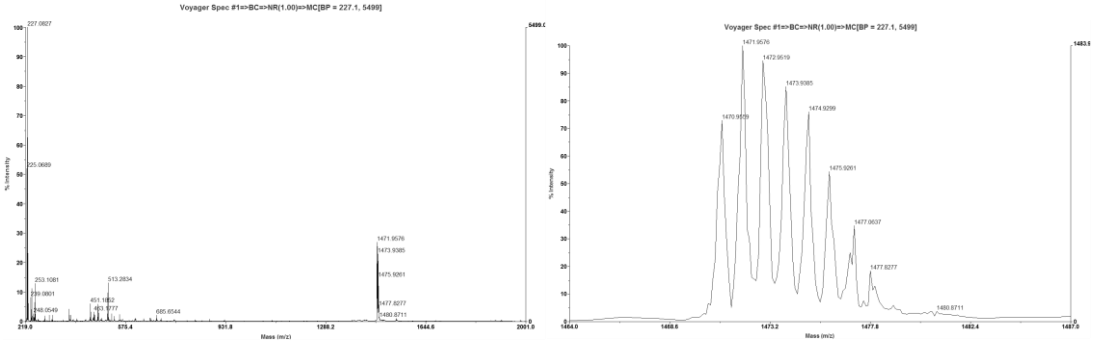

Figure 246. MALDI-MS spectrum of compound **SA15** (Matrix: Dithranol)

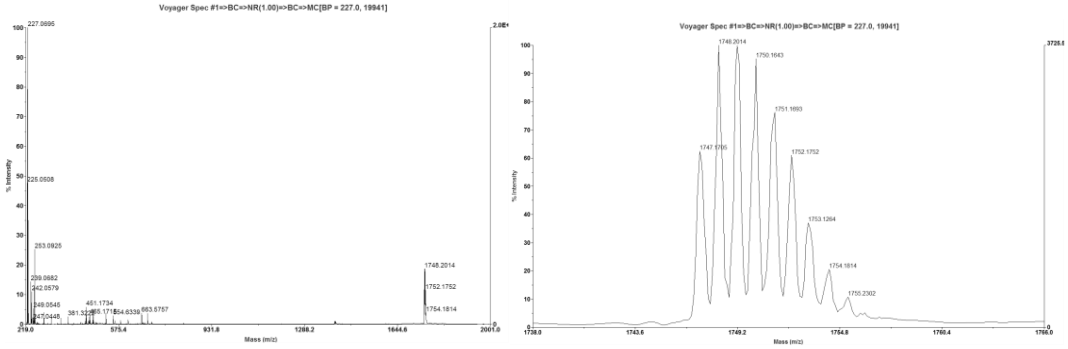

Figure 247. MALDI-MS spectrum of compound **SA16** (Matrix: Dithranol)

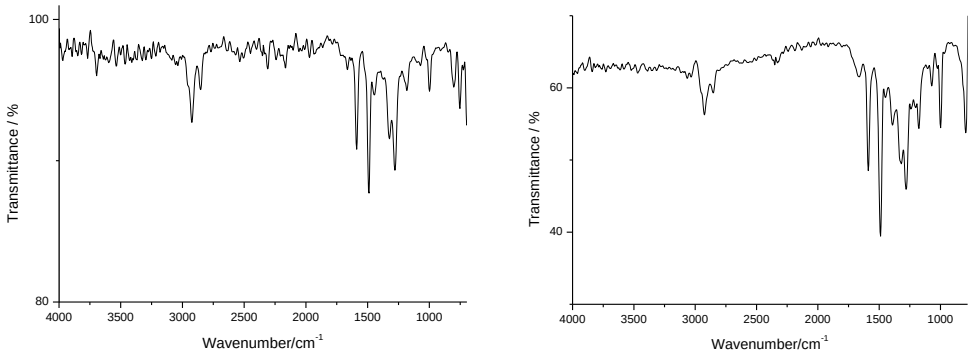

Figure 248. FT-IR spectra of compounds **SA17** (left) and **SA18** (right) (NaCl window)

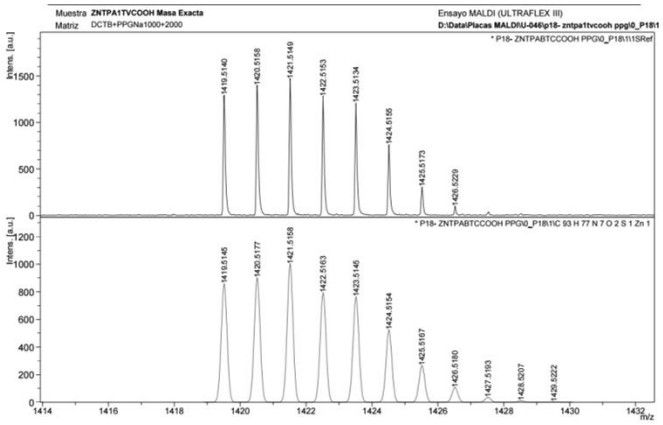

Figure 249. MALDI-MS spectrum of compound **SA17** (Matrix: Dithranol)

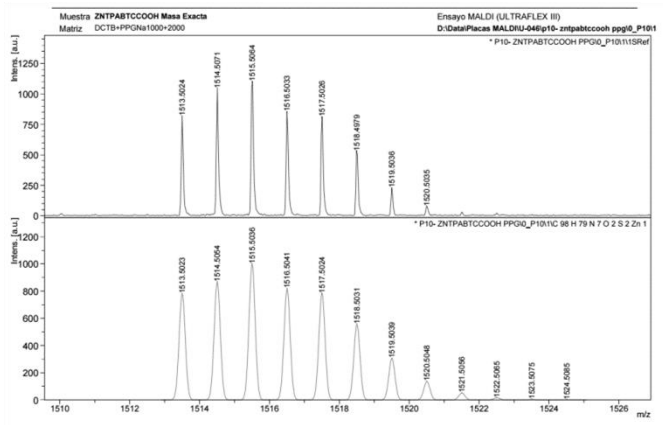

Figure 250. MALDI-MS spectra of compound **SA18** (Matrix: Dithranol)

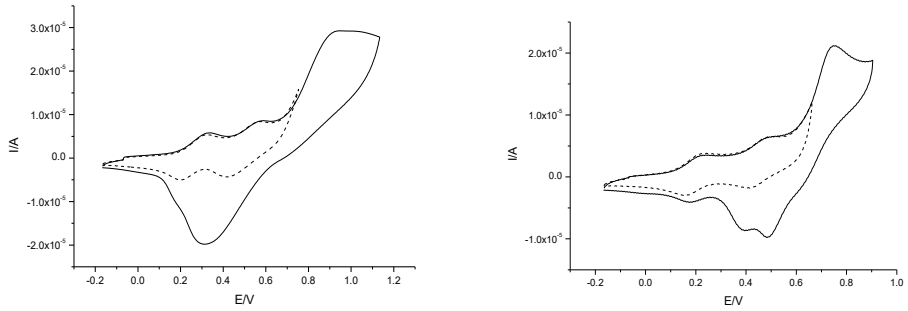

Figure 251. Cyclic Voltammetry (cathodic window) of compounds **SA17** (rigth) and **SA18** (left) (referred to Fc/Fc^{+})